DEVELOPMENT AND APPLICATION OF CORRELATIVE STED AND AFM TO INVESTIGATE NEURONAL CELLS

NATHAN CURRY

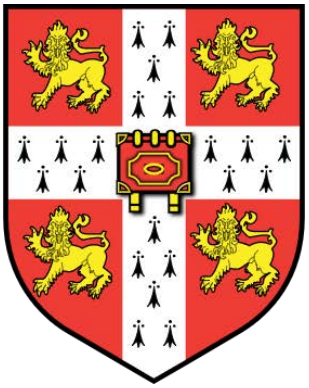

Supervisor – Professor Clemens Kaminski

This dissertation is submitted for the degree of Doctor of Philosophy

Department of Chemical Engineering and Biotechnology
Laser Analytics Group
Sidney Sussex College
University of Cambridge

January 2018

Nathan Curry: *Development and application of correlative STED and AFM to investigate neuronal cells,* PhD Thesis, © January 2018
SUPERVISORS:
Professor Clemens Kaminski

DECLARATION

This dissertation is the result of my own work and includes nothing which is the outcome of work done in collaboration except as declared in the Preface and specified in the text.

It is not substantially the same as any that I have submitted, or, is being concurrently submitted for a degree or diploma or other qualification at the University of Cambridge or any other University or similar institution except as declared in the Preface and specified in the text. I further state that no substantial part of my dissertation has already been submitted, or, is being concurrently submitted for any such degree, diploma or other qualification at the University of Cambridge or any other University or similar institution except as declared in the Preface and specified in the text.

It does not exceed the prescribed word limit for the relevant Degree Committee.

Sidney Sussex College, January 2018

Nathan Curry

Nathan Curry: *Development and application of correlative STED and AFM to investigate neuronal cells*, PhD Thesis © January 2018
SUPERVISORS:
Professor Clemens Kaminski

SUMMARY

Over the past three decades in cellular neuroscience there has been a shift towards the view of the "tripartite synapse", where, astrocytes – as well as the pre-synapse and post-synapse – are involved in synaptic signalling. The migration of astrocytes to form branched networks in the brain is, therefore, of great interest in understanding brain development and neuronal function.

Migration is a complex interplay between cytoskeletal reorganisation and cell mechanical stiffness. In order to improve understanding of this process, correlative measurements of cytoskeletal organisation and mechanical stiffness are required. To investigate astrocyte migration a technique combining atomic force microscopy (AFM) with stimulated emission depletion (STED) microscopy was developed.

First a custom STED microscope was developed. To facilitate the design of this system the theoretical performance of a range of STED techniques (cw-STED, time-gated STED, pulsed STED and RESOLFT) were compared, identifying that pulsed STED theoretically has the highest photon efficiency. A pulsed STED microscope, which uses adaptive optics, was then designed, developed and characterised. The microscope was found to achieve resolutions below 50 nm.

The STED microscope was combined with a commercial AFM to study live cells. Using the recently developed SiR-actin and SiR-tubulin dyes and AFM probes optimised for live cell mechanical property studies, images of the actin and tubulin cytoskeleton were correlated with AFM topography and mechanical stiffness measurements. It was found that, in astrocytes, actin contributes significantly both to astrocyte stiffness and topography. Investigations of migrating cells showed differences in actin organisation and mechanical stiffness between the basis and leading edge of migration. A further study was performed, investigating the effects of the gap-junction protein connexin30, which is expressed during the early stages of brain development, on migration. This protein was found to inhibit the actin reorganisation and mechanical stiffness changes observed in basal conditions.

Overall the combination of mechanosensitive AFM measurements with advanced microscopy, such as super-resolution, on live cells is a promising approach which will enable a range of investigations, for instance when studying cell structural remodeling during brain development or tumorigenesis.

Nathan Curry: *Development and application of correlative STED and AFM to investigate neuronal cells,* PhD Thesis

PUBLICATIONS

PUBLISHED

- **Curry N**, Ghézali G, Kaminski Schierle G, Rouach N, Kaminski CF, "Correlative STED and atomic force microscopy on live astrocytes reveals plasticity of cytoskeletal structure and membrane physical properties during polarized migration", *Front. Cell. Neurosci.* (2017), **11** (104)
- Lautenschläger J, Stephens A, Fusco G, Ströhl F, **Curry N**, Zacharopoulou M, Michel C, Laine R, Nespovitaya N, Fantham M, Pinotsi D, Zago W, Fraser P, Tandon A, George-Hyslop P, Rees E, Phillips J, De Simone A, Kaminski CF, Kaminski Schierle GS, "C-terminal calcium binding of α-synuclein modulates synaptic vesicle interaction", *Nature Communications* (2018), 9:712

SUBMITTED

- Ghézali G, Vasile F, **Curry N**, Fantham M, Ezan P, Cohen-Salmon M, Kaminskie CF, Rouach N, "Neuronal activity drives astroglial connexin 30 in perisynaptic processes and shapes its functions" *eLife*

IN PREPARATION

- Ghézali G, **Curry N**, Vasile F, Kaminski CF, Rouach N, "Connexin 30 controls actin cytoskeleton and membrane physical properties during polarized migration"

CONFERENCE PROCEEDINGS

- **Curry N**, Ghézali G, Kaminski Schierle G, Rouach N, Kaminski CF, "Live-cell STED/AFM correlates cytoskeletal structure and cell physical properties," *Frontiers in Optics OSA Technical Digest*, Optical Society of America, (2016), paper FF2A.1
- Mahou P, **Curry N**, Pinotsi D, Kaminski-Schierle GS, Kaminski CF, "Stimulated emission depletion microscopy to study amyloid fibril formation", *SPIE NanoScience+ Engineering*, VIII, 93310U

ACKNOWLEDGMENTS

I would like to start by thanking Clemens Kaminski for his support and guidance throughout my PhD. His enthusiasm, ideas and encouragement were all of incredible importance in bringing this thesis together.

My PhD also received significant support from two outstanding French researchers. First Pierre Mahou who led the design of the STED microscope, trained me in best practice in optics and ensured that I was asking the right questions. Importantly he impressed on me the importance of good characterisation of systems and knowing when things are good enough, two of the most important skills in research. He also encouraged me to be prepared to "shake a few trees" to ensure I was getting what I needed from other people, an invaluable skill. A final crucial role of Pierre was to force me to sit down and write. Preparing my thesis was made significantly easier by the time he encouraged me to invest preparing my first year report and similar.

The second French supervisor arrived shortly after Pierre left. Nathalie Rouach injected new life into the STED projects bringing with her challenging research questions and being prepared to take the time to adapt her work to the systems she was working with. Although intense the time spent working with Nathalie was consistently highly productive.

I was also lucky enough to receive significant supervision from many other PIs in the department. Particularly Gabriele Kaminski Schierle who took a huge amount of time to improve my understanding and skills in the biology aspects of my thesis and Eric Rees who was a source of good advice, good humour and interesting discussions.

Outside of the main projects presented here I was also lucky enough to receive a huge amount of advice, training and insight from France again. With Claire Michel and Romain Laine providing a huge amount of advice on becoming a better researcher. I have kept throughout my time in the lab an e-mail from Claire about one of my presentations of which I remain very proud to have received.

I would like to thank the entire LAG, MNG and QI groups particularly Amberley Stephens (led synaptic vesicle work), James Manton (image processing advice), Florian Ströhl (countless fruitful discussions), Janin Lautenschäger (working with primary cells) and Oliver Vanderpoorten (rebuilding the STED). Within the department Iain and John in IT, all of the mechanical workshop and Alastair Finlayson were hugely important.

Outside of the lab, I was lucky enough to work in a teaching role with the Sensors CDT while writing up. This was a hugely challenging task in terms of dividing my time. I would therefore like to thank the CDT staff, Oliver Hadeler, Zizi Hollander and Caroline Yan-Man-Shing, for their patience and support. Oliver offered me some pearls of wisdom during writing up and Zizi was incredibly good at helping me manage my workload.

I would like to thank Sidney Sussex college (particularly the graduate tutors and MCR) for making my time outside of the lab as enjoyable as the time in the lab. And Sidney Sussex Boat Club for giving me something to enjoy a little too passionately.

I would like to thank the photonics CDT for funding me and particularly Alex Macfaden, Martin Felle, Richard Colchester and Oliver Tedder for some great times working together. As well as the Sensors CDT for keeping me busy in my final year.

Finally I would like to thank my friends and family. Scott Galliflent-Holmes for some sage advice, significant patience and encouraging me to aspire to a reasonable work-life balance. My parents, Grandma and sister for everything.

CONTENTS

1 INTRODUCTION 1
- 1.1 Introduction 1
  - 1.1.1 Aims 1
  - 1.1.2 Motivation 1
  - 1.1.3 Structure of the thesis 3

2 INTRODUCTION TO CORRELATIVE AFM AND OPTICAL MICROSCOPY 5
- 2.1 AFM and mechanical property measurements 5
  - 2.1.1 Atomic force microscopy 5
  - 2.1.2 Force–distance interaction 6
  - 2.1.3 AFM imaging modes 7
  - 2.1.4 Measuring mechanical properties by force volume imaging 10
- 2.2 Correlative AFM and optical microscopy 11
  - 2.2.1 Instrumentation for correlative AFM and optical microscopy 12
  - 2.2.2 Co-registration of AFM and optical images 13
  - 2.2.3 Applications or correlative AFM and optical microscopy 14
  - 2.2.4 Correlative AFM and optical microscopy to study live and fixed cells 14
  - 2.2.5 Correlative AFM and optical super-resolution microscopy 15

3 INTRODUCTION TO STED AND RESOLFT MICROSCOPY 17
- 3.1 Introduction 17
  - 3.1.1 Fluorescence microscopy 17
  - 3.1.2 Confocal laser scanning microscopy 18
  - 3.1.3 Resolution enhancement by STED and RESOLFT 19
  - 3.1.4 Depletion patterns in STED and RESOLFT 21
  - 3.1.5 Effects that degrade STED/RESOLFT depletion patterns 25
  - 3.1.6 Instrumentation for generating and aligning depletion patterns and correcting aberrations 27
  - 3.1.7 Fluorescence depletion 29
  - 3.1.8 Stimulated emission depletion 30
  - 3.1.9 Reversible photoswitching fluorescent proteins (used in RESOLFT) 32
  - 3.1.10 Fluorescent labelling for live cell STED and RESOLFT 33
- 3.2 Photobleaching 34
  - 3.2.1 General discussion of photobleaching 34
  - 3.2.2 Photobleaching in confocal microscopy 36

3.2.3 Photobleaching in STED 39
3.2.4 Photobleaching in RESOLFT 41
3.2.5 Photobleaching limits signal in single STED and RESOLFT images 42
3.2.6 Reducing photobleaching 44
4 THEORETICAL AND PRACTICAL COMPARISON OF STED AND RESOLFT TECHNIQUES 51
4.1 Introduction 51
4.2 Definition of key parameters related to STED and RESOLFT resolution 52
4.2.1 Excited and ground states 52
4.2.2 Suppression factor 52
4.2.3 Peak and average saturation intensity, and total saturation energy 53
4.2.4 Resolution enhancement 54
4.2.5 Photon efficiency 55
4.3 Theoretical comparison of STED modes 55
4.3.1 General principle of STED 55
4.3.2 cw-STED 55
4.3.3 cw-STED with pulsed excitation 57
4.3.4 cw-STED with time-gated detection 59
4.3.5 Pulsed STED 63
4.3.6 Time-gated pulsed STED 65
4.3.7 Summary 70
4.4 Practical comparison of STED modes 70
4.4.1 cw-STED and time-gated cw-STED 70
4.4.2 Pulsed STED 72
4.4.3 Perspectives 73
4.4.4 Conclusions 73
4.5 RESOLFT 74
4.5.1 Theoretical discussion of RESOLFT 74
4.5.2 Practical considerations in RESOLFT 79
4.5.3 Summary 80
4.6 Conclusion 81
5 DEVELOPMENT OF A PULSED STED MICROSCOPE 83
5.1 Introduction 83
5.2 STED implementation 84
5.3 Temporal coalignment of excitation and depletion beams 84
5.3.1 Effects of temporal alignment on suppression factor 84
5.3.2 Time synchronised excitation and depletion pulses through supercontinuum generation 86
5.3.3 Temporal alignment of depletion and excitation pulses 89
5.4 Temporal shaping of depletion pulses 90
5.5 Depletion beam shaping 91

5.5.1 Implementation of spatial light modulator in the depletion path 91
5.5.2 Polarisation of the depletion beam 93
5.5.3 Aberration correction and day-to-day alignment using an SLM 93
5.6 Rigorous determination of resolution 94
5.6.1 Fluorescent bead preparation protocol 94
5.6.2 Measuring resolution 95
5.7 Conclusions 95
6 CORRELATIVE STED AFM ON MIGRATING ASTROCYTES 99
6.1 Introduction 99
6.2 Protocol for STED–AFM imaging on live astrocytes in culture 100
6.2.1 STED imaging of live cells 100
6.2.2 STED and AFM coregistration and coalignment 101
6.2.3 AFM probes and force calibration 102
6.2.4 AFM imaging 103
6.2.5 Calculation of cell Young's modulus 103
6.3 Correlative STED–AFM investigation of astrocyte cultures in basal conditions 104
6.3.1 Sample preparation 104
6.3.2 Live cell STED-AFM imaging of cytoskeletal proteins 104
6.3.3 Contribution of actin to cell topography 106
6.3.4 Contribution of tubulin to cell topography 107
6.3.5 Measurement of astrocyte stiffness 107
6.3.6 Contribution of actin to cell stiffness 107
6.3.7 Contribution of tubulin to astrocyte stiffness 111
6.3.8 Discussion 111
6.4 STED-AFM on migrating astrocytes 113
6.4.1 Scratch-induced migration assay 113
6.4.2 Cytoskeletal reogranisation during polarised migration 113
6.4.3 Subcellular changes in membrane stiffness in migrating astrocytes 113
6.4.4 Discussion 115
6.5 Connexin30, the cytoskeleton and cell mechanical properties 116
6.5.1 Introduction 116
6.5.2 Actin cytoskeleton organisation of migrating CX30 astrocytes 116
6.5.3 Stiffness changes in migrating Cx30-expressing astrocytes 117
6.5.4 Conclusions 122
7 APPLICATION OF STED TO *in vitro* AND FIXED TISSUE IMAGING 125

7.1 Introduction 125
7.2 STED imaging of amyloid fibrils *in vitro* 125
7.2.1 Introduction 125
7.2.2 Methods 126
7.2.3 Results and discussion 127
7.2.4 Conclusions 127
7.3 Sub-cellular location of connexin30 in fixed tissue 129
7.3.1 Introduction 129
7.3.2 Methods 130
7.3.3 Results and discussion 131
7.3.4 Conclusions 131
8 CONCLUSIONS AND OUTLOOK 135
8.1 Conclusion 135
8.1.1 Theoretical performance of STED and RESOLFT techniques 135
8.1.2 Development and characterisation of STED microscope 136
8.1.3 Development and application of correlative live-cell STED/AFM 138
8.2 Outlook 139
8.2.1 STED imaging in live cells 139
8.2.2 Two-colour imaging 140
8.2.3 Correlative FLIM and AFM 142

BIBLIOGRAPHY 143

LIST OF FIGURES

Figure 1 AFM approach and imaging. 6
Figure 2 Theoretical plot of a force–distance curve in AFM. 7
Figure 3 Theoretical plot of a force–distance curve used in force–volume imaging. 9
Figure 4 Schematic of a combined AFM and opitcal microscope. 12
Figure 5 Generalised schematic of optical and AFM coalignment. 14
Figure 6 Simple Jablonski diagram of fluorescence. 18
Figure 7 Excitation and emission spectra of ATTO 647N dye and common excitation and emission filters. 19
Figure 8 Schematic of a confocal microscope. 20
Figure 9 Principle of STED- and RESOLFT-type microscopies. 21
Figure 10 Diffraction-unlimited resolution in STED and RESOLFT. 22
Figure 11 Phase mask and intensity distributions for 1D resolution enhancement in STED. 23
Figure 12 Phase mask and intensity distributions for simple 2D resolution enhancement in STED. 24
Figure 13 Phase mask and intensity distributions for isotropic 2D resolution enhancement in STED. 24
Figure 14 Phase mask and intensity distributions for axial resolution enhancement in STED. 25
Figure 15 Schematic of the incorporation of a phase mask (or transmission SLM) in a STED or RESOLFT microscope. 28
Figure 16 A birefringent phase mask which produces a vortex beam for the depletion beam and gaussian beam for the excitation beam simplifies alignment. 28
Figure 17 Schematic of STED with dual adaptive elements. 29
Figure 18 The process of stimulated emission. 30
Figure 19 Excitation and depletion wavelengths used in STED microscopy of ATTO 647N dye. 31
Figure 20 Jablonski diagram of stimulated emission depletion. 31
Figure 21 Transitions in RESOLFT microscopy. 32
Figure 22 RESOLFT imaging. 33

Figure 23 Jablonski diagram showing photobleaching in confocal microscopy. 35
Figure 24 Photobleaching in confocal microscopy 38
Figure 25 Jablonski diagram showing photobleaching in STED microscopy. 39
Figure 26 Photobleaching in STED microscopy. 40
Figure 27 Increase in the rate of photobleaching in STED. 41
Figure 28 Fluorophores not at the depletion minimum undergo photobleaching before they are imaged. 43
Figure 29 Spatial profile of photobleaching rate in STED. 43
Figure 30 Photobleaching in MINFIELD STED [79]. 49
Figure 31 Stimulated emission depletion in fluorescence microscopy. 53
Figure 32 Suppression factor in STED or RESOLFT microscopy. 54
Figure 33 Temporal control in continuous wave STED. 56
Figure 34 CW STED with pulsed excitation. 58
Figure 35 Photon arrival times in cw-STED with pulsed excitation. 59
Figure 36 cw-STED with time-gated detection. 59
Figure 37 Resolution in time-gated cw-STED. 60
Figure 38 Saturation intensity reduction in time-gated cw-STED. 62
Figure 39 Photon efficiency optimisation in time-gated cw-STED. 62
Figure 40 Temporal control in pulsed STED. 63
Figure 41 Effect of depletion pulse duration on STED resolution. 67
Figure 42 Time-gated pulsed STED. 68
Figure 43 Saturation intensity reduction in time-gated pulsed STED. 69
Figure 44 Time-gated pulsed-STED is less photon-efficient than pulsed-STED. 69
Figure 45 Saturation intensity in RESOLFT microscopy. 76
Figure 46 Photon efficiency in RESOLFT, including depletion photons only. 77
Figure 47 Photon efficiency in RESOLFT, including depletion and readout photons. 78
Figure 48 Schematic of STED system. 85
Figure 49 Effect of temporal alignment on decay curves in pulsed STED. 86
Figure 50 Typical 2D plots of super-continuum spectrum as a function of wavelength. 88
Figure 51 Supercontinuum generated at 780 nm. 89

Figure 52 Fluorescence suppression as a function of depletion arrival time. 90
Figure 53 Spectral broadening of a 780 nm depletion pulse as it propagates through a PM-SMF. 92
Figure 54 Aberration corrected vortex beam. 94
Figure 55 Resolution characterisation of the STED microscope. 96
Figure 56 Correlative STED-AFM experimental set up. 101
Figure 57 Example measured force curve. 103
Figure 58 Confocal and STED images of actin cytoskeleton. 105
Figure 59 AFM force and height images of astrocytes. 106
Figure 60 Colocalisation of AFM topography and STED images. 106
Figure 61 Colocalisation of AFM topography and STED images of actin. 108
Figure 62 AFM topography does not correlate with STED images of tubulin. 109
Figure 63 Effects of transfection on astrocyte stiffness. 110
Figure 64 STED and AFM images of astrocytes treated with cytochalasin D. 110
Figure 65 Effects of depolymerising actin on cell stiffness. 111
Figure 66 STED and AFM images of astrocytes treated with nocodazole. 112
Figure 67 Effects of depolymerising tubulin on cell stiffness. 112
Figure 68 Actin reorganisation during polarised migration. 114
Figure 69 Tubulin reorganisation during polarised migration. 114
Figure 70 Reorganisation of astrocyte stiffness during polarised migration. 115
Figure 71 Actin structure in the basis of control migrating astrocyte. 118
Figure 72 Actin structure in the basis of connexin30 expressing migrating astrocyte. 119
Figure 73 Actin structure in leading edge of control migrating astrocyte. 120
Figure 74 Actin structure in leading edge of connexin30-expressing migrating astrocyte. 121
Figure 75 Reorganisation of astrocyte stiffness during polarised migration 122
Figure 76 Stiffness is not changed by expression of connexin 30 in basal conditions. 123

Figure 77 STED super-resolution imaging of α-synuclein fibrils. 128
Figure 78 STED image showing Cx30 is found in PAPs. 132
Figure 79 Design for two-colour STED. 141

LIST OF TABLES

Table 1 Approximate values for parameters related to photobleaching for a hypothetical fluorophore. 37
Table 2 Typical values of parameters affecting resolution in STED. 57
Table 3 Summary of supression factors and saturation intensities in different STED modes. 71
Table 4 Typical values of parameters effecting resolution in RESOLFT. 77

1 INTRODUCTION

1.1 INTRODUCTION

1.1.1 *Aims*

In this thesis, the contribution of the actin and tubulin cytoskeletal elements to the process of astrocyte polarised migration was investigated. In particular, the combined changes in the mechanical stiffness of migrating astroglial cells through the combination of atomic force microscopy (AFM, stiffness measurements) and stimulated emission depletion (STED) super-resolution imaging (cytoskeletal imaging) was studied. To achieve this, a custom STED microscope was developed for live cell imaging and combined with a commercial AFM.

1.1.2 *Motivation*

The brain is comprised of two main cell types, neurons and glial cells. Although glia are at least as numerous in the human brain as neurons [1, 2], historically neurons have been considered to be the main functional element in the brain. Glia were thought to be mainly structural and supportive elements [3].

Over the past three decades there has been a shift in this view as glial cells were found to express neurotransmitter receptors and respond to glutamate exposure. In particular, astroglia (commonly referred to as astrocytes), the most abundant cell type in the central nervous system (CNS), have been found to regulate ionic homeostasis, to regulate neurotransmitter levels in the extracellular space, and to release neuroactive molecules [3]. These findings led to the proposal of the "tripartite synapse", where, astrocytes – as well as the pre-synapse and post-synapse – are involved in synaptic physiology, processing synaptic information and regulating synaptic transmission [4].

The astrocyte sub-compartment that contributes to a single synapse is referred to as a perisynaptic astroglial process (PAP). Just as changes in the morphology of the post-synapse (dendritic spines) correspond to function [5], the morphology of PAPs has been found to regulate synaptic strength [6].

On a larger scale, the migration of whole astrocytes to their final destination in the CNS, the formation of multiple branches in mature astrocytes, and the formation of PAPs are important in brain development and neuronal function [7].

Cell motility and changes of shape can be driven by the cytoskeletal elements (actin and tubulin) [8] as well as cell mechanical stiffness [9], and are likely a complex interplay between both. Correlative measurements of cytoskeletal organisation and the modulus of the astrocytes will allow a greater insight into the migration process.

This requires the combination of a mechanosensitive imaging technique with an imaging method that can specifically identify the cytoskeletal elements in cells. Mechanical property measurements should be on live, intact, cells to minimise perturbations of these properties due to the fixing process. Individual cell mechanical properties can be measured using a range of methods including optical tweezers [10] and AFM [11]. AFM is well adapted to measuring the mechanical properties of attached cells [12] and can be used to target subregions of cells, but cannot be used to specifically identify sub-cellular elements such as actin or tubulin.

Fluorescence microscopy, on the other hand, is well adapted to specifically identifying proteins in cells but does not typically provide mechanical information. Fluorescence techniques can be combined with AFM to enable specific chemical identification, or sub-cellular imaging, and mechanical property measurements on the same cells [11]. Combined AFM and confocal microscopy have been used to correlate images of specifically labelled actin with cell topography [13]; however, it was found in this study that the resolution in confocal microscopy was insufficient to resolve small, dense bundles of actin filaments.

Optical super-resolution microscopy is able to resolve the cytoskeletal network [14], but there have been limited reports of combination with AFM, particularly for live cell imaging [15–18].

The previously developed scratch assay, which allows the study of the migration of cultured astrocytes [19] is combined with the imaging system developed in this work and used to investigate the effects of the gap-junction protein connexin30, which is expressed in mice from postnatal day 16 and is thought to be involved in synaptic pruning and synaptogenesis, on astrocyte mechanical properties and cytoskeletal organisation during migration. Notably, connexin30 has recently been found both to reduce astrocyte migration [20] – likely during late stages of brain development – and to regulate synaptic function in the adult brain [6]. Connexin30 also colocalises with the actin cytoskeleton [21].

In astrocyte cultures synaptic connections do not form, therefore to investigate the full effects of connexin30 it will be necessary to image in tissue slices. Although the focus will be on live cell imaging in culture, this must be considered as part of the microscope design.

In the context of this work, the AFM should be combined with a technique that has high resolution and is live cell compatible. It is also preferred that the system be compatible with imaging tissue cultures.

Stimulated emission depletion [22] is a super-resolution microscopy approach that can can achieve resolutions below 50 nm [23]. As a confocal-like technique, STED is well adapted to imaging in thick samples, such as tissue cultures. This technique also has relatively fast imaging times and is not significantly affected by the motion of live cells during acquisition.

There have been previous reports of STED microscopy combined with AFM; however, these have generally been limited to proof of concept work [17, 24–26], *in vitro* studies [27, 28] or fixed cell studies [17, 24]. This is due to a combination of the challenges associated with live cell AFM imaging (due to long acquisition times and the stiffness of probes [29]) and live cell STED imaging (due to limited live cell compatible dyes with good photophysical properties for STED, as well as the high intensities and photon doses required for high resolution STED). Furthermore, it has only been in the past 3–4 years that a wide range of commercial STED microscopes have become available – particularly the high resolution pulsed STED variant.

This work combines recent advances in AFM techniques and probe technologies with recently developed STED dyes for live cell imaging [30–33] to enable investigations of migrating astrocytes. To ensure the highest resolution and full flexibility a custom microscope system is developed based around the pulsed STED principle.

1.1.3 *Structure of the thesis*

As a commercial AFM system is used to the measurement of cell mechanical properties in this work, AFM technology will be introduced in the following chapter. First an introduction to the operating principle of AFM is presented focusing on the measurement of mechanical properties. In particular, the challenges associated with live cell AFM imaging are discussed. This is followed by an overview of correlative AFM and optical microscopy focusing on some of the opportunities and operational challenges associated with this. A particular focus is on the current state of the art in correlative AFM on live cells and also combinations with super-resolution microscopy.

Another key focus is the development of a high resolution STED microscope for live-cell imaging and combination with AFM. In order to do this an understanding of the physical principle of STED, as well as the key limitation of STED resolution and applications. Chapter 3 presents an introduction to STED and, the similar, RESOLFT technique. Challenges such as the optimisation of the spatial shape of the beams and photobleaching are treated in detail.

Building upon this, a range of STED modalities [34–37] as well as the similar RESOLFT (or reversible saturable optical fluorescence transition) technique [38], are considered in detail in chapter 4. In order to select between these, a theoretical comparison of the intensity and

photon dose required for a given resolution is presented. This builds upon previous work [37, 39] by deriving an equivalent expression for RESOLFT and calculating the photon efficiency to better allow comparison accross all techniques.

From this discussion it is decided that a pulsed STED system gives a theoretically optimal performance and a pulsed STED microscope is developed and characterised in chapter 5.

Following on from the testing of the microscope it is combined with an AFM and live cell stiffness measurements are performed on migrating and confluent astrocytes, which are correlated with the mechanical stiffness. In the first instance it is verified that stiffness changes in astrocytes can be measured by AFM and which cytoskeletal elements contribute to astrocyte stiffness, by using drug treatments to selectively depolymerise action and tubulin. Following on from this, the changes in mechanical properties of migrating cells are investigated. Finally, the effects of connexin30 on the cytoskeleton and mechanical stiffness in basal conditions and during migration are investigated. A key advantage of this system is that two distinct subcompartments of the same migrating cell can be individually identified and investigated.

STED microscopy was an entirely new technology to the lab and there was little experience of this technique in the lab at the start of this work. As a result of the work in this thesis a range of new research projects were made possible. Two of these are discussed in chapter 7. First it is then shown that the STED microscope can be applied both to *in vitro* studies of amyloid proteins and to performing studies on astrocytes in tissue samples by identifying the subcellular location of connexin30 in astrocytes in tissue. Finally some future modifications of the STED microscope and future work combining AFM mechanical property measurements with other advanced microscopies are proposed.

2

INTRODUCTION TO CORRELATIVE AFM AND OPTICAL MICROSCOPY

2.1 AFM AND MECHANICAL PROPERTY MEASUREMENTS

2.1.1 *Atomic force microscopy*

AFM belongs to the scanning probe microscopy family of techniques. These techniques are typically used to map the height of a sample.

In AFM the sample is imaged by scanning a nanoscale probe over the surface of the sample. The probe senses the separation between its tip and the sample by measuring the interation force (of the order pN–nN).

An AFM probe comprises a nanoscale tip mounted on a cantilever. A range of probes are available with various tip sizes and cantilever stiffness, chosen depending upon the sample and target resolution. AFM can be adapted to image stiff structures – for instance in materials science [40] – or softer biological structures [12, 41] by choosing a probe with an appropriate tip radius and cantilever stiffness. In general, cantilevers with a high spring constant are preferred for imaging samples with a high stiffness and a lower spring constant is preferred for low stiffness samples.

As the tip of the probe approaches the sample, the probe is repelled by the interaction force between the tip and the sample causing the cantilever to bend. To measure the bending of the probe, a laser is reflected off the tip of the probe onto a photodiode with four quadrants. As the cantilever bends the beam is deflected and the change in deflection is measured by the detector.

A pseudocolour image of the height of the sample, or other mechanical properties, is mapped by raster scanning the probe over the sample and measuring the interaction force. Unlike optical microscopy, AFM imaging is a near field technique and the resolution is not limited by optical diffraction. The fundamental lateral resolution of AFM is instead limited by the size of the tip and can be of the order 1 nm allowing the visualisation of the double helix of DNA [41, 42], and the structure of silicon [43, 44] and graphite [45]. Unlike other scanning probe techniques, AFM does not require a vacuum and can be performed in ambient conditions or in fluids including solvents, buffers and cell culture media [15].

2.1.2 *Force–distance interaction*

AFM imaging modes are best understood in the context of the force-distance interaction between the cantilever mounted probe and the sample. These forces are treated in detail by Cappella *et al.* [46]. A combination of attractive forces (such as van der Waals interaction) and repulsive forces (such as short range Coulombic interactions) contribute to the net force on the AFM probe. The cantilever bends as a result of these forces as shown in figure 1. A theoretical plot of the force on the probe as a function of tip–sample distance is shown in figure 2.

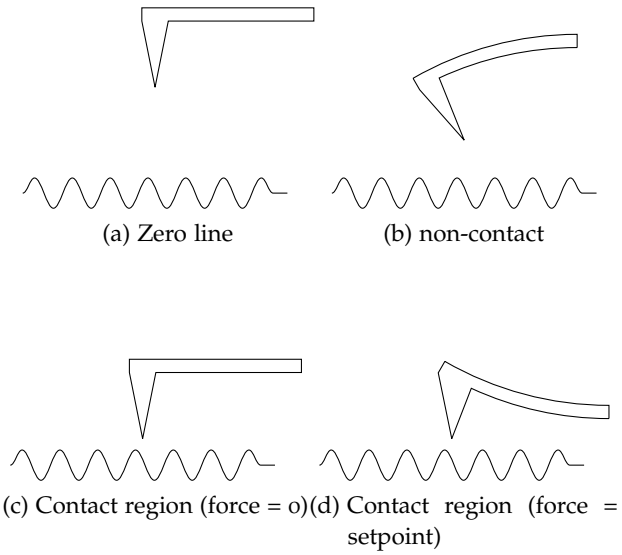

Figure 1: **AFM approach and imaging.** Solid lines represent the sample. 1a A tip far from the sample experiences a negligible force and is in a neutral position. 1b The cantilever is lowered such that the tip-sample distance decreases. The tip experiences a net attractive force towards the sample. 1c The tip is in the contact region of the sample. 1d The tip is in the contact region and experiences a net repulsive force and deflects away from the sample.

In general, when the tip–sample distances are large the interatomic forces are small between the tip and the sample. This establishes the zero line (ZL) shown in figures 1a and 2 [46, 47]. As the tip–sample distance decreases the attractive forces increase. The range in which attractive forces dominate the interaction is the non-contact region (figures 1b and 2). As the atoms in the tip and sample become closer together their electron clouds begin to repel each other electrostatically. This causes a repulsive force – reducing the net attractive force between the tip and sample. This region of the force-distance curve is the contact region [46, 47]. For small tip–sample separation, typically angstroms, the net interaction force becomes zero – this is shown in

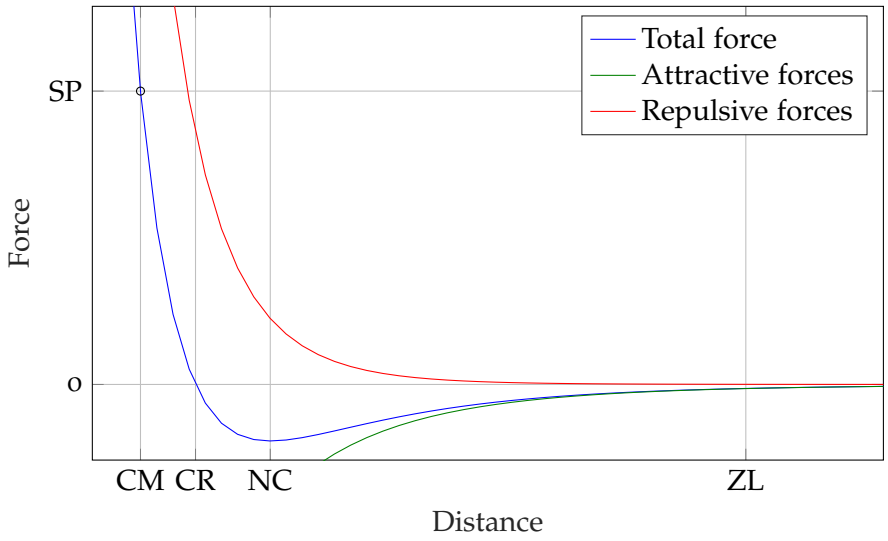

Figure 2: **Theoretical plot of a force–distance curve in AFM.** A combination of attractive and repulsive forces contribute to the force curve. The force curve can be divided into 3 main regions. The contact region (distance < CR) is where the tip is approximated as being in contact with the sample and there is a net repulsive force between the tip and sample. The non-contact region (NC < distance < ZL) contains the "jump to contact" and "jump from contact" point. The zero line (distance > ZL) is where the tip is far from the sample. A typical set point (SP) and corresponding tip–sample distance distance (CM) is shown for contact mode AFM imaging.

figure 1c and represented as CR in figure 2. The repulsive force between the samples then increases with deceasing separation.

For AFM imaging, the deflection of the probe is typically measured by reflecting a laser off the back of the probe with changes in angle detected on a four quadrant detector. AFM maps are formed by raster scanning the tip over the sample and measuring the interaction force at different positions [47]. Different methods can be used to estimate the height of the sample from the tip–sample interaction. These methods differ in which parts of the force–distance curve is used. The most common AFM modes in biological AFM are contact mode, tapping mode and peak force mode [41, 47–49] and are discussed in this section.

2.1.3 *AFM imaging modes*

Contact mode

In contact mode AFM [50] the probe is within the contact region of the force–distance curve. The probe experiences a repulsive force from the sample which is detected as a cantilever deflection. The height of the sample is mapped by raster scanning the sample with respect to the probe and measuring the interaction force between the tip and the

sample or – more commonly – the height of the probe necessary to maintain a constant force. In constant force scanning mode a z-piezo is used to adjust the sample height to maintain a constant force. The change in height required to maintain this force is the height for each AFM pixel [47].

Although this mode has been used for imaging both amyloid fibrils [51] or proteins on cell membranes [52] a major challenge in contact mode AFM is the relatively high force exerted by the probe on the sample, which may deform samples [47, 53]. In particular shear forces between the tip and sample may push or pull the sample during scanning leading to the sample being moved or deformed. The sample may also be compressed due the high forces used during imaging [41, 47]

Tapping mode

Tapping mode reduces the shear forces on the probe and sample by minimising the tip–sample contact time. In tapping mode the cantilever is oscillated at close to its resonant frequency, with a typical amplitude of 20–100 nm [47]. During scanning the tip–sample distance oscillates between the contact region and the zero line at a frequency of 50–50 kHz. The amplitude of the tip oscillation is measured using the four quadrant detector. As the tip–sample distance oscillates the tip has intermittent contact with the sample. Energy is lost from the oscillation due to this contact leading to a reduction in the amplitude of oscillation. The amplitude of oscillations is related to the average tip–sample distance. Similar to contact mode, the sample is raster scanned and the change in height required to maintain a constant amplitude is recorded and represented as a topographical map of the sample.

In neuroscience this mode has been used to categorise different morphologic structures of amyloid fibrils into twisted ribbons, helical ribbons, and nanotubes and to measure their periodicity [54]. In the context of cell studies tapping mode with small cantilevers (corresponding to faster force feedback [55] has been used to image bactrial organelles [56].

In tapping mode the probe oscillates between the zero line and contact region and therefore experiences a range of different force responses from the sample. However, only the average response is measured as a change in oscillation amplitude. Whilst the average force allows the sample height to be measured with high resolution and low average forces, this imaging mode does not allow other information about the sample, related to the force curve, to be measured [48, 49].

Force–volume imaging

In force volume imaging the entire force–distance curve is measured by gradually approaching the sample with the tip and measuring the cantilever deflection at each step [57]. Although the original implementations of this imaging mode were relatively slow (approximately 10 force curves per second) [57], recent developments in the field, such as peak force quantitative nanomechanics from Bruker [48], have increased the imaging speed to up to 1000 force curves per second. Forces are typically measured both during approach and retraction. An example force–distance curve is shown in figure 3.

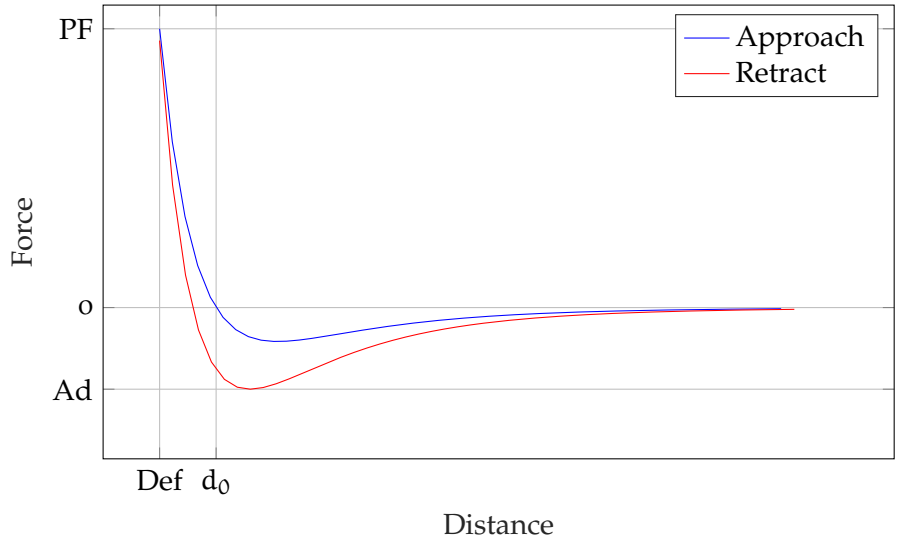

Figure 3: **Theoretical plot of a force–distance curve used in force–volume imaging.** Approach and retract curves used in force–volume imaging. The probe approaches the sample until the interaction force is equal to the user-defined peak force (PF). Mechanical properties can be calculated from this such as the Young's modulus which is equivalent to the gradient of the curve in the contact region (distance < d_0). The adhesion force, between the tip and the sample, can be calculated from the difference between the minimum force of the retract curve and the zero line. The deformation of the sample – how much the tip indents the sample – is the distance between the start of the contact region (d_0, force = 0) and the distance at the peak force (Def).

Fitting this curve allows mechanical properties – including adhesion, Young's modulus and the deformation of the sample – to be calculated. A further advantage of force–volume imaging is that it allows precise force control and automated feedback, such that forces can be minimised on the sample in high resolution AFM imaging of DNA [41, 42] or imaging of soft structures such as microvilli on live cells [29].

In this thesis, a key aim is the measurement of mechanical properties of live cells. Force–volume imaging is the AFM imaging mode

that allows this and is discussed in more detail in the following section.

2.1.4 *Measuring mechanical properties by force volume imaging*

Deformation

The deformation parameter is the extent to which the sample changes shape during interaction with the cantilver. It is measured based on the approach curve and is the difference between the tip–sample distance where the interaction force is 0 (d_0) and the tip–sample distance where the force is at the setpoint value (SP). The set-point is defined by the user, therefore this parameter changes based upon user settings. The measured deformation includes both plastic and elastic deformations.

For high resolution AFM topography imaging a minimal deformation is preferred as this reduces sample damage; therefore, lower peak force setpoints are typically used in high resolution AFM imaging [41, 42]. In order to measure the mechanical properties by AFM, some deformation is required. The peak force set points must be sufficiently high to deform the sample; however, excessive deformations can lead to artifacts in mechanical property measurements because either the tip can no longer be approximated as conical or spherical, or the substrate contributes to the mechanical property image [57, 58].

Adhesion

The adhesion force is the minimum force in the retraction curve and corresponds to the attractive force between the probe and the sample [57]. This can arise due to any attractive force between the tip and the sample. Adhesion is of particular interest when using tips functionalised to interact with the sample. Ganchev *et al.* [59] used gold coated AFM tips to identify Cys residues corresponding to where β-sheet of an amyloid protein core starts. In live–cell studies, functionalised tips have been used to locate and quanitfy virus binding sites [12].

Young's modulus

The Young's modulus, or sample stiffness, can be estimated from the measured force curve by fitting the approach or retract curve in the contact region ($d < d_0$). This corresponds to the mechanical stiffness that is investigated in this study. A range of models can be used to estimate the modulus, a simple example is the Derjaguin-Muller-Toporov (DMT) model where a spherical tip of radius R and low deformation (less than the tip diameter) are assumed [60]

$$F - F_{adh} = \frac{4}{3} E^* \sqrt{R(d - d_0)^3}, \tag{1}$$

where F_{adh} is the adhesion force between the tip and sample. The constant of proportionality E^* is the reduced modulus given by [58]

$$\frac{1}{E^*} = \frac{1-{\nu_P}^2}{E_P} + \frac{1-{\nu_S}^2}{E_S}, \tag{2}$$

where $E_{P,S}$ is the modulus of the tip and the sample, respectively, and $\nu_{P,S}$ is the Poisson ratio of the tip and the sample, respectively. It is generally assumed in AFM modulus measurements that the tip is much stiffer than the sample ($E_P \gg E_S$) and undergoes negligible deformation such that

$$E_S \simeq (1-\nu_P)E_P. \tag{3}$$

E_S is therefore estimated by fitting an appropriate force distance equation (such as equation 1) to measured force–distance curves. The DMT model discussed above is one example of models used to estimate mechanical properties from nanoindentations. Other models, such as the Hertz modulus, developed by Sneddon [61], can be used to estimate the modulus in the case of conical tips or large indentations [62].

Stiffness measurements of live cells are becoming of increasing importance. In particular AFM has been used to differentiate between normal and cancerous cells [63] and to correlate actin cytoskeleton density and strucure with mechanical stiffness in cancer and normal cells in basal conditions [64, 65]. The work presented in this thesis goes these reports by allowing AFM imaging to be correlated with super-resolution microscopy images.

2.2 CORRELATIVE AFM AND OPTICAL MICROSCOPY

AFM is a higher resolution technique than most optical microscopy techniques and, using force–volume measurements, allows measurements of sample stiffness and adhesion, which cannot be measured optically. AFM can be complemented by optical microscopy in many ways. This can include using the faster imaging speed of an optical microscope to quickly screen a sample and select regions of interest for high resolution AFM imaging [15, 66] or combining chemical identification – from fluorescent labelling of the sample – with high resolution AFM imaging to correlate structure with chemical species [67]. Correlating AFM with fluorescent labelling is particularly advantageous in live cell studies where cells which have been treated (for instance genetically encoded with a fluorescent protein) can be identified against a non-transfected population. This has been used in studies of changes in cells upon viral transduction [12]

In this section, the instrumentation for correlative AFM and optical microscopy is discussed. In particular the modifications required to both an AFM and optical microscope for imaging to be performed on the same platform and the calibration of both techniques so that images can be directly combined.

2.2.1 *Instrumentation for correlative AFM and optical microscopy*

Although it is possible to image a sample from above the AFM probe, this is typically limited to long working distance, low numerical aperture imaging systems. To incorporate AFM with an optical microscope it is usually preferred to use an inverted optical microscope and image from below the sample. Commercial AFMs have been designed that can be mounted directly on an inverted optical microscope, in place of the translation stage, as in figure 4.

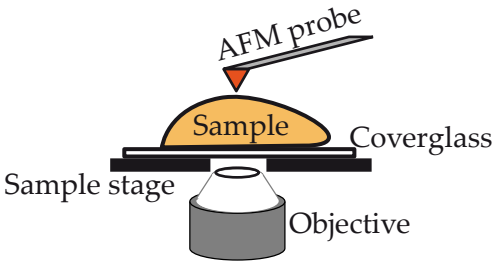

Figure 4: **Schematic of a combined AFM and opitcal microscope.** AFM can be added to an inverted optical microscope in place of the translation stage. Generally a stiff stage is preferred for AFM but a hole is necessary to allow access for the objective, reducing the support for the sample. Optical microscopy also requires the sample to be mounted on transparent coverglass, which has a greater roughness than common AFM substrates such as mica.

For high resolution AFM imaging mica is generally used as a flat substrate. Mica has poor optical properties as it has a low transmission and high birefringence and cannot usually be combined with optical imaging as the sample must be mounted on a transparent substrate, typically coverglass. Coverglass has a greater roughness (0.5 nm) than mica (0.05 nm) [68] or other common AFM substrates. This leads to an increased noise on height measurements in AFM. To correlate optical images with high height precision AFM images some groups use coverslips with a thin layer of mica glued to them [68–70]. The work presented in this thesis uses AFM imaging on cells, which are rough relative to glass, so this is not required for this work.

AFM is generally performed on a stiff surface to minimise vertical movement of the sample during imaging. However, for optical imaging from below, sample stage must have a hole to allow access for the objective, as in figure 4. To minimise vertical movement, the AFM sample holder has a smaller hole than would be used on a conventional sample holder for optical microscopy. Whilst this is beneficial in AFM imaging it limits the areas which can be imaged on the sample, meaning care must be taken during sample preparation to ensure that the sample is in the optical field of view.

A final instrumentation consideration when combining advanced optical microscopes, particularly super-resolution microscopes, is that

either the detectors or lasers used in these systems often require cooling – using built in fans. These can cause noise in the AFM images and should be decoupled from the AFM or, switched off during imaging, or water cooling should be used.

AFM and optical images can be taken simultaneously or sequentially. The choice between these two depends upon the type of AFM used and the type of experiment being performed. In both simultaneous and sequential imaging light scattering off the AFM probe may contribute to noise. In sequential imaging, it is usually best to withdraw the tip from the sample and turn off the AFM laser to minimise noise from the AFM.

During simultaneous AFM and fluorescence microscopy imaging, near-field interactions between the tip and the fluorophore (including tip-enhanced fluorescence or tip-induced quenching) [15, 71] may change the the signal. In some studies tip–fluorophore interactions are used to allow near-field fluorescence imaging [71].

2.2.2 *Co-registration of AFM and optical images*

Regardless of whether AFM and optical image are acquired simultaneously or sequentially optical images will usually have different pixel size and orientation to AFM images. The scale in these images may also differ due to different calibrations. These are represented in figure 5. To allow images to be overlaid a transformation must be defined between the optical and AFM images. Usually this is performed within the AFM software. The tip or the sample is moved to three (or more) known positions, by the software, and an optical image is taken in each position. The difference between the position of the tip (or a feature of the sample) is used to estimate the transformation between the AFM and optical images.

The number of points used to define the transform limits the correction. Three points allow a rotation and rescale of the pixels in both lateral dimensions. This assumes that only a linear transform is required. More points are required to account for field curvature [25]. Measuring this transform is referred to as coregistration throughout this thesis. This transformation ensure the pixel size and orientation of AFM and optical images is calibrated. It does not coalign the AFM and optical images in space.

Coalignment can be achieved in imaging software by translating the optical image with respect to the AFM image such that common features to both images are coaligned. The features can either be intrinsic contrast in both images or a fiduciary marker that is present in both images.

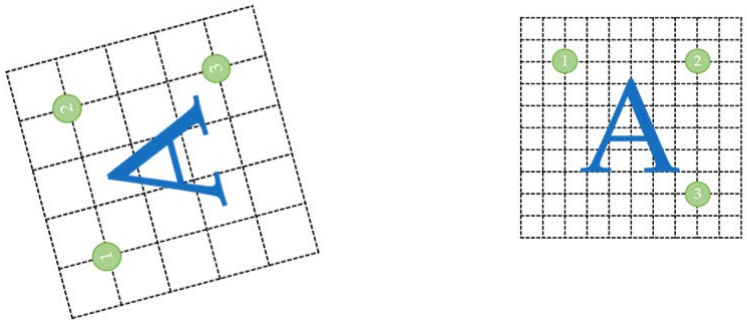

(a) STED image (b) AFM image

Figure 5: **Generalised schematic of optical and AFM coalignment.** The optical image has different orientation and pixel size to the AFM. To allow these images to be overlaid, a transform must be identified. The AFM software moves the sample (or tip) to three known positions (1, 2, 3) and optical images are taken. The change in the position of the sample (or tip) in the optical image is used to estimate the transformation.

2.2.3 *Applications or correlative AFM and optical microscopy*

Upon the design and implementation of a correlative optical and AFM imaging system a range of new applications are enabled [15]. Of particular relevance to this thesis is imaging of live cells and AFM combined with optical super-resolution. Developments in these fields are discussed in this section.

2.2.4 *Correlative AFM and optical microscopy to study live and fixed cells*

An early example of correlative imaging investigated actin focal adhesions with optics and AFM [72]. Optical contrast, from confocal microscopy, was used to identify actin and paxillin and AFM was used to image in high resolution. In this study, the cells were deroofed [73] to provide the AFM access to the cytoskeletal structure within the cell. The AFM provided structural detail about the cytoskeleton which was not accessible with an optical approach and allowed the quantification of the widths of actin filaments.

A recent example of correlative live-cell imaging that is relevant to this thesis includes mechanical property measurements on live cells that had been genetically modified to express viral binding sites, co-expressed with fluorescent proteins [12]. Optical images identified cells expressing a virus receptor and AFM probes, functionalised with a virus, were used to perform adhesion measurements to identify binding sites. Although the optical microscopy technique used in this work is relatively simple it used a novel sample chamber to improve

live cell imaging. A heated stage was used to maintain cells at 37 °C. Unlike previous work a chamber with a sliding glass ceiling, with access for the AFM probe, was used. This allowed carbon dioxide to be added to the air above the sample maintaining the correct environment for the cells. Evaporation of cell culture medium was also minimised by the presence of this ceiling. Both of these improvements allowed longer term live cell imaging.

An example that required more advanced optical imaging was correlating the actin cytoskeletal structure through confocal imaging of labelled actin with topography images from AFM [13]. These images revealed a good correlation between actin and the cell topography but, interestingly, not all filaments observed in the AFM images could be observed in the optical image. The authors hypothesised that this was because the smaller, dense, filament networks were below the optical diffraction limit so could not be observed. This suggested a need for optical super-resolution to be correlated with AFM in investigations of the actin cytoskeleton.

2.2.5 *Correlative AFM and optical super-resolution microscopy*

AFM has previously been correlated with the super-resolution techniques STED [17, 24–26], *d*STORM (direct stochastic optical reconstruction microscopy) [18, 27, 28, 70] and PALM (Photoactivated localization microscopy) [18]. Each of these combinations have been used for correlative imaging on either fixed or live cells.

In the first reported example of correlative STED and AFM, Harke *et al.* [24] demonstrate correlative STED and AFM on fluorescent beads and on fixed COS7 cells where tubulin was fluorescently labelled. Subsequently it was shown, by the same research group [17], that both STED and *d*STORM could be combined with AFM on fixed cells. Both studies act as proof-of-concept work, demonstrating that super-resolution cytoskeleton images can be combined with height and stiffness measurements on fixed cells.

Building upon this AFM was used by Chacko *et al.* [25, 26] for nanomanipulation of fluorescent beads and fixed cells. In these experiments STED imaging was used as a reporter of responses to mechanical stimuli.

Live cell STED imaging is limited by the availability of STED dyes which are compatible with live cell imaging. Recent advances in STED labelling have led to organic dyes that are membrane permeable and compatible with live cells [30–33]. Outside of the study presented in this thesis, these dyes have not been reported in examples of correlative STED and AFM, although Abberior Instruments have shared related experiments on their website [74]

Live cell PALM has been correlated with AFM by Odermatt *et al.* [18]. Fast AFM scans were used to investigate the cell membrane

structure. These images were correlated with PALM images showing focal adhesions. Using this technology, the authors were able to demonstrate correlative time-lapse live-cell imaging.

Each of these reports of correlative super-resolution imaging and optical microscopy on live or fixed cells have been limited to proof-of-concept studies on cell lines. One reason for this is that both super-resolution microscopy and AFM, particularly on live cells, require complex systems and significant day-to-day alignment. In the following chapters new technologies including AFM probes optimised for live cell imaging [29] and to reduce the complexity of mechanical property measurements [12], well as new live cell super-resolution dyes [30–33] are used to facilitate routine, biologically relevant, studies combining optical super-resolution and AFM.

3

INTRODUCTION TO STED AND RESOLFT MICROSCOPY

3.1 INTRODUCTION

In this chapter, the physical principles of STED and RESOLFT are introduced. To place these techniques in context, a brief introduction to confocal microscopy is provided. The increase in resolution in STED and RESOLFT, through the photoinduced saturation of non-fluorescent states [23], is then discussed. The experimental requirements for STED and RESOLFT are then explained, focussing on the generation of a spatially shaped depletion pattern and the photophysical processes exploited to deplete fluorescence.

A major challenge in STED and RESOLFT is the high photon doses required, which lead to phototoxicity and photobleaching. The process of photobleaching and how this is effected by the STED or RESOLFT process is explained. This allows some advances in STED and RESOLFT, designed to reduce [36, 38, 75–79] or mitigate [80] photobleaching to be placed in context.

3.1.1 *Fluorescence microscopy*

The photophysical process in a conventional fluorescence microscope, such as a confocal microscope, is best described by Jablonski diagrams [81]. A simplified example is shown in figure 6. This represents a typical fluorescence process in which a molecule in the ground state is transferred to the first excited state ($[S_0, V_0] \rightarrow [S_1, V_N]$, where V_N represents the vibrational energy levels of the singlet states S_M) by the absorption of a photon of energy $h\nu_{exc} = hc/\lambda_{exc}$, where h is Planck's constant, c is the speed of light and ν_{exc}, λ_{exc} are the frequency and wavelength of excitation light, respectively. The rate of excitation is proportional to the product $\sigma_{exc} I_{exc}$, where σ_{exc} is the absorption cross-section and I_{exc} is the intensity measured in photons.cm^{-2}.s^{-1}.

The fluorophore loses energy through vibrational relaxation, transferring to the lowest energy level of the excited state ($[S_1, V_0]$), then relaxes to the ground state ($S_1 \rightarrow [S_0, V_N]$) by emitting another photon of energy $h\nu_{fl}$, with wavelength λ_{fl}. The energy of the emitted photon is lower than that of the absorbed photon due to the energy loss through vibrational relaxation. This corresponds to a longer wavelength; the change in wavelength is referred to as the Stokes shift [81].

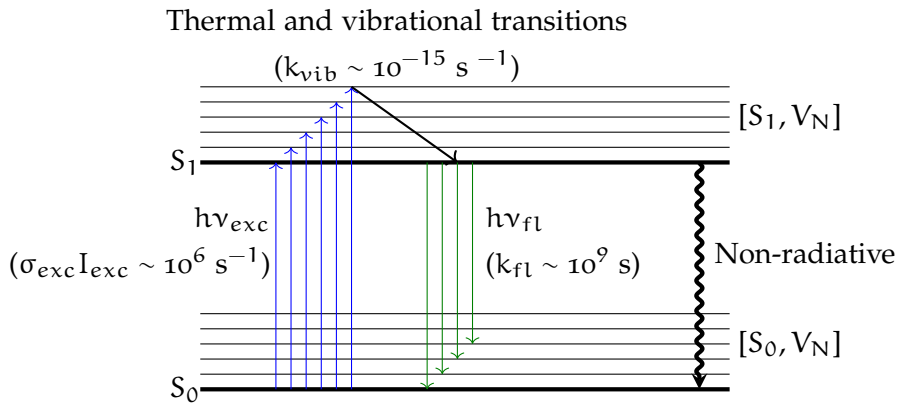

Figure 6: **Simple Jablonski diagram of fluorescence.** Molecules are excited from the ground state (S_0) to an excited state ($[S_1, V_N]$) through the absorption of a photon of energy $h\nu_{exc}$. Thermal and vibrational transitions transfer the molecule to the lowest energy level of the excited state (S_1). The molecule then transfers to the lower electronic energy level ($[S_0, V_N]$). This process releases a photon of energy $h\nu_{fl}$. S_0 and S_1 represent the ground and and first excited singlet states, respectively. V_N represent the vibrational energy states associated with S_0 and S_1. A molecule in the excited state can also decay by a non-radiative transition. The rate of excitation scales with the excitation intensity (I_{exc}) and absorption cross section at the excitation wavelength (σ_{exc}). The rates of vibrational decay and fluorescence emission are given by k_{vib} and k_{fl}.

As the fluorescence emission is spectrally distinct from the excitation, fluorescence emission can be separated from excitation using bandpass filters (figure 7). Fluorescence is effectively detected against a dark background making this a highly sensitive technique [81]. Furthermore, fluorescent dyes can be conjugated specifically to a range of targets, making this a technique that can be used to image targeted biological structures (such as the cytoskeleton).

3.1.2 *Confocal laser scanning microscopy*

Confocal laser scanning microscopy is a powerful and widely used technique in the life sciences [81] that allows 3D imaging of fluorescently labelled biological samples. A schematic of a confocal microscope is shown in figure 8. In confocal microscopy an excitation laser is focused on the sample by a microscope objective (with numerical aperture, NA). Fluorescence emission is collected by the same objective and imaged onto a pinhole. The pinhole is used to reject out-of-focus light, allowing axially resolved imaging. An image is formed

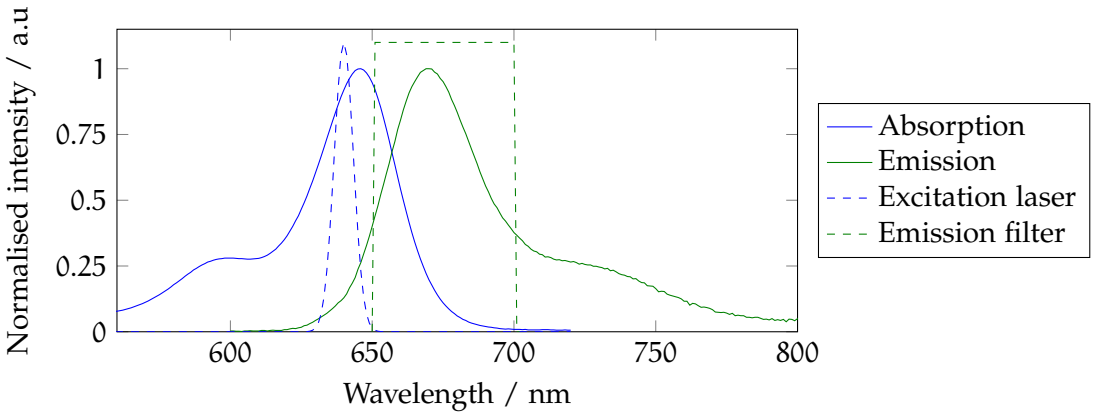

Figure 7: **Excitation and emission spectra of ATTO 647N dye and common excitation and emission filters.**

by scanning the focal volume with respect to the sample. Pixel grey values are the fluorescence intensity detected at each position.

The resolution in confocal microscopy is limited by the size of the focal spot. The full-width half-maximum (FWHM) radius (Δr) of the focal spot produced by an objective with numerical aperture $NA = n\sin\alpha$ focusing light of wavelength λ is

$$\Delta r = \frac{\lambda}{2n\sin\alpha} = \frac{\lambda}{2NA}, \tag{4}$$

where n is the refractive index of the medium in which the objective is working and α is the maximal half-angle of the light cone that can exit the lens. For an oil immersion objective ($n = 1.516$), an objective with $NA = 1.4$ and light of wavelength $\lambda = 640$ nm the FWHM of the focal spot would be 230 nm. This would not allow the resolution of smaller features, such as the cytoskeletal elements investigated in this work [13].

The STED and RESOLFT techniques are based upon confocal microscopy but allow higher resolution imaging, whilst retaining the axial sectioning of confocal microscopy.

3.1.3 *Resolution enhancement by STED and RESOLFT*

In STED and RESOLFT microscopy the effective size of the spot scanned over the sample is reduced. This is achieved by overlaying the Gaussian focal spot of the excitation laser with a depletion laser, which reduces the fluorescence emission by using a light-induced transition to suppress fluorescence [23]. The depletion laser is spatially shaped into an optical vortex beam, commonly referred to as a doughnut beam [23], such that it has an intensity minimum at its centre (coaligned with the maximum of the excitation laser) [82]. This confines fluorescence emission to the centre of the focal spot and reduces the size of the effective focal spot from which fluorescence can

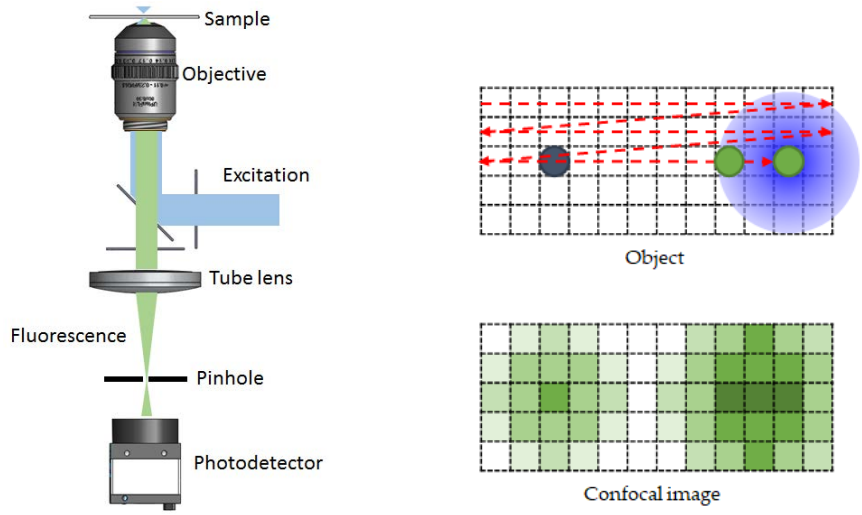

(a) Schematic of confocal microscope

(b) Image formation

Figure 8: **Schematic of a confocal microscope.** The excitation light is focused on the sample and the fluorescence intensity measured. The fluorescence is focused onto a pinhole which is used to reject out-of-focus light. An image is formed by scanning the focal volume with respect to the sample. 8b represents image formation in confocal microscopy.

be emitted. The coaligned depletion and excitation beams are scanned across the sample. This allows features that could not be separated in a conventional confocal image to be resolved in STED or RESOLFT (figure 9).

Like the excitation spot, the depletion patterns are also diffraction limited. However, it is possible to achieve resolutions far beyond the diffraction limit, and theoretically unbounded, by saturating the off-switching transition.

A saturation intensity (I_S) is defined as the depletion laser intensity for which the fluorescence emission will be reduced by a factor of $1/e$. This is represented by the horizontal dashed line in figure 10a. The separation between points at which the depletion intensity (I_{depl}) is equal to the saturation intensity ($I_{depl}(r = r_S) = I_S$), decreases for increasing depletion power ($P \propto I_{av}$, where I_{av} is the spatial average of the depletion intensity). This corresponds to a saturation of the depletion transition. Figure 10b shows suppression of a uniformly fluorescent sample in response to a 1D vortex beam of increasing intensity. The full-width half-maximum (FWHM) decreases for increasing depletion intensity. This corresponds to a decrease in the area from which fluorescence can be emitted, as represented in figure 10c leading to improved resolution. The resolution enhancement in STED and RESOLFT is more rigorously treated in chapter 4.

(a) Diffraction limited excitation spot

(b) Depletion beam transfers molecules to dark state

(c) Effective focal spot

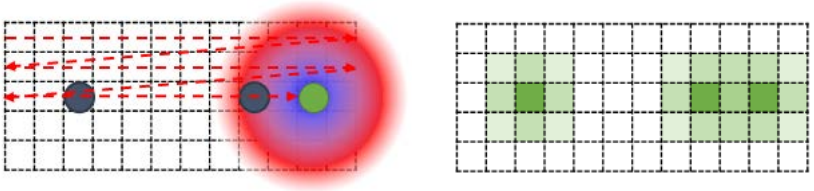

(d) STED/RESOLFT scan of object

(e) STED/RESOLFT image

Figure 9: **Principle of STED- and RESOLFT-type microscopies.** STED and RESOLFT are point scanning techniques, similar to confocal microscopy. As well as of scanning with a diffraction-limited excitation focal spot (9a), the beam is overlaid with a depletion laser (9b, $\lambda_{\mathtt{depl}}$ – shown in red). This beam drives a depletion transition – that is distinct from fluorescence. Therefore, fluorescence can be assumed to originate from the centre of the focal spot – giving a smaller effective focal spot size (9c). This reduces the effective size of the spot scanned over the sample (9d) and therefore allows the separation between small features to be resolved (9e). Green beads are fluorescing and grey beads are not fluorescing or depleted. For illustrative purposes, larger beads are shown in 9d, 9e than in 9a, 9b.

Both the generation of a high resolution vortex beam and the photophysical principles used to deplete fluorescence are important in STED and RESOLFT. In the following sections these are discussed in more detail.

3.1.4 *Depletion patterns in STED and RESOLFT*

In STED and RESOLFT, resolution derives from the spatial shape and intensity of the depletion beam. A range of depletion patterns have been developed depending on whether imaging requires 1D, 2D, 3D or isotropic resolution enhancement. The generation of these phase patterns is discussed in this section.

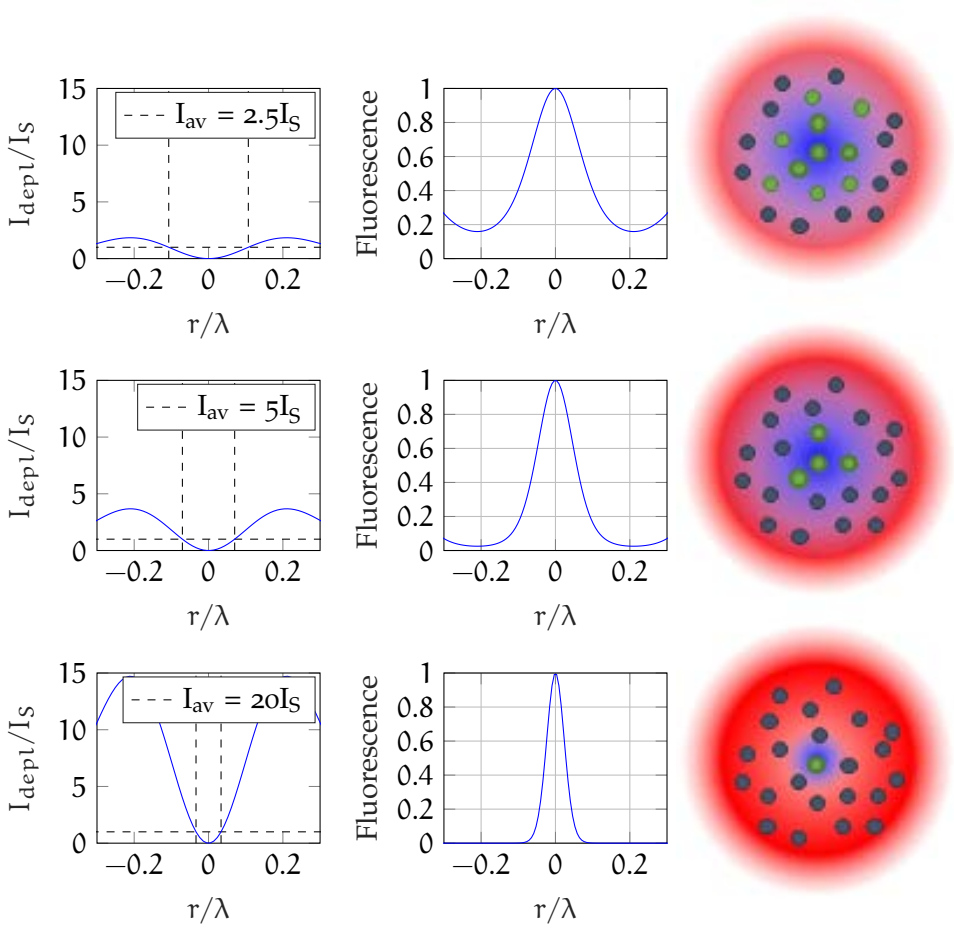

(a) Depletion pattern (b) Fluorescence suppression (c) 2D representation

Figure 10: **Diffraction-unlimited resolution in STED and RESOLFT.** 10a The intensity in the image plane of a vortex beam with increasing average intensity (I_{av}), proportional to the depletion power. Although the profile of the vortex beam is diffraction-limited, the distance between points (vertical dashed lines) at which the depletion intensity exceeds the saturation intensity (I_S, horizontal dashed line) decreases as a function of increasing depletion power. This corresponds to a non-linear suppression of fluorescence as a function of distance from the centre of the pattern. The FWHM of the fluorescence suppression pattern (10b) decreases as a function of depletion power. This corresponds to a decrease in the area from which fluorescence is emitted as a function of increasing intensity, as represented in 10c.

3.1.4.1 *Depletion phase patterns*

In STED and RESOLFT, depletion patterns are typically generated by imaging a phase pattern in the back aperture of the objective. A phase pattern in the back aperture corresponds to an intensity distribution at the focus. Different phase patterns can be used and some of these are introduced here, based upon a detailed review by Keller *et al.* [82].

1D STED

A 1D depletion pattern can be efficiently generated [82] from a phase mask where one half is π out of phase with the other half (11a). In the focal plane, at the centre, rays from one half will be π out of phase with the other half, leading to destructive interference. Constructive interference occurs outside of the centre, due to the different path lengths, generating a focus with an intensity minimum at the centre and bright side lobes 11. Laterally the intensity scales with r^2 about the minimum.

(a) Phase mask (b) Intensity map (x,y) (c) Intensity map (x,z)

Figure 11: **Phase mask and intensity distributions for 1D resolution enhancement in STED.** 11a shows the phase mask which, if applied to the depletion beam in the back aperture, will give the intensity distributions shown in 11b and 11c in the focal plane. Simulated by Dr. Pierre Mahou.

2D STED – simple

A simple extension of the 1D STED beam profile to 2D is achieved by splitting the beam into quarters with a π phase shift between each quarter (12a). In this case, similar interference takes place to in the 1D case, but in two orthogonal directions. This gives a central zero as shown in figure 12, which can be used for resolution enhancement in 2D. As the intensity distribution is not radially symmetric, resolution enhancement is not isotroptic in the lateral dimensions. Hereafter this depletion pattern will be referred to as 2D-simple.

2D STED – helical

For an isotropic resolution enhancement in the lateral dimensions, a helical phase mask is used. This can be thought of as the 1D phase

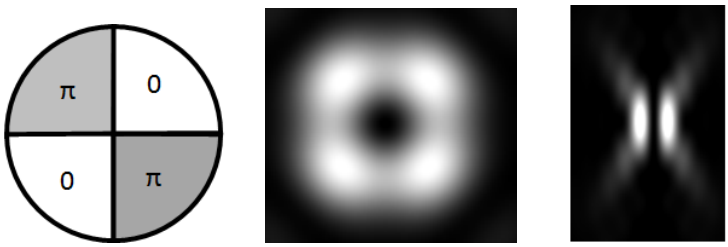

(a) Phase mask (b) Intensity map (x,y) (c) Intensity map (x,z)

Figure 12: **Phase mask and intensity distributions for simple 2D resolution enhancement in STED.** 12a shows the phase mask which, if applied to the depletion beam in the back aperture, will give the intensity distributions shown in 12b and 12c in the focal plane. Simulated by Dr. Pierre Mahou.

mask being rotated to all angles. In this case half of each diagonal is π out of phase with its other half. This is shown in figure 13. This gives an isotropic vortex beam (sometimes referred to as a doughnut beam) in the focal plane. For the depletion patterns shown in figure 12 and 13 the intensity scales laterally with r^2 close to the minimum. Hereafter this depletion pattern will be referred to as 2D-helical.

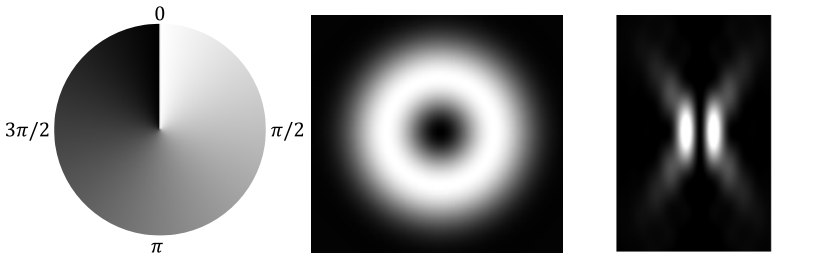

(a) Phase mask (b) Intensity map (x,y) (c) Intensity map (x,z)

Figure 13: **Phase mask and intensity distributions for isotropic 2D resolution enhancement in STED.** 11a shows the phase mask which, if applied to the depletion beam in the back aperture, will give the intensity distributions shown in 13b and 13c in the focal plane. Simulated by Dr. Pierre Mahou.

3D STED – bottle

The helical phase mask generates an isotropic enhancement in lateral resolution, but does not enhance the resolution axially, compared to confocal microscopy. Axial resolution enhancement can be achieved using the circular phase mask shown in figure 14. This has a phase difference of π between the centre of the beam and the outside. At the focus this will interfere destructively. Unlike the helical phase mask, destructive interference occurs only near focus and the depletion pattern has lobes above and below the focal plane which enhance axial resolution.

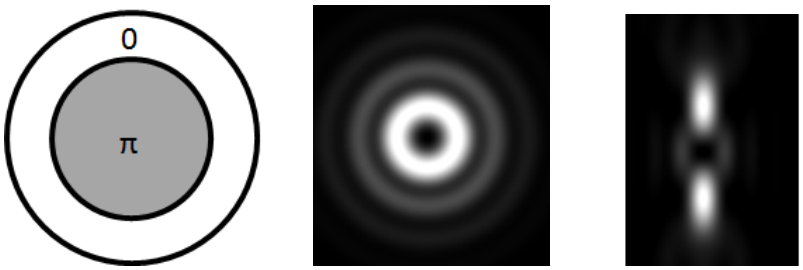

(a) Phase mask (b) Intensity map (x,y) (c) Intensity map (x,z)

Figure 14: **Phase mask and intensity distributions for axial resolution enhancement in STED.** 14a shows the phase mask, which if applied to the depletion beam in the back aperture, will give the intensity distributions shown in 14b and 14c in the focal plane. Simulated by Dr. Pierre Mahou.

This beam profile is sometimes referred to as a bottle beam. Laterally the intensity scales with $r_{norm}{}^4$. Therefore, the intensity around the central minimum ($r_{norm}{}^4 < 1$, where $r_{norm}{}^4$ is the normalised lateral coordinate normalised with respect to the beamwaist [83–85]), scales slower than in the case of the helical phase mask. This means that laterally the resolution is not as high as in the helical phase mask case for a given intensity. Hereafter this depletion pattern will be referred to as 3D-bottle.

Generally users prefer high lateral resolution. To achieve 3D STED or RESOLFT with high lateral resolution the bottle beam can be superimposed incoherently on a vortex beam, generated using the 2D-helical mask [84]. This can result in challenging alignment [86] and high photon doses on the sample as fluorescence suppression is required in beams.

Regardless of the phase mask used, a common requirement is a high contrast between the low intensity minimum and the high intensity lobes, as well as a steep gradient about the minimum. The gradient and intensity at the minimum can be degraded by optical aberrations and misalignment of the system [86, 87]

3.1.5 *Effects that degrade STED/RESOLFT depletion patterns*

Optical aberrations can be induced by the misalignment of the system and by the sample [88]. Aberrations degrade the resolution in STED and RESOLFT by reducing the sharpness of the depletion pattern [89]. Coma, astigmatism and spherical aberrations and their effects on the sharpness of vortex and bottle beam depletion patterns are considered. Other effects that degrade the sharpness of a vortex beam include misalignment of the phase mask to the depletion beam [90] and the incorrect polarisation of the depletion beam [91–93]. Although not

directly related to the depletion pattern, the coalignment between excitation and depletion is also crucial.

Coma

Coma is an optical aberration which arises due to rays arriving off-axis in a lens. The effect of coma on a gaussian beam is to induce a focal spot with a comet-like tail, as different parts of the beam focus to different positions due to the change in the pupil.

For a 2D-helical phase mask, coma leads to an asymmetric depletion pattern, with lower intensity in one half than the other. The position of the intensity minimum is shifted [86].

For a 2D-helical phase pattern, theoretical data suggest that coma does not increase the intensity at minimum of the depletion pattern, but does decrease the intensity in one direction of the pattern [94]. This leads to asymmetric resolution enhancement.

The 3D-bottle beam is more affected by coma and there is an increase in intensity at the minimum. Like the 2D-helical beam, the position of the intensity minimum is shifted; however, it has recently been shown [86] that this is in the opposite direction to the 2D-helical beam. This means that particular care must be taken to minimise, or correct for, coma in isotropic 3D STED and RESOLFT systems.

Astigmatism

Astigmatism is a similar aberration to coma and originates from rays propagating in two perpendicular planes having different focii. For a 2D-helical beam, the radial symmetry of the depletion pattern is broken and the profile shows two high intensity lobes. Along one axis, peaks become dimmer and further apart. Again this leads to an asymmetric resolution enhancement [94].

Spherical aberrations

In microscopy, spherical aberrations commonly arise due to changes in refractive index, for instance between immersion oil (refractive index 1.516) and cell culture medium (1.33). The effects of spherical aberrations increase with depth in the sample, or further changes in refractive index [95, 96]. For a 2D-helical beam, spherical aberrations degrade the sharpness of the pattern, decreasing the gradient about the centre of the focal spot, leading to a decrease in resolution. Therefore spherical aberrations must be compensated for when imaging live cells or in thick samples.

Alignment of phase mask

For isotropic resolution enhancement the depletion beam must be centred on the phase mask. The profile of a 2D-helical beam or 3D-

bottle beam in the focal plane appears similar for a misaligned phase mask to that of coma, leading to similar effects on microscope resolution. When aligning a STED or RESOLFT microscope it is important to use the 3D profile of the beam to differentiate between phase mask misalignment and coma [90]. This problem is overcome simply by translating the phase mask relative to the depletion beam. It may be necessary to realign the depletion and excitation beams.

Coalignment of excitation and depletion beams

Excitation and depletion beams should be aligned such that the depletion minimum is coaligned with the excitation maximum, in all three dimensions. A lateral offset leads to a decrease in signal, while an axial offset leads to a reduction in resolution in the excitation focal plane.

Polarisation of depletion beam

As reported by Hao *et al.* [91], circular polarisation is required to generate a radially symmetric depletion pattern, with an intensity zero at the centre, for both a vortex beam and a bottle beam. In the case of the vortex beam, the handedness of the circular polarisation must match the handedness of the helical phase mask.

Importantly, in the focal plane, the depletion pattern for an eliptical depletion beam resembles that of a depletion beam with astigmatism, although axially this is not the case. Similar to differentiating between coma and phase mask misalignment, the 3D profile of the beam must be measured.

In order to generate the highest resolution STED images, all of the above issues need to be corrected. Methods for generating depletion patterns and correcting for aberrations are discussed next.

3.1.6 *Instrumentation for generating and aligning depletion patterns and correcting aberrations*

In order to generate the depletion pattern, a phase controlling element is introduced into the depletion beam path.

The simplest example is a phase plate [97], designed for either a 2D-helical depletion pattern pattern or a 3D-bottle pattern. A schematic of how this type of system might be incorporated is shown in figure 15. This mask must be aligned such that it is centred on the depletion beam. The depletion beam must then be coaligned with the excitation beam, such that the depletion minimum is centred on the excitation maximum. In the event of mechanical or thermal drift, both beams must be realigned.

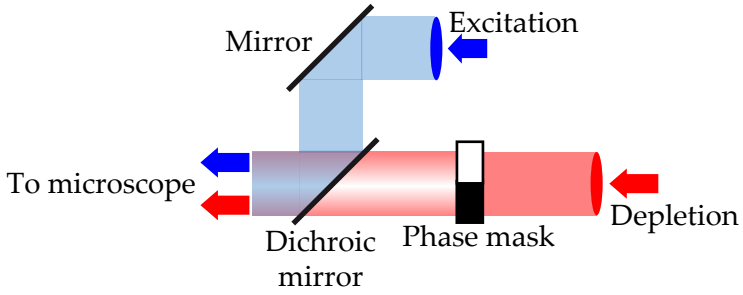

Figure 15: **Schematic of the incorporation of a phase mask (or transmission SLM) in a STED or RESOLFT microscope.** The phase mask must be translated such that a radially symmetric vortex beam is produced in the image plane. The excitation beam must then be centred on this beam (for instance by adjusting the mirror and dichroic mirror). Where an SLM is used, a linear phase ramp can be displayed on the SLM to allow fine adjustment of the position of the depletion beam in the image plane.

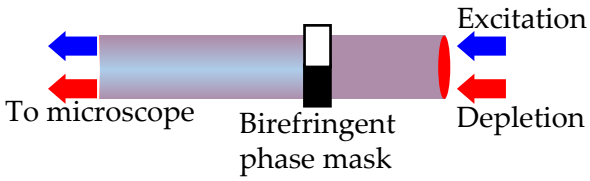

Figure 16: **A birefringent phase mask which produces a vortex beam for the depletion beam and gaussian beam for the excitation beam simplifies alignment.** Excitation and depletion lasers from a common source, such as a single mode fibre, are coaligned by design [98] – reducing the alignment steps involved.

To simplify the alignment of a STED microscope, a novel phase plate was developed by Reuss *et al.* [98]. A birefringent element is used, which causes the depletion beam to have opposite polarisations in opposing quarters whilst leaving the excitation beam unchanged. This gives rise to a depletion pattern similar to that used in the 2D simple mask (figure 12). This system simplifies alignment if excitation and depletion beams come from a common source, for instance if both lasers are coupled into the same optical fibre [98] or a supercontinuum source is used [99]. This phase mask can only produced the 2D-simple pattern and so does not give isotropic resolution enhancement (2D-helical is required for this). A schematic of how the phase plate is incorporated into a microscope system is shown in figure 16.

Both phase plates previously described are passive elements. Whilst the centring and positioning of the phase mask can be optimised by steering the excitation or depletion beam, these systems cannot correct for aberrations. An alternative is to use an active phase controlling element, which can generate a depletion pattern and correct aberrations, such as a spatial light modulator (SLM) [89]. An SLM is

a pixelated optical element, with which the phase of light propagating through each pixel can be controlled electronically. The user can display any phase pattern on the SLM, corresponding to any phase mask discussed in section 3.1.4.1. The phase pattern displayed on the SLM can also be used to change the position of the depletion beam in the image plane and correct for aberrations [88].

The phase pattern on an SLM is specific to the wavelength being used and is only compatible with linearly polarised light. An independent SLM would be required to correct aberrations of an excitation beam. Aberrations in fluorescence emission cannot be corrected for using an SLM due to the polarisation dependence. Recently developed STED microscopes [100, 101] use an SLM to generate the vortex beam and a deformable mirror, in a common optical path, to correct for aberrations in the depletion, excitation and emission channels, as shown in figure 17. A major advantage of using this system is that preliminary aberration correction can be performed *in situ* by optimising the intensity of a confocal image, which is simpler than automated approaches for *in situ* aberration correction of the depletion beam only [100].

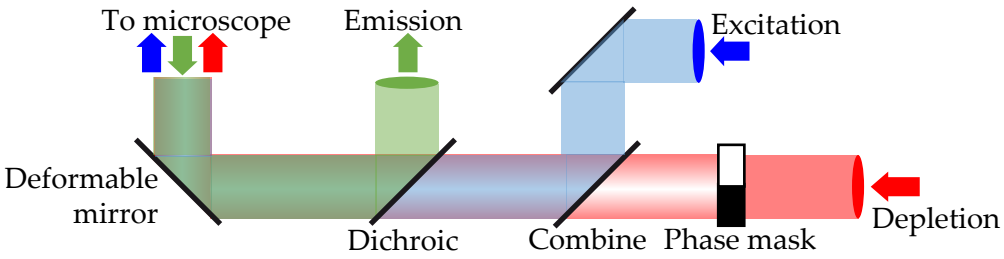

Figure 17: **Schematic of STED with dual adaptive elements.** A phase mask is used to spatially shape the depletion beam in the image plane. This is combined with an excitation beam. A deformable mirror that is common to both beams (and the fluorescence emission) corrects for aberrations. An SLM is typically used as the phase mask as this allows control of the depletion beam's 3D position and fine control of aberrations on the depletion beam [100].

This approach, with dual adaptive elements, is expensive and beyond the reach of most labs. In this project, where large numbers of images and imaging in thick samples are required, a single SLM is used for generating a vortex beam, correcting for aberrations on the depletion beam and simplifying day-to-day alignment.

3.1.7 *Fluorescence depletion*

Having generated a depletion pattern, it is important to consider the photophysical methods that can be used to induce off-switching of fluorophores. The established methods for this are stimulated emis-

sion depletion (STED) and the use of reversible photoswitchers (RESOLFT). These are discussed in more detail in the following sections.

3.1.8 *Stimulated emission depletion*

Stimulated emission depletion (STED) microscopy is one of the oldest far-field super-resolution microscopy techniques, and was first proposed in 1994 by Hell *et al.* [22]. STED uses the light driven process of stimulated emission to deplete fluorescence.

Stimulated emission is a light-driven process in which a molecule in an excited state will interact with a photon and transfer to a lower energy level. This process creates a new photon that is identical to the incident photon in phase, frequency, polarisation and direction of travel. This is shown for a two-level molecule in the higher energy state B in figure 18. The probability of interaction with a photon is defined by the stimulated emission cross-section $\sigma_{depl}(\lambda)$, commonly defined in units of cm^{-2}.

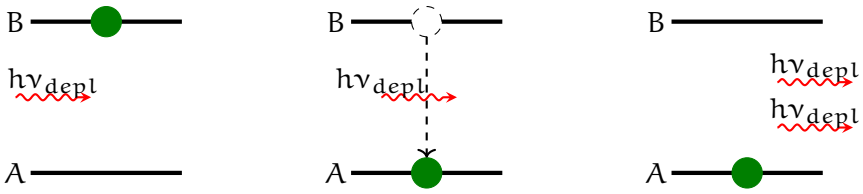

(a) Before emission (b) During emission (c) After emission

Figure 18: **The process of stimulated emission.** A molecule in the energy state B transfers to state A when interacting with a photon of energy $h\nu_{depl} = \Delta E_{B\to A} = E_B - E_A$. In this process a photon is emitted with the same energy, polarisation, direction and phase as the incident photon. The rate of this process is related to the stimulated emission cross-section and the intensity of photons.

Stimulated emission depletion microscopy takes advantage of both the Stokes shift and the broad emission spectrum of a fluorescent dye. This allows stimulated emission to be driven at a different wavelength to excitation and for stimulated emission to be spectrally separated from fluorescence emission. In figure 19 examples of the excitation, emission and depletion wavelength are overlaid on the spectrum of the common STED dye ATTO 647N [102, 103]. A modified Jablonski diagram (based upon figure 6) is shown in figure 20 for stimulated emission driven at λ_{depl}.

For resolution enhancement the rate of stimulated emission in the depletion region (figure 20b) must be greater than the rate of spontaneous (fluorescence) emission (k_{fl}). This corresponds to an average depletion intensity intensity 3–4 orders of magnitude greater than excitation intensities used in conventional confocal microscopy [23,

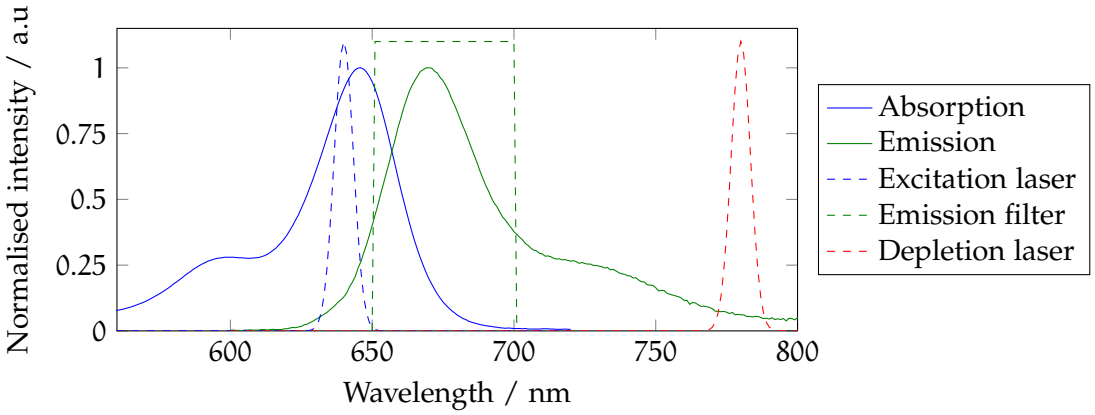

Figure 19: **Excitation and depletion wavelengths used in STED microscopy of ATTO 647N dye.** The depletion wavelength (λ_{depl}) is chosen to be within the emission spectrum of the dye but far from the emission maximum. This minimises excitation from the depletion beam and allows spectral separation of spontaneous and stimulated emission [102, 103].

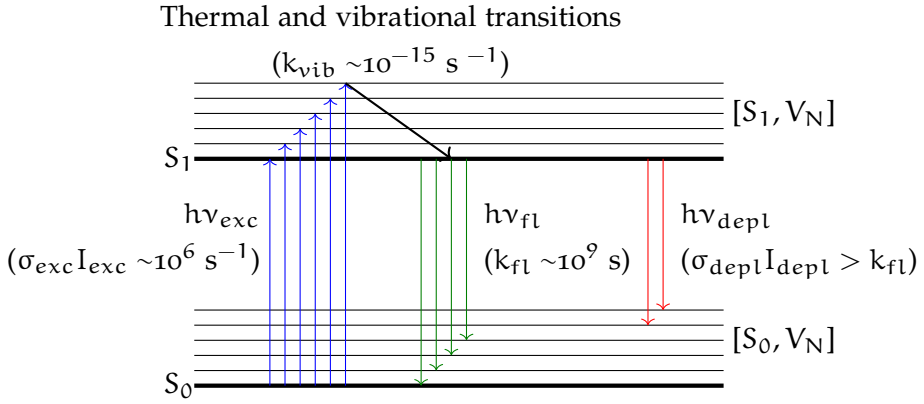

(a) STED Jablonski diagram

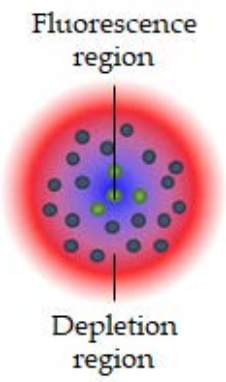

(b) Excitation and depletion beam profiles

Figure 20: **Jablonski diagram of stimulated emission depletion.** Molecules excited from the ground state ($[S_0]$) to an excited state ($[S_1, V_N]$) decay via thermal and vibrational transitions to the $[S_1, V_0]$ energy level. From this state molecules decay either by spontaneous emission (fluorescence, rate k_{fl}) or by stimulated emission (induced by a depletion laser, rate $\sigma_{depl} I_{depl}$). The rate of stimulated emission can be increased by increasing the intensity of the depletion laser. The depletion laser is shaped into an annular ring (red in 20b). The intensity is set such that stimulated emission dominates in the depletion region and fluorescence dominates in centre. The size of the fluorescence region decreases for increasing I_{depl}.

83], which can lead to photodamage and increase photobleaching. As shown in figure 10 (and derived in chapter 4) further increases in depletion intensity are required to achieve higher resolution. Aiming to reduce the high intensity required for STED, whilst retaining the advantages, Hofmann *et al.* [38] proposed the RESOLFT technique, which achieves STED-like resolution at confocal excitation intensities.

3.1.9 *Reversible photoswitching fluorescent proteins (used in RESOLFT)*

RESOLFT microscopy is based upon the STED principle but uses fluorophores that can be photoswitched by photoisomerisation between a fluorescent on-state and a non-fluorescent off-state [38]. A schematic of the transitions of a reversibly photoswitchable fluorescent protein showing the relevant transitions is presented in figure 21. Intermediate states are not shown [104].

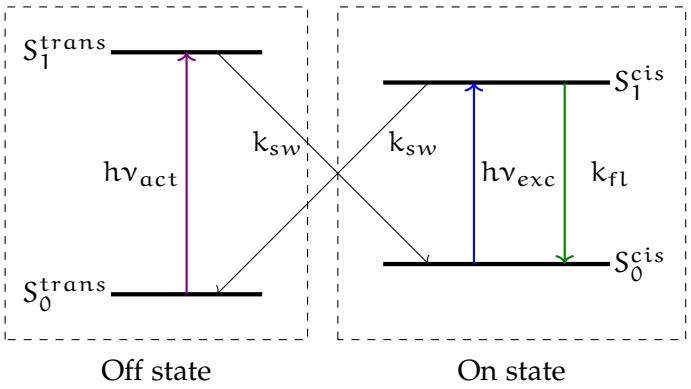

Figure 21: **Transitions in RESOLFT microscopy.** The fluorophores exist in a non-fluorescent isomer off-state. Activation by light at energy $h\nu_{act}$ can lead to photoswitching to an isomer on-state at a rate k_{sw}. In the on-state, excitation at $h\nu_{exc}$ to S_1^{cis} can lead to either fluorescence emission (rate k_{fl}) or photoswitching to the non-fluorescent state (rate k_{sw}). Only relevant transitions are shown [104]

A common fluorophore in RESOLFT is rsEGFP [105]. rsEGFP is initially in an off-state (trans isomer) and can be converted to the on-state (cis isomer) through absorption of a photon at the activations wavelength (λ_{act} = 405 nm for rsEGFP. In the on-state the fluorophore can absorb light at the excitation wavelength (λ_{exc} = 480–491 nm is typically used for rsEGFP). In the excited state (S_1^{cis}) the molecule can either fluoresce (rate k_{fl}) or switch back to the off-state (rate k_{sw}). For RESOLFT imaging a molecule in the off-state is first photoactivated with a Gaussian beam at λ_{act}. It is then depleted by illumination with a vortex shaped beam at the excitation wavelength. Fluorophores remaining in the on-state are confined to a sub-diffraction limit volume. The on-state is then read out by a gaussian shaped read-out beam

(again at the excitation wavelength). The sequence and a timeline is shown in figure 22.

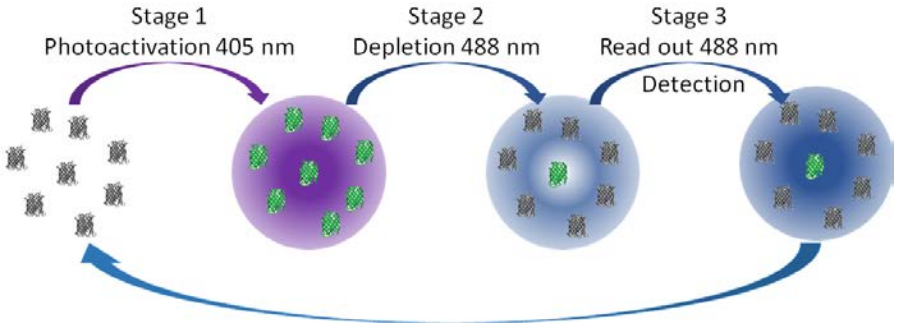

(a) RESOLFT cycle

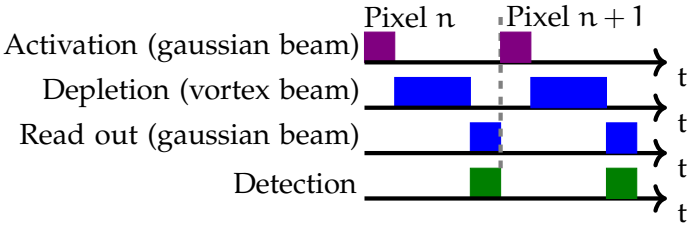

(b) RESOLFT timeline

Figure 22: **RESOLFT imaging.** A gaussian beam is used to photoactivate the fluorophores in a diffraction-limited volume. A vortex beam at the excitation wavelength depletes the fluorescence outside of the centre of the volume. Fluorescence is read out with a gaussian beam at the excitation wavelength. Detection occurs only during the read-out phase.

Compared to the fluorescence lifetime, the on isomer state is long-lived, meaning that the intensity required to saturate the off-state before reading out the fluorescence signal is lower than that required in STED microscopy. The RESOLFT depletion intensity can be comparable to intensities used in confocal microscopy [38, 105–107].

It is important to note that, in spite of the lower intensity requirement, the same number of fluorophores must be depleted in STED and RESOLFT to saturate the depletion channel. Therefore, RESOLFT typically has a long depletion stage (0.1–10 ms), at low intensities, in order to have sufficient depletion events. This leads to longer acquisition times and a larger photon dose on the sample than in confocal microscopy. The total number of depletion photons needed in STED and RESOLFT is compared in chapter 4.

3.1.10 *Fluorescent labelling for live cell STED and RESOLFT*

The main aim of this thesis is to apply STED or RESOLFT (with AFM) to imaging live cells. It is therefore required that sub-cellular features of living cells can be fluorescently labelled.

In STED, although stimulated emission can be driven on any fluorophore, only a limited subset of fluorophores have been found to perform well in STED [108–110]. Generally a fluorophore should have a long fluorescence lifetime, high quantum yield, large stokes shift and low photobleaching. Organic dyes are more likely to have these properties than fusion proteins but organic dyes are more difficult to introduce into live cells and to specifically target sub-cellular components [111]. On the other hand fusion proteins can be genetically coexpressed in live-cells with specific targets but few fluorescent proteins have been reported for STED imaging [109]. In the context of this work the lack of fluorescent proteins for STED may be mitigated by recently developed dyes that selectively target the cytoskeleton of live-cells [31].

In contrast to STED, RESOLFT has only been reported for imaging a limited range of fluorescent proteins. This is due to the requirement that fluorophores be reversibly photoswitchable. The most commonly used reversibly photoswitchable fluorescent proteins are rsEGFP [38], and rsEGFP2 [106]. rsEGFP2 has a higher rate of photoswitching k_{sw} and can therefore be depleted in a shorter time. Other fluorescent proteins for RESOLFT have been developed including a red variant for two colour imaging (rsCherryRev1.4) [112] and the highly photostable GMars-Q for long term imaging [113].

3.2 PHOTOBLEACHING

3.2.1 *General discussion of photobleaching*

In the previous descriptions of confocal, STED and RESOLFT microscopy only, radiative transitions between the S_0 and S_1 energy levels were considered. For simplicity, the process of photobleaching was not discussed.

Photobleaching is an irreversible chemical degradation of a fluorophore into a non-fluorescent species [114–117]. Photobleaching occurs from excited states where molecules have more energy and a greater probability of reacting with their surrounding. In one reaction mechanism molecules molecules in an excited state form a cation–electron pair (M^+e^-, quantum yield ϕ_{ion}). The cation–electron pair can either recombine or undergo an escape reaction forming a free radical cation and a solvated electron (quantum yield ϕ_{solv}). A free radical cation is chemically unstable in a polar solvent and reacts forming a molecule that is no longer fluorescent. The quantum yields ϕ_{ion} and ϕ_{solv} increase for higher energy levels. It is therefore important to consider energy levels beyond S_1; some of these energy levels and associated transitions are shown in figure 23 [116].

From the S_1 state, as well as decaying radiatively to the S_0 state (rate k_{fl}) or undergoing photobleaching (rate B_{S_1}), molecules can be

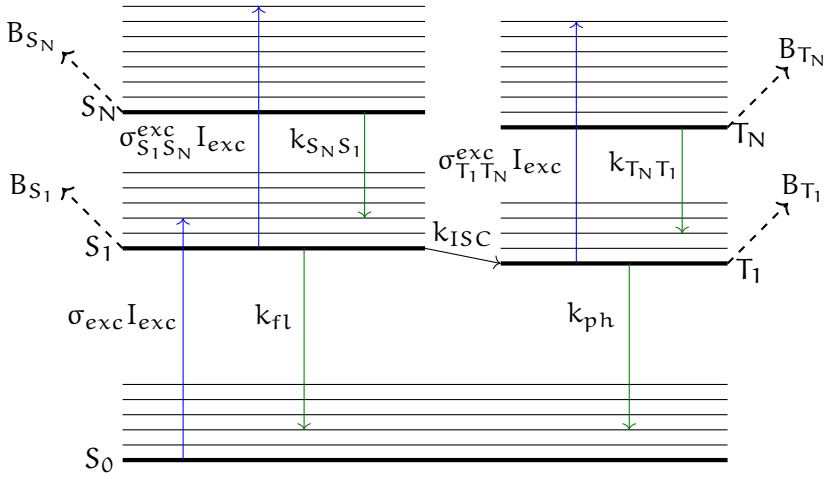

Figure 23: **Jablonski diagram showing photobleaching in confocal microscopy.** Molecules in higher energy states (S_1, S_N, T_1, T_N) have more energy than those in the ground state and are therefore more reactive. Molecules in the excited states have a probability of reacting (B_{S_1}, B_{T_1}, B_{S_N}, B_{T_N}) with other molecules in their environment and becoming non-fluorescent (photobleached). A molecule in the excited singlet state S_1 can be excited by the absorption of a photon to higher energy singlet states (S_N). Molecules in the S_N state are more reactive than those in the S_1 state and have a greater chance of reacting. A further photobleaching mechanism involves a molecule in the singlet state transferring to the triplet state (T_1) through intersystem crossing (rate k_{ISC}). This state is highly reactive with triplet oxygen and is longer lived than the singlet state ($k_{ph} < k_{fl}$). This increases the time in which the molecule can react with another molecule or be excited to a more reactive state (T_N). Rates of excitation to higher states are described by the absorption cross section at the excitation wavelength σ^{exc}_{XY} and the excitation intensity I_{exc}. The rates of decay from the excited states S_N and T_N are $K_{S_NS_1}$ and $K_{T_NT_1}$.

excited to higher energy states by the absorption of a photon. Higher energy singlet states are denoted S_N. These more energetic states have greater energy and, therefore, greater ionisation and solvation quantum yields (ϕ_{ion} and ϕ_{solv}). If a molecule is in a higher energy state, the probability of photobleaching is increased. Notably the probability of being excited from S_1 to S_N 9rate of decay $K_{S_NS_1}$) is dependent on the intensity of the excitation laser ($\sigma^{exc}_{S_1S_N} I_{exc} \sim 10^6\ s^{-1}$, for intensities typically used in confocal microscopy), which is low relative to the rate of fluorescence emission ($k_{fl} \sim 10^9\ s^{-1}$).

Another important transition is intersystem crossing (rate $k_{isc} \sim 10^5$–$10^6\ s^{-1}$ [116, 118]) from the singlet to the triplet state. From the first triplet state (T_1) a molecule can transition to a higher energy state (T_N, rate of decay $K_{T_NT_1}$) or decay to the ground state (S_0) through phosphorescence. The rate of phosphorescence ($k_{ph} \sim 10^5\ s^{-1}$) is much

lower than the rate of fluorescence emission, corresponding to the triplet state being longer lived than the singlet state. The rate of phosphorescence is also comparable to the rate of light-induced excitation to T_N ($\sigma^{exc}_{T_1T_N} I_{exc} \sim 10^6\ s^{-1}$). Therefore, transitions to higher energy states and photobleaching from the triplet state become more likely.

Overall, the probability of a molecule being photobleached depends upon the energy state it is in. Throughout this discussion the overall probability that a molecule not in the ground state will be photobleached is P_B. The rate of photobleaching (r_B) is the product of the probability of photobleaching and the rate of excitation (r_{exc}).

$$r_B = P_B \times r_{exc}. \tag{5}$$

Photobleaching imposes an upper limit on the amount of fluorescence that can be detected. The total amount of fluorescence signal available from a fluorophore is proportional to the number of times it can be excited to S_1 before the population has been reduced by $1/e$ by photobleaching. This will be referred to throughout this thesis as N_{cyc}, where

$$\frac{1}{e} = (1 - P_B)^{N_{cyc}}, \tag{6}$$

and is calculated for confocal, STED and RESOLFT microscopy.

3.2.2 *Photobleaching in confocal microscopy*

For a continuous wave confocal microscopy system the probability of photobleaching was calculated by Eggeling *et al.* [116, 117] as

$$P_B = \left(\frac{B_{S_1} + \frac{k_{ISC}}{k_{ph}} B_{T_1}}{k_{fl}} \right) + \left(\frac{\frac{\sigma^{exc}_{S_1S_N}}{K_{S_NS_1}} B_{S_N} + \frac{\sigma^{exc}_{T_1T_N}}{K_{T_NT_1}} \frac{k_{ISC}}{kph} B_{T_N}}{k_{fl}} \right) I_{exc}. \tag{7}$$

Notably, the probability of photobleaching scales linearly with the excitation intensity.

Some of the constants in equation 7 can vary significantly between fluorophores and experimental conditions. For instance, the rate of phosphorescence can range from $10^3\ s^{-1}$ (Oregon Green in the absence of oxygen [78, 119]), to $10^6\ s^{-1}$ (Rhodamine 6G [116], ATTO 532 [78, 120]). Similarly, excited state absorption cross-sections ($\sigma_{S_1S_N}$, $\sigma_{T_1T_N}$) can vary significantly between fluorophores and can lead to large differences in photobleaching [110]. For comparison between techniques the values given in table 1 are used.

The probability of photobleaching, rate of photobleaching and number of cycles before the population is reduced to $1/e$ (equation 6) are plotted in figure 24.

Parameter		Value	Comments and reference
Absorption cross-section at λ_{exc}	σ_{exc}	10^{-16} cm^2	10^{-15}–10^{-17} cm^2 quoted in [81]
Rate of fluorescence emission	k_{fl}	10^9 s^{-1}	Quoted in [81]
Rate of phosphorescence	k_{ph}	10^5 s^{-1}	Measured value for ATTO 647N [118]
Singlet state absorption	$\sigma^{exc}_{S_1S_N}$	10^{-17} cm^2	Order of magnitude for Rhodamine 6G [116]
Triplet state absorption	$\sigma^{exc}_{T_1T_N}$	5×10^{-17} cm^2	Order of magnitude for Rhodamine 6G [116]
Rate of intersystem crossing	k_{ISC}	10^5 s^{-1}	Measured value for ATTO 647N [118]
Rate of relaxation fron S_N	$k_{S_NS_1}$	5×10^{12} s^{-1}	Order of magnitude for Rhodamine 6G [116]
Rate of relaxation fron T_N	$k_{T_n T_1}$	5×10^{12} s^{-1}	Order of magnitude for Rhodamine 6G [116]
Rate of photobleaching from S_N	B_{S_N}	10^8 s^{-1}	Order of magnitude for Rhodamine 6G [116]
Rate of photobleaching from T_N	B_{T_N}	10^8 s^{-1}	Assumed to be the same as B_{S_N} [116]
Rate of photobleaching from S_1 and T_1	$B_{S_1} + \frac{k_{ISC}}{k_{ph}} B_{T_1}$	5×10^2 s^{-1}	Order of magnitude for Rhodamine 6G [116]
Excitation wavelength	λ_{exc}	640 nm	Excitation wavelength of ATTO 647N [102, 103]
STED depletion wavelength	λ_{depl} (STED only)	765 nm	Depletion wavelength of ATTO 647N [102, 103]
Depletion cross-section	σ_{depl} (STED only)	10^{-16} cm^2	Typical value quoted in [23]
Singlet state absorption (depletion wavelength)	$\sigma^{depl}_{S_1S_N}$ (STED only)	10^{-17} cm^2	Assumed to be the same as for excitation
Triplet state absorption (depletion wavelength)	$\sigma^{depl}_{T_1T_N}$ (STED only)	10^{-17} cm^2	Assumed to be the same as for excitation
Anti-Stokes excitation (depletion wavelength)	σ_{AS} (STED only)	$5{\times}10^{-21}$ cm^2	Measured for ATTO 647N [121]
Rate of photoswitching	k_{sw} (RESOLFT only)	2×10^5 s^{-1}	Estimated from data presented in [113]

Table 1: **Approximate values for parameters related to photobleaching for a hypothetical fluorophore.** Parameters are quotes for STED and RESOLFT, which are discussed in the following sections. The fluorophore is a hybrid of ATTO 647N and Rhodamine 6G.

As previously noted, throughout this thesis I_{exc} and I_{depl} is represented in photons.cm^{-2}.s^{-1}. This is converted into the more common terms of W cm^{-2} by multiplication by the photon energy

$$E_p = \frac{hc}{\lambda}. \tag{8}$$

For conventional excitation intensities of 1–10 kW cm^{-2} the rate of photobleaching scales approximately linearly with intensity. At higher intensities the quadratic term becomes dominant. The number of cycles decreases for increasing intensity, approximately 2×10^6 cycles are available.

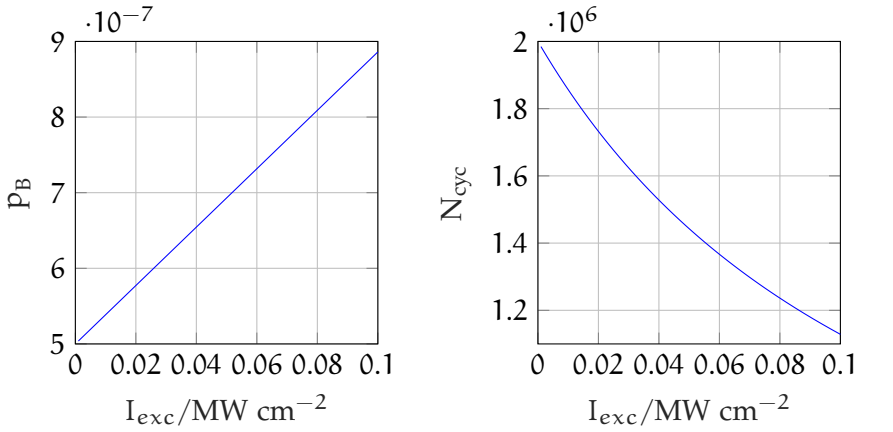

(a) Probability of photobleaching (b) Cycles before population reduced to $1/e$

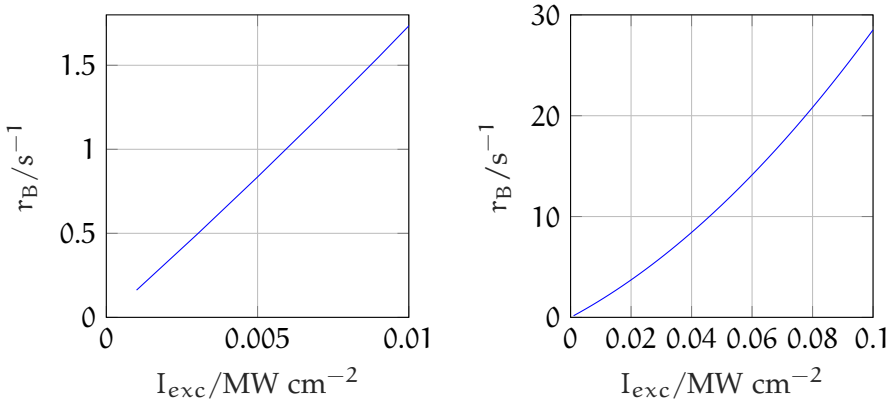

(c) Low excitation intensity (d) High excitation intensity

Figure 24: **Photobleaching in confocal microscopy.** 24a The probability of photobleaching upon excitation to the S_1 state scales linearly with the excitation intensity. 24b The number of cycles before the population is reduced by $1/e$ decreases with increasing intensity. 24c The rate of photobleaching ($r_B = P_B \times \sigma_{exc} I_{exc}$)is approximately linear for intensities commonly used in confocal microscopy (1–10 kW cm^{-2}) and scales quadratically at higher values (24d).

3.2.3 *Photobleaching in STED*

STED requires a depletion laser intensity 3–4 orders of magnitude greater than the confocal excitation laser. Figure 25 shows some of the transitions that the depletion laser can induce. Firstly the high intensity depletion laser can drive excitation of molecules in the S_1 or T_1 states to higher energy states, in which they have a higher probability of photobleaching.

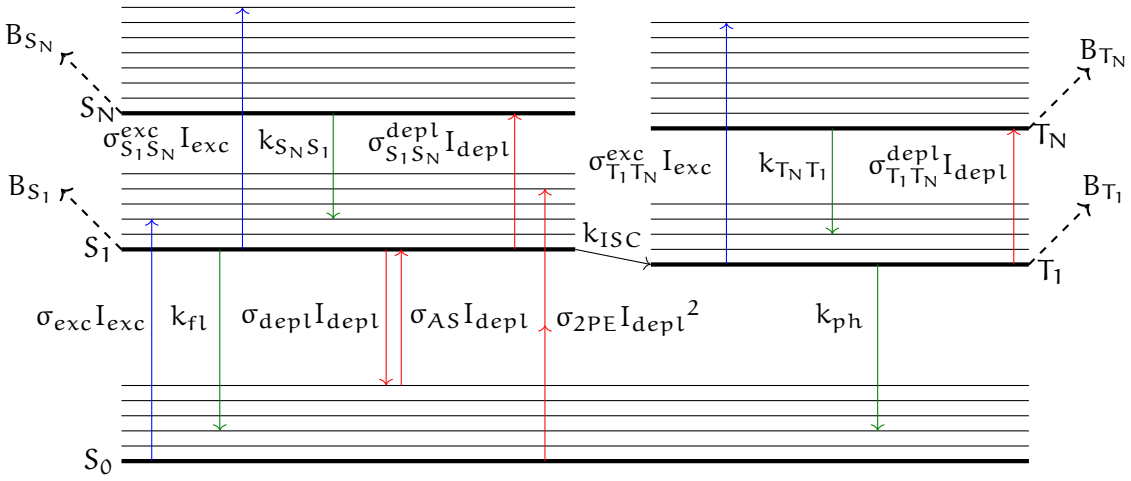

Figure 25: **Jablonski diagram showing photobleaching in STED microscopy.** The depletion laser in STED is 3–4 orders of magnitude more intense than the excitation laser. This laser can increase the rate of transitions to the higher energy states. On the other hand, the depletion laser also decreases the lifetime of the S_1 state, reducing the average population of the excited state and – potentially – the likelihood of higher order excitation. The depletion laser also has a low likelihood of causing excitation to the S_1 state either through anti-Stokes excitation or multi-photon excitation (when using pulsed lasers).

The depletion laser also drives stimulated emission from the S_1 state to the ground state (rate $\sigma_{depl} I_{depl}$), which reduces the lifetime of the excited state and competes with processes such as intersystem crossing, higher order excitation and photobleaching. Modifying equation 7 to reflect the influence of the depletion laser gives

$$P_B = \left(\frac{B_{S_1} + \frac{k_{ISC}}{k_{ph}} B_{T_1}}{k_{fl} + \sigma_{depl} I_{depl}} \right) + \left(\frac{\frac{\sigma^{exc}_{S_1S_N}}{K_{S_NS_1}} B_{S_N} + \frac{\sigma^{exc}_{T_1T_N} k_{ISC}}{K_{T_NT_1} kph} B_{T_N}}{k_{fl} + \sigma_{depl} I_{depl}} \right) I_{exc} + \left(\frac{\frac{\sigma^{depl}_{S_1S_N}}{K_{S_NS_1}} B_{S_N} + \frac{\sigma^{depl}_{T_1T_N} k_{ISC}}{K_{T_NT_1} kph} B_{T_N}}{k_{fl} + \sigma_{depl} I_{depl}} \right) I_{depl}. \quad (9)$$

P_B and N_{cyc} are plotted for the hypothetical fluorophore described in table 1, with an excitation laser intensity of 10 kWcm^{-2}. P_B in STED is 10–20 times larger than for confocal microscopy with the same excitation laser intensity. P_B begins to saturate when $\sigma_{depl} I_{depl} \gg k_{fl}$. The increase in P_B leads to a reduction in the number of fluorescence cycles the population can undergo, which tends towards 4.5% of the equivalent value in confocal microscopy. This limits the number of STED images that can be acquired as part of a time series or z-stack.

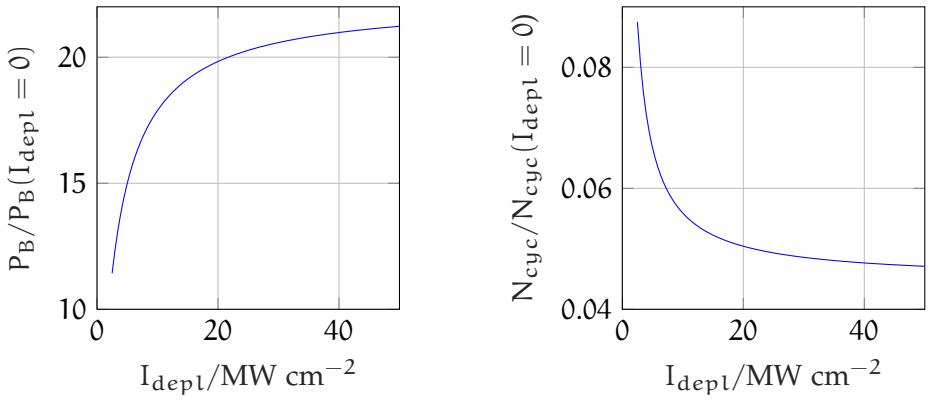

(a) Relative probability of photobleaching (I_{exc}=10 kWcm^{-2})

(b) Cycles before population reduced to $1/e$ (I_{exc}=10 kWcm^{-2})

Figure 26: **Photobleaching in STED microscopy.** 26a The probability of photobleaching upon being excited to the S_1 state for increasing depletion intensity. For the fluorophore in table 1 the probability of photobleaching is 10–20 times higher than in confocal microscopy and increases for increasing depletion laser intensity. Notably, this begins to saturate for $\sigma_{depl} I_{depl} \gg k_{fl}$. 26b Similarly, the number of cycles before the population is reduced to $1/e$ decreases with increasing intensity and tends towards 4.5% of the equivalent value in confocal microscopy. 50 MW cm^{-2} is the depletion intensity required for 50 nm resolution for this fluorophore.

Another consideration is reexcitation from S_0 to S_1 by the depletion laser. This can either be by anti-Stokes excitation (rate, $\sigma_{AS} I_{depl}$) or two-photon excitation (rate, $\sigma_{2PE} {I_{depl}}^2$) when using pulsed lasers. The motivation for using pulsed lasers and strategies to reduce two-photon excitation by the depletion laser are discussed in chapters 4 and 5. For this discussion it is assumed that two-photon reexcitation is negligible. Reexcitation by the depletion laser leads to an increased rate of excitation to the S_1 state compared to confocal microscopy. The rate of photobleaching, including anti-Stokes reexcitation with the depletion beam, is plotted in figure 27a.

In the depletion intensity range commonly used in STED (greater than the saturation intensity, 2.5 MW cm^{-2}), the rate of photobleaching scales linearly with depletion intensity. Similarly, the rate of pho-

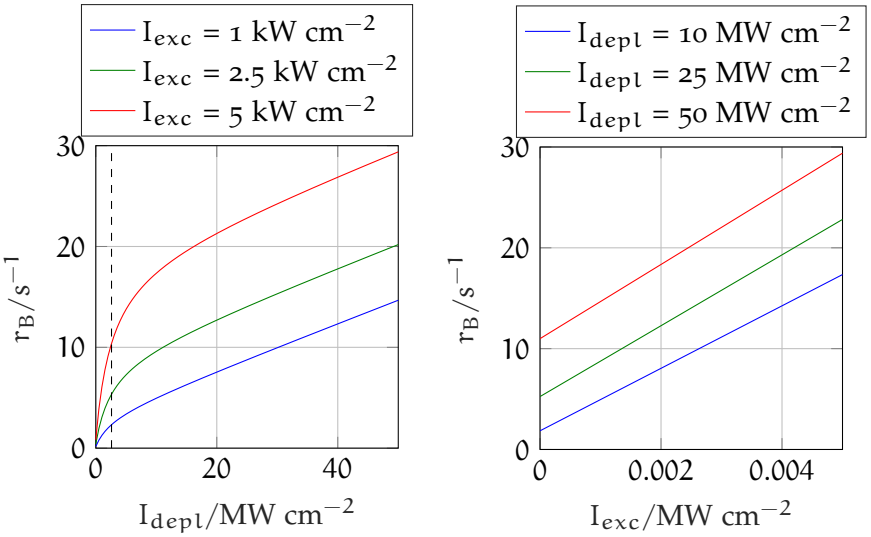

(a) Fixed excitation intensity

(b) Fixed depletion intensity

Figure 27: **Increase in the rate of photobleaching in STED.** Where $r_B = p_B \times (\sigma_{exc} I_{exc} + \sigma_{AS} I_{depl})$. The rate of photobleaching is up to 30 times higher than in confocal microscopy. 27a For depletion intensities higher than the saturation intensity (I_S, dashed black line) the rate of photobleaching scales approximately linearly with depletion intensity. 27b The rate of photobleaching in STED scales linearly with excitation intensity.

tobleaching scales linearly with excitation intensity. As the overall rate of depletion scales linearly with intensity, it can be assumed that total photobleaching is proportional to total photon dose in STED microscopy.

3.2.4 *Photobleaching in RESOLFT*

As previously discussed, RESOLFT is an alternative to STED that uses confocal like intensities and; therefore, potentially has a lower rate of photobleaching than STED. The probability of photobleaching in RESOLFT is described by a modified version of equation 7, which includes the alternative decay channel of photoswitching (k_{sw}):

$$P_B = \left(\frac{B_{S_1} + \frac{k_{ISC}}{k_{ph}} B_{T_1}}{k_{fl} + k_{sw}} \right) + \left(\frac{\frac{\sigma^{exc}_{S_1 S_N}}{K_{S_N S_1}} B_{S_N} + \frac{\sigma^{exc}_{T_1 T_N} k_{ISC}}{K_{T_N T_1} k_{ph}} B_{T_N}}{k_{fl} + k_{sw}} \right) I_{exc}. \quad (10)$$

For existing reversibly photoswitchable fluorophores, k_{sw} is approximately 2×10^5 s^{-1}. This is small relative to k_{fl} (~10^9 s^{-1}), implying the probability of photobleaching in RESOLFT is similar to in figure 24a.

Resolution enhancement in RESOLFT still requires saturation of the off-state. Unlike STED, saturation is achieved by depleting for a

longer time (of the order of milliseconds). This corresponds to a large amount of cycles being used to form a single image.

It will be shown in chapter 4 and during the discussion of protected STED [77] (section 3.2.6.2) that a total of $\frac{\sigma_{exc} I_{exc} + k_{fl} + k_{sw}}{k_{sw}}(1 - e^{-1})$ cycles are required to reduce the population of the on-state state to $1/e$. This corresponds to $\sim 3 \times 10^3$ cycles required every time the fluorophore is switched to the off-state and therefore the amount of photobleaching per image is 3×10^3 more than in equivalent confocal microscopy imaging.

At confocal intensities, the hybrid fluorophore in table 1 typically has 2×10^6 cycles before being photobleached (figure 24c). Therefore a fluorophore will only be able to be switched off $\frac{2 \times 10^6}{3 \times 10^3} \simeq 600$ times before it is photobleached (figure 24b). This limit is comparable to previously reported values of switching fatigue [104, 106, 113].

The limit also corresponds to approximately 30 times fewer images than in STED at the same resolution, although developing fluorophores with increased k_{sw} will reduce both photobleaching and the effects of switching fatigue.

3.2.5 *Photobleaching limits signal in single STED and RESOLFT images*

Due to the spatial shaping of the depletion beams in STED and RESOLFT, molecules may be interacting with the depletion or excitation laser when not emitting signal photons (for instance the flourophore in figure 28). This can mean that molecules have been photobleached before they are imaged. In this section the spatial shape of the depletion beam, and therefore the spatial dependence of photobleaching, is considered.

Figure 29 shows a spatial profile of the rate of photobleaching for the hybrid fluorophore described in table 1 during STED imaging. For a depletion intensity of of 50 MW cm^{-2}, commonly used in STED, a peak rate of photobleaching 15 times higher than in confocal microscopy is observed, for this fluorophore. Crucially, this photobleaching occurs in the side-lobes, over a larger area than in confocal microscopy. This means that photobleaching is at its highest rate when the fluorophore is not being detected. This implies that high depletion intensities may reduce the signal to be too low for imaging, even in the first STED image – imposing a practical limit on the maximum depletion intensity and therefore resolution [79].

In summary, this suggests that minimising the depletion intensity required for a given resolution is crucial for enabling high resolution STED imaging, z-stacks and time lapse images

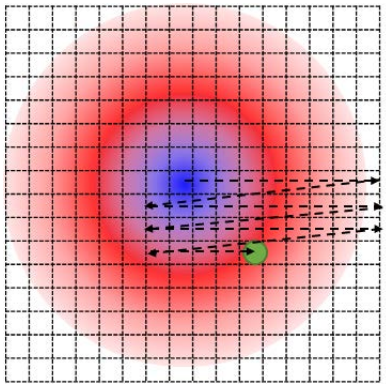

Figure 28: **Fluorophores not at the depletion minimum undergo photobleaching before they are imaged.** The fluorophore (green circle) undergoes both excitation and depletion. Both of these interactions can lead to photobleaching. Photobleaching can occur in each of the pixels prior to the fluorophore being at the depletion minimum leading to a reduction in available signal before the fluorophore is detected. The pixel size in this schematic corresponds to 10 nm.

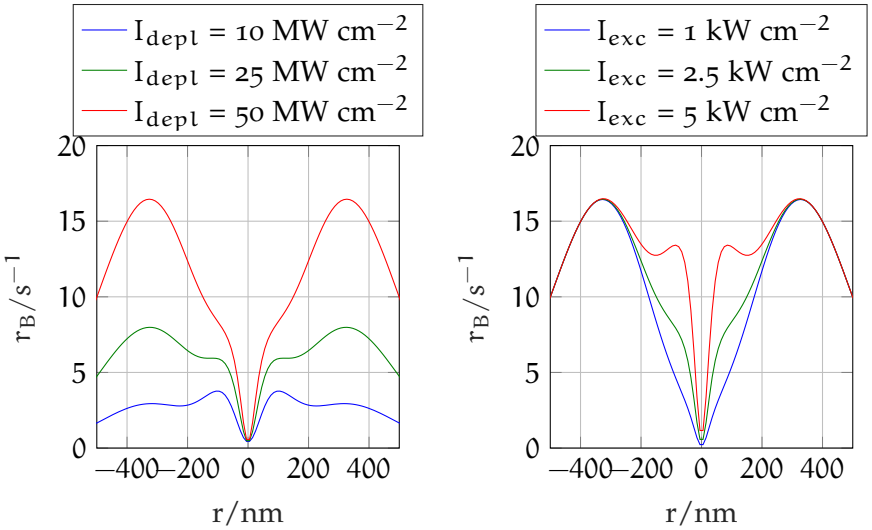

(a) $I_{exc} = 2.5$ kW cm^{-2} (b) $I_{depl} = 50$ MW cm^{-2}

Figure 29: **Spatial profile of photobleaching rate in STED.** Where $r_B = p_B \times (\sigma_{exc} I_{exc} + \sigma_{AS} I_{depl})$. 29a For fixed excitation, increasing the depletion intensity increases the rate of photobleaching in the side lobes due to a combination of the increased probability of photobleaching and anti-Stokes excitation. 29b For fixed depletion, increasing excitation intensity increases photobleaching at the centre of the PSF due to increases excitation.

3.2.6 *Reducing photobleaching*

For conventional intensities and fluorophores, the rate of photobleaching can be approximated as scaling linearly with intensity in STED and RESOLFT. Therefore, the amount of photobleaching can be approximated as being dependent on the total photon dose.

Both STED and RESOLFT require a certain intensity, or total photon dose, to achieve a given resolution, which is calculated in chapter 4; however, photobleaching in STED and RESOLFT can limit the available signal in a single image, leading to a limit on the amount of depletion and therefore achievable resolution of an image.

Photobleaching is considered a key limitation of STED and RESOLFT. A range of new techniques have been proposed to reduce photobleaching in STED and RESOLFT, some of these are discussed in the following section.

3.2.6.1 *General strategies*

Selection of photostable dyes

The scaling of r_B with respect to excitation or depletion intensity depends upon the photophysical properties of the fluorophore. Choosing a fluorophore with a low overall probability of photobleaching (P_B) or, in STED, low σ_{AS} reduces the rate of photobleaching. Hotta *et al.* [110] investigated two fluorophores with similar absorption and emission spectra but different σ^{depl}_{S1SN}, observing that the fluorophore with a lower excited state absorption-cross section photobleaches less in STED. Similarly many users choose a long wavelength for depletion to minimise σ_{AS}, at the expense of reducing σ_{depl}.

For live cell imaging users are often constrained to imaging fluorescent proteins or live cell compatible dyes. Fluorescent proteins are typically less photostable than organic dyes, which has imposed a limit on the application of STED to imaging live cells. Notably, where STED has been performed on live-cells it has generally been limited to cells labelled with the yellow fluorescent protein (YFP), which has been found to have good photophysical properties for STED.

As will be discussed in chapter 4, the laser sources best optimised for STED are designed for the depletion of red dyes and therefore are not compatible with imaging yellow fluorescent proteins. Recently, organic dyes which are compatible with STED live-cell imaging have been developed [30–33].

Antifading agents

Similar to choosing more photostable, fluorophores antifading agents, which reduce the rate of photobleaching, can be introduced to the imaging medium [122]. The mechanism for one set of these agents

involves acting as a reducing or oxidising agent that reduces the population of triplet or radical states [123]. Alternatively, reagents can be introduced that remove molecular oxygen [124], reducing triplet state reactivity but increasing the triplet state population.

These methods can increase the number of images that can be acquired during imaging. Although these methods are well adapted to imaging fixed samples [124], they are generally not compatible with live cell imaging [125].

Replacing photobleached dye with non-photobleached dyes

In live cell imaging, reducing photobleaching by changing the fluorophore or imaging medium is challenging and therefore photobleaching may be unavoidable, particularly during long-term imaging. If photobleached fluorophores could be replaced with fluorophores that have not been photobleached this would assist long-term imaging.

In certain cases, optical microscopy is being used to investigate sub-compartments of a larger cell, for instance dendritic spines of neurons. If only a single neuron is expressing a fluorescent protein which is free to diffuse throughout the cytosol, but remain within the cell, dendritic spines can be differentiated against a dark background. A small imaging area, for instance a dendrite, can be selected and imaged. Over time the fluorescent protein within the imaging volume will be photobleached; however, this is replaced by the diffusion of non-photobleached fluorescent protein from elsewhere in the cell [126].

A range of fluorescent labelling strategies can be used in this type of study including cytosolic YFP [5, 127], LifeAct-YFP [128, 129] (which binds transiently to actin), and LifeAct-mNeptune2.5 [109], as well as organic dyes introduced into live cells by patch-clamps [130].

3.2.6.2 *Strategies specific to STED*

D-Rex, T-Rex and resonant scanners

Although in STED and confocal microscopy, for conventional depletion and excitation intensities, the rate of photobleaching scales linearly with intensity. Outside of these ranges, notably for high excitation intensities or low depletion intensities, the rate of photobleaching begins to scale non-linearly (figure 24d, 27a). Reducing the excitation intensity, such that it is in the linear range of figure 24d, or reducing the depletion intensity, such that it is in the non-linear range of figure 27a, will lead to an overall reduction in the amount of photobleaching.

Particularly in STED, the minimum value of the depletion laser intensity is limited by the resolution that is required, and therefore

cannot be lowered. STED requires high intensities such that the probability of stimulated emission is greater than the probability of fluorescence emission (which typically occurs within nanoseconds). Intensity-dependent photobleaching occurs due to excitation from the S_1 state to S_N or the T_1 state to T_N. Typically, the triplet state has a lifetime of hundreds of microseconds. Controlling the depletion intensity such that the intensity is high when the S_1 state is populated – to allow stimulated emission depletion – but low (or zero) when only the T_1 state is populated will allow high resolution STED with lower photobleaching.

This is achieved in D-Rex/T-Rex STED [102] by using pulsed lasers for excitation and depletion. Depletion pulses immediately follow excitation pulses and deplete the S_1 state to allow super-resolution imaging. There is a time of up to 2 µs between each excitation–depletion pulse train. In this time any fluorophores in the triplet state will decay to the singlet state [102, 131–133]. This reduces the average depletion intensity such that it is in the non-linear range in 27a. For instance, using T-REX STED Donnert *et al.* [102, 134] reported STED with reduced photobleaching and higher resolution using an average depletion intensity of 200 kW cm^{-2}. Due to the long time between pulses (4 µs) this imaging technique is relatively slow.

An alternative approach is investigated by Wu *et al.* [**Schneider2015**, 78, 133] using resonant scanners to increase the scan speed such that the time averaged depletion intensity is reduced to 10 $MWcm^{-2}$ leading to an approximately 2-fold decrease in total photobleaching.

Although the low imaging speeds of T-REX would not be ideal for live cell imaging, the use of resonant scanners is a potentially viable approach.

Protected STED

Figures 28 and 29 show that the rate of photobleaching is typically high around the side lobes where the depletion intensity is highest. This is related to excitation from the ground state by the depletion laser.

In order to be photobleached, fluorophores must be excited from the S_0 state to a higher energy state. Danzl *et al.* [77] propose that if fluorophores in the depletion region could be placed in a state where they could not be excited then photobleaching would be reduced. One such state is the off-state of a reversibly photoswitchable fluorescent protein, such as those used in RESOLFT. In this technique, so-called protected STED, fluorophores are photoactivated with a Gaussian beam; fluorophores outside of the centre are then off-switched using a vortex shaped RESOLFT laser. Finally, the fluorescence signal is read-out using an excitation beam overlaid with a vortex-shaped depletion beam.

It will be shown in chapter 4 that the number of molecules remaining in the on-state ($N_{on}(I_R, t_R)$) in RESOLFT after illumination for time t_R at intensity I_R is

$$N_{on}(I_R, t_R) = e^{-\frac{\sigma_{exc} I_R k_{sw}}{\sigma_{exc} I_R + k_{fl} + k_{sw}} t_R}, \tag{11}$$

where the initial population is one. The number of molecules photobleached (N_B^{RES}) in time t_R is the probability of photobleaching multiplied by the number of molecules transitioned to the excited state in this time:

$$\begin{aligned} N_B^{RES} &= P_B^{RES} \int_0^{t_R} \sigma_{exc} I_R N_{on}(I_R, t) \\ &= \frac{P_B^{RES}(\sigma_{exc} I_R + k_{fl} + k_{sw})}{k_{sw}} \left(1 - e^{-\frac{\sigma_{exc} I_R k_{sw}}{\sigma_{exc} I_R + k_{fl} + k_{sw}} t_R}\right) \end{aligned} \tag{12}$$

where the probability of photobleaching in RESOLFT is described by equation 10 and is referred to here as $P_B^{RES}(I_R)$. The number of molecules photobleached during the STED phase is

$$\begin{aligned} N_B^{STED} &= P_B^{STED} \int_0^{t_S} (\sigma_{exc} I_{exc} + \sigma_{AS} I_{depl}) N_{on}(I_R, t) \\ &\simeq r_B^{STED} t_S e^{-\frac{\sigma_{exc} I_R k_{sw}}{\sigma_{exc} I_R + k_{fl} + k_{sw}} t_R}, \end{aligned} \tag{13}$$

where t_S is the STED imaging time and $r_B^{STED}(I_{exc}, I_{depl})$ is the rate of STED photobleaching shown in figure 27. Due to the relatively short STED readout times it is assumed that photoswitching is negligible.

The total photobleaching in protected STED is $N_B^{TOT} = N_B^{RES} + N_B^{STED}(t_R)$ and the improvement over STED only ($N_B^{STED}(t_R = 0)$) is therefore described by the expression

$$\begin{aligned} N_B^{TOT} = \\ \left(r_B^{STED} t_S - \frac{P_B^{RES}(\sigma_{exc} I_R + k_{fl} + k_{sw})}{k_{sw}}\right) \left(1 - e^{-\frac{\sigma_{exc} I_R k_{sw}}{\sigma_{exc} I_R + k_{fl} + k_{sw}} t_R}\right), \end{aligned} \tag{14}$$

suggesting that, providing the total photobleaching in RESOLFT is less than in STED, the improvement will increase for increasing t_R. This principle was verified experimentally by Danzl *et al.* [77] for rsEGFP2, where photobleaching was reduced by a factor 4 in protected STED over conventional STED. A secondary advantage of this technique is that the RESOLFT process is also enhancing the resolution, and this may lead to a reduction in required depletion intensity. The imaging time of this technique is comparable to the imaging time in RESOLFT.

Although protected STED uses fluorescent proteins and is therefore compatible with live cells, it is yet to be demonstrated that the protected STED on rseGFP2 is less photobleaching than conventional STED on, for instance, YFP, which is more commonly used in STED. The imaging time is also long compared to conventional STED.

Minimising photobleaching outside of the centre of the depletion spot

A key aim of protected STED is reducing photobleaching in the regions where the STED depletion laser is most intense. As previously discussed, this has an impact on the achievable signal in single image STED imaging.

A range of new STED imaging techniques have been recently proposed, which aim to reduce the exposure of fluorophores to the depletion laser and, therefore, photobleaching. One such technique is MINFIELD [79]. In this technique, fields of view are chosen that are less than 200 × 200 nm^2 in area. This corresponds to imaging the area shown in figure 30a. Figure 30b shows the distribution of the rate of photobleaching. Notably, for a 200 × 200 nm^2 area, the peak rate of photobleaching is 5 s^{-1} (a three-fold improvement over standard STED (figure 29). This method reduces both the maximum rate of photobleaching and the number of cycles the fluorophore will undergo during a single image (compare figure 30a to figure 28). Gottfert *et al.* [79] measured an up to 100-fold decrease in photobleaching in MINFIELD over standard STED.

MINFIELD requires a small field of view compared to conventional STED (200 × 200 nm^2). This technique is therefore well adapted to imaging sparse sub-diffraction limit features. It allows either higher resolution, single-shot imaging through allowing higher depletion intensities to be used or acquiring z-stacks. Although multiple frames can be acquired in MINFIELD, time-lapse movies can only be acquired of strucutures that do not move out of the, small, imaging volume.

In principle, MINFIELD could be combined with RESOLFT imaging; however, acquisition times in RESOLFT may prevent this if the sample moves out of the field of view during acquisition. Similarly the method could be combined with D-REX/T-REX to further reduce photobleaching but the increase in imaging time may be prohibitive.

MINFIELD is not well adapted to imaging larger structures such as actin networks in live cells. Alternative techniques which modulate the intensity to minimise unnecessary photodamage have been proposed. In the RESCue STED [75] technique it is recognised that the fluorophore in figure 28 will not emit signal but may still be photobleached by the depletion beam. Therefore, the depletion and excitation lasers are turned off in pixels where the signal is below a given threshold, minimising the time fluorophores not at the depletion minimum are exposed to the high intensity depletion beam.

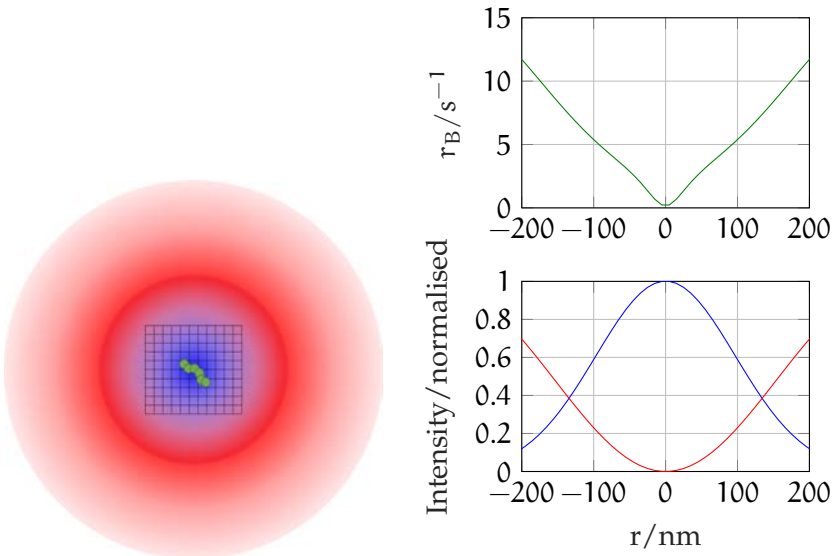

(a) MINFIELD FOV

(b) Rate of photobleaching close to depletion minimum

Figure 30: **Photobleaching in MINFIELD STED [79].** 30a Schematic representing the field of view where STED imaging is performed in MINFIELD. A subdiffraction limit field of view is selected based on a confocal image and the feature is then imaged in high resolution. 30b A line profile showing that by selecting a 200 × 200 nm^2 field of view the maximum rate of photobleaching is reduced to 5 s^{-1} (a three-fold improvement on standard STED (figure 29)). The green line represents the rate of photobleaching, blue the normalised excitation PSF and red the normalised depletion PSF.

Similarly, DyMIN [76] modulates the depletion intensity in response to the fluorescence signal such that the depletion intensity is just high enough to quench fluorescence, up to a maximum depletion intensity defined by the target resolution. DyMIN further reduces unnecessary exposure to high intensity depletion beams. Total photobleaching in DyMIN is slightly higher than in MINFIELD; however, this technique can be used for imaging larger fields of view and notably live cells.

Many of these strategies are highly advanced, but could be retrofitted to a system if necessary. It is therefore prudent to build a STED or RESOLFT system that can achieve the highest possible resolution and consider adding these modifications if necessary. To a first approximation photobleaching in STED and RESOLFT is proportional to photon dose. Intensity should also be minimised [135]. In the following section, the relationships between the resolution of STED, RESOLFT and their variants with photon dose and intensity is investigated theoretically to allow comparison of these techniques.

4

THEORETICAL AND PRACTICAL COMPARISON OF STED AND RESOLFT TECHNIQUES

4.1 INTRODUCTION

Aim

In the previous discussion it was decided that STED and RESOLFT type microscopies were introduced and the major challenge of photobleaching was outlined. In this chapter different techniques in STED and RESOLFT microscopy are compared in terms of the intensity and photon dose required to achieve a given resolution. By considering theoretical and practical considerations the type of microscope to be developed in this work is selected.

Motivation

Since the first proposal of STED microscopy in 1994 by Hell *et al.* [22] and demonstration in 2002 [136] a range of microscopes have been developed based around this principle. In general these techniques differ in the type of laser used for depletion (pulsed or cw) and the depletion intensity required for a given resolution. It has been suggested that STED with pulsed or cw lasers (hereafter pulsed STED and cw-STED) can be further improved by using time-gated detection which rejects lower resolution early emitted photons [36, 137].

Although each of these STED modes (pulsed STED [39], cw-STED [39], time-gated pulsed STED [37, 137] and time-gated cw-STED [37, 137]) have been well described in the literature in terms of their suppression factor it is difficult to directly compare some STED modes in the common term of saturation intensity (I_S), which indicates the depletion intensity required for a given resolution [37, 39]. This makes both the direct comparison of STED modes and the identification of limiting factors in STED resolution challenging.

This is particularly relevant in RESOLFT [38], where theoretical values for the suppression factor and saturation intensity are less commonly discussed. These values are also more difficult to compare to those for STED techniques as, although the time averaged intensities in RESOLFT are lower than in STED, the longer dwell times in RESOLFT may mean that a comparable total number of depletion photons are required. Finally, in RESOLFT, more fluorescence photons are typically detected per fluorophore due to the photoswitching mechanism, making RESOLFT and STED difficult to directly compare in terms of theoretical resolution. Therefore it is more relevant to com-

pare STED and RESOLFT in terms of total photon efficiency – total number of depletion photons required per signal photon.

The consideration of photon efficiency in STED is also relevant in modes that use time-gated detection. In these techniques signal photons are inherently rejected to allow the reduction of depletion intensity. This potentially leads to a reduced SNR and therefore longer exposure times. This suggests that saturation intensity alone does not tell the full story [138].

Structure

In this section STED and RESOLFT microscopy techniques are discussed in terms of the photophysics of dyes during depletion. The origin and theory of increases in resolution due to pulsed depletion and time gating are discussed in detail and the techniques are compared in terms of theoretical resolution. To assist direct comparisons, particularly with RESOLFT, the parameter γ_S is defined, which is the number of depletion photons required per fluorescence photon.

Having considered the theoretical performance of the techniques' practical limitations such as laser sources available, compatible fluorescent markers, experimental complexity and cost of systems are discussed allowing a design strategy for the microscope developed in this thesis to be formed.

4.2 DEFINITION OF KEY PARAMETERS RELATED TO STED AND RESOLFT RESOLUTION

4.2.1 *Excited and ground states*

For simplicity the fluorophores used in STED are approximated as a four level system represnted in figure 31, where states A' and A represent the ground state and states B' and B represent the excited state. States A and B are the lowest energy levels of the ground and excited state. A' and B' represent higher vibrational energy states.

4.2.2 *Suppression factor*

The suppression factor ($\eta(r)$) is the factor by which the depletion laser quenches fluorescence and is defined as the ratio of fluorescence detected in the presence of a depletion laser of intensity $I_{depl}(r)$ to that without a depletion laser:

$$\eta(r) = \frac{N_F(I_{depl})}{N_F(I_{depl} = 0)} = \frac{\int_{t_0}^{t_1} n_F(t, I_{depl})dt}{\int_{t_0}^{t_1} n_F(t, I_{depl} = 0)dt}, \tag{15}$$

where N_F is the total number of fluorescence photons emitted in a given time and $n_F(t)$ is the instantaneous number of fluorescent pho-

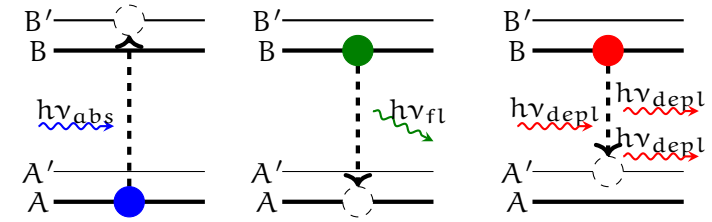

(a) Fluorescence excitation (b) Fluorescence (spontaneous) emission (c) Stimulated emission (depletion)

Figure 31: **Stimulated emission depletion in fluorescence microscopy.** In STED the molecule is excited from the dark ground state (A) to a vibrational energy level (B′) of the bright, excited, state (B) (31a). Thermal transitions transfer the molecule to the lowest energy excited state (B). A molecule in this state can return to the ground state (B $\rightarrow$ A) through spontaneous emission (fluorescence) as in 31b or through stimulated emission in the presence of a photon of energy $h\nu_{depl}$ (31c), The wavelength (λ_{depl}) and therefore $h\nu_{depl}$ can be selected such that it is spectrally distinct from λ_{fl}.

tons emitted. t_0 and t_1 are the times at which detection starts and finishes, respectively.

An example suppression factor PSF is plotted in figure 32 for a common approximation of the suppression factor ($\eta(r) = e^{-I_{depl}(r)/I_S}$) where the depletion intensity distribution is given by the Laguerre-Gaussian (LG_{01})

$$I_{depl}(r) = \epsilon r^2 e^{-2r^2/\omega^2}, \tag{16}$$

where $\epsilon = 4I_{av}/\omega^2$ is a factor related to the distribution of the STED intensity, and ω is the $1/e$ waist of the electric field [37], I_{av} is the average intensity of the depletion beam and r is the distance from the centre of the PSF. The STED or RESOLFT PSF is the product of the suppression factor and confocal PSF ($h_{S,R} = \eta \times h_C$).

It is shown in this chapter that the shape of $\eta(r)$ varies depending upon the STED mode. However it is behaviour for low r (and $I_{depl}(r)$) that is most relevant to STED [79] and to first approximation these modes all have the same shape.

4.2.3 *Peak and average saturation intensity, and total saturation energy*

The saturation intensity (I_S) is the average depletion intensity required to reduce the probability of fluorescence emission to $1/e$. For STED with pulsed depletion $I_S = I_S^{peak} t_p/t_{duty}$ where t_p and t_{duty} are the pulse duration and time between pulses, respectively. I_S^{peak} is the peak pulse intensity required to reduce the probability of fluorescence emission to $1/e$. For comparison with RESOLFT the total

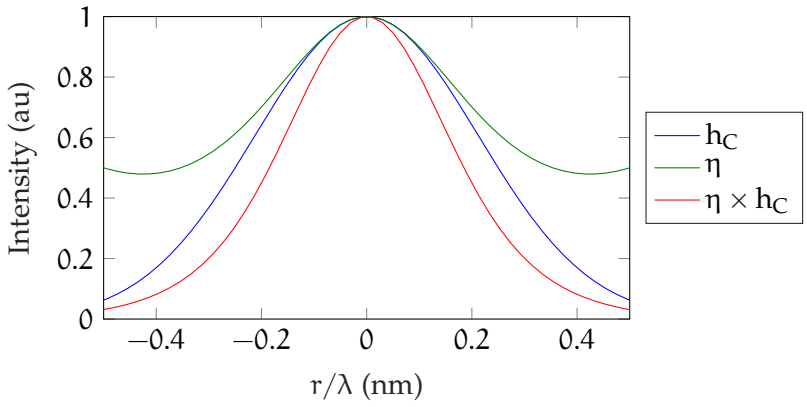

Figure 32: **Suppression factor in STED or RESOLFT microscopy.** The suppression factor PSF ($\eta = e^{-I_{depl}(r)/I_S}$) is shown for $I_{av} = I_S$ relative to the confocal PSF (h_C). The STED/RESOLFT PSF ($h_C \times \eta$) is shown – representing a resolutio enhancement relative to confocal. The STED/RESOLFT FWHM is $\Delta r_{S,R} = h_C/\sqrt{2}$

energy ($E_S = I_S t_S$) as typical exposure times in RESOLFT are longer than in STED.

Generally a lower saturation intensity (or energy) is preferred for STED as it reduces the power requirements of the depletion laser and thus the likelihood of photobleaching and photodamage to the sample for a given resolution.

4.2.4 *Resolution enhancement*

For a confocal PSF $h_C = e^{-4r^2/\omega^2}$ the FWHM is $\Delta r_C = \omega\sqrt{\ln 2}$. For the suppression factor $\eta(r) = e^{(-I_{depl}(r)/I_S)}$ the STED or RESOLFT PSF is

$$h_{S,R} = \exp\left(-\frac{4r^2}{\omega^2} - \frac{4I_{av}r^2}{I_S\omega^2}e^{-r^2/\omega^2}\right), \tag{17}$$

which close to the centre of the PSF can be approximated as

$$\lim_{r\to 0} h_{S,R} = e^{-\frac{4r^2}{\omega^2}\left(1+I_{depl}/I_S\right)}, \tag{18}$$

and the FWHM as [97]

$$\Delta r_{S,R} = \frac{\omega\sqrt{\ln 2}}{\sqrt{1+I_{depl}/I_S}} = \frac{\Delta r_C}{\sqrt{1+I_{depl}/I_S}}. \tag{19}$$

A STED or RESOLFT PSF for $I_{depl} = I_S$ is shown in figure 32 – the resolution enhancement is $1/\sqrt{2}$. The resolution in STED and RESOLFT is theoretically only limited by the ratio of I_{av} to I_S.

4.2.5 *Photon efficiency*

In practice STED or RESOLFT resolution is limited, in part, by the depletion intensity that can be delivered to the sample and therefore either by the power of the depletion laser source or by photobleaching or photodamage induced by the depletion laser. It is advantageous to reduce the saturation intensity either by choosing fluorophores that have low saturation intensities or by employing STED modes that have reduce saturation intensity such as pulsed depletion or time resolved detection.

Although time resolved detection reduces the saturation intensity for STED microscopy techniques with pulsed excitation it is important to consider that some signal photons are rejected by these techniques. Therefore for the same SNR more excitation and depletion cycles are required and therefore a higher total photon dose will be needed.

To allow comparison between time-gated and non time-gated detection the saturation photon efficiency γ_S is defined as ratio of time averaged fluorescence emission at $r = 0$ ($n_F(r = 0)$) to the saturation intensity:

$$\gamma_S = \frac{n_F(r = 0)}{I_S}, \tag{20}$$

A higher γ_S implies a lower photon dose. The numerator in this term is similar to the peak SNR discussed by Vicidomini *et al.* [137].

In the following section four STED modes (cw-STED, time-gated cw-STED, pulsed STED and time-gated pulsed STED) as well as some specific variants (cw-STED with pulsed excitation, pulsed STED with short pulses) are discussed in the context of their suppression factors, peak and average saturation intensities, and their photon efficiency. These methods are then contrasted in terms of practical constraints such as available laser sources, fluorophores and experimental complexity.

The same parameters are then discussed for RESOLFT and this method is compared with STED.

4.3 THEORETICAL COMPARISON OF STED MODES

4.3.1 *General principle of STED*

4.3.2 *cw-STED*

A relatively simple and low cost version of STED microscopy can be carried out using continuous wave (cw) lasers [35]. In this configuration the sample is continuously illuminated with lasers of wavelength λ_{abs} and λ_{depl} and fluorescence continuously collected. This is illustrated in figure 33.

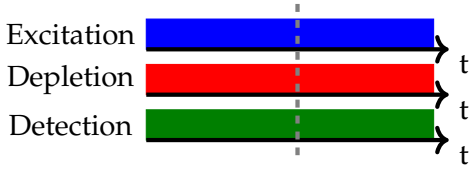

Figure 33: **Temporal control in continuous wave STED.** In cw-STED the sample is continuously illuminated at both the excitation and depletion wavelength ($\lambda_{exc}, \lambda_{depl}$) and fluorescence emission (λ_{em}) is continuously collected. The system is considered to reach a steady state.

Suppression factor in cw-STED

Assuming that states A' and B' (figure 31) have lifetimes much shorter than the lifetimes of A and B – that is to say molecules in A' and B' decay instantaneously to A and B, respectively – the rate equation for the change of population of state B (N_B) can be written as

$$\frac{dN_B(t)}{dt} = -(k_{fl} + k_{depl})N_B(t) + k_{exc}N_A(t), \tag{21}$$

where k_{fl} ,k_{depl} and k_{exc} are the rates of fluorescence emission, stimulated emission and fluorescence excitation respectively. Assuming the system is in the steady state ($\frac{dN_B(t)}{dt} = 0$) and all molecules are in either state A or state B ($N_A(t) + N_B(t) = 1$) this can be written as

$$N_B = \frac{k_{exc}}{k_{fl} + k_{depl} + k_{exc}}. \tag{22}$$

The number of fluorescent photons, n_F, emitted per unit time can be written as

$$n_F(k_{depl}) = k_{fl}N_B(t) = k_{fl}\frac{k_{exc}}{k_{fl} + k_{depl} + k_{exc}}. \tag{23}$$

The suppression factor $\eta(k_{depl})$ is the ratio of photons emitted through fluorescence with to that without a depletion laser

$$\eta(k_{depl}) = \frac{n_f(k_{depl})}{n_f(k_{depl} = 0)} = \frac{k_{fl} + k_{ex}}{k_{fl} + k_{ex} + k_{depl}}. \tag{24}$$

For typical excitation intensities (table 2) the rate of fluorescence excitation $k_{exc} = \sigma_{exc}I_{exc}$ (σ_{exc} is the absorption cross section at the excitation wavelength and I_{exc} is the excitation intensity) is much lower than the rate of emission ($k_{exc} \ll k_{fl}$) and depletion ($k_{exc} \ll k_{depl}$). The suppression factor can therefore be approximated as

$$\eta \simeq \frac{k_{fl}}{k_{fl} + k_{depl}} = \frac{1}{1 + \sigma_{depl}\tau_{fl}I_{depl}}, \tag{25}$$

where $\tau_{fl} = 1/k_{fl}$ is the fluorescence lifetime and k_{depl} is the product of the depletion laser intensity and the stimulated emission cross section at the depletion wavelength ($I_{depl}\sigma_{depl}$).

Saturation intensity in cw-STED

The saturation intensity I_S is average depletion intensity at which $\eta = 1/e$. Therefore in the continuous wave case the saturation intensity is

$$I_S = \frac{e-1}{\sigma_{depl}\tau_{fl}} \simeq \frac{1.7183}{\tau_{fl}\sigma_{depl}}. \tag{26}$$

The saturation intensity can be calculated for the common STED fluorophore ATTO 647N based upon the parameters in table 2. To achieve a resolution of 50 nm, based on equation 17, the intensity I_{depl} required is $\sim 40 \times I_S$, corresponding to $\sim 20 \times 10^{25}$ photons/s or ~ 50 MWcm^{-2}. Assuming a diffraction limited depletion pattern this corresponds to available laser power of 250 mW where $P = \pi\omega^2 I_{av}$. This is comparable to values reported by Vicidomini *et al.* [36].

Parameter	Value	Comments and reference
σ_{exc}	10^{-16} cm^2	absorption cross-section10^{-15}–10^{-17} cm^2 quoted in [81]
I_{exc}	10 kWcm^{-2}	Order of magnitude intensity used in cw-STED [35, 139]
τ_{fl}	3.5×10^{-9} s	Typical fluorescence lifetime of ATTO 647N
σ_{depl}	10^{-16} cm^2	Typical depletion cross-section quoted in [23]
λ_{exc}	640 nm	Excitation wavelength of ATTO 647N [102, 103]
λ_{depl}	765 nm	Depletion wavelength of ATTO 647N [102, 103]
NA	1.4	Numerical aperture of a common high resolution objective
Γ	80 MHz	Repetition rate of Ti:S laser commonly used in STED

Table 2: **Typical values of parameters affecting resolution in STED.**

Photon efficiency in cw-STED

The rate of fluorescence emission at $r = 0$ where $I_{depl} = 0$ is

$$n_F(r=0) = k_{fl}N_B = k_{fl}\frac{k_{exc}}{k_{fl}+k_{exc}} \simeq \sigma_{exc}I_{exc}, \tag{27}$$

for conventional excitation intensities. γ_S is therefore

$$\gamma_S = \frac{n_F}{I_S} = \frac{\tau_{fl}\sigma_{depl}\sigma_{exc}I_{exc}}{e-1}. \tag{28}$$

In the following sections this parameter will be compared in other STED and RESOLFT modes.

4.3.3 *cw-STED with pulsed excitation*

CW-sources with sufficient power for STED depletion are relatively common and instruments using cw depletion are relatively simple

to implement as no temporal alignment is required. Pulsed sources with sufficient power for fluorescence excitation can also be used and include supercontinuum sources, for arbitrary wavelength selection, and sources for 2-photon excitation. The steps involved in this STED mode are represented in figure 34.

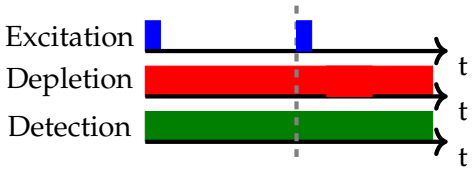

Figure 34: **CW STED with pulsed excitation.** Here excitation is from a pulsed laser source but depletion is with a cw laser. The suppression factor can be shown to be the same as for STED with all cw lasers [37, 39]. This mode could be used for 2-photon excitation STED [140–142]

Suppression factor and saturation intensity in pulsed cw-STED

At $t = 0$, immediately after a square pulse of peak intensity I_{exc}^{peak} and duration $t_{exc} \ll \tau_{fl}$ the excited state population is $N_B(t = 0) = \sigma_{exc} I_{exc}^{peak} t_{exc}$. The rate of decay from the excited state is

$$\frac{dN_B}{dt} = -(k_{depl} + k_{fl})N_B, \tag{29}$$

and the suppression factor is

$$\eta(k_{depl}) = \frac{\int_0^\infty N_B(k_{depl})}{\int_0^\infty N_B(k_{depl} = 0)} = \frac{k_{fl}}{k_{fl} + k_{depl}}, \tag{30}$$

this is the same as the approximation for conventional cw-STED in equation 25. Therefore I_S can also be written as

$$I_S = \frac{e - 1}{\sigma_{depl}\tau_{fl}}. \tag{31}$$

γ_S in cw-STED with pulsed excitation

As the time between pulses t_{duty} is long relative to the fluorescence lifetime it is assumed that all molecules have decayed $N_B(t_{duty}) = 0$. The average fluorescence at $r = 0$ in one duty cycle is therefore

$$n_F(r = 0) = \frac{\sigma_{exc} I_{exc}^{peak} t_{exc}}{t_{duty}} = \sigma_{exc} I_{exc}, \tag{32}$$

where $I_{exc} = I_{exc}^{peak} t_{exc}/t_{duty}$ is the intensity averaged over one duty cycle. γ_S is therefore

$$\gamma_S = \frac{n_F(r = 0)}{I_S} = \frac{\tau_{fl}\sigma_{depl}\sigma_{exc} I_{exc}}{e - 1}, \tag{33}$$

analagous to cw-STED.

4.3.4 *cw-STED with time-gated detection*

In cw-STED with pulsed excitation the amount of molecules that have been depleted by stimulated emission increases over time as more depletion photons arrive at the sample. Molecules emitting earlier after excitation have, therefore, been less affected by the depletion beam. Fluorescence is therefore more likely to have been emitted from the centre of the PSF at later time points [36, 37]. Figure 35 shows a comparison between $N_B(t, I_{depl})$ and $N_B(t, I_{depl} = 0)$, corresponding to the depleted region and centre of the PSF, as a function of time after the depletion pulse. For increasing t the suppression factor $\eta = N_B(t, I_{depl})/N_B(t, I_{depl} = 0)$ decreases. Suggesting that starting detection later after excitation (as in figure 36) will decrease the average suppression factor, increasing the resolution.

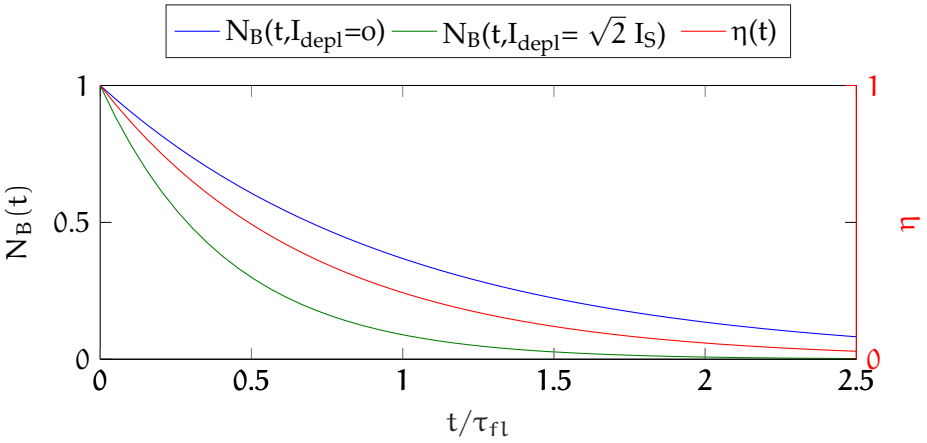

Figure 35: **Photon arrival times in cw-STED with pulsed excitation.** Excited state population in cw-STED for regions at the centre ($N_B(t, I_{depl} = 0)$) and depleted region ($N_B(t, I_{depl})$). The suppression factor (ratio of $N_B(t, I_{depl})$ to ($N_B(t, I_{depl} = 0)$) decreases – corresponding to higher resolution.

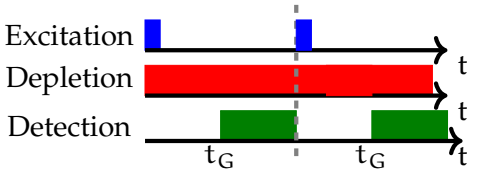

Figure 36: **cw-STED with time-gated detection.** Fluorescence emission is collected only at later time points (t_g) after the excitation pulse. This excludes lower resolution photons emitted early after the pulse at the expense of total signal.

The contribution of early and late emitted photons is shown in figure 37. The PSF emitted before a time gate t_g is lower resolution than the PSF emitted after t_g. The PSF emitted after t_g (corresponding to the PSF in time-gated cw-STED) is also higher resolution than the to-

tal PSF (corresponding to cw-STED). The affect is more pronounced for longer time gates (cw-STED, FWHM = 71 nm; time-gated t_g = 300 ps, 67 nm; t_g = 1000 ps, 59 nm).

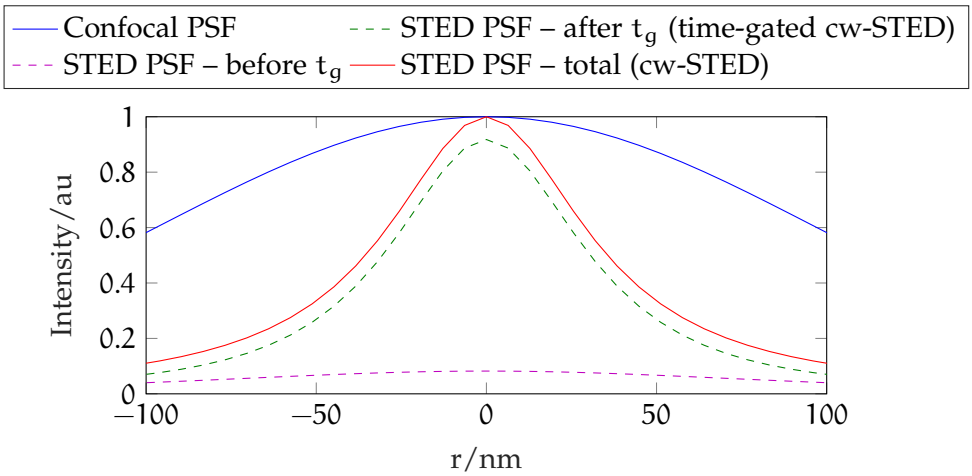

(a) t_g=300 ps, τ_{fl}=3.5 ns

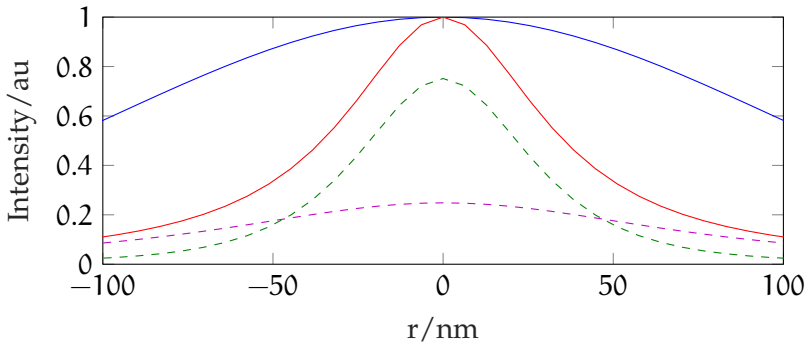

(b) t_g=1000 ps, τ_{fl}=3.5 ns

Figure 37: **Resolution in time-gated cw-STED.** The confocal, cw-STED and time-gated cw-STED PSFs are compared for (37a) 300 ps and (37b) 1000 ps time gates. Time-gated cw-STED has better resolution than conventional cw-STED, although there is a reduction in signal. For illustrative purposes fluorescence emitted prior to the time gate is shown.

Suppression factor in time-gated cw-STED

The suppression factor in time-gated cw-STED is

$$\eta(I_{depl}) = \frac{\int_{t_g}^{\infty} N_B(t, I_{depl})dt}{\int_{t_g}^{\infty} N_B(t, I_{depl}=0)dt} = \frac{1}{1+\tau_{fl}\sigma_{depl}I_{depl}} e^{-\sigma_{depl}I_{depl}t_g}. \tag{34}$$

Substituting in the suppression factor in cw-STED from equation 25 shows that time gated STED has a lower suppression factor for increasing t_g

$$\eta_{cw/tg} = \eta_{cw}(I_{depl})e^{-\sigma_{depl}I_{depl}t_g}. \tag{35}$$

As predicted the suppression factor scales exponentially with an increasing time gate. The effect of this on I_S and γ_S is discussed here.

Saturation intensity in time-gated cw-STED

The suppression factor (equation 34) is dependent on the depletion intensity and time gate. There is not a simple expression for the saturation intensity (I_S) but the saturation time gate (t_{gS}) can be represented, by rearranging equation 34 where $\eta(I_S, t_{gS}) = 1/e$, as

$$t_{gS} = \frac{\ln\left|\frac{e}{1+\sigma_{depl}I_S\tau_{fl}}\right|}{\sigma_{depl}I_S}. \tag{36}$$

Interestingly this can be written in terms of the the reduction of saturation intensity in time-gated cw-STED ($I_S^{cw/tg}$) over cw-STED (I_S^{cw}) based upon equation 26 as

$$\frac{t_{gS}}{\tau_{fl}} = \frac{\ln\left|\frac{e}{1+(e-1)\frac{I_S^{cw/tg}}{I_S^{cw}}}\right|}{(e-1)\frac{I_S^{cw/tg}}{I_S^{cw}}}, \tag{37}$$

suggesting that the improvement in saturation intensity of time-gated STED is dependent only on the ratio of time-gate duration and the fluorescence lifetime. Based upon this equation the reduction of saturation intensity in time-gated cw-STED ($\frac{I_S^{cw/tg}}{I_S^{cw}}$ is plotted as a function of t_{gS}/τ_{fl} in figure 38.

γ_S for time-gated cw-STED

For longer time gates the saturation intensity decreases, however for the same excitation intensity, this will lead to a reduction in in fluorescence emission detected. Only fluorescence emitted after t_g is detected such that the average fluorescence emission over one duty cycle (duration t_{duty})

$$n_F(r=0) = \sigma_{exc}I_{exc}\int_{t_g}^{\infty} N_B(I=0,t)dt = \sigma_{exc}I_{exc}e^{-t_G/\tau_{fl}}. \tag{38}$$

Based upon equation 28 the improvement in photon efficiency in time gated cw-STED, over cw-STED ($\gamma_S^{cw/tg}/\gamma_S^{cw}$) is

$$\frac{\gamma_S^{cw/tg}}{\gamma_S^{cw}} = \frac{I_S^{cw}e^{-t_g/\tau_{fl}}}{I_S^{cw/tg}(t_g)}. \tag{39}$$

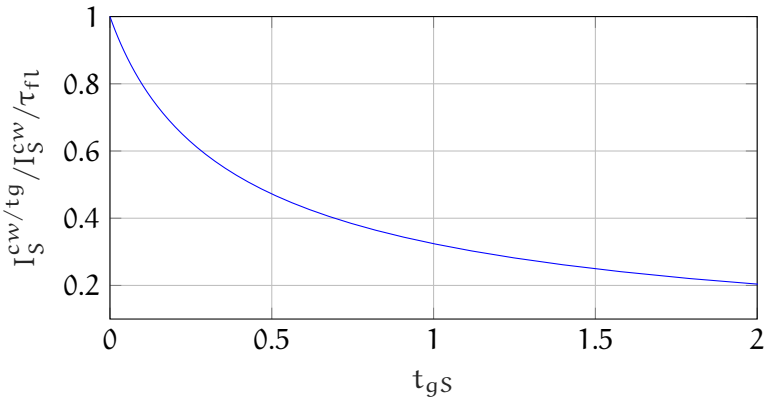

Figure 38: **Saturation intensity reduction in time-gated cw-STED.** The saturation intensity is reduced in time-gated cw-STED ($I_S^{cw/tg}$) for increasing time gates relative to cw-STED (I_S^{cw}). The improvement in saturation intensity is dependent only on the time gate duration relative to the fluorescent lifetime.

$\gamma_S^{cw/tg}/\gamma_S^{cw}$ is calculated by dividing the intensities shown in figure 38. This is plotted in figure 39. The photon efficiency of time-gated cw-STED initially improves up to an optimum time gate $t_G = 0.46\tau_{fl}$ and is then degraded as the loss in signal would lead to a longer acquisition time – for a given signal level – and therefore higher photon dose. The theoretically optimised time gate is similar to the time gate used in previous reports of time-gated cw-STED [143]

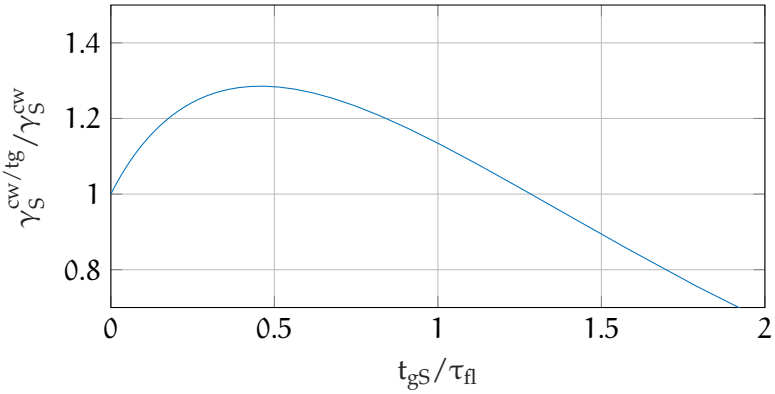

Figure 39: **Photon efficiency optimisation in time-gated cw-STED.** The photon efficiency is higher in time-gated cw-STED for time gates less than half the lifetime. An optimum time gate occurs at $t_g = 0.46\tau_{fl}$. For higher lifetime the loss in signal overcomes the reduction in depletion intensity.

At the optimum time gate the saturation intensity is $0.49I_S^{cw}$ and the photon efficency is $1.29\gamma_S^{cw}$. By using the analytically found opti-

mum time gate expressions for the optimum saturation intensity and photon efficiency can be found as

$$\begin{aligned} I_S(0.46\tau_{fl}) &= 0.49\frac{(e-1)}{\sigma_{depl}\tau_{fl}} \\ \gamma_S(0.46\tau_{fl}) &= 1.29\frac{\sigma_{exc}I_{exc}\sigma_{depl}\tau_{fl}}{(e-1)} \end{aligned} . \tag{40}$$

simple expressions for the these parameters have not been reported which has made direct comparison of time-gated cw-STED with other STED modes challenging.

4.3.5 *Pulsed STED*

In time-gated cw-STED it was found that early emitted photons degrade the resolution and therefore detection is limited to later time points after the depletion laser has had a more significant significant effect. An alternative is to concentrate the depletion photons to early time points after the excitation pulse by using a pulsed depletion laser of duration t_p, as represented in in figure 40.

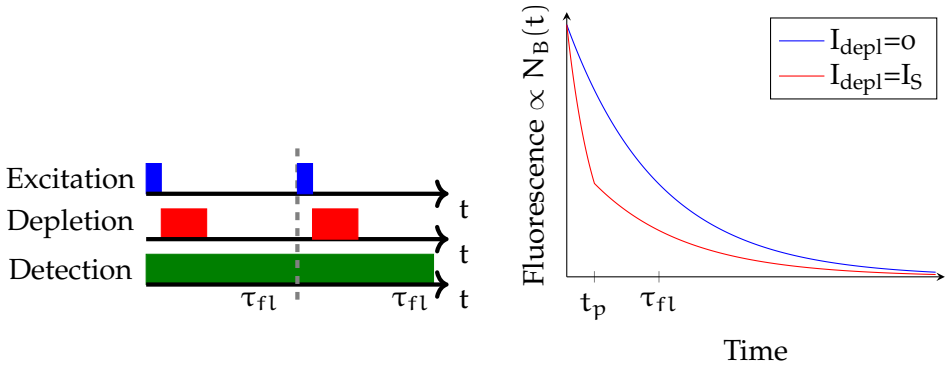

(a) Pulse sequence

(b) Population of the excited state

Figure 40: **Temporal control in pulsed STED.** 40a In pulsed STED both the excitation and depletion lasers are pulsed. These pulses are separated in time, such that there are is no re-excitation of depleted molecules during acquisition. Excitation pulses (duration 100 ps) transfer fluorophores in to an excited state. The depletion pulse (duration 200–300 ps) deplete the excited state after excitation. Usually pulses are much shorter than the fluorescence lifetime τ_{fl}, such that minimal fluorescence is emitted during the pulse. 40b The probability distribution for fluorescence at time (t) after excitation by a pulsed laser. The blue line shows the probability decay without a depletion laser. By concentrating the depletion power into time t_p the depletion can be maximised for a lower average intensity.

Suppression factor in pulsed STED

For pulsed excitation the population of the excited state $N_B(t)$ will vary as a function of time (t) after excitation as described by the rate equation

$$\frac{dN_B}{dt}(t) = -k_{fl}N_B(t) - \sigma_{depl}I_{depl}(t)N_B(t), \tag{41}$$

where the terms $k_{fl}N_B(t)$ and $\sigma_{depl}I_{depl}(t)N_B(t)$ represent the number of photons emitted at time (t) by fluorescence and stimulated emission, respectively. In the pulsed STED case, the pulse is assumed to be a square pulse of duration t_p, starting at $t = 0$ (immediately after excitation), with intensity peak power I_{depl}^{peak} – such that

$$I_{depl}(t) = \begin{cases} I_{depl}^{peak} & 0 \leqslant t \leqslant t_p \\ 0 & t > t_p \end{cases}. \tag{42}$$

The population of the excited state is therefore

$$N_B(t) = \begin{cases} e^{-(k_{fl}+\sigma_{depl}I_{depl}^{peak})t} & 0 \leqslant t \leqslant t_p \\ e^{-\sigma_{depl}I_{depl}^{peak}t_p}.e^{-k_{fl}t} & t > t_p \end{cases}. \tag{43}$$

The suppression factor (from equation 15) for one image cycle (where $t_{duty} \gg \tau_{fl}$ such that $t \to \infty$) is therefore

$$\eta = \frac{k_{fl}\int_0^\infty N_B(I,t)dt}{k_{fl}\int_0^\infty N_B(I=0,t)dt} = \frac{k_{fl}\left(\int_0^{t_p} N_B(I,t)dt + \int_{t_p}^\infty N_B(I,t)dt\right)}{k_{fl}\int_0^\infty N_B(I=0,t)dt}, \tag{44}$$

giving

$$\eta = e^{-(k_{fl}+\sigma_{depl}I_{depl}^{peak})t_p} + \frac{k_{fl}}{k_{fl}+\sigma_{depl}I_{depl}^{peak}}\left(1 - e^{-(k_{fl}+\sigma_{depl}I_{depl}^{peak})t_p}\right), \tag{45}$$

where the first term represents fluorescence emitted after the depletion pulse and the second term fluorescence emitted during the depletion pulse. This equation can be expressed in terms of the ratio of the pulse duration to the fluorescence lifetime, $\alpha = t_p/\tau_{fl}(= t_p k_{fl})$, and the energy density of the pulse, $E = I_{depl}^{peak}t_p$,

$$\eta = e^{-(\alpha+\sigma_{depl}E)} + \frac{\alpha}{\alpha+\sigma_{depl}E}\left(1 - e^{-(\alpha+\sigma_{depl}E)}\right). \tag{46}$$

For short pulses relative to the fluorescence lifetime ($t_p \ll \tau_{fl}$) α tends to zero ($\alpha \to 0$). This corresponds to concentrating all of the depletion at $t = 0$ when the population of the excited state is at its maximum and gives the lowest suppression factor for a given E. In this case the suppression factor can be approximated as

$$\eta(I_{depl}) = e^{-\sigma_{depl}I_{depl}t_p}. \tag{47}$$

Saturation intensity in pulsed STED (short pulses)

For pulses of finite duration there is not a simple solution for I_S, however, for short pulses the peak satuation intensity (I_S^{peak}) can be defined as

$$I_S^{peak} = \frac{1}{\sigma_{depl} t_p}. \tag{48}$$

Although, instantaneously, this intensity is high – the average intensity (I_S) of the pulse over its duty cycle is lower

$$I_S = \frac{1}{\sigma_{depl} t_{duty}}, \tag{49}$$

where t_{duty} is the time between pulses.

The ratio between I_S for cw-STED (I_S^{cw}) and the average for pulsed STED (I_S^p) is given by

$$\frac{I_{S_p}}{I_{S_{cw}}} = \frac{\tau_{fl}}{t_{duty}(e-1)}, \tag{50}$$

showing that, for a duty cycle greater than the fluorescence lifetime, the average depletion power in pulsed STED will be less than that in cw. This is because the power is concentrated in the time when it can be effective – before fluorescence has been emitted [35]. For ATTO 647N, pulsed STED has an I_S six times lower than cw-STED, corresponding to 3×10^{25} photons, 8 MWcm^{-2} or 40 mW in the back aperture of a 1.4 NA objective.

γ_S for short pulses

Similar to in section 4.3.3 the fluorescence emission is

$$n_F(r=0) = \frac{\sigma_{exc} I_{exc}^{peak} t_{exc}}{t_{duty}}, \tag{51}$$

such that

$$\gamma_S = \frac{n_F(r=0)}{I_S} = \sigma_{depl}\sigma_{exc} I_{exc} t_{duty}. \tag{52}$$

4.3.6 *Time-gated pulsed STED*

In the previous discussion the saturation intensity is calculated, and minimised, for infinitesimally short pulses immediately after the excitation pulse [37]. In a more complete model, proposed by Leutenegger *et al.* [39], it is proposed that depletion pulse durations of $t_p \simeq 20$–30 ps are a more efficient use of power. This is because of the short but finite relaxation time between B′ and B.

In practice it has been found that excitation pulses of duration 50–70 ps and depletion pulses of duration t_p = 100–300 ps are more

effective [39]. This is thought to be due to a combination of minimising synchronization jitter [39], reducing photobleaching [144] – which scales with peak intensity [116] – and reduction of multiphoton re-excitation processes [39, 145].

For pulse durations that tend towards the fluorescence lifetime (τ_{fl}), photons emitted during the pulse begin to contribute to the overall PSF. Similar to the case in section 4.3.4, photons emitted during the pulse have been less effectively depleted and so fluorescence emission is less confined to the center of the PSF.

The suppression factor (equation 46) can be divided into two parts

$$\begin{aligned} \eta_{during} &= \frac{k_{fl}}{k_{fl} + \sigma_{depl} I_{depl}} \left(1 - e^{-(k_{fl} + \sigma_{depl} I_{depl}) t_p}\right), \\ \eta_{after} &= e^{-(k_{fl} + \sigma_{depl} I_{depl}) t_p} \end{aligned} \tag{53}$$

and

$$\eta_{total}(r) = \eta_{during} + \eta_{after}. \tag{54}$$

The PSF resulting from each of these components is plotted in figure 41,where $I_{depl} = \frac{4 I_{av} r^2}{\omega^2} e^{-r^2/\omega^2}$ and $I_{av} = 40 I_S^p$ is used for resolution ~50 nm (I_S^p is the saturation intensity for STED with infinitely short depletion pulses).

For short pulses relative to the lifetime (t_p = 300 ps, τ_{fl} = 3.5 ns; figure 41a the total PSF – typically detected – is comparable the PSF detected only after the depletion pulse ($FWHM_{total}$ = 51.7 nm, $FWHM_{after}$ = 50.3 nm). For either longer pulses (t_p = 1000 ps, τ_{fl} = 3.5 ns; figure 41c) or shorter lifetime fluorophores (t_p = 300 ps, τ_{fl} = 1 ns; figure 41b) the contribution of fluorescence emitted during the pulse is more pronounced leading to either a decrease in signal in the fluorescence emitted after the pulse or a decrease in resolution in the total PSF (Longer pulse – $FWHM_{after}$ = 50.3 nm, FWHM $_{total}$ = 54.9 nm; shorter lifetime – $FWHM_{after}$ = 50.3 nm, FWHM $_{total}$ = 55.1 nm)

This suggests that excluding fluorescence emitted during the pulse may have a benefit for short lifetime dyes or STED with longer pulse durations. Time-gated detection [37, 39], similar to in section 4.3.4, can be used to exclude fluorescence emitted during the pulse. This is represented in figure 42 and the impact of this on resolution is considered in this section.

It has recently been proposed both by Castello *et al.* [138] and Oracz *et al.* [121] that longer pulse durations, with lower peak powers but the same average power, lead to reduced non-linear photobleaching suggesting that fluorescence emitted during the pulse may become increasingly relevant in STED.

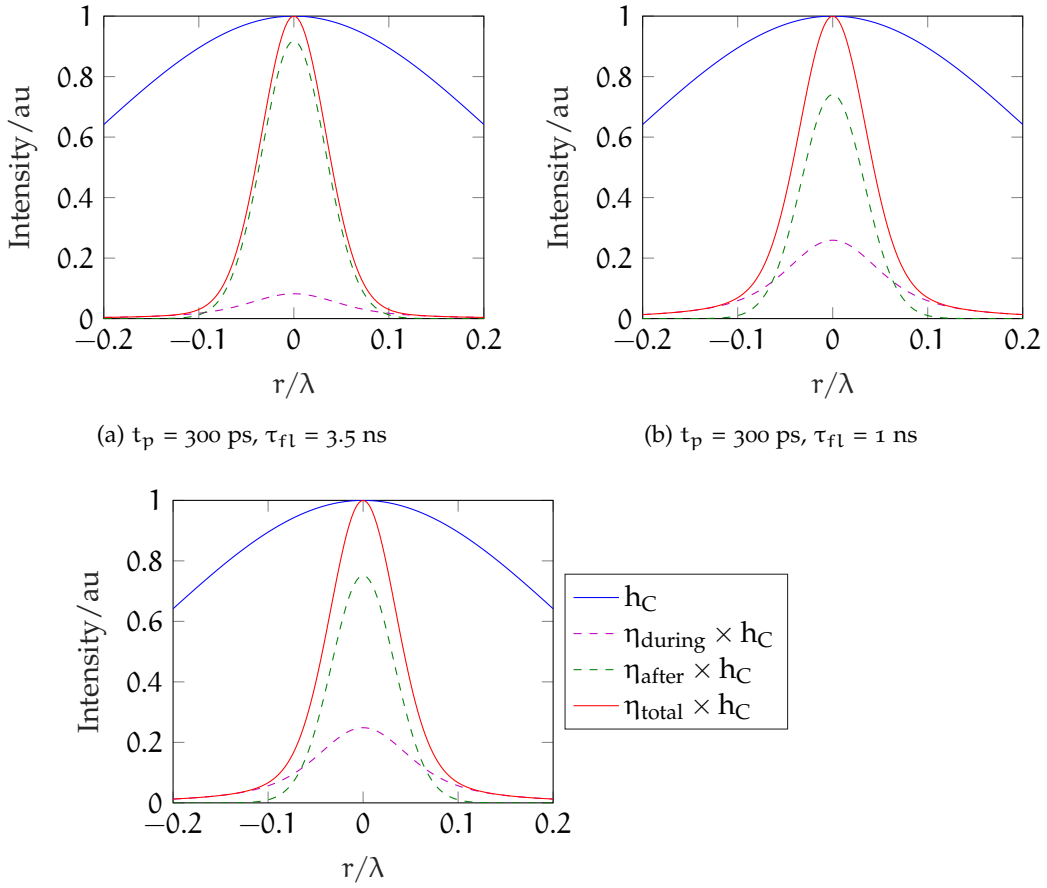

(a) t_p = 300 ps, τ_{fl} = 3.5 ns

(b) t_p = 300 ps, τ_{fl} = 1 ns

(c) t_p = 1000 ps, τ_{fl} = 3.5 ns

Figure 41: **Effect of depletion pulse duration on STED resolution.** In pulsed STED, the STED PSF ($\eta_{total} \times h_C$) is a combination of photons emitted during the depletion pulse ($\eta_{during} \times h_C$) and after the depletion pulse ($\eta_{after} \times h_C$). Photons emitted during the pulse have a lower resolution than those emitted after the pulse as fewer molecules have been depleted by the depletion beam. Although in the typical case (41a) where the pulse duration is much shorter than the lifetime this effect is negligible, for short lifetimes (τ_{fl}, 41b) or long pulses (41c) photons emitted during the depletion pulse degrade resolution. Time-gated detection excludes photons emitted during the pulse, increasing the resolution at the expense of total signal.

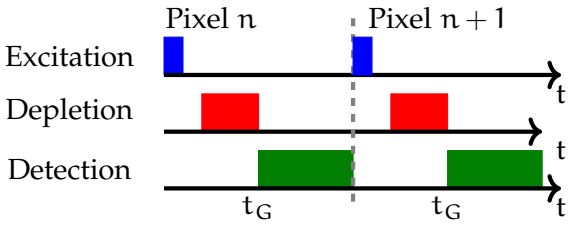

Figure 42: **Time-gated pulsed STED.** Fluorescence emission is collected only after the depletion pulse. This excludes low resolution fluorescence emission before the depletion laser has taken effect and excludes background related to the IRF and jitter on depletion pulse arrival times.

Suppression factor in time-gated pulsed-STED

Because time-gated pulsed-STED excludes fluorescence emitted during the pulse the suppression factor is similar to that in pulsed-STED with infinitely short pulses.

$$\eta = \frac{k_{fl}\int_{t_g}^{\infty} N_B(I,t)dt}{k_{fl}\int_{t_g}^{\infty} N_B(I=0,t)dt} = e^{-\sigma_{depl} I_{depl} t_p}. \tag{55}$$

Saturation intensity in time-gated pulsed-STED

The saturation intensity is where $\eta = 1/e$ and can be calculated as

$$I_S = \frac{1}{\sigma_{depl} t_p}. \tag{56}$$

This suggests that for longer (~ns) pulses time-gated detection allows the same resolution as STED with short pulses of the same average intensity. time-gated pulsed STED is compared to conventional pulsed STED with increasing pulse duration (I_S for conventional pulsed STED is calculated analytically) in figure 43. Showing that time-gated pulsed STED has the same I_S as STED with infinitesimal short pulses. Increasing the depletion pulse duration may reduce non-linear photobleaching [121, 138], with time gating ensuring that there is no increase in I_S. Like time-gated cw-STED (section 4.3.4) some signal is rejected in time-gate pulsed STED and this is considered here.

γ_S in time-gated pulsed STED

Only fluorescence emitted after t_g is detected such that the average fluorescence is

$$n_F(r=0) = \sigma_{exc} I_{exc} k_{exc} \int_{t_g}^{\infty} N_B(I=0,t)dt = \sigma_{exc} I_{exc} e^{-t_G/\tau_{fl}}, \tag{57}$$

such that

$$\gamma_S = \sigma_{depl}\sigma_{exc} I_{exc} t_{duty} e^{-t_g/\tau_{fl}}, \tag{58}$$

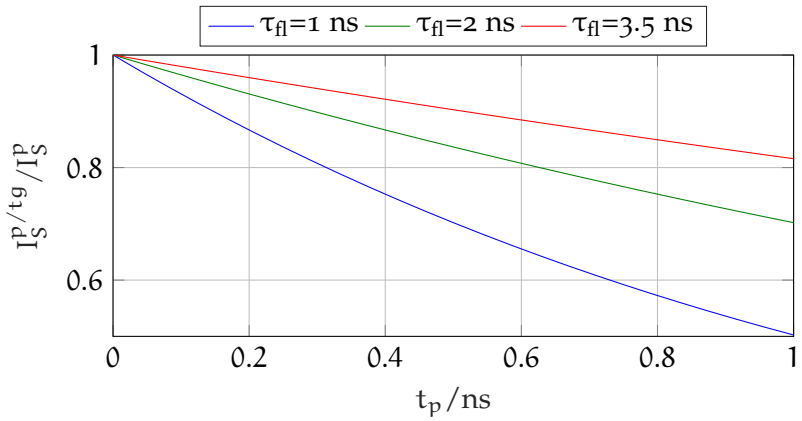

Figure 43: **Saturation intensity reduction in time-gated pulsed STED.** The ratio of average saturation intensities of time-gated pulsed STED and conventional pulsed STED, $I_S^{p/tg}$ and I_S^p, showing that for conventional pulse durations and fluorophores the saturation intensity is lower in time-gated pulsed STED.

indicating that more depletion photons will be required for a longer t_g than with short pulses and no time gating. This is shown in figure 44, which suggests that for any pulse duration pulsed STED will outperform time-gated STED in terms of photon efficiency. This metric does not take into account other benefits associated with time gating which include reduced effect of temporal jitter and reduced background from scattered light.

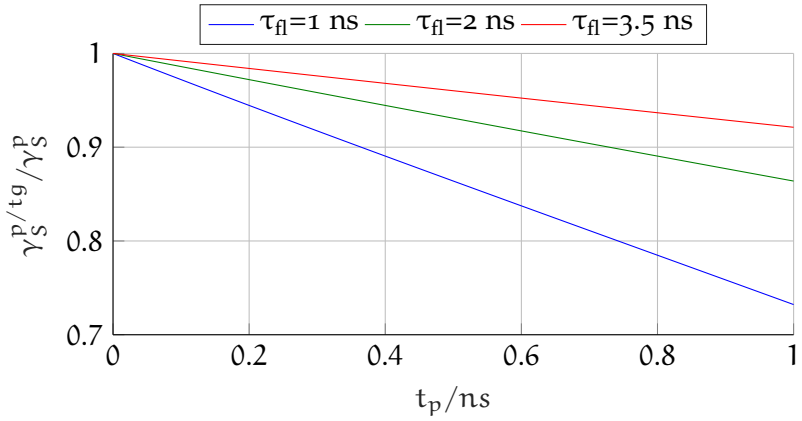

Figure 44: **Time-gated pulsed-STED is less photon-efficient than pulsed-STED.** Although the saturation intensity is lower in time-gated pulsed-STED the reduction in signal due to not collecting all fluorescence suggests that this is less photon efficient. This does not take into account other benefits of time-gating, including reducing the affects of temporal jitter. In this plot $t_g = t_p$

4.3.7 *Summary*

The suppression factor, peak and average saturation intensity and photon efficiency are summarised in table 3. time-gated detection in cw-STED reduces the saturation intensity and increases the photon efficiency by factors of 0.49 and 1.29, respectively (for an optimum time gate of $t_G = 0.46\tau_{fl}$), implying that time-gated cw-STED outperforms conventional cw-STED.

Comparing saturation intensity and photon efficiency in time-gated cw-STED to equivalent values in pulsed-STED (short pulses) gives

$$\frac{I_S^p}{I_S^{cw/tg}} = \frac{\tau_{fl}}{0.49(e-1)t_{duty}} \simeq 0.84\frac{\tau_{fl}}{t_{duty}}, \tag{59}$$

$$\frac{\gamma_S^p}{\gamma_S^{cw/tg}} = \frac{t_{duty}(e-1)}{1.29\tau_{fl}} \simeq 1.33\frac{\tau_{fl}}{t_{duty}}, \tag{60}$$

For standard 40 MHz or 80 MHz lasers used in STED, t_{duty} is 25 ns and 12.5 ns, which are greater than the lifetime of most fluorescent dyes (3.5 ns for ATTO647N). Therefore pulsed STED will typically have a lower saturation intensity and higher photon efficiency than time-gated cw-STED, giving a better resolution for a given depletion power or photon dose.

Time-gated detection can also be used in pulsed-STED. This reduces the saturation intensity when pulse durations are long relative to the fluorescence lifetime, however this leads to reduced photon efficiency compared to pulsed-STED. The main benefits associated with time-gated detection include rejecting scattered light, reducing the effects of temporal misalignment or jitter, and rejecting fluorescence emitted by dyes with a short lifetime component [137].

4.4 PRACTICAL COMPARISON OF STED MODES

In the previous discussion STED with pulsed depletion was found to have the lowest saturation intensity and highest photon efficiency of the STED modes – corresponding, in principle to reduced photobleaching and photodamage for a given resolution. Another constraint which must be considered when developing a STED microscope are the system cost and complexity, and compatible fluorescent markers. Here the STED modes are discussed in the context of these practical considerations.

4.4.1 *cw-STED and time-gated cw-STED*

STED requires an excitation and depletion laser sources which, are spatially coaligned. The excitation and depletion lasers should be

STED mode	η	I_S	γ_S
cw-STED (cw excitation)	$\frac{1}{1+\sigma_{depl} I_{depl} \tau_{fl}}$	$\frac{e-1}{\sigma_{depl}\tau_{fl}}$	$\frac{\sigma_{exc} I_{exc} \sigma_{depl} \tau_{fl}}{e-1}$
cw-STED (pulsed excitation)	$\frac{1}{1+\sigma_{depl} I_{depl} \tau_{fl}}$	$\frac{e-1}{\sigma_{depl}\tau_{fl}}$	$\frac{\sigma_{exc} \bar{I}_{exc} \sigma_{depl} \tau_{fl}}{e-1}$
Time-gated cw-STED	$\frac{k_{fl}}{k_{fl}+\sigma_{depl} I_{depl}} e^{-\sigma_{depl} I_{depl} t_G}$	$\frac{0.49(e-1)}{\sigma_{depl}\tau_{fl}}^{\dagger}$	$\frac{1.29\sigma_{exc} I_{exc} \sigma_{depl} \tau_{fl}}{(e-1)}^{\dagger}$
Pulsed STED	$\frac{k_{fl}+\sigma_{depl} I_{depl} e^{-(k_{fl}+\sigma_{depl} I_{depl}) t_p}}{k_{fl}+\sigma_{depl} I_{depl}}$	*	*
Pulsed STED ($t_p \ll \tau_{fl}$)	$\sim e^{-\sigma_{depl} I_{depl} t_p}$	$\sim \frac{1}{\sigma_{depl} t_{duty}}$	$\sim \sigma_{exc} I_{exc} \sigma_{depl} t_{duty}$
Time-gated pulsed STED ($t_p \leqslant t_g$)	$e^{-\sigma_{depl} I_{depl} t_p}$	$\frac{1}{\sigma_{depl} t_{duty}}$	$\sigma_{exc} I_{exc} \sigma_{depl} t_{duty} e^{-t_G/\tau_{fl}}$

Table 3: **Summary of supression factors and saturation intensities in different STED modes.** The suppression factor $\eta(I_{depl}, t_p, t_g)$, average saturation intensity $I_S(\tau_{fl}, t_{duty})$ and photon efficiency γ_S are described for all STED modes. † indicates values found analytically for $t_g = 0.46\tau_{fl}$. * indicates where a simple solution does not exist due to the dependence of η on pulse duration or time gate length.

at the excitation and depletion wavelengths of the fluorophore and have sufficient intensity for efficient excitation or depletion (excitation ~100 µW [83], depletion 10–100 mW [23], section 4.3.2). cw-STED can work with cw or pulsed excitation lasers, although time-gated cw-STED is limited to pulsed excitation only. As relatively low laser powers are required for excitation this imposes very few constraints on laser sources in terms of cost or wavelength selection. Low cost diode lasers can be used, as well as flexible solutions such as supercontinuum sources, which allow tuning of the excitation wavelength. Multiphoton excitation can also be used which allows imaging in thick samples and reduced autofluorescence from biological samples [142, 146].

The range of available depletion lasers is constrained by the requirement for high laser powers at the correct wavelength. For cw-STED there are now a range of commercially available sources for common depletion wavelengths (590 nm and 775 nm) at relatively low cost.

As with any confocal laser scanning system, beam quality of both excitation and depletion lasers should be considered. For time-gated cw-STED a depletion laser with low intensity noise should be used [147].

There is additional complexity in time-gated STED as either a time correlated single photon counting module [36] or a photon counter

coupled to an FPGA must be used to allow time resolved detection [138]. This must be triggered by the excitation laser.

Overall cw-STED is a simple and relatively low cost implementation of STED microscopy that can be designed for imaging common fusion proteins (YFP, depletion 590 nm) or organic dyes (ATTO 647N, depletion 775 nm). The cost and complexity associated with STED optimised for either target is similar, such that a STED microscope can be designed for fluorescent target – although this must be decided before the microscope is designed or purchased.

The addition of time-gated detection adds to the cost of the microscope but reduces the saturation intensity by approximately 50% and increases photon efficiency by 30%. This is generally considered to be worthwhile.

Until the recent development of lower cost, high power pulsed diode and fiber lasers, time-gated cw STED was used in many commercial STED systems.

4.4.2 *Pulsed STED*

As previously discussed, pulsed-STED has a better theoretical performance than cw-STED and has generally been found to achieve better resolutions [138]. The instrumentation requirements for pulsed STED can, however, be challenging compared to cw-STED. Pulsed STED requires the combination of two time synchronised laser pulses. The excitation and depletion pulses must be of the correct duration (50–70 ps and 100–300 ps respectively) and the depletion should arrive immediately after excitation, for maximum efficiency. The repetition rate should also be high for faster imaging – typically ~20–80 MHz is used [97, 139].

Further to the experimental challenges of temporal coalignment, a further restriction in pulsed STED is the availability of lasers with sufficiently high pulse power for STED at relevant wavelengths. A commonly used depletion source in home-built systems is the titanium sapphire laser (Ti:S). A Ti:S laser emits 100 fs pulses with a repetition rate of 76 MHz and powers of up to 3 W. The wavelength range of a Ti:S laser can be 700–1040 nm [89], therefore this system is limited to red and near infrared dyes such as ATTO 647N and STAR 600. Further experimental complexity is introduced when using a Ti:S laser as the pulse duration is of the order of 100 fs, which is too short for STED depletion and needs to be stretched by propogation through glass and through an optical fibre.

For live cell imaging pulsed STED has generally been limited to green fluorescent proteins [128], due to the limited availability of dyes and fluorescent proteins with good photophysical properties for STED [109]. Until recently pulsed STED on commonly used green dyes and fluorescent proteins required an optical parametric oscilla-

tor (OPO) pumped by a titanium sapphire laser to generate shorter wavelength pulses [148]. Although this enables research on tissue slices [5, 127] and living mouse brains [128], this technique is costly and beyond the reach of many labs.

New developments in fluorescent labelling technology for STED have generated fluorophores which are compatible both with infrared STED and live cell imaging. The silicon rhodamine (SiR) dye series [30–33] for instance have enabled a range of studies in live cells.

4.4.3 *Perspectives*

Laser technology

New laser sources have been developed recently for STED microscopy. These are typically pulsed fiber lasers, some of which have tunable repetition rates and pulse durations and can be externally triggered. Sources are available that operate at 775 nm and 590 nm with good pulse durations for STED and lower cost than a Ti:S laser or OPO.

These new laser sources reduce the cost and complexity of pulsed STED and, although few systems using this technology have been published, they are likely to make pulsed-STED, particularly, on fluorescent proteins more achievable for many labs.

Long lifetime fluorescent dyes

As previously discussed, the ratio of saturation intensity in time-gated cw-STED and pulsed STED is

$$\frac{I_{S_p}}{I_{S_{Gcw}}} = \frac{\tau_{fl}}{0.49(e-1)t_{duty}}. \tag{61}$$

State-of-the-art pulsed STED systems use lasers with a duty cycle of 12.5 ns or 25 ns. Based on the above, cw-STED would have an equivalent saturation intensity for dyes with a lifetime of 10 ns or 20 ns, respectively. Pulsed-STED imaging of nitrogen vacancies in nanodiamonds (with 11 ns lifetimes) has achieved 8 nm resolution [149] and 10 ns lifetime organic STED dyes are being more commonly reported [150, 151], which should theoretically allow time-gated cw-STED experiments with comparable performance to current state-of-the-art pulsed-STED systems.

4.4.4 *Conclusions*

In this section the mechanisms through which pulsed STED, cw-STED and time-gated STED enhance resolution in STED microscopy were discussed with the aim of selecting the optimal method for this work. The saturation intensity and photon efficiency were considered. By considering a simple expression for photon efficiency a theoretically

optimal time-gate for time-gated cw-STED could be found as 0.47 fluorescence lifetimes. This allows the estimation of I_S and γ_S for time-gated cw-STED and the direct comparison to pulsed STED. Calculated optimal time gates agree with previously published works in which time-gated STED is used [137].

Direct comparison of cw-STED and time-gated cw-STED suggests that, for optimal time gates, time-gated cw-STED will have better resolution for a given depletion intensity and will have a lower total depletion photon dose. For current state-of-the-art STED dyes, STED with pulsed depletion has a lower average saturation intensity than time-gated cw-STED as well as higher photon efficiency, at the expense of increased cost and experimental complexity. New laser sources are being developed which decrease the cost and experimental complexity of pulsed STED, as well as new organic dyes which allow cw-STED to achieve comparable resolutions as current state-of-the-art pulsed STED.

Time-gated detection in pulsed STED has little effect on the saturation intensity unless long depletion pulses are used. Time-gated pulsed STED has a lower photon efficiency than conventional pulsed STED, although this reduction is relatively small. time-gated detection rejects scattered light from the excitation and depletion laser, as well as short lifetime components of fluorescence emission, and is less sensitive to the temporal alignment of excitation and depletion pulses.

The analysis presented here suggests that pulsed STED is the highest resolution STED technique with the lowest depletion intensity requirements. This imaging mode is the most experimentally complex. A further constraint associated with this STED technique is that the lasers required for STED on fluorescent proteins are expensive and beyond the reach of most labs. Finally, although the average depletion intensity is lowest, the peak depletion intensity is the highest of all STED modes. An alternative technique, RESOLFT (or reversible saturable optical fluorescence transition) has been proposed [38, 105, 152], which is lower cost, can be used to image fluorescent proteins and uses low (comparable to confocal) laser intensities for depletion. The theoretical performance of this technique is also considered in the following section.

4.5 RESOLFT

4.5.1 *Theoretical discussion of RESOLFT*

Suppression factor in RESOLFT

For the suppression factor, $t = 0$ is considered as the start of stage 2 (figure 22a). It is assumed that at $t = 0$ the probability of a fluo-

rophore being in the on state (S_0^{cis} or S_1^{cis}) is 1 ($N_{on}(0) = 1$). The population of each on state, $S_{0,1}^{cis}$, is given by

$$N_{0,1}^{cis}(t) = \epsilon_{0,1} N_{on}(t), \tag{62}$$

where $\epsilon_{0,1}$ is the probability a molecule, which is in the on-state, being in S_0^{cis} or S_1^{cis}.

As the transition between the on state and off state is much slower than the internal, fluorescent, transitions (analagous case to that discussed in [78]) it can be assumed that $\epsilon_{0,1}$ will reach a steady state allowing ϵ_1 to be written as

$$\epsilon_1 = \frac{\sigma_{exc} I_{depl}}{\sigma_{exc} I_{depl} + k_{fl} + k_{sw}}, \tag{63}$$

where I_{depl} is the intensity of the depletion laser (operating at the excitation wavelength). This allows the rate of change of the population of the on state to be written as

$$\frac{dN_{on}}{dt} = -k_{sw}\epsilon_1 N_{on} = -\frac{\sigma_{exc} I_{depl} k_{sw}}{\sigma_{exc} I_{depl} + k_{fl} + k_{sw}} N_{on}. \tag{64}$$

Solving this gives

$$N_{on}(I_{depl}, t) = e^{-\frac{\sigma_{exc} I_{depl} k_{sw}}{\sigma_{exc} I_{depl} + k_{fl} + k_{sw}} t}. \tag{65}$$

As the on state is long-lived, the population is assumed not to decay in the absence of a depletion beam $N_{on}(I_{depl} = 0) = 1$. The suppression factor is therefore

$$\eta = \frac{N_{on}(I_{depl}, t)}{N_{on}(I_{depl}, t = 0) = 1} = e^{-\frac{\sigma_{exc} I_{depl} k_{sw}}{\sigma_{exc} I_{depl} + k_{fl} + k_{sw}} t}. \tag{66}$$

Saturation intensity

The saturation intensity can be shown to be

$$I_S = \frac{k_{sw} + k_{fl}}{\sigma_{depl}(k_{sw} t_{depl} - 1)} \simeq \frac{k_{sw} + k_{fl}}{\sigma_{depl} k_{sw} t_s}, \tag{67}$$

where t_s is the duration of the depletion part of the RESOLFT cycle and is much larger than $1/k_{sw}$ (necessary for the system to reach a steady state). t_s can also be considered as the saturation time at a given depletion intensity. The saturation intensity of a fluorophore with $k_{sw} = 2 \times 10^5\ s^{-1}$ and $k_{sw} = 7 \times 10^4\ s^{-1}$ (estimated for rsEGFP2 from data presented by Wang *et al.* [113]) is shown in figure 45.

For a depletion intensity comparable to confocal microscopy (10 $kWcm^{-2}$ [35, 81]) the saturation time for rsEGFP2 is 583 µs. This corresponds to a total photon dose of 1.4×10^{19}. The total number of depletion photons in RESOLFT ($E_S^{RESOLFT} = I_S t_{depl}$) per cycle can be compared to

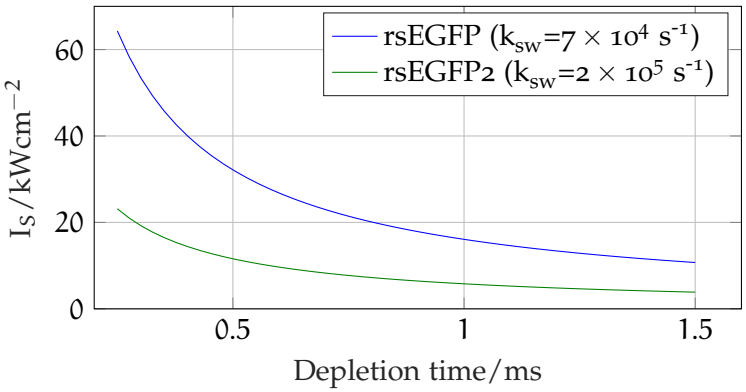

Figure 45: **Saturation intensity in RESOLFT microscopy.** The saturation intensity calculated from the simple model derived in this work. rsEGFP2 is a faster photoswitcher than rsEGFP and therefore will have a lower saturation intensity for a given depletion time. k_{sw} is estimated based upon data presented by Wang *et al.* [113]

the corresponding value in pulsed-STED ($E_S^{p-STED} = I_S t_{duty}$). Assuming the depletion cross section is the same in both cases gives

$$\frac{E_S^{RESOLFT}}{E_S^{p\text{–}STED}} \simeq \frac{k_{sw} + k_{fl}}{k_{sw}}., \tag{68}$$

suggesting that the depletion photon dose per cycle will always be larger in RESOLFT.

However, unlike in STED, the same fluorophore can emit multiple fluorescent photons per cycle, meaning that fewer cycles may be required and photon efficiency – signal photons per depletion photons – must be considered.

Photon efficiency in RESOLFT

The number of fluorescent photons emitted during the read out part of the cycle ($t = 0$) when the read out laser is activated, duration t_R) at the centre of the PSF is

$$\begin{aligned} N_F &= \sigma_{act} I_{act} t_{act} \int_0^{t_R} k_{fl} e_1 N_{on}(t) dt \\ &\simeq \sigma_{act} I_{act} t_{act} \frac{k_{fl}}{k_{sw}} \left(1 - e^{-\frac{k_{sw}\sigma_{depl} I_R}{k_{sw}+k_{fl}} t_R}\right), \end{aligned} \tag{69}$$

where I_R is the intensity of the read out beam, $\sigma_{act} I_{act} t_{act}$ is the number of fluorophores photoswitched into the on state during the activation phase and the rate of excitation is much less than the rates of photoswitching or fluorescence.

The photon efficiency is the total fluorescence read out per depletion photon

$$\gamma_S = \frac{N_F}{E_S} = \frac{\sigma_{act} I_{act} t_{act} \sigma_{depl} k_{fl}}{k_{sw} + k_{fl}} \left(1 - e^{-\frac{k_{sw}\sigma_{depl} I_R}{k_{sw}+k_{fl}} t_R}\right). \tag{70}$$

Which can be compared to the photon efficiency in pulsed STED (equation 52) where the I_{act}, t_{act} have been chosen such that the number of fluorophores in the on-state is comparable to pulsed STED:

$$\frac{\gamma_S^{RESOLFT}}{\gamma_S^{p-STED}} = \frac{k_{fl}}{k_{sw}+k_{fl}}\left(1-e^{-\frac{k_{sw}\sigma_{depl}I_R}{k_{sw}+k_{fl}}t_R}\right). \tag{71}$$

The photon efficiency varies as a function of the total number of readout photons ($I_R \times t_R$). Setting the read out intensity to 10 kWcm^{-2} (chosen to be comparable to confocal microscopy ([35, 81]) the evolution of the photon efficiency in RESOLFT with readout time is shown in figure 46. Parameters used in the simulation are given in table 4.

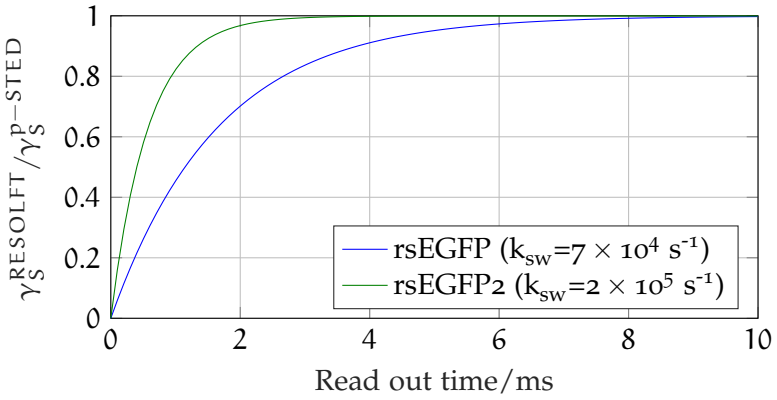

Figure 46: **Photon efficiency in RESOLFT, including depletion photons only.** The ratio of γ_S in RESOLFT and pulsed STED showing that STED and RESOLFT have comparable γ_S for a long read out cycle. This plot assumes that only depletion photons contribute to γ_S. The read out intensity is 10 kWcm^{-2}. k_{sw} is estimated based upon data presented by Wang *et al.* [113]

Parameter	Value	Comments and reference
σ_{exc}	10^{-16} cm^2	Absorption cross-section, range 10^{-15}–10^{-17} cm^2 quoted in [81]
I_R	10 kWcm^{-2}	Same excitation intensity I_{exc} used in STED (table 2)
τ_{fl}	3.5×10^{-9} s	Fluorescence lifetime of common fluorophores [81]
σ_{depl}	10^{-16} cm^2	Typical depletion cross-section quoted in [23]
λ_{depl},λ_R	491 nm	Depletion and read out wavelength of rsEGFP2 [106, 112]
NA	1.4	Numerical aperture of common high resolution objective

Table 4: **Typical values of parameters effecting resolution in RESOLFT.**

The photon efficiency tends towards the same photon efficiency as pulsed STED for long readout time (of the order ms) as more fluorescence is read out. In this case the photon dose for readout becomes

comparable with the photon dose for depletion. Therefore it would be more correct to write equation 70 as

$$\gamma_S = \frac{N_F}{E_S + I_R t_R} = \frac{\sigma_{act} I_{act} t_{act} \sigma_{depl} k_{fl}}{k_{sw} + k_{fl} + \sigma_{depl} k_{sw} I_R t_R} \left(1 - e^{-\frac{k_{sw}\sigma_{depl} I_R}{k_{sw}+k_{fl}} t_R}\right). \tag{72}$$

The activation photon dose is assumed to be negligible. Again this is compared to pulsed STED and plotted in figure 47. This plot suggests that there is an optimum readout time for RESOLFT, as well as that the photon efficiency is lower than in pulsed STED – but can be better than time-gated cw-STED.

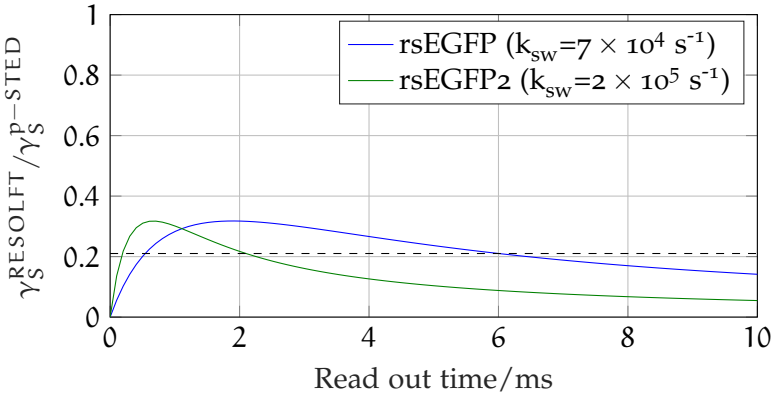

(a) 123 nm resolution

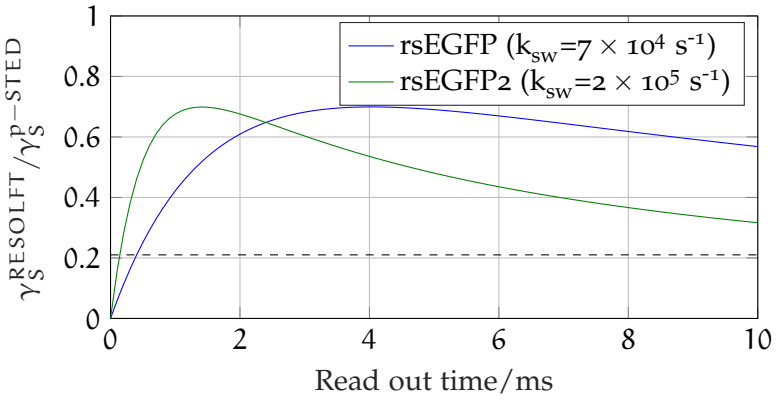

(b) 50 nm resolution

Figure 47: **Photon efficiency in RESOLFT, including depletion and readout photons.** When readout photons are included there is an optimum t_R (for a given readout intensity). The photon efficiency is also generally less than STED. As only the depletion photon dose scales with the resolution in RESOLFT the theoretical optimum readout time and photon efficiency changes depending on the depletion conditions. The photon efficiency of time-gated cw-STED is illustrated as a dashed line.

When including readout photons in the photon efficiency it is important to note that only the depletion photon dose changes if an

increased resolution is required. For higher resolution the theoretical optimum readout time decreases and the photon efficiency – relative to STED with equivalent resolution – increases.

Notably the theoretically optimum depletion and readout times in RESOLFT are in the range of milliseconds. This is significantly longer the pixel dwell times commonly used in STED or confocal microscopy. In spite of the reduction in average intensity, and therefore non-linear photodamage, the increase in dwell time leads to lower overall photon efficiency than pulsed-STED, and therefore comparable total photon dose. Further study is required to understand the relative contributions of linear and non-linear photodamage and this is beyond the scope of this work.

In the following section the practical considerations in RESOLFT are discussed.

4.5.2 *Practical considerations in RESOLFT*

Intrumentation

Due to the lower intensities used in RESOLFT there are fewer constraints on the laser sources used than in STED. In general the main requirement is that the laser can be switched on and off for durations of tens of µs, as well as electronics to control this. A further consideration is that, unlike STED, RESOLFT usually requires 3 lasers (activation, depletion and readout lasers) to be spatially coaligned making spatial alignment more challenging than in STED.

Imaging speed

As discussed in the previous section for efficient super-resolution imaging RESOLFT currently requires long pixel dwell times of the order 0.09–2 ms [106, 107, 112] depending upon the laser intensities used. Modelling in the previous section suggests that increasing the photoswitching time constant k_{sw} will reduce pixel dwell time [153].

Current pixel dwell times are long compared to STED microscopy where dwell times of the order 30 µs are typically used. The dwell times in RESOLFT make imaging large fields of view or 3D volumes challenging.

However the low intensities required for RESOLFT permit parrelised RESOLFT imaging with 1000 vortexes for faster imaging [154], although this system is relatively complex.

Fluorescent labels

The reversibly photoswitchable rsEGFP2 [106] is the most commonly used fluorescent protein in RESOLFT due to its faster off-switching kinetics. For two colour RESOLFT imaging a red fluorescent protein

rsCherryRev1.4 [112] was developed and has been used to demonstrate two colour RESOLFT imaging, although this fluorescent protein has a lower k_{sw} and therefore requires longer imaging times.

A positive photoswitching protein, kohinoor, has been recently developed **[Tiwari2015]** that uses three independent wavelengths for on-switching, off-switching and fluorescence readout.

Switching fatigue

Reversibly photoswitchable fluorescent proteins can typically only undergo 250 switching cycles before their intensity is reduced by a factor 2 [104]. This limits the number of images which can be taken in a time series or when taking a 3D image.

Fluorescent proteins such as GMars-Q [104, 113] have recently been developed for long-term imaging due to their reduced switching fatigue.

Residual fluorescence

It has been reported that there remains a fluorescent signal from fluorophores in the off state. For rsEGFP2 this off state fluorescence is of the order 2–3% of the signal from on state fluorophores [153]. This signal will degrade the resolution and may increase the number of switching cycles and the amount of photobleaching.

4.5.3 *Summary*

The new theoretical framework developed in this section to describe the saturation intensity in RESOLFT allows a simple calculation of photon efficiency. Using the expression for photon efficiency it can be seen that the photon efficiency in RESOLFT varies as a function of the readout time. An optimum readout time can be determined from this model, based upon the photoswitching time constant, fluorescent lifetime, readout intensity and target resolution. This framework would allow the estimation of optimal parameters for RESOLFT imaging.

The photon efficiency in RESOLFT is less than the equivalent value for pulsed-STED but RESOLFT uses lower cost and lower intensity cw-laser sources. Although an extra laser source is required in RESOLFT the overall experimental complexity is lower due to simpler temporal alignment. The imaging speed and the current lack of bright photostable reversible switching fluorophores limits the viability of RESOLFT for many experiments.

4.6 CONCLUSION

The four main STED modes were considered in this section. Of these pulsed STED was found to have the highest photon efficiency. This technique is also the most complex and uses the highest peak laser intensities.

Pulsed STED was compared to the RESOLFT technique which was found to have a lower photon efficiency. RESOLFT is known to have a longer acquisition time and is currently limited to fluorophores which exhibit low photostability and brightness.

Based upon this pulsed-STED is chosen as the preferred technique to develop for this project. A major trade off with pulsed STED is that the most common implementation, using near-infra-red depletion, is optimised for far red dyes and is not compatible with common fluorescent proteins [109]. Alternative instruments for STED GFP and YFP imaging can be built but are more costly [5]. Recently developed SiR dyes can be used for imaging live cells with near-infra-red depletion. These are optimised for directly targeting cellular structures such as actin and tubulin but SNAP tag conjugates are also available allowing any cellular target expressing SNAP-tags to be labelled [101].

In the following section a pulsed STED microscope optimised for far red organic dyes will be designed and implemented.

5 DEVELOPMENT OF A PULSED STED MICROSCOPE

5.1 INTRODUCTION

Aim

In this chapter a pulsed STED microscope is developed for super-resolution imaging living cell cultures or cleared tissue. Design considerations including laser sources, vortex beam generation and temporal alignment are discussed and the spatial resolution of the system is tested.

Motivation

In the previous chapter the relative merits of the different STED and RESOLFT modes were discussed. Models for photon efficiency of all modes suggests that pulsed STED is the optimum approach.

In practice a pulsed STED system requires pulsed excitation and depletion sources to be temporally aligned. The most established and widely used depletion laser source in custom STED microscopes is the titanium sapphire (Ti:S) laser, which typically features a pulse duration of 100 fs. The optimal pulse duration for depletion has been found to be 100–300 ps [39], therefore the femtosecond pulses must be stretched in time.

Finally it is necessary to generate the STED depletion pattern and to coalign this with the excitation beam. For optimal performance the depletion pattern should be a vortex with a strict intensity minimum at the centre and steep intensity gradient. Spectral broadening and optical aberrations, particularly those iduced by thick or scattering samples, degrade the intensity minimum and should be minimised.

Structure

In this chapter the design and implementation of a STED microscope is described in which these challenges are addressed. Temporal synchronisation between excitation and depletion lasers is achieved by generating a supercontinuum source using the depletion laser from which excitation lines are selected. Excitation lines are, therefore, inherently synchronised with the depletion laser. Depletion and excitation pulses are temporally coaligned using an optical delay line. Correct pulse durations are obtained by dispersing pulses in glass and in optical fiber. Spatial coalignment and aberration correction are controlled by a spatial light modulator (SLM). The resolution of the

microscope is tested and found to be of the order of 50 nm in ideal conditions.

5.2 STED IMPLEMENTATION

A schematic of the STED microscope is shown in figure 48, part numbers and manufacturers are provided in the figure caption for key components.

In brief the system is based upon a commercial RESOLFT microscope provided by Abberior instruments (Göttingen). A titanium sapphire laser (Ti:S) operating at 765 nm is used as the depletion laser. The power from this source is divided between two optical paths. One path is the depletion path. In this path laser pulses are temporally stretched by propagation in 50 cm of SF66 glass and 100 m polarisation maintaining single mode fiber. A spatial light modulator (SLM) is used to spatially shape the beam into a vortex beam and correct aberrations. An optical delay line is used to control the arrival times of depletion pulses relative to excitation pulses.

The second path is used to generate the excitation beam. The pulsed laser pumps a photonic crystal fiber (PCF), generating a supercontinuum. From this an excitation line at 640 nm is selected. This temporally stretched by propagation in a 30 m optical fiber. Both beams are then coaligned in the image plan of a microscope.

The microscope frame is an Olympus IX83 and the imaging objective is a 100X/1.4NA oil immersion objective (UPLSAPO 100X, Olympus). Beam scanning is performed using galvanometric mirrors (Quad scanner, Abberior instruments). These allow a 80 x 80 μm^2 field of view (FOV) to be scanned with a line frequency of up to 2 kHz. Two avalanche photodiodes (SPCM-AQRH Excelitas technologies) are used. One is used for STED fluorescence detection (emission filter: ET685-70, Chroma). The second photodiode is used to detect fluorescence from green or UV dyes, with confocal resolution. Fluorescence excitation is from a 405 nm (Cobolt-06-MLD-405 nm) or 488 nm (Cobolt 06-MLD-488 nm, Cobolt) diode laser. Fluorescence emission is separated from excitation using a dichroic mirror (zt-594-RDC, Chroma) and emission filter (Brightline HC 550/88, Semrock).

The design, implementation and characterisation of sub-systems used for STED are described in detail in following sections.

5.3 TEMPORAL COALIGNMENT OF EXCITATION AND DEPLETION BEAMS

5.3.1 *Effects of temporal alignment on suppression factor*

In pulsed STED excitation and depletion must be temporally syncronised for optimal depletion. Illustrative examples of the effects of

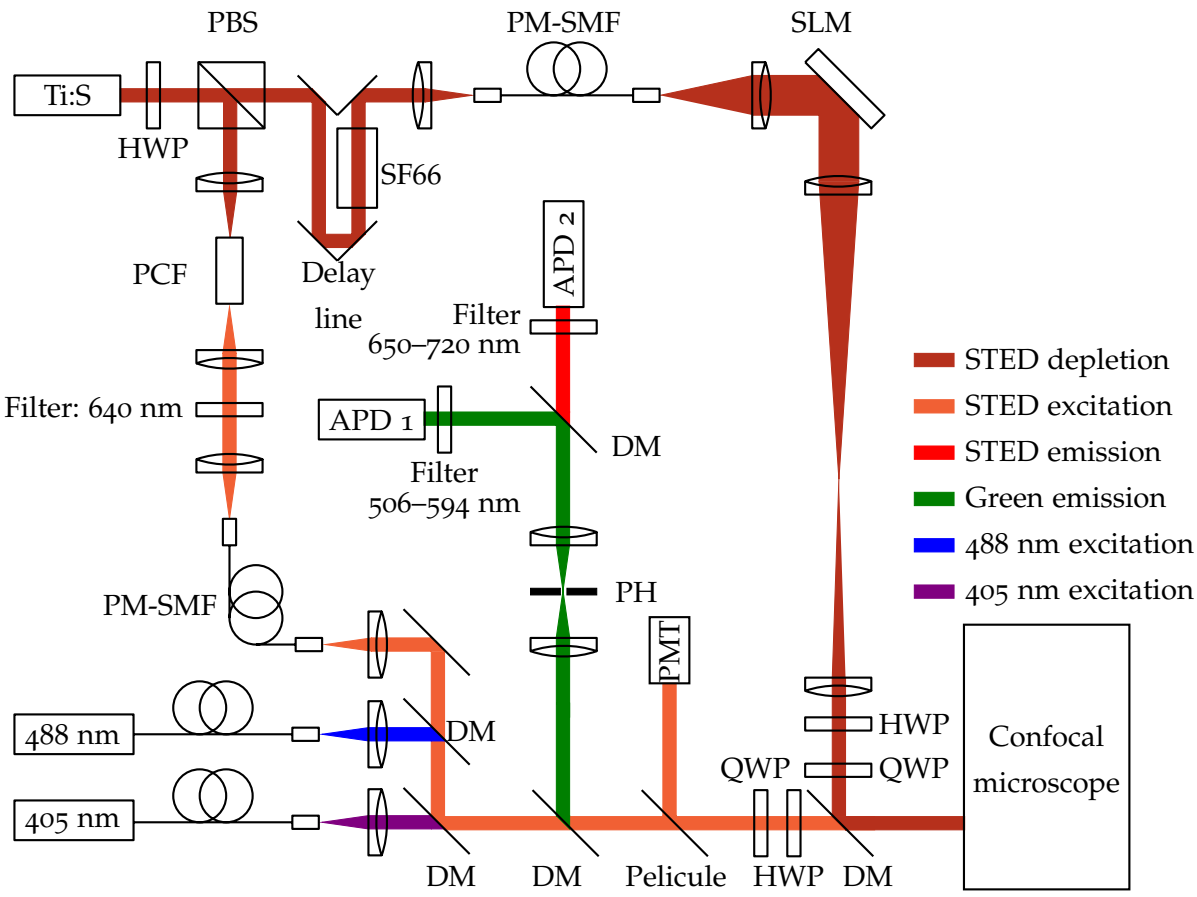

Figure 48: **Schematic of STED system.** Ti:S laser (Mai-Tai, Spectra-physics) is tuned to a wavelength of 765 nm; a half-wave plate (HWP) is used in conjunction with a polarisation beam splitter (PBS, Thorlabs) to control the optical power in the depletion channel and excitation channel. In the excitation channel, light is focused on a photonic crystal fibre (PCF, SCG-800, Newport). This generates a supercontinuum. A 640 nm (bandwidth 8 nm) line is selected using a bandpass filter (LD01-640/8-12.5, Semrock) and this is focused into a polarisation maintaining single mode fibre (PM-SMF, Thorlabs)) to stretch the pulse in time. Depletion light propagates along a motorised variable delay line (Thorlabs) and through a SF66 glass block to pre-chirp the pulse before it is sent through a polarisation maintaining single mode fibre (PM-SMF). Depletion light is sent through a phase mask (spatial light modulator, SLM, Hamamatsu) to generate a vortex beam. Both beams are recombined in a confocal microscope (Arberrior instruments). The vortex beam can be imaged using scattered light from gold nanoparticles detected by a photomultiplier tube (PMT). Fluorescence emission is imaged onto a pinhole (PH) and detected on an avalanche photodiode (APD). STED emission is detected on APD 2. Continuous wave 488 nm and 405 nm laser sources are also available for confocal imaging of GFP or DAPI – fluorescence emission from these fluorophores is detected on APD 1.

arrival times of excitation and depletion pulses (approximated as top hat functions of width 50 ps and 300 ps) are presented in figure 49 for a depletion intensity of I_S. The suppression factor increases for incorrect offset suggesting the need for stable and precise temporal alignment in pulsed STED/

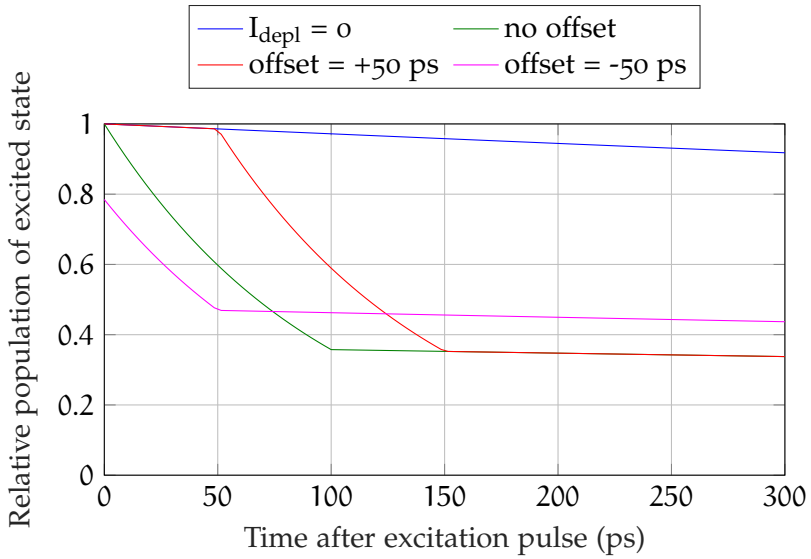

Figure 49: **Effect of temporal alignment on decay curves in pulsed STED.** Decay curves for STED microscopy with rectangular excitation and depletion pulses (durations 50 ps and 300 ps). Three depletion pulse arrival times are considered. Immediately after the excitation pulse (no offset) 50 ps after the exciation pulse (offset = +50 ps) and 50 ps before the end of the depletion pulse (offset = -50 ps). The suppression factor increases for pulses arriving before or after the depletion pulse, compared to no offset (1.02 (+50ps), 1.06 (-50ps)). The depletion intensity used in this plot is I_S.

Here the temporal alignment of excitation and depletion pulses is discussed and excitation and depletion sources which allow for temporal alignment with low jitter are implemented.

5.3.2 *Time synchronised excitation and depletion pulses through supercontinuum generation*

Time synchronised excitation pulses are commonly generated using a diode laser that is electronically synchronised with the depletion source [99]. Laser drivers used in pulsed STED have a temporal jitter of 20 ps corresponding to approximately 2% noise on the suppression factor. Laser diodes can only operate at fixed wavelengths so this does not allow the system to be adapted to image a range of fluorophores [99].

A more flexible system is to use the Ti:S as a depletion laser and to use some of the power to pump a photonic crystal fibre. This generates a super-continuum, which includes a broad range of wavelengths and is inherently time synchronised. One, or more, of these wavelengths can be selected for fluorescence excitation. Different excitation – and depletion – lines can be selected for different fluorophores [99, 155]. Temporal alignment can then be precisely tuned using an optical delay line. Pulses are generated from the same source and their arrival times controlled only by optical path length. A large change in optical path length (for example 1 mm) corresponds to a small change in arrival time (3.3 ps). This system is therefore more stable than an electronically triggered system.

For this STED microscope a supercontinuum is generated by pumping a photonic crystal fibre (PCF) with the depletion laser. A commercial PCF (SCG-800, Newport) was selected, which has a zero-dispersion wavelength of 750 nm, such that depletion pulses of wavelength greater than 750 nm will operate in the anomalous dispersion regime, which is generally used for super-continuum generation [156]. This fibre has been used in previous reports of STED microscopy [89].

In a PCF, light propagates along a narrow (1–2 μm) core. This gives a large intensity, leading to a range of non-linear effects including Raman scattering, four-wave mixing, self phase modulation and soliton generation [156]. A combination of these effects generates new spectral frequencies. A review of the physics of supercontinuum generation can be found here [157].

The PCF is a tapered fiber, such that the core diameter is larger at the input and output of the fibre than in the middle. This simplifies coupling into the fibre and reduces the likelihood of damage due to dust at the entrance to the fibre, ensuring the long term reliability of the system.

The PCF is mounted on an XYZ translation stage (M-562F-XYZ, Newport). By selecting in and out coupling objectives that match the numerical aperture of the fibre (NA=0.4, M-20X, Newport) and expanding the depletion beam to fill the back aperture of these objectives it was found that coupling efficiencies of 60–70% were repeatably achievable.

To ensure that this PCF is suitable for generating STED excitation, the supercontinuum spectrum is measured for a range of pump powers and wavelengths. This fiber must generate sufficient intensity at the excitation wavelength (640 nm). The pump wavelength to generate this excitation line should be suitable for STED (750–780 nm) and the pump power should be sufficiently low that sufficient energy remains available for the depletion path.

For testing of the PCF, a spectrometer (USB 4000, Ocean Optics) was used to measure the spectrum at the output. Neutral density and

infra-red filters were used to remove the pump wavelength and to prevent saturation of the spectrometer. The PCF was tested at a range of wavelengths and pump powers.

The supercontinuum spectrum was measured as a function of pump power and wavelength. The pump wavelength range was between 760 nm and 820 nm. Typical two dimensional plots of the supercontinuum spectrum as a function of pump power are presented for pump wavelengths of 780 nm and 820 nm in figure 50. These are similar to spectra measured for other wavelengths. The spectra shown here correlate with those shown in the application note for the fibre [158].

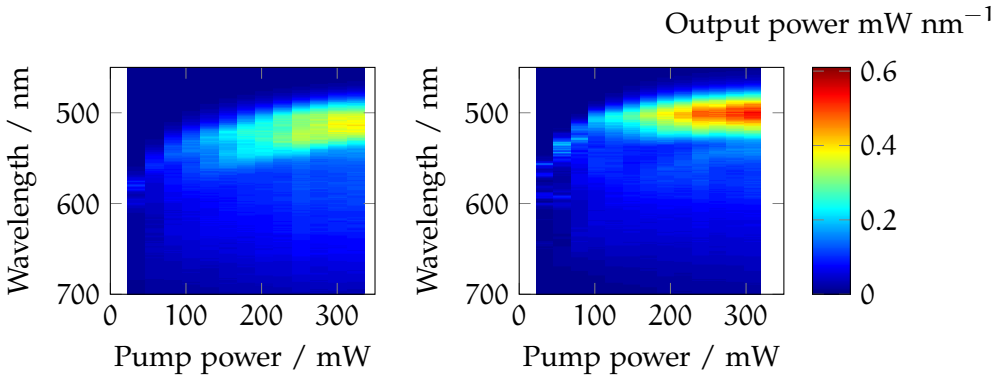

(a) 780 nm pump (b) 820 nm pump

Figure 50: **Typical 2D plots of super-continuum spectrum as a function of wavelength.** Typical plots showing that for larger pump powers the spectrum of the generated super-continuum is more intense and slightly blue shifted. There does not appear to be a significant difference between pump wavelengths. The pump wavelength has been removed using a short pass filter. Colour bar applies to both plots.

Figure 51 shows the spectrum of the PCF when pumped at 780 nm at a range of powers up to 301 mW, close to the maximum recommended pump power. This is overlaid with the bandpass of the excitation filter (640 ± 8 nm) for the ATTO 647N dye (LD01-640/8-12.5, Semrock). Pump powers of 160 mW and 301 mW produce similar output powers at 640 nm. A pump power of 160 mW was chosen for the STED microscope as this will generate adequate power (up to 500 µW in the back aperture) for excitation and is below the damage threshold of the fibre.

This spectrum also shows powers generated at shorter wavelengths. Therefore other wavelengths could be coupled from this supercontinuum to allow, for instance, two colour STED imaging [101].

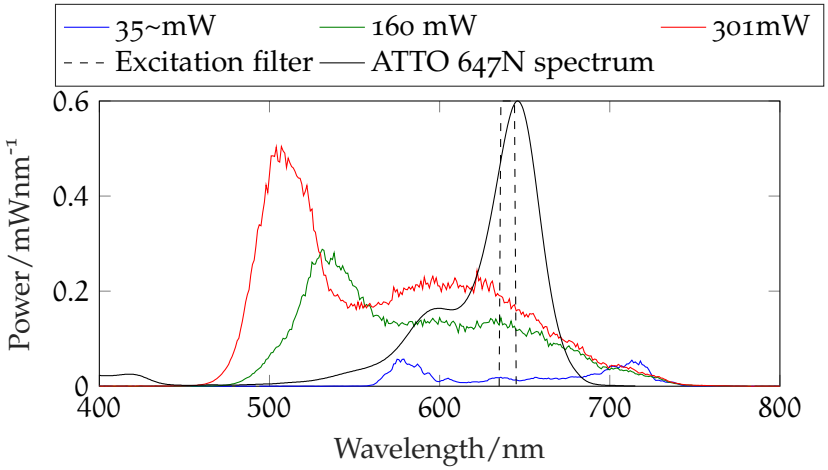

Figure 51: **Supercontinuum generated at 780 nm.** This shows powers of the order 0.2 $mWnm^{-1}$ at 640 nm, the wavelength that will be used for STED. For illustrative purpose the excitation filter that will be used, as well as the normalised absorption spectrum of ATTO 647N, are shown. The 785 nm pump was removed by an IR filter to avoid saturating the detector.

5.3.3 *Temporal alignment of depletion and excitation pulses*

In figure 49 it is shown that depletion pulses must arrive after excitation pulses for optimum depletion. As excitation and depletion pulses are derived from the same source they are inherently triggered. The arrival times of laser pulses are controlled by changing the optical path length of the depletion laser using an optical delay line.

To allow pulses to be temporally coaligned an optical rail of length 50 cm is used in the depletion path. Coarse temporal control is achieved by manually moving the trolley on this rail. For fine alignment a computer controlled motorised linear translation stage (PT1/M-Z8, Thorlabs) is used. To simplify alignment of the delay line and minimise beam walk off an optical delay line mirror mount (9848-KT, Newport) is used.

Coarse temporal alignment is achieved by measuring the pulse arrival times using a fast photodiode. Arrival times are measured relative to an electronic trigger from the titanium sapphire source and the delay line is manually adjusted to minimise the offset between the maxima of depletion and excitation peaks.

Delays are optimised by measuring the fluorescence suppression on a fluorescent bead sample (F8783, ThermoFisher) for different delays. The delays are controlled by the motorised translation stage moving in 1 mm steps (corresponding to a change in delay of 6.67 ps). Three images are taken; one with excitation only, one with excitation and depletion and a final image with excitation only – to confirm the reduction in intensity in the depletion image is due to suppression of fluorescence and not photobleaching. Depletion beam profile is gaus-

sian and the excitation and depletion beams are coaligned, such that all fluorescence can be suppressed.

The suppression is calculated by segmenting the image. A mask is applied to the first excitation only image, to select fluorescent beads, and then calculating the ratio of intensity in the depletion image to the average of the excitation only images.

A plot of suppression as a function of the change in delay is shown in figure 52. The delay line position which minimises the suppression factor (in this case corresponding to 35 ps) is chosen. The motorised delay stage is programmed to initialise to this position.

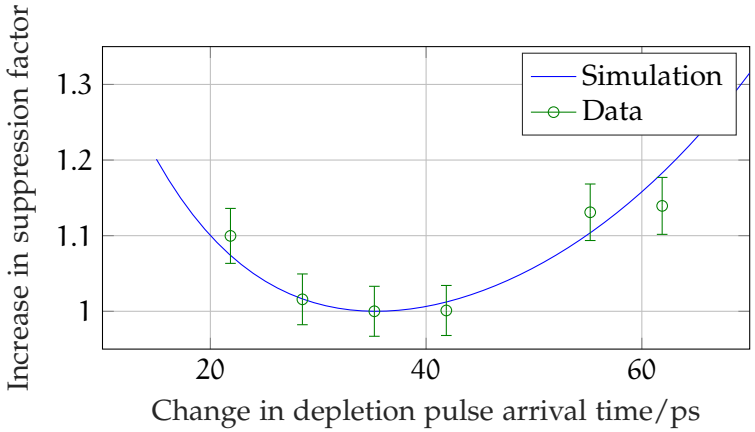

Figure 52: **Fluorescence suppression as a function of depletion arrival time.** This shows good agreement with the simulation based upon equation 41 for changing depletion arrival times of Gaussian excitation and depletion pulses pulses and allows the arrival time to be optimised for this microscope system as 35 ps. Simulation was performed with $t_{depletion}$=100 ps and I_{depl}=20I_S.

5.4 TEMPORAL SHAPING OF DEPLETION PULSES

Laser pulses generated by the Ti:S laser have a pulse duration of $t_{P_0} = 100$ fs. This is shorter than the pulse durations found to be optimum for STED (50-70 ps excitation and 100-300 ps depletion). To achieve the correct pulse durations, pulses are stretched in time by propagation in a polarisation-maintaining single mode fibre of length (L). The fibre lengths were selected based upon group velocity dispersion (GVD) inside the fibre where

$$t_p = t_{P_0}\sqrt{1+\left(\frac{4\ln 2 \times GVD \times L}{{t_{P_0}}^2}\right)^2}, \tag{73}$$

where t_p is the pulse duration after propagation through the fibre, L is the length of the fibre and t_{P_0} is the initial pulse duration. The fibre lengths were calculated – for a silica core fibre – to be 30 m and

100 m for the excitation and depletion beams, respectively, giving pulse durations of 56 ps and 100 ps.

Due to the high peak intensities of the pulses required for the depletion beam, non-linear effects, particularly self-phase modulation, can generate new wavelengths in the fibre. This spreads the energy out over a broader range of wavelengths reducing the depletion efficiency of the beam. The generation of shorter wavelengths can also lead to re-excitation of depleted fluorophores. Furthermore, the phase mask used to generate the vortex beam is wavelength dependent so new wavelengths could reduce quality of the intensity zero. To minimise this effect the optical power is spread out in time, prior to fibre incoupling. This reduces the peak intensity in the fibre. Depletion pulses are pre-chirped (stretched in time) by propagation through two 24 cm SF66 glass blocks (IC optical systems). SF66 glass was chosen due to its high group velocity dispersion.

The spectrum after the fibre is measured as a function of depletion power, for no glass, 24 cm glass and 48 cm glass (two glass blocks). These spectra are shown in figure 53.

When no pre-chirping is used there is an increase in bandwitch from 8 nm in the minimum power case (3 mW) to 63 nm for 294 mW output power. Increasing the pre-chirping by adding 24 cm and 48 cm of SF66 glass decreases the bandwidth at high intensities. The spectra for similar powers are shown in figures 53b and 53c. Output power of 300 mW corresponds to 29 nm bandwidth (24 cm glass) and 19 nm (48 cm glass, 310 mW). This is typical of those used in other STED experiments [83].

5.5 DEPLETION BEAM SHAPING

In the previous sections the temporal shaping and alignment of the excitation and depletion beams was implemented. Next, the spatial shaping of the depletion beam and its alignment to the excitation beam is considered. As discussed in section 3.1.6 there are a range of methods for generating a depletion pattern. Of these a spatial light modulator (SLM) is preferred as a versatile solution that allows aberration correction and simplifies day-to-day alignment of the system. The implementation of the spatial light modulator is described in this section.

5.5.1 *Implementation of spatial light modulator in the depletion path*

After propagation in the polarisation maintaining single mode fibre (PM-SMF), the depletion beam is expanded to fill a spatial light modulator (SLM) (Hammamatsu). To minimise diffraction effects from the pixel size of the SLM and to maintain good phase modulation, the angle of incidence onto the SLM is minimised to ~4°.

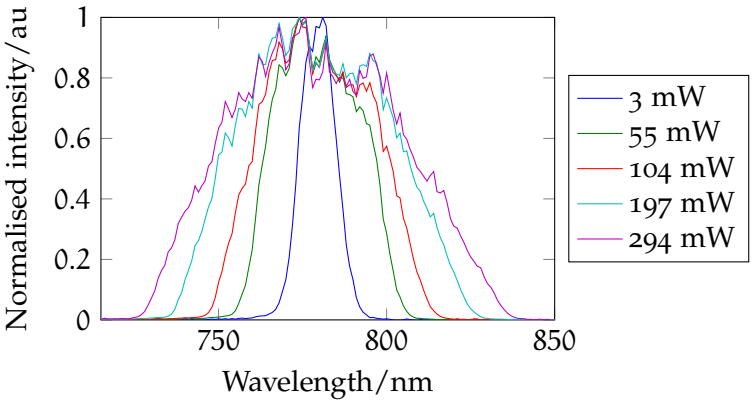

(a) No glass block

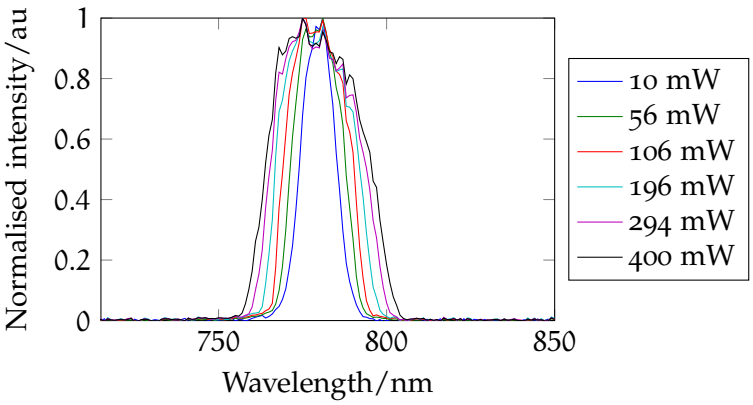

(b) 24 cm glass block

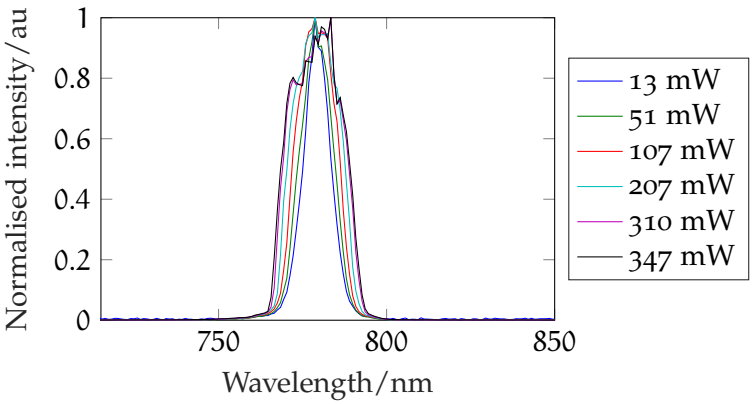

(c) 48 cm glass block

Figure 53: **Spectral broadening of a 780 nm depletion pulse as it propagates through a PM-SMF.** 53a shows the spectrum of the depletion pulse measured after propagation through a 100 m polarisation-maintaining single mode fibre. Spectral broadening occurs due to the high peak intensity. 53b and 53c show the broadening is reduced when the pulse is pre-chirped by propagation through 24 cm and 48 cm of glass, respectively.

The SLM is imaged onto the back aperture of the objective using an optical relay. To ensure a diffraction limited vortex pattern, whilst minimising power losses, the magnification of the optical relay was selected to just overfill the back aperture of the objective.

A linear phase ramp is applied to the SLM to separate the modulated light from the zero order. To reduce unnecessary light on the sample, the zero order was removed by mounting a variable slit in the Fourier plane of the optical relay.

5.5.2 *Polarisation of the depletion beam*

As previously shown by Hao *et al.* [91], the magnitude of the zero and symmetry of STED vortex beams is dependent upon the polarisation of the depletion beam, and that polarisation should be circular in the back aperture. The polarisation of the depletion beam is adjusted by rotating a quarter wave-plate and half wave-plate and measuring the polarisation in the back aperture by rotating a polariser and measurieng the intensity.

5.5.3 *Aberration correction and day-to-day alignment using an SLM*

A Matlab GUI was developed to allow the user to select a phase mask (helical, gaussian or bottle beam) apply linear phase ramps, adjust defocus or perform first order aberration correction.

Depletion point spread functions (PSFs) are measured by imaging the scattered light from sub-diffraction limit (80 nm) gold nanoparticles. Scattered light is deflected onto a PMT by a pelicule beamsplitter mounted in the detection path. The pelicule beamsplitter is mounted on a flip mount and removed from the beam path during imaging, to prevent signal loss.

Excitation and depletion beams are coaligned by sequential imaging of gold nanoparticles with the excitation beam and depletion beam. The gradient of the linear phase ramp and weighting of the defocus Zernike polynomial are adjusted manually to coalign the beams. The 3D PSF of an aberrated vortex beam has been described in detail by Deng *et al.* [94] and Patton *et al.* [100].

The fine alignment of the STED microscope is verified by imaging 100 nm fluorescent beads or 20 nm fluorescent beads. Sequential confocal and STED imaging are used to verify that the STED PSF is centred on the confocal PSF, corresponding to the best signal to noise ratio. To achieve this, the depletion beam is moved with respect to the excitation beam, by changing the linear phase, to achieve this.

Final spherical aberration and defocus adjustments must be made on the sample which is being imaged as these are imaging medium dependent. Both defocus and spherical aberration are adjusted, in the GUI, such that the resolution is the best possible.

An aberration corrected vortex beam is shown in figure 54. This shows a homogeneous doughnut shape with an intensity minimum in the centre. Fitting the vortex pattern to equation 16,

$$I_{depl}(r) = \epsilon r^2 e^{-r^2/\omega^2},$$

gives $\omega = (394 \pm 3)$ nm. For $\omega = \frac{\lambda}{2NA\sqrt{\ln(2)}}$ and NA =1 .4, $\lambda = (764 \pm 6)$ nm, suggesting that the vortex pattern is diffraction limited. The plot profile through the centre is also shown. The residual intensity is of the order of 3%. This residual intensity may be due to the relatively large size (80 nm) of the gold nanoparticles used to visualise the vortex beam, or artifacts due to incorrect polarisation [159]. If the intensity at minimum is 3%, this corresponds to a reduction in signal to 65% at the peak [159] (for depletion intensity of $20I_S$, corresponding to 50 nm resolution of ATTO 647N).

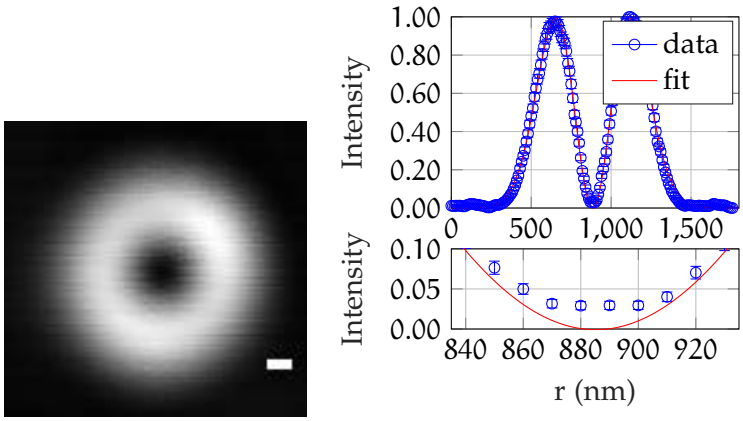

(a) Vortex beam (b) Beam profile

Figure 54: **Aberration corrected vortex beam.** 54a A vortex beam after aberration correction using the SLM imaged as scattered light from an 80 nm gold nanoparticle. The scale bar is 100 nm. 54b A cross-section through the vortex beam. A fit to this profile suggests the vortex beam is diffraction limited. The residual intensity in the null is of the order 3%.

5.6 RIGOROUS DETERMINATION OF RESOLUTION

5.6.1 *Fluorescent bead preparation protocol*

The resolution of the STED microscope is characterised by imaging sub-diffraction limit fluorescent beads. 20 nm dark red beads are mounted on a 1.5H coverslip by first washing the coverslip with 1M pottasium hydroxide for 20 minutes. Potassium hydroxide is removed by washing with deionised water. To ensure beads adhere to the coverslip the coverslips are incubated with poly-L-lysine for 20

minutes and washed with deionised water. The coverslip is then incubated with a bead solution for 20 minutes before excess solvent is removed and the sample is mounted in 2,2′ -thiodiethanol or phosphate buffered saline. Coverslips are attached to the microscope slide using nail polish.

Bead dilution is adjusted to obtain a uniform distribution of fluorescent beads with density of the order 0.25 beads.μm^{-2}. A stock solution is diluted in steps of 100 times dilution in 97% ethanol to achieve the target concentration, typically $1{:}10^7$. At each dilution step the beads are centrifuged to remove any aggregated beads. Beads are taken from the centre of the tube. To ensure individual beads, the bead solution is sonicated for 5 minutes immediately before mounting [160].

5.6.2 *Measuring resolution*

Confocal and STED images at incremental intensities are taken with a pixel size of 20 nm. Resolution is measured by calculating the average full-width half-maximum of all measured beads. A 2D Lorentzian profile is fitted to each bead and a histogram of the distribution of their FWHM is plotted.

An average FWHM of 378 nm (standard deviation = 46 nm, 116 beads) is measured for confocal microscopy. The average FWHM is plotted as a function of increasing depletion laser intensity. This is fitted to the STED resolution equation. At 16 $MWcm^{-2}$, the highest intensity used, the average FWHM is 46.5 nm (standard deviation = 10.9 nm, 162 beads) suggesting an increase in resolution by a factor of eight. This is comparable with many previously reported STED microscope systems.

5.7 CONCLUSIONS

In this chapter the developmental steps of the STED microscop used in this work were illustrated and design considerations explained. A titanium sapphire laser operating at 765 nm is used both as a depletion laser and to generate excitation lines through supercontinuum generation. Both depletion and excitation pulses are stretched in duration by propagation through a single mode fiber to 56 ps and 100 ps, respectively, to minimise non-linear effects, such as two-photon excitation, in the sample. Prechirping of the depletion pulse before propagation in the fibre was investigated to minimise the generation of new spectral components. Prechirping in 24 cm and 48 cm of SF66 was tested and 48 cm was found to be most appropriate, minimising spectral broadening to 19 nm. The addition of more glass may further decrease spectral broadening; however, design constraints of the system have limited this. A spatial light modulator (SLM) is used to

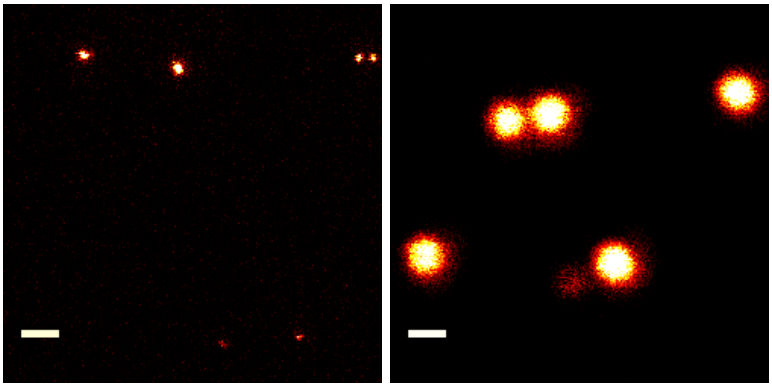

(a) STED (b) Confocal

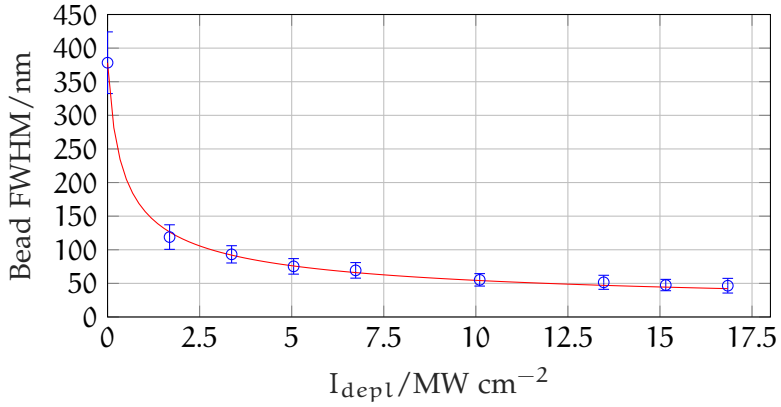

(c) Resolution scaling in STED

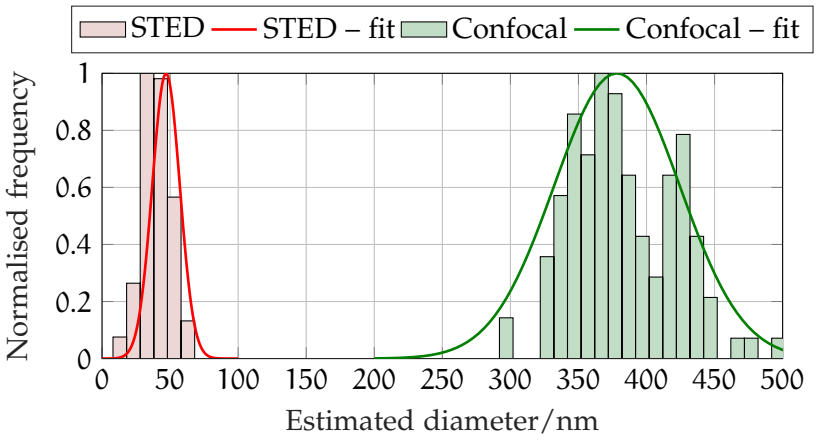

(d) Distribution of bead sizes in STED and confocal

Figure 55: **Resolution characterisation of the STED microscope.** 55a, 55b Typical STED and confocal images. Scale bars are 500 nm. 55c Resolution improves for increasing depletion intensity. The FWHM of 100–200 beads was measured by fitting a 2D Lorentzian function. Error bars are the standard deviation 55d The distribution of bead FWHM for STED (16 MWcm^{-2}, depletion intensity) and confocal microscopy. Mean values were STED: 46.5 nm (standard deviation = 10.9 nm, 162 beads) and confocal: 378 nm (standard deviation = 46 nm, 116 beads).

generate a vortex beam for depletion. A strategy to precompensate for aberrations induced by the optical system and to ensure coalignment between excitation and depletion lasersm is presented. It is demonstrated that diffraction limited vortex beams can be produced using the SLM with an intensity minimum at the centre of 3% of the peak intensity.

The resolution of the STED microscope was tested on fluorescent beads and resolutions of 50 nm are typically observed. This is less than the localisation precision of STORM [161] but STED is less prone to labelling artifacts and can be applied to imaging both live cells and tissue.

In the next chapter this microscope is combined with a commercial AFM to allow combined mechanical property measurements and STED imaging on live cells. This is applied to studying astrocyte migration.

6

CORRELATIVE STED AFM ON MIGRATING ASTROCYTES

6.1 INTRODUCTION

Aim

In this chapter the changes in cytoskeletal organisation and astrocyte stiffness, during polarised migration is investigated, in both basal conditions and in cells expressing connexin 30 (a condition found during the late stages of development). To achieve this an atomic force microscope (AFM) is added to the STED microscope developed in chapter 5.

Motivation

The morphology of astrocytes and astrocytic processes has been shown to be important in synaptic function [162–166]. During development astrocytes develop from migrating glial progenitor cells to polarised highly ramified motile signalling elements [3, 7, 167]. In adults astrocytes undergo polarised migration in response to wounds or trauma in the central nervous system [19, 168], and (in neuroglioma) astrocytes can develop into highly motile tumour cells [169–171]. Astrocyte morphology is also associated with the gap junction protein connexin 30 (Cx30), where Cx30 knockdown astrocytes have been found to invade the synaptic cleft, regulating synaptic strength [6].

Morphological changes in cells such as polarisation, branching or migration are likely associated with changes in the mechanical properties of the cell, such as the cell stiffness [163]. It has also been shown that astrocyte morphological plasticity depends upon the cytoskeletal elements actin and tubulin [8, 172, 173].

Atomic force microscopy (AFM) is one technique which allows the study of cell mechanical properties, including stiffness and the topography of cells. However, this technique alone does not allow the specific identification of individual elements contributing to the cell structure. Correlating AFM with optical microscopy has been previously reported *in vitro* [17, 24–28], on tissue slices and on fixed or live cells [13, 17, 24–26]. In particular, AFM has been correlated with confocal microscopy imaging of the actin cytoskeleton however, due to the limited resolution, actin filaments in dense structures could not be observed [13].

Correlating AFM images with STORM and STED super-resolution *in vitro* has been previously reported and has been performed on

fixed cells [26]. However, as yet, correlative STED and AFM has not been applied to live cell imaging or to studies of astrocytes and astrocyte migration.

Structure

In this chapter a protocol for live cell STED/AFM imaging is developed to allow the correlation of astrocyte cytoskeletal structure with membrane topography and stiffness in confluent and migrating astrocytes. This protocol is tested and used to investigate the contribution of actin and tubulin to astrocyte topography is characterised by correlating specifically labelled STED images of each cytoskeletal element with the membrane topography. The contribution of actin and tubulin to astrocyte stiffness is investigated by measuring the mechanical properties of the cells in response to drug treatments that depolymerise the either actin or tubulin.

Having tested the system in basal conditions, the system is applied to studying astrocyte migration. Migration is induced in astrocyte cultures, using the scratch assay [19], and differences in stiffness between the basis and leading edge of migration are measured. Changes in cytoskeletal structure as also considered, with the help of STED imaging. Following on from the investigation of cytoskeletal organisation, astrocytes expressing Cx30 are investigated and the effects on polarised migration are discussed.

6.2 PROTOCOL FOR STED–AFM IMAGING ON LIVE ASTROCYTES IN CULTURE

6.2.1 *STED imaging of live cells*

STED imaging is performed using the system developed in chapter 5. To allow AFM imaging, the stage of the microscope is replaced with a compatible AFM system (BioScope Resolve, Bruker) as illustrated in figure 56. The optical system is unchanged. STED images are acquired using the Imspector software (Aberrior Instruments).

STED excitation power was 10–20 µW (λ_{exc} = 640 nm, 6–12 kWcm^{-2}) and depletion power was 100-150 mW (λ_{depl}=765 nm, 43–64 MWcm^{-2}), both measured in the back aperture. At the start of each experiment the depletion beam profile and coalignment of excitation and depletion beams were verified by imaging gold nanoparticles and fluorescent beads as described in section 5.5.3. The imaging system was optimised for imaging in cell culture medium by adjusting the defocus and spherical aberration Zernike polynomials displayed on the SLM to obtain the best STED image, as judged by the user. Images were acquired as z-stacks with an 80 x 80 µm^2 lateral FOV and z height of 1.5–3.75 µm depending upon the height of the cell being imaged.

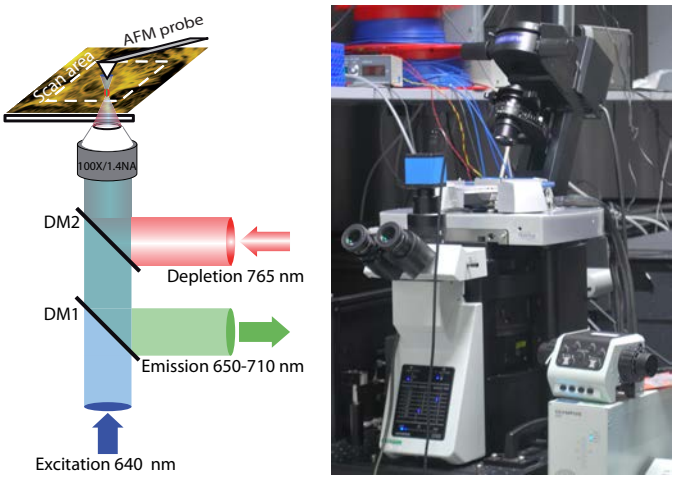

(a) (b)

Figure 56: **Correlative STED-AFM experimental set up.** 56a Conceptual schematic of STED and AFM set up fully described in figure 48. The AFM probe is centred on the optical field of view prior to imaging. AFM images can then be taken in user defined regions of interest within the optical field of view. 56b A photograph of the STED-AFM system *in situ*.

The pixel sizes were 50x50 nm^2 laterally and 500-750 nm axially. Pixel dwell times of 35 µs were used giving a total acquisition time of 5–7.5 minutes per image stack.

Some STED images were combined with confocal images of GFP or mVenus, to identify transfected cells. These images were taken after the STED images, as the 488 nm excitation laser was found to contribute to photobleaching of the SiR dyes [31] used for STED.

6.2.2 *STED and AFM coregistration and coalignment*

The AFM used was a sample scanning AFM. In sample scanning AFM, the sample is moved laterally for AFM imaging whilst the tip only moves axially. The STED system is a beam scanning system, where the laser is scanned over the sample using galvonometric mirrors. Prior to imaging the size and orientation of the STED pixels must be calibrated with respect to the AFM movement (coregistration), and AFM and optical fields of view must be centred on one another (coalignment). These procedures are briefly described.

Coregistration

During the coregistration procedure, the AFM stage was translated by the NanoScope software to three known xy positions. A confocal image of a fluorescent bead sample was captured in each position. A common feature from all three images was selected and the the

transformation required to translate an optical image into an AFM image was calculated by the AFM software. Coregistration must be performed once per microscope objective and per pixel size (in the optical image) and can be used for all subsequent experiments.

Coalignment

Alignment between optical and AFM images was performed for every experiment. First, for coarse coalignment, the AFM tip was centred on the optical field using confocal images of scattered light to locate the AFM tip and manually adjusting the tip position. Optical images of the tip and sample were imported into the NanoScope acquisition software using the MIROView tool. The transformation calculated during the coregistration process was applied by the software. AFM regions of interest were defined based upon the optical image. Fine coalignment was achieved by aligning features that are common to both imaging modalities. Typically borders between cells were clearly observed in STED and AFM. The optical image was translated, in software, with respect to the AFM image for a good agreement between the optical image and all AFM images.

6.2.3 *AFM probes and force calibration*

AFM on cells in culture or in tissue is a challenge in AFM as cells can have a wide range of heights relative to the length of the AFM tip [29]. This can lead to shadowing or blind spots in the image if the cantilever comes into contact with the sample.

A further challenge when performing AFM force measurements is that the spring constant and deflection sensitivity of the AFM probe must be precisely calibrated before every experiment. This process can be time consuming and generally requires measuring the force-distance curve on a substrate which is infinitely stiff compared to the tip. For live cell experiments this can be measured on a region of coverglass which does not contain any cells; however, any contaminants on the surface will change the measured value. It is usually preferred to measure the spring constant on a separate substrate. This process can be time consuming and can be affected by user errors.

To overcome these challenges, probes recently developed by Bruker [29] (PFQNM-LC, Bruker) were used for AFM imaging. These probes have taller tips (17 μm) than conventional probes, to prevent the cantilever touching the sample. The spring constant of these probes has been precalibrated using a vibrometer, meaning that only the deflection sensitivity needs to be measured prior to imaging. This process is fully automated and takes less than 5 minutes, using the "no-touch calibration" function in the NanoScope acquisition software (Bruker). These AFM probes have been used in previous reports of AFM mi-

croscopy for imaging soft structures such as microvilli [29] and for measuring virus adhesion forces [12].

6.2.4 *AFM imaging*

AFM imaging was performed on a commercial system (BioScope Resolve, Bruker) using the NanoScope software. The imaging mode used was "PeakForce QNM (PFQNM) in fluid – live cells". The scan rate was 0.271 lines per second and images were 256 x 256 pixels corresponding to 15.75 minutes per image. A field of view of 18 x 18 μm^2 was used for all images. Typically four AFM images were acquired per optical field of view. Peak force setpoints were adjusted to optimise the shape of the force curve and were typically 300–500 pN. The force curve is measured and saved for each pixel for offline analysis. An example force curve is shown in figure 57.

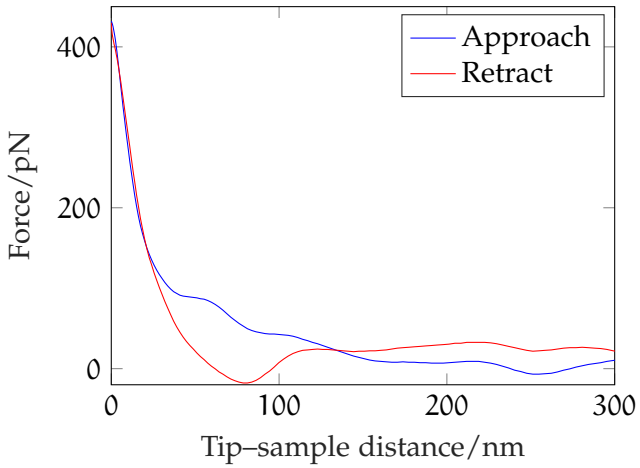

Figure 57: **Example measured force curve.** Measured on a live astrocyte in culture.

6.2.5 *Calculation of cell Young's modulus*

The probes used in this work (PFQNM-LC, Bruker) have a spherical tip that merges tangentially into a cone. The spherical tip has a diameter of 130 nm. The cone has an opening angle of 15° [29]. The cone–sphere model proposed by Briscoe *et al.* [60] describes the force of this type of indenter and this model is used to calculate the Young's modulus of the sample.

Every force curve during imaging was saved and analysed offline using the NanoScope Analysis software (Bruker) producing a 256 x 256 map of Young's modulus values (an example stiffness map is shown in figure 59c). Cell stiffness is heterogeneous over the AFM field of view so, to estimate the stiffness of a given region of a cell, the average stiffness in the AFM image was calculated. Where an AFM FOV

includes multiple cells, or a cell and glass, an average value is measured for individual cells by cropping the AFM image. Where multiple AFM images are acquired on the same cell, the cell stiffness is the average of the stiffnesses of each image.

This protocol was used to combine mechanical stiffness data with STED images of the cytoskeleton, but could be generalised to any live-cell study.

6.3 CORRELATIVE STED–AFM INVESTIGATION OF ASTROCYTE CULTURES IN BASAL CONDITIONS

6.3.1 *Sample preparation*

Primary cortical astrocyte cultures were prepared by Nathalie Rouach and Gregory Ghezali. Following dissection cell cultivation, further treatments and fluorescent labelling were performed by the author, Nathalie Rouach and Gregory Ghezali. Experiments were carried out according to the guidelines of the European Community Council Directives of January 1st 2013 (2010/63/EU) and of the local animal welfare committee, and all efforts were made to minimize the number of animals used and their suffering.

The protocol was previously described by Koulakoff *et al.* [174] and is outlined briefly here. Brains were removed from mouse CD-1 newborn (mouse) pups (postnatal days 1–3, P1-P3). Cortices were dissected in cold PBS-glucose (33 mM). Meninges were withdrawn and cortices were mechanically dissociated. Astrocytes were seeded on polyornithine-coated glass coverslips in DMEM containing 10% fetal calf serum, 10 Uml^{-1} penicillin, and 10 μgml^{-1} streptomycin (GIBCO) and incubated at 37 °C, 5% CO2. After one week, when cells had reached confuency, 1 µM cytosine-arabinoside was added to the cell culture for three days to eliminate proliferating microglial cells. Medium was changed every three days. Cells were imaged after 2–3 weeks in culture.

6.3.2 *Live cell STED-AFM imaging of cytoskeletal proteins*

Fluorescent labelling

As discussed in section 4.4.2, sample preparation for STED microscopes with near-infrared depletion is challenging due to an absence of fluorescent proteins with suitable photophysical properties. The recently developed silicon rhodamine (SiR) organic dyes [30–33] are well adapted for live cell super-resolution imaging. In particular, the dyes are membrane permeable and have low cytotoxicity [31]. The SiR dyes have been applied to live cell STED super-resolution imaging with NIR depletion due to their high brightness and photostabil-

ity. They are also fluorogenic and therefore have a low background due to non-specific binding [111].

Of particular relevance to this study are the dyes SiR-actin and SiR-tubulin. These dyes are conjugated to drugs, which bind specifically to F-actin and tubulin (desbromo-desmethyl-jasplakinolide and docetaxel, respectively). Astrocytes were incubated for 1 hour in culture medium containing 1 µM SiR-actin or SiR-tubulin. Staining medium was removed and replaced with HEPES complemented medium prior to imaging.

STED imaging of actin cytoskeleton

To illustrate the benefits of STED imaging, STED and confocal images of actin filaments, in live astrocytes, labelled using SiR-actin are shown in figure 58. STED imaging allows better resolution of actin filaments than confocal and resolves filaments that cannot be resolved by confocal imaging.

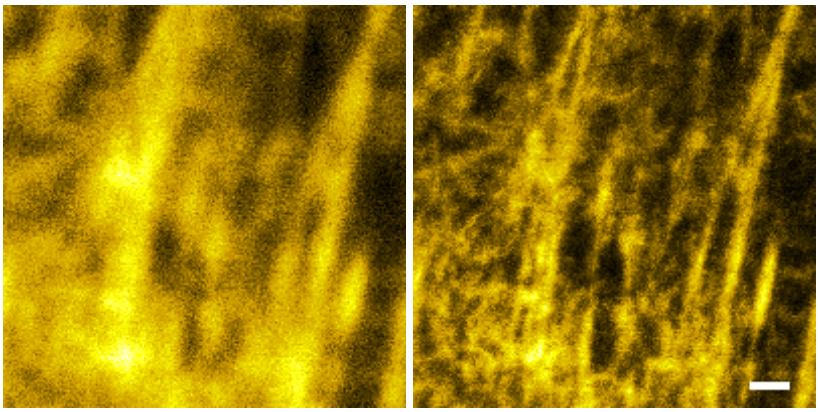

(a) Confocal (b) STED

Figure 58: **Confocal and STED images of actin cytoskeleton.** The actin cytoskeleton, labelled with SiR-actin, is better resolved in STED (58b) than in confocal (58a). This allows the resolution of individual actin filaments and dense filament meshworks. Scale bar is 1 µm.

Correlating AFM height and stiffness images and STED images

A typical AFM topography and stiffness map, measured on a live astrocyte in basal conditions, is shown in figure 59. The topography reveals a polarised structure, which is thought to be cytoskeletal structures sensed through the cell membrane. The stiffness map reveals high and low stiffness regions, with the high stiffness regions corresponding to the filamentous structures present in the topography image.

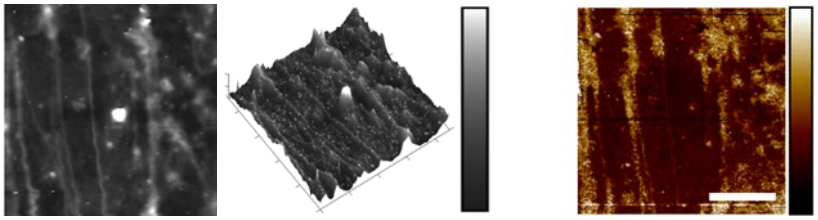

(a) AFM height map (b) 3D height map (grey scale 0–402.5 nm) (c) AFM Young's modulus map (colourscale -11.4–62.5 kPa)

Figure 59: **AFM force and height images of astrocytes.** 59a, 59b Show AFM topography images of the same field of view on live astrocytes. The images show polarised fibrillar elements. 59c Map of the Young's modulus (stiffness) of the astrocyte calculated using the cone-sphere model. The average stiffness is calculated for each cell. The scale bar is 5 µm.

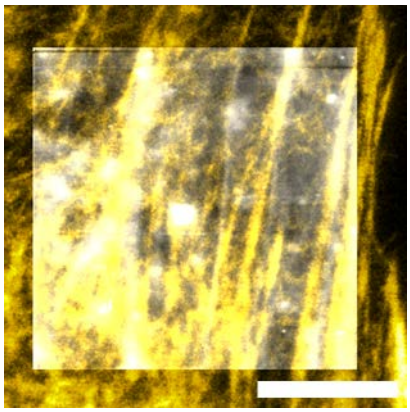

Figure 60: **Colocalisation of AFM topography and STED images.** The AFM height image represented in 59a is overlaid on the STED image of actin in 58b showing that both modalities can be correlated to image the same feature. Scale bar is 5 µm.

AFM topography maps can be overlaid on the corresponding optical images (figure 60). Furthermore, AFM topography images and stiffness maps are already directly correlated as they were measured from the same force curves, allowing the correlative imaging of all three modalities. Interestingly the polarised structures in AFM topography image appear to correlate with the fluorescently labelled actin cytoskeleton. This is further investigated in the next section.

6.3.3 *Contribution of actin to cell topography*

AFM height images show highly polarised structural elements in astrocytes. To identify the nature of these structures they are compared with STED images of actin from the same cell. Actin revealed similarly polarised structures within confluent astrocytes, as shown in

figure 61. A line profile through the optical and AFM images (figure 61b) shows that many actin fluorescence intensity peaks and AFM peaks are co-located. This suggests that actin is a contributor to cell astrocyte topography. Similarly the Pearsons correlation coefficient is 0.2 (figure 61c). This is in agreement with previous reports that have suggested that this is also the case for endothelial cells [13].

6.3.4 *Contribution of tubulin to cell topography*

The contribution of tubulin to cell topography is contrasted with actin. Correlative AFM and STED images of tubulin, labelled with SiR-tubulin, are shown in figure 62. STED images of tubulin do not show a clear polarisation orientation and the tubulin structures do not correlate with astrocyte topography (Pearsons coefficient = 0.04, figure 62c). This is unlike the actin images.

6.3.5 *Measurement of astrocyte stiffness*

AFM stiffness measurements allow quantitative information about cells to be determined. The application of AFM stiffness measurements to live astrocytes is investigated here.

In the first instance it is verified that AFM stiffness measurements can be performed on transfected cells as this will enable a range of studies, for instance investigating the mechanical properties of astrocytes expressing Cx30. The stiffness of non-transfected astyrocytes is compared with the stiffness of GFP expressing astrocytes.

The correlated stiffness maps allow the average stiffness of individual cells to be measured. The mean stiffness of astrocytes is measured as 27.9 $\pm$ 2.6 kPa n = 38. The range of observed stiffness values was high and is likely due to heterogeneity of astrocytes. It is found that transfection with GFP does not alter cell stiffness (23.2 $\pm$ 3.3 kPa, n = 12, $p > 0.05$, Mann Whitney test, figure 67) and therefore that the transfection process does not perturb cell stiffness.

6.3.6 *Contribution of actin to cell stiffness*

As actin contributes to the topographical structure of cells, it is investigated whether there is a similar contribution to cell stiffness. The actin network is disturbed by treatment with cytochalasin D (30 µM, 1 hour) prior to staining with SiR-actin. Treatment with cytochalasin D depolymerised the actin filaments as, shown in figure 64. The topography of the cells was also changed and the polarised structures in figure 61 were not observed.

Because actin was depolymerised, individual cells could not be identified and GFP labelling was used to delineate individual astrocytes. Actin disruption was found to descrease astrocyte stiffness

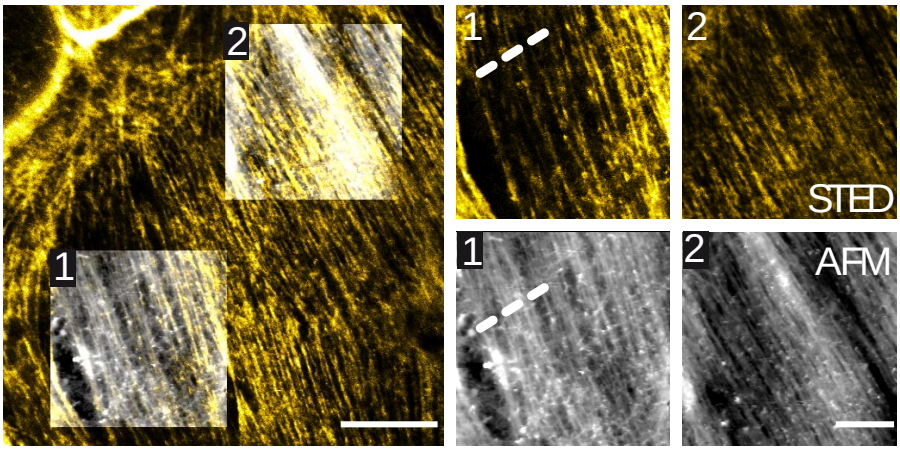

(a) STED image of actin (yellow) correalted with AFM topography (grayscale)

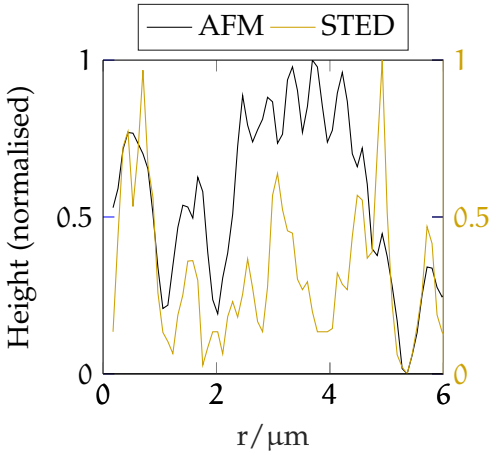

(b) Line profile through dashed region

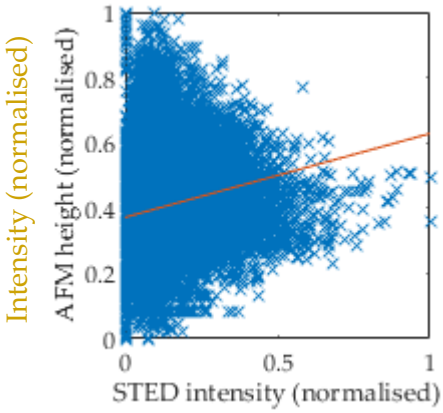

(c) Correlation of pixel values

Figure 61: **Colocalisation of AFM topography and STED images of actin.** 61a AFM topography images (grayscale) show good agreement with STED images of specifically labelled actin (SiR-actin). This suggests that actin is a major contributor to the measured cell topography of astrocytes. The AFM colour scale represents ranges in height of 455 nm and 464 nm in regions 1 and 2 respectively. The scale bars are 10 µm (large image) and 5 µm (small images). 61b Line profile through the dashed region. the positions of the peaks generally agree in both imaging modalities. 61c Scatter plot of corresponding pixel values between STED and AFM showing a positive correlation with Pearsons coefficient = 0.2.

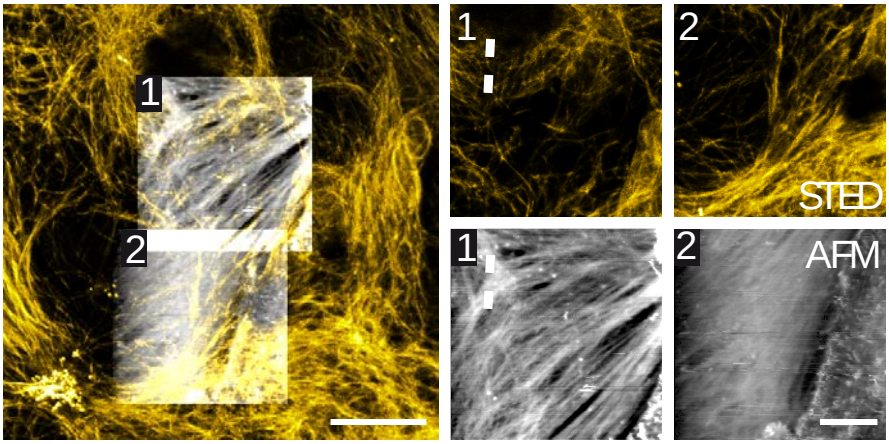

(a) STED image of tubulin (yellow) correalted with AFM topography (grayscale)

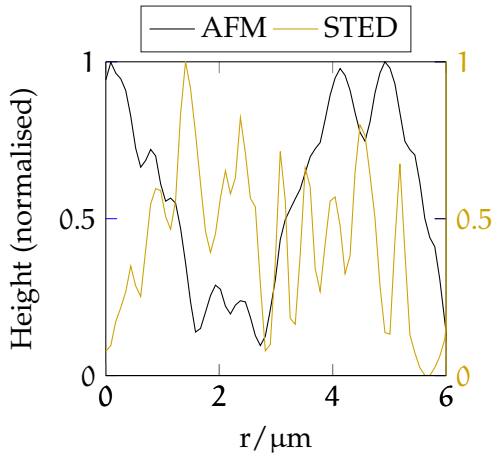

(b) Line profile through dashed region

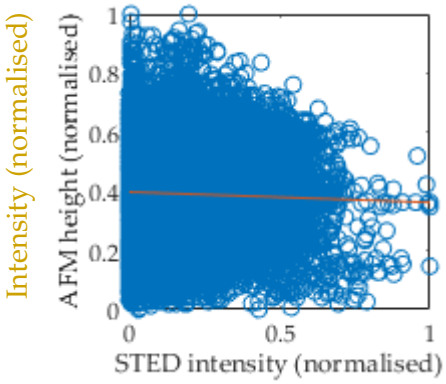

(c) Correlation of pixel values

Figure 62: **AFM topography does not correlate with STED images of tubulin.** 62a Tubulin (labelled with SiR-tubulin) is imaged in STED microscopy. Tubulin images are overlaid with AFM images of the cell topography. The cell topography shows polarised filaments with different direction and organisation to the tubulin image. This suggests that tubulin contributes less to cell topography than actin. AFM images are grayscale with gray values representing height ranges of 680 nm in region 1 and 388 nm in region 2. The scale bars are 10 µm (large image) and 5 µm (small images). 62b Line profile through the dashed region, showing limited agreement between the peaks of STED and AFM images. 62c Scatter plot of corresponding pixel values between STED and AFM reflecting a low correlation between tubulin and astrocyte topography (Pearsons coefficient = 0.04).

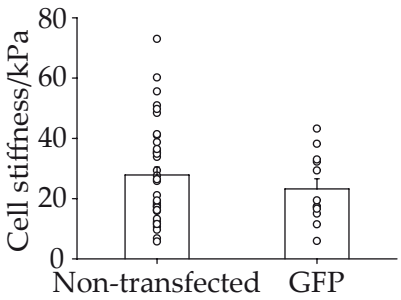

Figure 63: **Effects of transfection on astrocyte stiffness.** The mean cell stiffness of control (non-transfected, n = 38) and GFP-transfected astrocytes (n = 12), showing no significant effect of GFP transfection on stiffness ($p > 0.05$, Mann-Whitney test), suggesting that the transfection process does not affect the stiffness of astrocytes.

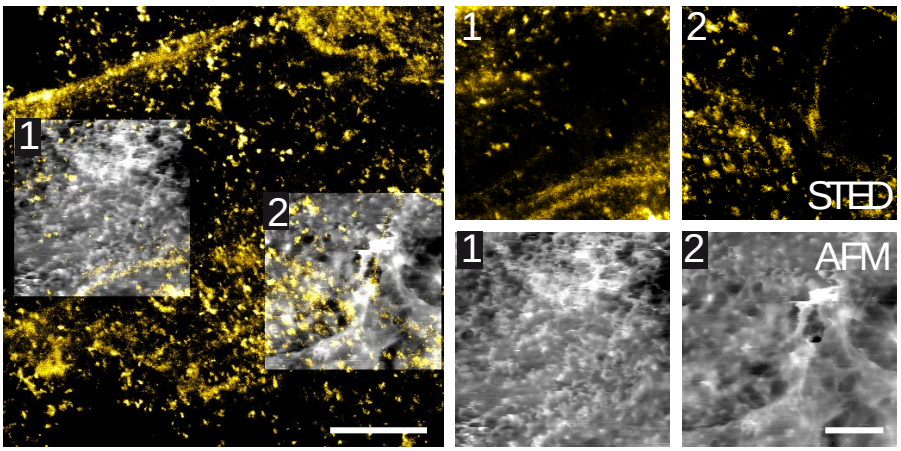

Figure 64: **STED and AFM images of astrocytes treated with cytochalasin D.** Actin is depolymerised by treatment with cytochalasin D. Depolymerisation of actin (STED images) is accompanied by changes in the cell topography relative to basal conditions. Polarised filaments are not observed in either imaging mode. The grayscale AFM images represent height scales of region 1: 1394 nm, region 2: 1320 nm. Scale bars are 10 μm (large images) and 5 μm (small images).

(GFP: 23.2 ± 3.3 kPa, n = 12; GFP + cytochalasin D: 14.5 ± 1.9 kPA, n = 10, p<0.05, unpaired *t* test). This suggests that, as well as contributing to the cell topography, actin also contributes to cell stiffness.

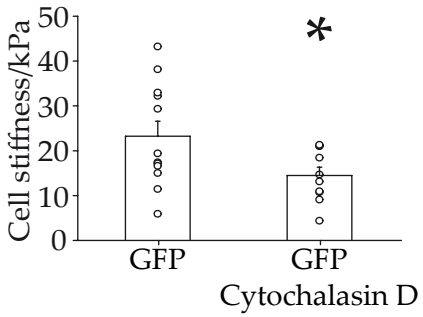

Figure 65: **Effects of depolymerising actin on cell stiffness.** Treatment with cytochalasin D (30 μM, 1 h) reduced the stiffness of astrocytes relative to control (GFP, n = 12; GFP + cytochalasin D, n = 10, p < 0.05, unpaired *t* test). Asterisk indicates statistical significance (* represents p < 0.05). GFP fluorescence was used to allow the identification of individual cells.

6.3.7 *Contribution of tubulin to astrocyte stiffness*

As in the previous study the involvement of tubulin in cell stiffness is investigated by depolymerising the tubulin cytoskeleton. Astrocyte cultures are treated with nocodazole (16 μM, 1 hour) prior to staining. Tubulin is depolymerised, as shown in figure 66. Again GFP labelling is used to identify inidividual astrocytes. Unlike actin, a change in astrocyte stiffness is not observed when tubulin is disrupted (GFP: 23.2 ± 3.3 kPa, n = 12; GFP + nocodazole: 26.2 ± 5.5 kPa, n = 7, p > 0.05, Mann–Whitney test). Overall this suggests that the actin cytosekelton is a major contributor to astrocyte mechanical properties.

6.3.8 *Discussion*

In this section STED and AFM were correlated together to investigate the contributions of the cytoskeletal proteins to the physical properties of live astrocytes. Using this method it was found, through correlative imaging, that actin contributes to the topography of astrocytes. Pharmacological treatments and AFM Young's modulus measurements were used to show that actin contributes to cell stiffness through. This is in contrast to tubulin which was not found to correlate with astrocyte topography and a change in stiffness was not observed in the case of tubulin depolymerisation.

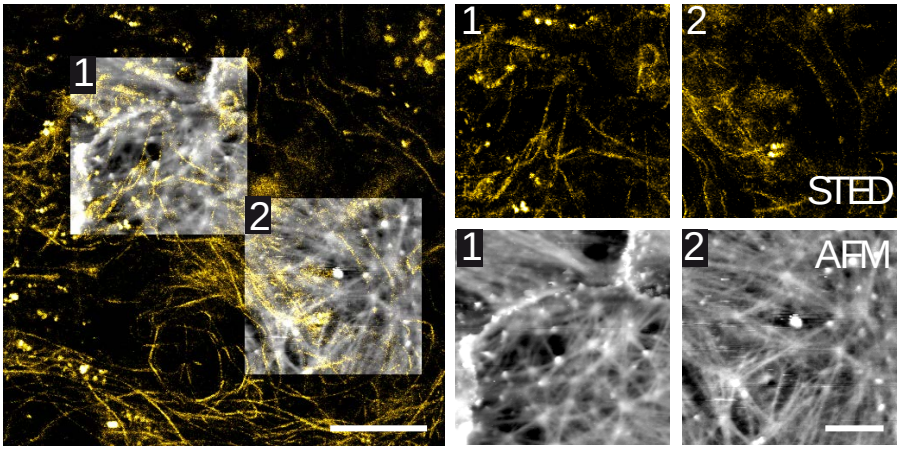

Figure 66: **STED and AFM images of astrocytes treated with nocodazole.** Tubulin is depolymerised by treatment with nocodazole (16 µM, 1 h). Both the tubulin cytoskeleton and AFM topography different to that in basal conditions. The grayscale AFM images represent height scales of: region 1: 680 nm, region 2: 388 nm. Scale bars are 10 µm (large images) and 5 µm (small images).

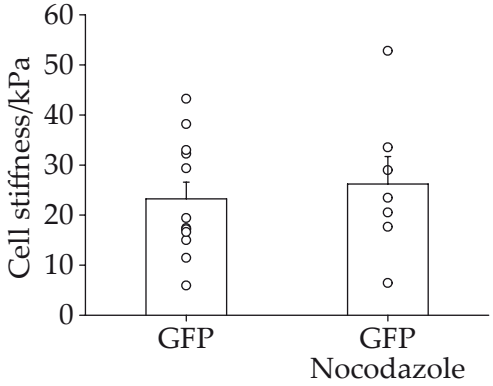

Figure 67: **Effects of depolymerising tubulin on cell stiffness.** Treatment with nocodazole (15 µM, 1 h) did not lead to a measurable change in astrocyte stiffness relative to GFP transfected control cells (GFP: 23.2 ± 3.3 kPa, n = 12; GFP + nocodazole: 26.2 ± 5.5 kPa, n = 7, $p > 0.05$, Mann-Whitney test).

The contribution of the actin cytoskeleton to cell topography has been previously established on a range of cell lines [13, 175], as well as the contribution of actin stress fibers to cell stiffness [64, 176].

The effects of tubulin on cell stiffness have been less well studied [177]. It was found here that tubulin does not contribute to astrocyte topography. This is similar to endothelial cells [175] however, in contrast to this result, tubulin has been found to be a significant contributor to axonal stiffness [178]. This suggests that the contribution of microtubules to cell stiffness is cell type – or cellular compartment – dependent.

Having demonstrated that correlative STED and AFM imaging can be used to characterise the cytoskeleton and physical properties of astrocytes in basal conditions, the technique is applied to investigate astrocyte cytoskeleton organisation and physical properties during polarised migration.

6.4 STED-AFM ON MIGRATING ASTROCYTES

6.4.1 *Scratch-induced migration assay*

Polarised migration is induced in confluent astrocyte cultures using a scratch assay [19]. In brief, a wound is made in the dish by scraping in a straight line with a 20 µL pipette tip (~300 µm). To simplify finding the region of the wound three wounds are made in a star shape. Astrocytes migrate in a direction perpendicular to the scratch. Migrating astrocytes are imaged 6–8 hours after making the scratch, when the cells will have reached their maximum migration distance.

6.4.2 *Cytoskeletal reogranisation during polarised migration*

A migrating astrocyte (scratch-induced) is shown in figure 68. Actin stress fibres parallel to the direction of migration concentrate in the leading edge of migration. Figure 69 shows the tubulin structure in a migrating astrocyte. The tubulin cytoskeleton shows a greater organisation than in the basal condition, with polarised filaments in the direction of migration in both the basis and leading edge of the migrating astrocytes.

6.4.3 *Subcellular changes in membrane stiffness in migrating astrocytes*

To investigate whether cytoskeleton remodelling in polarized migration alters the subcellular mechanical properties, cell stiffness is measured using AFM. In this case the AFM is used to probe two different regions of the migrating cells, the leading edge and the basis. Paired values can be compared from the same cell and an increase in stiff-

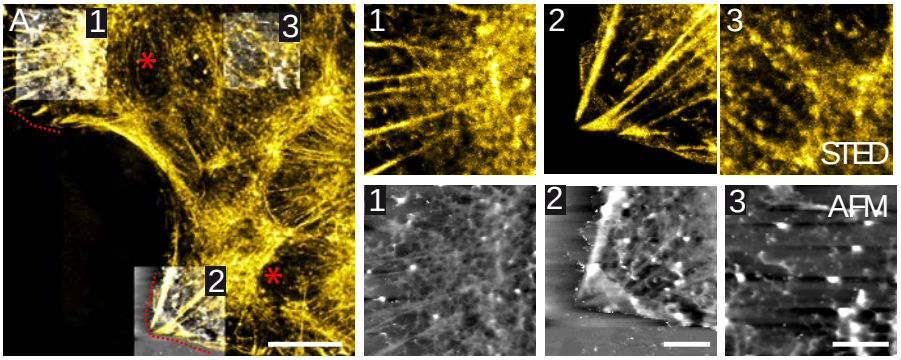

Figure 68: **Actin reorganisation during polarised migration.** STED images (SiR-actin) of the actin cytoskeleton are correlated with AFM images. In the leading edge (indicated by red dashed line, corresponding to regions 1 and 2) stress fibres pointed in the direction of migration are observed in both images. In the basis (*, region 3) actin is less organised. AFM height range: region 1: 564 nm, region 2: 814 nm, region 3: 942 nm. Scale bars are 10 µm (large images) and 5 µm (small images).

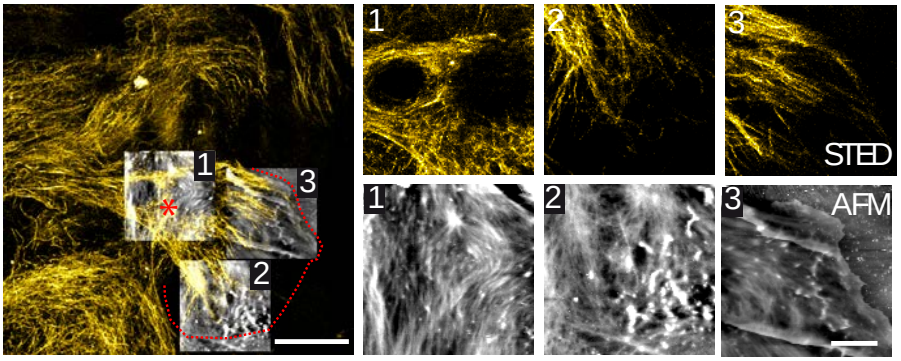

Figure 69: **Tubulin reorganisation during polarised migration.** Tubulin is labelled with SiR-tubulin and imaged using STED microscopy. The astrocyte topography is imaged by AFM. STED images of tubulin show structures in the basis (*, region 1) and leading edge (dashed line, regions 2 and 3) are polarised in the direction of migration, unlike in basal conditions where microtubules are not linearly polarised. AFM images do not correlate with STED images of tubulin images. AFM height range: region 1: 297 nm, region 2: 322 nm, region 3: 396 nm. Scale bars are 10 µm (large image) and 5 µm (small images).

ness is observed in the leading edge (30.5 ± 4.3 kPa, n = 16) compared to the basis (16.3 ± 2.9 kPa, n = 16, $p < 0.001$, paired t test, figure 70).

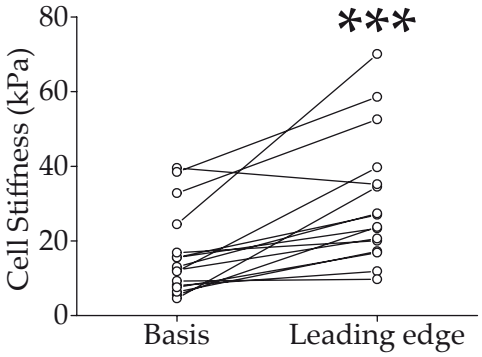

Figure 70: **Reorganisation of astrocyte stiffness during polarised migration.** Cellular stiffness is increased in the leading edge of migration (30.5±4.3 kPa, n=16) relative to the basis of the protrusion (16.3 ± 2.9 kPa, n = 16, $p < 0.001$, paired t test). Each data point represents a stiffness measurement in the basis or leading edge. Lines join data points from the same cell.

6.4.4 *Discussion*

As a result of astrocyte migration both the actin and tubulin cytoskeletons were found to be rearranged after more than 8 hours of migration relative to cells in basal conditions. The actin cytoskeleton formed stress fibres in the leading edge. These actin filaments are thought to push the cell membrane forwards [8, 179, 180]. Tubulin is polarised in the direction of migration throughout the astrocyte.

The changes in the actin and tubulin cytoskeleton corresponded to changes in astrocyte stiffness, an increase in stiffness was observed in the leading edge of migration relative to the basis. The increase in stiffness corresponded to an increase in actin stress fibres in the leading edge. In section 6.3.6 it was shown that actin is a major contributor to astrocyte stiffness. Furthermore, actin stress fibres have previously been reported to have high stiffness [181] suggesting that the increase in actin filaments in the leading edge of migration leads to an increase in stiffness.

Tubulin was also found to be rearranged compared to basal conditions. Although tubulin was not found to contribute directly to astrocyte stiffness in basal conditions it is well known that tubulin contributes to polarised migration. Tubulin has been reported to be important in establishing the directionality of migration and the remodelling of the tubulin cytoskeleton is necessary to establish retraction in the basis [182, 183]. Together microtubules and actin have been found to influence each other's dynamics and contribute to cell mi-

gration either by generating a force at the plus end or controlling regulators promoting actin rearrangement [8, 184, 185].

The combination of STED and AFM to study cytoskeletal elements and cell mechanical properties during polarised migration is a promising approach in functional cell biology. This method was demonstrated for the simple case of actin and tubulin, for which there is a commercial solution for direct labelling [31], but other approaches such as SNAP-tag labelling could be used to label arbitrary protein targets [30, 101, 186].

In the next section the STED-AFM, approach for investigations in neuroscience is applied to the study of astrocytes and the gap-juntion protein connexin30.

6.5 CONNEXIN30, THE CYTOSKELETON AND CELL MECHANICAL PROPERTIES

6.5.1 *Introduction*

Connexin30 (Cx30) in mouse models is associated with spatial memory [166, 187–189] and response to pain anxiety and stress [166, 187]. Interestingly connexin30 expression is reduced in the brains of humans suffering from major depression [166, 190] and (human) suicide completers [166, 191]. Some of these pathologies may be associated with the effects of connexin30 on synaptic strength, cell migration and invasion of synapses [6].

The effects of Cx30 on migration are investigated in this section. It has previously been reported that connexin30 colocalises with actin [21] and, in the previous section, it was found that actin is important in establishing astrocyte stiffness and that the actin cytoskeleton is remodelled during migration. It has also been found that, for cancer cells, invasive and motile cells have lower stiffness (in the central or overnucleus region) [176]. Taken together, this suggests that connexin30 could be related to cytoskeletal organisation and its effects on cell stiffness.

In this section, the reorganisation of the actin cytoskeleton and mechanical properties of Cx30-expressing astrocytes is investigated.

6.5.2 *Actin cytoskeleton organisation of migrating CX30 astrocytes*

To investigate whether Cx30 interacting with actin alters the remodelling of cytoskeletal structures during migration, correlative STED-AFM imaging was performed on astrocytes labelled with SiR-actin, as described in section 6.2. Astrocyte cultures were prepared as described in section 6.3.1. Astrocytes were transfected with mVenus-connexin30 or GFP 24–48 hours prior to the experiment. Eight hours before imaging, migration was induced using the scratch assay de-

scribed in detail in section 6.4.1. One hour prior to imaging actin was labelled by incubation cell culture medium containing SiR-actin (1 μM).

Following scratching the wound-edge control astrocytes initiated polarised migration and some protruding cells formed. An example image of a migrating control (non-Cx30-expressing) astrocyte and a Cx30-expressing astrocyte are shown in figures 71 and 72, respectively. The actin organisation and the correlation with cell topography is discussed for the basis and leading edge of migration.

Basis

In control migrating astrocytes – those not expressing Cx30 – actin was highly organised in an array of polarised actin fibres (figure 71). In addition, STED images of actin filaments correlate with the astrocyte topography AFM images, both showing polarised structural elements with similar orientation (Control: STED: 82°; AFM: 79°, measured using the FibrilTool FIJI macro [192]). STED images actin filaments co-localise with the major polarised elements in the AFM topography image.

In Cx30-expressing astrocytes, actin fibres are thinner and less dense than in control astrocytes (figure 72). STED images of actin filaments and AFM images of astrocyte topography also show weaker correlation in the basis of cx30-expressing migrating astrocytes. They display different orientations (Cx30: STED: 75°; AFM: 55°, FibrilTool FIJI macro [192]) and the AFM topography image shows features not present in the actin filaments. Finally correlating the values of corresponding pixels in STED and AFM shows a higher correlection in GFP astrocytes than Cx30 astrocytes (GFP: 0.14, Cx30 0.01, Pearson's coefficient). This suggests a reduced contribution of actin to cell topography.

Leading edge

In the migration leading edge, similar but stronger effects of Cx30 on actin fibres were observed. Whilst in control conditions stress fibers were observed pointing in the direction of the wound, in Cx30-expressing cells actin was less organised (figures 73 and 74 – control and Cx30-astrocytes respectively). Correlated AFM images also revealed reduced correlation with astrocyte topography compared to control conditions (GFP: 0.08, Cx30 0.02, Pearson's coefficient). Overall this suggests that Cx30 impairs actin remodelling and the formation of stress fibres during polarised migration.

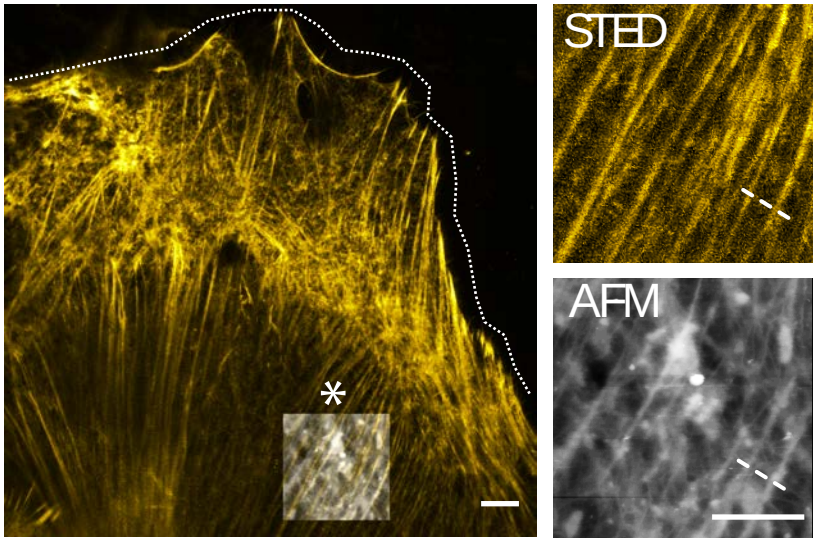

(a) STED image of actin (yellow) correalted with AFM topography (grayscale)

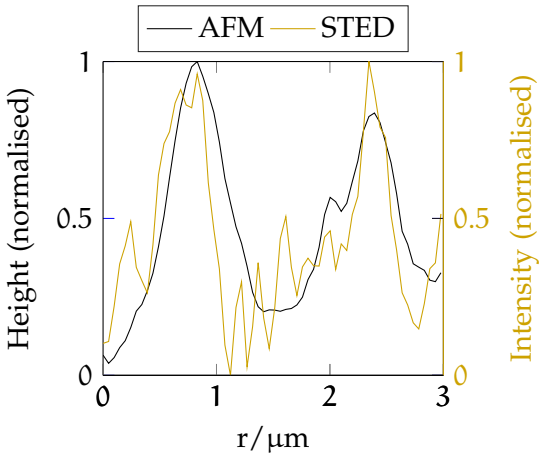

(b) Line profile through dashed region

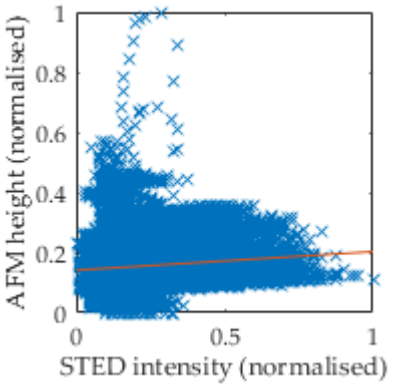

(c) Correlation of pixel values

Figure 71: **Actin structure in the basis of control migrating astrocyte.** In the basis actin fibres are observed to be polarised in the direction of migration (82°, with respect to the wound – FibrilTool FIJI macro). AFM topography maps correspond to the actin filaments and show similar polarity (79°). 71b represents a line profile through the dashed region showing that fluorescently labelled actin corresponds to the major features in the AFM topography. 71 Scatter plot of corresponding AFM heights and STED values showing positive correlation (Pearsons coefficient = 0.14). The AFM colour scale represents ranges in height of 496 nm. Dotted lines represent the leading edge, the star represents the basis. All scale bars correspond to 5 µm.

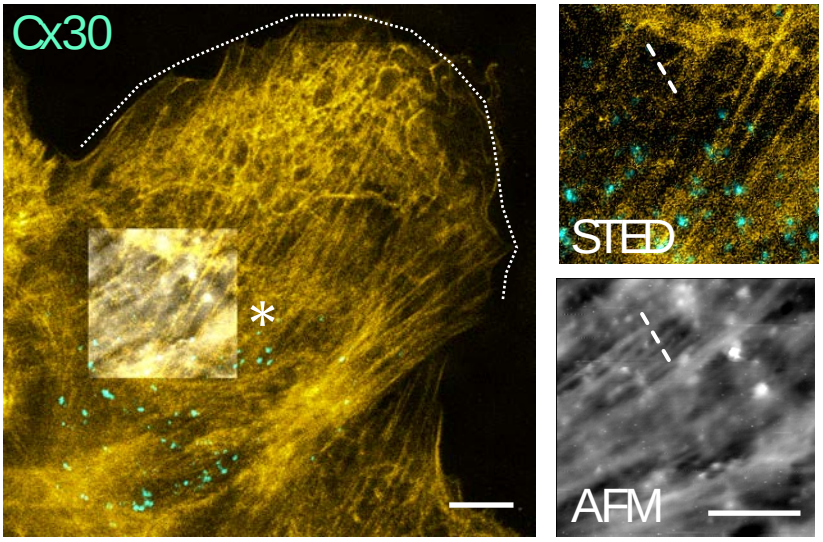

(a) STED image of actin (yellow) correalted with AFM topography (grayscale)

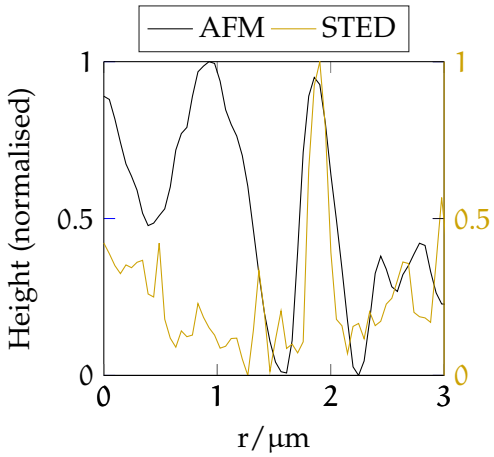

(b) Line profile through dashed region

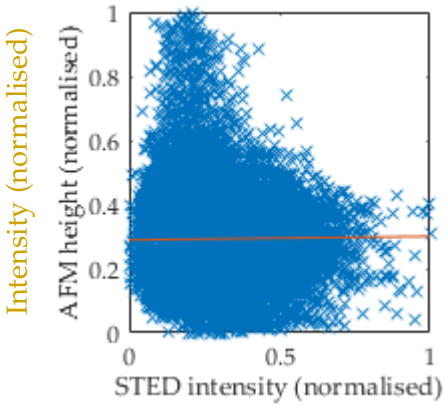

(c) Correlation of pixel values

Figure 72: **Actin structure in the basis of connexin30 expressing migrating astrocyte.** Unlike the control astrocyte, in Cx30-astrocytes the actin structure has a different polarisation to the AFM topography. STED images of actin show a polarisation angle of 75° compared to 55° in AFM. 72b A line profile (dashed line) showing that, although some features do appear in STED and AFM images, other cellular elements, as well as actin, are involved in establishing the topography of Cx30-expressing astrocytes in the basis. Similarly 72c shows a scatter plot of corresponding height and intensity values showing limited positive correlation (Pearson's coefficient 0.01). The AFM height range is 385.7 nm. All scale bars correspond to 5 µm.

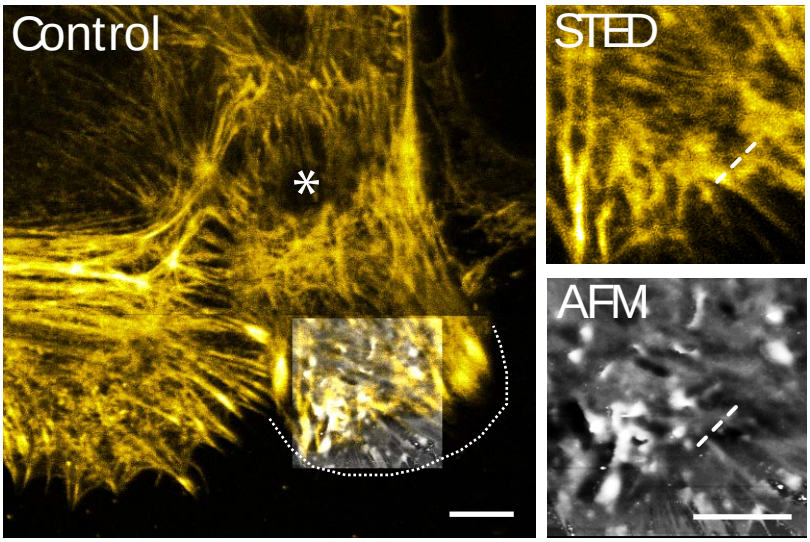

(a) STED image of actin (yellow) correalted with AFM topography (grayscale)

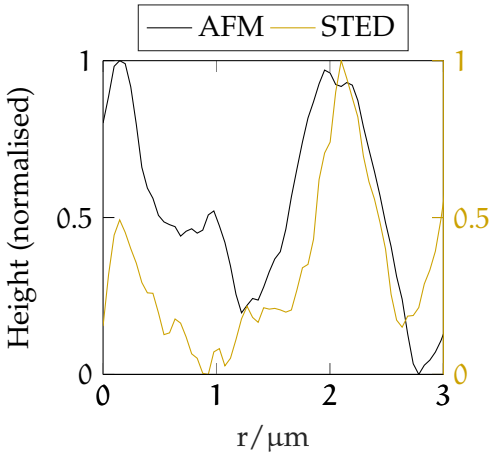

(b) Line profile through dashed region

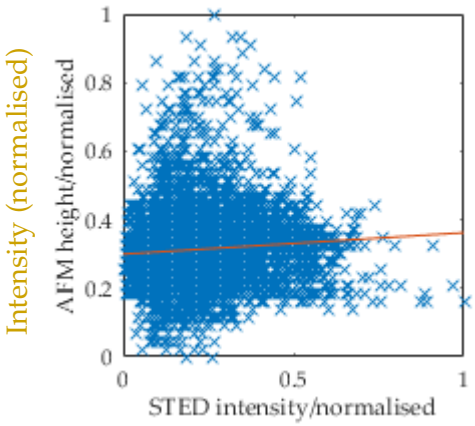

(c) Correlation of pixel values

Figure 73: **Actin structure in leading edge of control migrating astrocyte.** Stress fibers are observed orientated in the direction of migration. These fibers appear in the STED and an AFM topography images as shown in the line profile in 73b for the dashed line. Dotted line indicates the leading edge and * indicates the basis. Scale bars are 5 µm. 73c Scatter plot of corresponding height and intensity pixels showing small positive correlation (Pearson's coefficient = 0.08). The AFM height map represents a range of 564 nm.

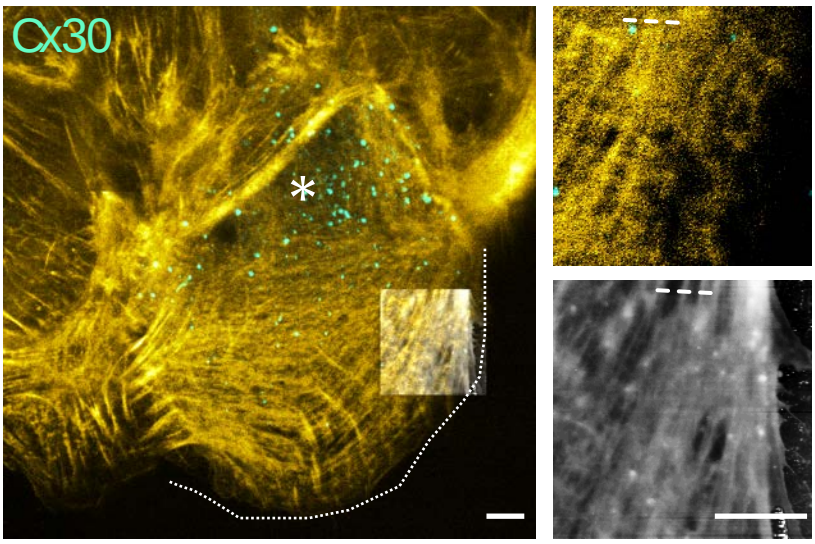

(a) STED image of actin (yellow) correalted with AFM topography (grayscale)

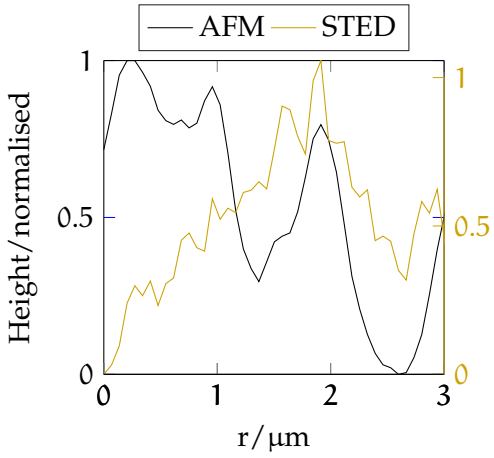

(b) Line profile through dashed region

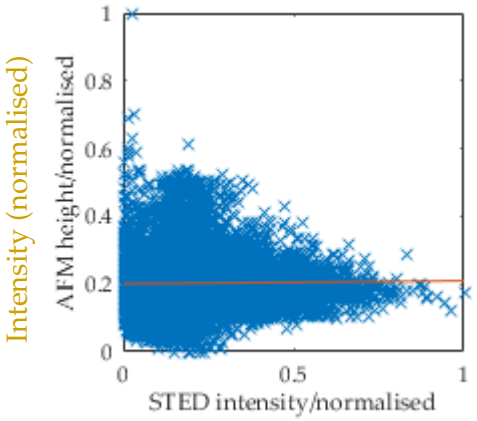

(c) Correlation of pixel values

Figure 74: **Actin structure in leading edge of connexin30-expressing migrating astrocyte.** Fewer stress fibers and lower actin organisation are observed than in control conditions. AFM topography shows reduced agreement with the optical image (74b, dashed line). Similarly 74c shows low correlation between the AFM height and STED intensity values for corresponding pixels (Pearson's coefficient = 0.02). Dotted line indicates the leading edge and * indicates the basis. Scale bars are 5 μm. The AFM height map represents a range of 417 nm.

6.5.3 *Stiffness changes in migrating Cx30-expressing astrocytes*

AFM stiffness measurements were used to investigate whether the observed inhibition of actin rearrangement influences the change in mechanical properties previously observed for migrating astrocytes. The stiffness of the basis and leading edge of migrating astrocytes transfected with GFP (control) or Cx30 is measured. The stiffnesses of the basis and leading edge are compared for the same cell. As in section 6.4, GFP control cells exhibited an increase in mechanical stiffness in the leading edge relative to the basis (leading edge: 27.6 ± 3.8 kPa vs basis: 14.6 ± 3.4 kPa, n = 11, $p < 0.01$, paired *t* test, figure 75a). However, in Cx30 expressing astrocytes no significant change was observed (edge: 15.1 ± 3.5 vs basis: 13.8 ± 2.4, n = 9, $p > 0.05$, paired *t* test, figure 75b). This indicates that Cx30 primarily impaired actin remodelling in the leading edge compartment and is consistent with the finding that actin contributes significantly to astrocyte stiffness and that actin is more disorganised in the leading edge of Cx30-expressing astrocytes.

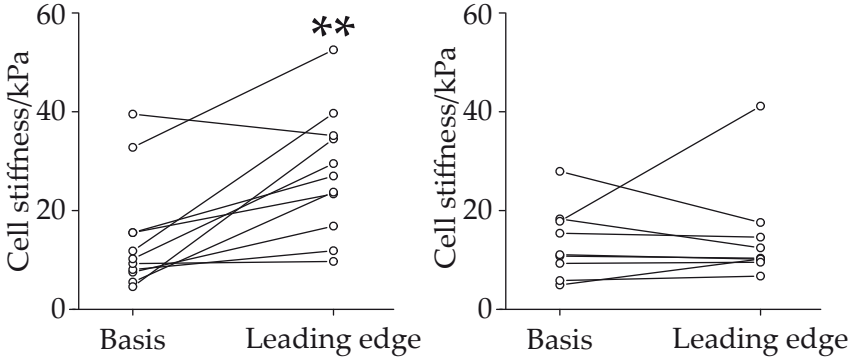

(a) GFP-expressing (b) Cx30-expressing

Figure 75: **Reorganisation of astrocyte stiffness during polarised migration** occurs for control (GFP) astrocytes (leading edge: 27.6 ± 3.8 kPa vs Basis: 14.6 ± 3.4 kPa, n = 11, $p < 0.01$, paired *t* test, 75a) but not for cx30-expressing astrocytes (edge: 15.1 ± 3.5 kPa vs basis: 13.8 ± 2.4 kPa, n = 9, $p > 0.05$, paired *t* test, 75b).

Interestingly Cx30 had no significant effect on stiffness in non-migrating astrocytes (GFP: 23.2 ± 3.3 kPa, n = 12; Cx30: 18.3 ± 3.1 kPa, n = 12, $p > 0.05$, t test, figure 76).

6.5.4 *Conclusions*

Overall it has been shown that correlative STED and AFM on live cells is a powerful technique for correlating changes in subcellular features

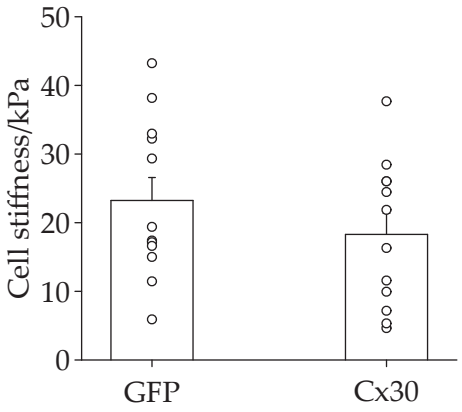

Figure 76: **Stiffness is not changed by expression of connexin 30 in basal conditions.** (GFP: 23.2 ± 3.3 kPa, n = 12; Cx30: 18.3 ± 3.1 kPa, n = 12, $p > 0.05$, t test).

of different phenotypes with stiffness. This was demonstrated by investigating the effects of the gap-junction protein connexin30.

It was found that the actin structure in migrating astrocytes is perturbed in connexin30-expressing astrocytes compared to control migrating cells. In the basis this corresponded to a reduction in density and thickness of actin in connexin 30 astrocytes. Correlation with astrocyte topography was also reduced in connexin30-expressing astrocytes, with other cytoskeletal elements appearing to dominate the AFM signal.

Changes in actin structure in connexin30-expressing cells, compared to control, were more pronounced in the leading edge, revealing a reduced organisation of actin stress fibres in the leading edge.

In control cells stiffness increases in the leading edge relative to the basis, whilst in connexin30 cells no change is observed. This correlates with the observation that connexin 30 leads to the biggest change in actin organisation in the leading edge of migration, as well as the finding that actin is a major contributor to astrocyte stiffness.

Further work on this project, carried out by Gregory Ghézahli, shows that connexin30 expressing astrocytes also migrate slower than control cells [20] – similar to connexin30 expressing HeLa cells [6]. Suggesting that, in astrocytes, increased migration speed is associated with an increase in leading edge stiffness and in actin stress fibres. This correlates with work on cell lines that have been genetically modified to change their motility, where stiffness was found to increase in motile cells [176, 193–195].

This technology will have applications in investigating the plasticity of cell mechanics that occur during cell migration, adhesion and division in physiological and pathological conditions. For instance, both cell stiffness [63–65] and cytoskeletal structure [196] have been found to be important in the migration of cancerous cells. Further de-

velopments to the system, such as the addition of a perfusion chamber, will allow longer term imaging of cells as well as measurements of cell stiffness before and after drug treatment.

7

APPLICATION OF STED TO *IN VITRO* AND FIXED TISSUE IMAGING

7.1 INTRODUCTION

The STED microscope developed in chapter 5 is well adapted to a range of imaging projects beyond correlative STED and AFM. Some of the other projects where this technology was applied are introduced in the following sections.

7.2 STED IMAGING OF AMYLOID FIBRILS *in vitro*

7.2.1 *Introduction*

Aim

The viability of the STED microscope developed in chapter 5 is tested for imaging self assembly structures such as amyloid fibrils.

Motivation

Neurodegenerative diseases, such as Alzheimer's, Parkinson's and Huntingdon's disease, are associated with the aggregation of proteins and peptides into fibrillar structures [197, 198]. The study of the dynamics of these processes can lead to a better understanding of the cause of these diseases and assist progress in the search for therapeutic intervention [199].

Biophysical techniques can be used to study protein aggregation and give information about, for instance, aggregation kintetcs [200, 201]. These techniques generally average over a large number of aggregating molecules and cannot be used to read out the length or shape of individual fibrils.

High resolution microscopy methods such as atomic force microscopy (AFM) and electron microscopy (EM) have been applied to studying fibril growth with resolutions lower than 1 nm. But these studies are limited to excised tissue *in vitro* [202] and do not allow the specific imaging of components of the fibril, such as fibril seeds [27, 203] or structural components [28].

The use of single molecule localisation was pioneered for the study of aggregated proteins by Kaminski Schierle *et al.* [197, 204]. This super-resolution technique is well adapted to studies in fixed cells with resolutions down to 20 nm and has been used to investigate

amyloid fibril growth kinetics [27, 203] and the coaggregation of extracellular and intra-cellular tau protein [205].

Single molecule localisation techniques have image acquisition times of the order minutes and are very sensitive to background. Therefore, in order to image inside live cells and with imaging depths greater than 100 nm, other microscopy techniques are necessary.

STED offers slightly worse spatial resolutions than localisation approaches (50 nm) but with imaging times of tens of seconds and depths of the order micrometres within cells. The high complexity of this system has generally limited its application in biological applications. The STED microscope developed in this thesis is tested for imaging amyloid fibrils.

Collaborator contributions

This project was in collaboration with Pierre Mahou. Dora Pintosi provided the α-synuclein seeds, monomers and the fibrilisation protocol based upon previous work [203]. Optimisation of the indirect immunostaining protocol was lead by the author in collaboration with Pierre Mahou. The imaging protocol was optimised by Pierre Mahou and the author. the image analysis was performed by Pierre Mahou and the author.

7.2.2 *Methods*

Amyloid fibril elongation and sample preparation

α-synuclein fibrils were elongated by incubating unlabelled seed fibrils with unlabelled monomer for 24 hours at 37 °C at concentrations of 2 μM (seeds) and 19.95 μM (monomers) in phosphate buffer [203].

Fibrils were mounted on Labtek 8 well chambered coverglass (155409, ThermoFisher). Labtek wells were first prepared by incubating with 1 M pottasium hydroxide (100 μL) to clean. It was found empirically that α-synuclein fibrils adhered better to coverglass which was prepared by incubation with poly-l-lysine (100 μL). Both incubation steps were 20 minutes.

Finally fibrils were mounted by incubation for 20 minutes. To control fibril density the incubated solution is further diluted by a factor 10 in phosphate buffer (10 μL fibril solution, 90 μL phosphate buffer). After incubation fibrils were then washed three times with phosphate buffer.

Indirect antibody labelling

α-synuclein was fluorescently labelled by indirect immunochemistry. The sample is first blocked, to reduce non-specific binding. The block-

ing solution was 5% goat serum in PBS/0.05% Tween. The well was incubated for two hours at room temperature.

The primary antibody was mouse monoclonal anti-α-synuclein (LB509, abcam). This binds specifically to α-synuclein. The antibody was diluted to 1:150 in 5% goat serum, PBS/0.05% Tween solution. The incubation time was one hour. The sample was washed three times and then blocked for 20 minutes with blocking solution. The secondary antibody was goat-anti-mouse functionalised with ATTO 647N (50185, Sigma-Aldrich). This binds to the mouse antibodies. The antibody was diluted to 1:150 in 5% goat serum, PBS/0.05% Tween solution. The incubation time was one hour. The sample was washed three times prior to mounting.

Sample mounting

Samples were mounted in 97% TDE (2,2'-Thiodiethanol, 166782, Sigma-Aldrich) a mounting medium which can be in water diluted to match the refractive index of immersion oil [206]. The refactive index was measured using a refractometer using a refractometer.

STED imaging

The STED microscope was as described in chapter 5. STED excitation and depletion powers were 10-20 μW and 100-150 mW respectively. Pixel size was 15 nm and dwell time was 35 μs. STED images were taken immediately before a confocal image to allow comparison of resolution.

7.2.3 *Results and discussion*

A comparison of STED and confocal images of the same α-synuclein fibrils is shown in figure 77. The resolution of the STED and confocal images is compared by fitting a lorentzian function to line profiles through the fibrils. Resolution is enhanced from 321 nm (standard deviation = 27, n = 10 fibrils) to 66.8 nm (standard deviation = 8.3, n = 10 fibrils).

This is comparable to the resolution obtained for indirect immunostained fibrils imaged in *d*STORM [197] and implies that STED can be used in similar studies to those reported using *d*STORM. However STED has the advantages of being able to image far from the coverslip, at higher imaging speed and with reduced sensitivity to labelling artifacts.

7.2.4 *Conclusions*

The viability of STED imaging to study amylid fibril growth kinetics was demonstrated here. It is shown that a 5 fold resolution enhance-

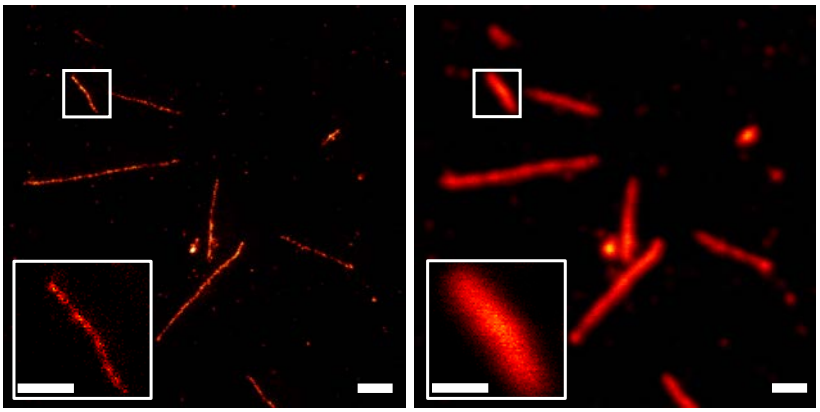

(a) STED (b) Confocal

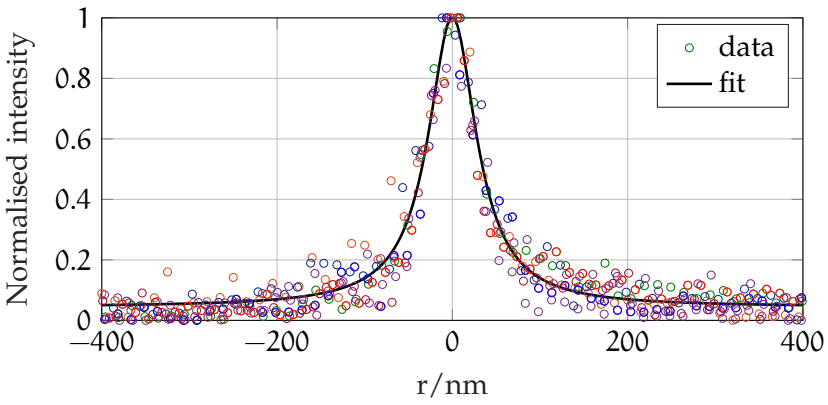

(c) STED

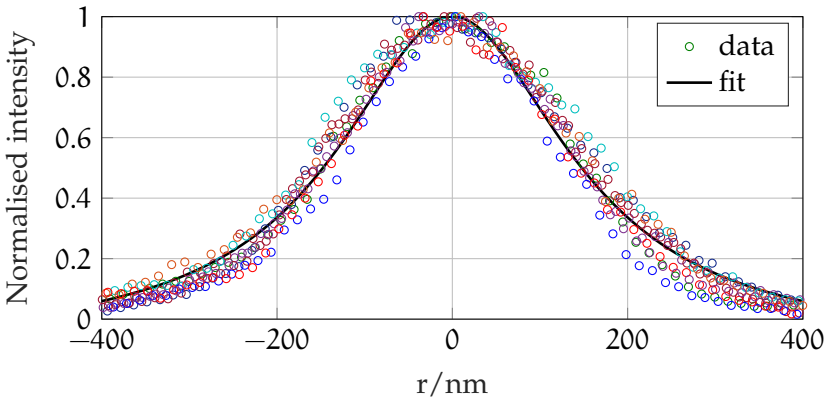

(d) Confocal

Figure 77: **STED super-resolution imaging of α-synuclein fibrils.** 77a, 77b STED and confocal images of α-synuclein fibrils. Images were taken sequentially of the same field of view. STED images were acquired before confocal images. The inset shows a zoom of the region indicated in the figure. Scale bars are 1000 nm (full image) and 500 nm (inset). 77c, 77d Line profiles through 10 fibrils in STED and confocal. A Lorentzian is fitted to each line profile and the FWHM is found. The average values are 66.8 nm (STED, standard deviation = 8.3, n = 10 fibrils) and 321 nm (confocal, standard deviation = 27, n = 10 fibrils). The fit shown uses the average FWHM.

ment can be achieved on indirectly immunostained α-synuclein fibrils. This result is comparable to *d*STORM measurements on similar samples.

This STED microscope was further applied by Pierre Mahou to a range of projects investigating the self-assembly of amyloid fibrils [27, 28] and to organic self assembly structures [207].

7.3 SUB-CELLULAR LOCATION OF CONNEXIN30 IN FIXED TISSUE

7.3.1 *Introduction*

Aim

The location of the gap-junction protein connxein30 (Cx30, also studied in section 6.5) within mature astrocytes, in a mouse brain, is investigated, demonstrating that the STED microscope developed in this work can be applied to imaging in fixed tissues.

Motivation

In chapter 6 the effects of Cx30 on astrocyte migration was investigated in cell culture and it was found that Cx30 disrupts actin reorganisation during migration. Similarly, in the brain, it has been found that knocking-down Cx30 leads to the invasion of the synaptic cleft by perisynaptic astroglial processes (PAPs) [6]. Cx30 is also known to contribute to neurotransmission by fuelling active synapses with nutrients [208] and by facilitating extracellular glutamate and pottassium uptake to regulate synaptic strength [209]. Together this suggests the involvement of Cx30 in synaptic function.

As PAPs are the relevant nanodomain for astrocytes to interact with synapses [3] Ghézali [20] hypothesised that Cx30 is present in PAPs and found, by Western Blot, that Cx30 is enriched both in PAPs and in synaptosomes. Although this suggests that PAP membranes do contain high levels of Cx30 this is yet to be demonstrated by direct imaging.

In cell culture astrocytes do not develop PAPs as there are no synapses. Therefore it is required that Cx30 imaging is performed in brain tissue slices where PAPs have formed. Of the super-resolution techniques STED is best adapted to imaging in thick samples such as tissue and has been applied to imaging in organotypic hippocampal slice cultures [5], as well as in mouse brains *in vivo* [109, 128]. These studies used fluorescent proteins to allow super-resolution imaging of post-synapses. They also use glycerol objectives and correction collars to correct for spherical aberrations induced by the sample at high imaging depths [210].

For this investigation into the sub-cellular localisation of Cx30 dynamic studies on live slices are not required. Instead fixed slices, where Cx30 has been fluorescently labelled by immunostaining can be applied. Although this imaging approach is simpler case than previous reports [5, 109, 128], due to the use of fixed tissues, this builds upon the investigation of Cx30 described in section 6.5 and demonstrates the application of the STED microscope to imaging in thick samples, such as fixed tissues.

Collaborator contributions

This project was part of a larger project led by Grégory Ghézali and Nathalie Rouach investigating the effects of Cx30 on PAP shape and functions. Brain slices were prepared and stained by Ghézali. The mounting media and fluorescent labelling was recommended by the author. Imaging conditions were optimised by the author and image acquisition performed by the author.

7.3.2 *Methods*

Acute hippocampal slice preparation

Acute hippocampal slices from GFAP-EGFP mice (postnatal days 21–30, 300–400 µm thickness) were prepared by Ghézali using established protocols [211]. Slices were fixed overnight at room temperature with 4% paraformaldehyde, then washed three times with PBS and pre-incubated for 1 hour with PBS-1% gelatin in the presence of 1% Triton-X100.

Following fixing Cx30 in brain slices was stained by overnight incubation at 4 °C with the primary antibody, Cx30 rabbit polyclonal (1:500 dilution, 71-2200, Zymed Laboratories), and washed three times. Secondary antibody, goat anti-rabbit IgG conjugated to ATTO 647N (1:500 dilution, 40839-1ML-F, Sigma-Aldrich), was applied for 1–2 hours at room temperature.

After washing slices were mounted in ProLong Gold Antifade Mountant (P36930, ThermoFisher). This mountant has a refractive index of 1.47, which is less than that of immersion oil (1.516), however it was found empirically that the SNR was higher for this sample than when TDE was used (section 7.2.2), likely due to the reduction in photobleaching. Spherical aberrations due to the change in refractive index could be adequately compensated for using the SLM.

STED and confocal imaging

The STED microscope used throughout this work was used here to image the sub-cellular location of Cx30. The depletion power was 100–150 mW in the back-aperture and the excitation power was 10–20 µW.

The pixel size was 50 nm. Z-stacks were acquired of the 3D structure. The z step size was 1 µm. The pixel dwell time was 10 µs and five line accumulations were acquired. The size of the lateral field of view was 80 x 80 μm^2.

Astrocytes were identified by confocal imaging of EGFP, which is coexpressed with the astrocyte marker GFAP (Glial fibrillary acidic protein). EGFP images were acquired after the STED images, to minimise the impact of photobleaching on STED SNR. EGFP images were of the same field of view. A pixel dwell time of 7 µs and 5 line accumulations were used. The excitation power was 20–30 µs. Imaging depth varied depending upon the distribution of astrocytes in the tissue, typical depths were 5–10 µm.

STED and confocal images were deconvolved using the Richardson-Lucy algorithm in the DeconvolutionLab FIJI plugin. The STED PSF was an average STED PSF measured on 20 nm beads. The confocal PSF was simulated using the PSF Generator FIJI plugin.

7.3.3 *Results and discussion*

Confocal images of astrocytes combined with STED images of Cx30 in acute slices show that Cx30 is expressed throughout the aborisation of astroglial processes, where PAPs are located [3], as shown in figure 78. Cx30 is not expressed in the cell body.

This corresponds to Ghézali's other findings [20] using Western Blots which show that Cx30 is enriched in synaptosomes. This finding was further investigated using three colour SIM imaging, which found that Cx30 revealing that Cx30 is in close procimity to synaptic markers [20].

Overall the finding that Cx30 is located in PAPs supports previous findings that Cx30 is involved in neuroglial regulation and synaptics regulation [6]. The presence of Cx30 in PAPs may also be involved in the regulation of astroglial coverage. It was shown in section 6.5 that Cx30 regulates migration of astrocytes and it is likely that Cx30 stabilises PAPs preventing their invasion of the synaptic cleft.

7.3.4 *Conclusions*

Of the most commonly used super-resolution techniques (STED, SIM and single molecule localisation microscopy) STED occupies the unique space of potentially providing resolutions below 100 nm and penetration depths of tens of microns [128]. Making it a technique that is highly suitable for investigations of sub-cellular features in acute tissue slices.

Whilst the main focus of this work was on the migration of astrocytes in culture, many studies require the interplay of different cell

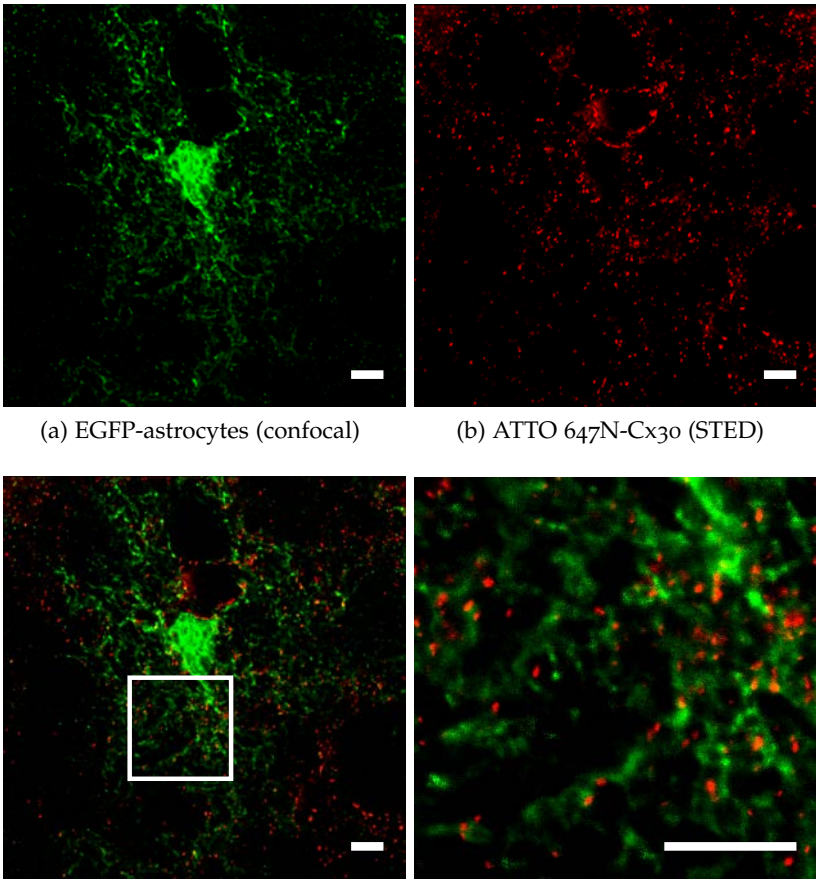

(a) EGFP-astrocytes (confocal) (b) ATTO 647N-Cx30 (STED)

(c) Merge (d) Zoom

Figure 78: **STED image showing Cx30 is found in PAPs.** Single plane image of an astrocyte (78a, EGFP) and Cx30 (78b, ATTO 647N) in an acute hippocampal slice. The merged imaged (78c) and zoom of indicated region (78d) show that Cx30 is predominantly found in PAPs. Other dense regions of Cx30 likely correspond to other astrocytes not expressing EGFP. Scale bars are 5 µm in all images.

types *in situ*. The study presented in this section shows one such application of STED microscopy.

In this work it was required to use antibody stained, fixed slices. In order to build upon this it would be interesting to investigate cytoskeletal dynamics in astrocytes in live slices. For this a fluorescent protein that is compatible with the high resolution STED microscope developed during this thesis would be required. Wegner *et al.* [109] recently reported the use of the plasmid Lifeact-mNeptune2 to study actin dynamics in neurons in the brains of living mice. Similar studies in acute slices, expressing Lifeact-mNeptune2, could be possible with the microscope presented in this work.

8

CONCLUSIONS AND OUTLOOK

8.1 CONCLUSION

This thesis describes the development of a STED microscope and its application to a range of neuroscience projects, particularly focusing on an investigation of cytoskeletal reorganisation and its impact on the mechanical stiffness of migrating astrocytes through the combination with live-cell AFM mechanical property mapping. The work can be divided into three main phases. First, the current technology landscape in STED and RESOLFT microscopy was investigated, leading to the optimal design of the STED microscope. As part of this phase a theoretical model for RESOLFT was developed, which allowed the comparison of RESOLFT with major STED modes in terms of intensity and photon efficiency, for a given resolution. In phase two, a pulsed STED microscope was designed, constructed and characterised. In phase three, the STED microscope was combined with an AFM to access complimentary information during studies of live cells. In particular cytoskeletal rearrangement was investigated in migrating astrocytes using STED microscopy and mechanical stiffness was measured using AFM. The microscope was also provided to a range of other projects and some of these were described.

Key outcomes of each of these phases are summarised in this section.

8.1.1 *Theoretical performance of STED and RESOLFT techniques*

The overall aim of this work was to correlate super-resolution images of live-cells with AFM images. A secondary aim was to be able to image in thick samples. STED and RESOLFT were identified as the best techniques to achieve this. There have been a range of different techniques developed in STED and RESOLFT, which have varying cost, complexity and photon dose requirements. Although the relative merits of these systems are well known within the community, and theoretical models for saturation intensity have been developed [37, 39], direct comparison between STED modes – and particularly between STED and RESOFT – remains challenging.

To allow the derivation of simple models, based upon previous work by Moffitt *et al.* [37] and Leutenegger *et al.* [39], for direct comparison between cw-STED, pulsed STED and time-gated STED, the figure of merit of photon efficiency was defined.

A theoretical optimum time gate in time-gated cw-STED is identified, based upon maximising photon efficiency, as 0.46 fluorescence lifetimes, which is comparable to values in previous reports of time-gated STED [143]. The optimum saturation intensity in time-gated cw-STED could be identified using the time gated of $0.76\tau_{fl}$, which further permitted the direct comparison between STED modes in terms of optimum photon efficiency.

Modelling of STED techniques suggested that, for the same fluorophore, pulsed STED has the best photon efficiency, followed by time-gated cw-STED and then cw-STED. Time-gated pulsed STED was found to have a comparable theoretical photon efficiency to conventional pulsed STED, in spite of associated advantages such as the rejection of scattered light and improved tolerance for temporal alignment.

In contrast to STED, there has been limited discussion of the photon efficiency in RESOLFT. In this work, a model for the-light induced decay of the on-state of a reversibly photoswitchable fluorescent molecule was derived, using an approximation previously applied to kinetics in photobleaching [78]. This model allowed the derivation of a simple expression for the saturation intensity and photon efficiency in RESOLFT.

Based upon these models, STED and RESOLFT can be ranked from best to worst in terms of depletion photon efficiency as pulsed STED, RESOLFT, time-gated cw-STED and cw-STED. The theoretical model does not take into account that pulsed lasers are generally considered to lead to more photodamage than cw-lasers [135]. Neither does this model consider the availability of cost-effective laser sources to deplete commonly used fluorophores. For instance, pulsed STED on commonly used GFP and YFP requires expensive laser sources beyond the reach of most labs. Finally, due to limited characterisation data of the state of the art rsEGFP used in RESOLFT, parameters such as the absorption cross-section have been assumed and are likely overestimates.

Overall it was decided that pulsed STED would be the optimum system for this work as all of the target applications (live-cell cytoskeletal imaging and cleared tissue imaging) could be performed without the need for fluorescent proteins [31].

8.1.2 *Development and characterisation of STED microscope*

The STED microscope was designed based upon well-established systems. A titanium-sapphire laser was used to generate depletion pulses, due to its high pulse power and tunable wavelength, which allows it to operate at the depletion wavelength of many near infra-red fluorophores. A super-continuum source, generated by pumping a photonic crystal fiber (PCF) with the depletion laser, was used as a ver-

satile excitation source. A spatial light modulator (SLM) was used to generate aberration-corrected vortex beams. This system was initially proposed by Auksorius *et al.* [155]. To simplify the system design and day-to-day alignment, a commercial PCF was used [89]. This fiber was characterised and a pump power was chosen that generates sufficient power at the STED excitation wavelength (640 nm).

This approach was chosen, in part, due to the versatility of being able to select a range of excitation wavelengths for multi-colour imaging [101]. However, it is important to note that care must be taken to ensure that optical path lengths of both colours are designed correctly to ensure that both excitation pulses arrive simultaneously.

As well as allowing aberration correction when imaging in thick samples, the SLM also simplifies alignment as it allows the user to adjust the centring of the STED phase mask and the position of the depletion beam in the image plane using a computer-controlled element.

The depletion pulse arrival time was controlled by a delay line and this was optimised to maximise depletion. This approach was found to be stable and only required reoptimisation following changes to the optical system.

The depletion and excitation pulse durations were set by propagating through optical fibres. 30 m was used for excitation and 100 m for depletion. Pulse durations following the fibre were estimated as 56 ps and 100 ps. To prevent unwanted supercontinuum generation in the optical fibre pre-chirping of the depletion pulses through propagation in Schott SF66 glass was investigated. It was found that a minimum of 50 cm of SF66 glass was required to reduce spectral broadening.

Following optimisation the resolution of the microscope was characterised as 50 nm on idealised test samples. This is worse than the STORM microscope commonly used in this lab to study amyloid fibrils, which achieves 20 nm resolution [161, 197], however STED has the advantage of being compatible with imaging in cell culture medium or in thick samples.

This system requires approximately weekly reoptimisation of fiber coupling and of phase mask alignment due to thermal drift. Full reoptimisation generally takes a user 30–45 minutes. Once aligned the system can be used by non-specialist users.

The stability of the STED microscope could be improved by incorporating recent advances in fiber laser technology. Since the implementation of this microscope, new laser sources have been developed for STED that have the advantages of being lower cost than a titanium-sapphire laser and having tunable pulse durations in a range that includes the optimum STED pulse duration. These sources include a pulsed laser operating at 590 nm, which is compatible with imaging YFP [127]. Finally, these sources can be externally triggered, meaning that they can be used used with two-photon excitation lasers.

These sources will likely outperform a titanium-sapphire laser in STED development as they vastly reduce the complexity of the system as they do not require fibre coupling for pulse stretching. However the STED microscope developed during this work achieves all of the aims of this work.

8.1.3 *Development and application of correlative live-cell STED/AFM*

STED super-resolution imaging was combined with atomic force microscopy (AFM) to study migrating astrocytes. Recent advances in AFM technology have allowed fast mechanical property measurements to be performed on live cells, including improvements in AFM imaging techniques [29] and AFM cantilever design [12, 29].

Meanwhile, significant progress has been made in STED microscopy through the development of the SiR-dyes, which allow STED compatible labelling of the cytoskeleton [31], nucleus [32], lysosomes [33] and SNAP-tag [30] conjugated proteins in live-cells.

These advances were combined to investigate cytoskeletal dynamics in living astrocytes. Combining STED and AFM topography imaging showed that astrocyte topography correlates with fluorescently labelled actin structures and does not correlate with tubulin organisation. This goees beyond previous reports [13, 175] which have correlated cell topography with actin strcuture as the STED super-resolution allows the identification of smaller filaments than would be possible with conventional techniques.

The viability of AFM measurements of mechanical properties was investigated for measuring the stiffness of astrocytes in basal conditions [12]. First it was shown that this technique could be used to measure the mechanical stiffness of transfected cells, by verifying that there was no change in mechanical stiffness of GFP expressing astrocytes compared to untransfected cells. Drug treatments which depolymerised select cytoskeletal elements showed that actin is a major contributor to astrocyte stiffness, unlike tubulin. Interestingly, the relative contribution of actin and tubulin to cell stiffness appears to be cell type dependent. In astrocytes and endothelial cells [175] tubulin does not contribute to cell siffness but in axons tubulin is a significant contributor [178]. This suggests that the cytoskeletal elements which contribute to cell stiffness are cell dependent.

This technique was used to investigate migrating astrocytes. The migration, and morphological changes, of astrocytes is important in studies of neuronal development [3, 7, 167], responses to wounds and trauma [19, 168], and in glioma type tumours [169–171]. Both mechanical stiffness [163] and cytoskeletal organisation [8, 172, 173] have been implicated in astrocyte migration. The combination of AFM and STED imaging allowed the combined effects of stiffness and cytoskeletal organisation to be studied in super-resolution.

Tubulin and actin organisation was investigated in migrating astrocytes. An increase in tubulin organisation was observed with microtubules pointing in the direction of migration, meanwhile the actin structure was disrupted in the basis compared to the leading edge of migration, which showed increased stress fibers. The mechanical stiffness in the basis and in the leading edge was compared and it was found that the stiffness of the leading edge was increased compared to the basis within the same migrating astrocyte. It is likely that the change in stiffness, and migration of astrocytes, is caused by the coordinated interplay between multiple different cytoskeletal elements [8, 11, 172, 177, 179].

The gap-junction protein connexin30 is thought to impact upon astrocyte function and it has been shown that connexin30 expression leads to reduced astrocyte migration [6, 20]. Correlative AFM and STED experiments show that that, while there are small changes in actin organisation in the basis, there are larger changes in the leading edge of astrocyte migration. In connexin30 astrocytes, unlike control astrocytes, there are fewer actin stress fibers and this corresponds to a reduction in stiffness in the leading edge, where no change in stiffness is observed compared to the basis in connexin30 astrocytes.

This suggests that connexin30 acts to inhibit migration and stabilise astrocyte morphology by preventing the reorganistation of the actin cytoskeleton into stress fibers which are involved in the polarised migration function.

It was noted that primary astrocytes were highly heterogeneous in terms of measured mechanical stiffness and that this technique worked best when comparing changes in mechanical stiffness within the same cell, for instance comparing the mechanical stiffness in the leading edge and basis subcompartments, as opposed to comparing changes across different populations of cells. For investigating changes in mechanical properties due to drug treatments it would be more interesting to measure stiffness changes over time, on the same cell, with time lapse STED and AFM imaging of perfused cells. A commercial perfusion system could be added or the system recently proposed by Alsteeens *et al.* [12] could be used.

8.2 OUTLOOK

The work presented in this thesis may be advanced in a range of directions and the microscopy techniques developed here will be used in a range of upcoming projects.

8.2.1 *STED imaging in live cells*

Current applications of the STED are limited by the design of the STED system preventing imaging of fluorescent proteins. Whilst SiR-

SNAP [30] has been proposed as an approach for imaging any target in live cells this requires the engineering of proteins fused with the SNAP-tag and the optimisation of imaging procedures. These techniques will only be compatible with cleared tissues or live cells as they still require an external dye molecule.

There has been recent work involving the development of red fluorescent proteins for STED that achieve 80 nm resolution in living tissue [109]. These fluorescent proteins would be compatible with the microscope developed here and could be investigated.

As previously mentioned new pulsed laser sources have also been developed that would allow lower cost STED imaging of YFP. As they are fibre lasers these could be implemented in the current STED system, with minimal changes. Some of these sources can be externally triggered, meaning that the excitation could be used either through supercontinuum generation or 2-photon excitation directly from the titanium sapphire laser.

8.2.2 *Two-colour imaging*

Two colour STED would enable, for instance, investigations of actin and tubulin structures in the same cell in the investigations in chapter 6 or investigations of the colocalisation of synaptic vesicales and amyloid fibrils. Building upon the projects described in this thesis. A design is proposed in figure 79 for a two-colour STED system. This is based upon the system proposed by Göttfert *et al.* [212]. A similar system was recently applied to live cell imaging on protein targets coexpressing SNAP and HALO tags and labelled with SiR-SNAP or ATTO590 [101].

The systems reported previously [101, 212] used laser diodes for excitation. The STED microscope designed here uses a supercontinuum course from which excitation lines are chosen. A dichroic mirror (DM) and clean up filters are used to select excitation lines at 590 nm and 640 nm. These are coupled into PM-SMFs. Both excitation beams and the depletion beam are coaligned in the image plane of the microscope.

The 640 nm, 590 nm and depletion beams must all have optimised arrival times for STED depletion. The path lengths of the 590 nm and 640 nm excitation beams are adjusted in free space – through redesigns of the system – to ensure that the lasers have the correct arrival times.

The implementation of this system is challenging as it requires the 3D spatial and temporal coalignment of three pulsed lasers. Drift of any one beam will decrease the SNR in one or more detection channels, as excitation maxima will no longer be coaligned with the depletion minimum. This will make initialisation of this system more time consuming and may limit its usability.

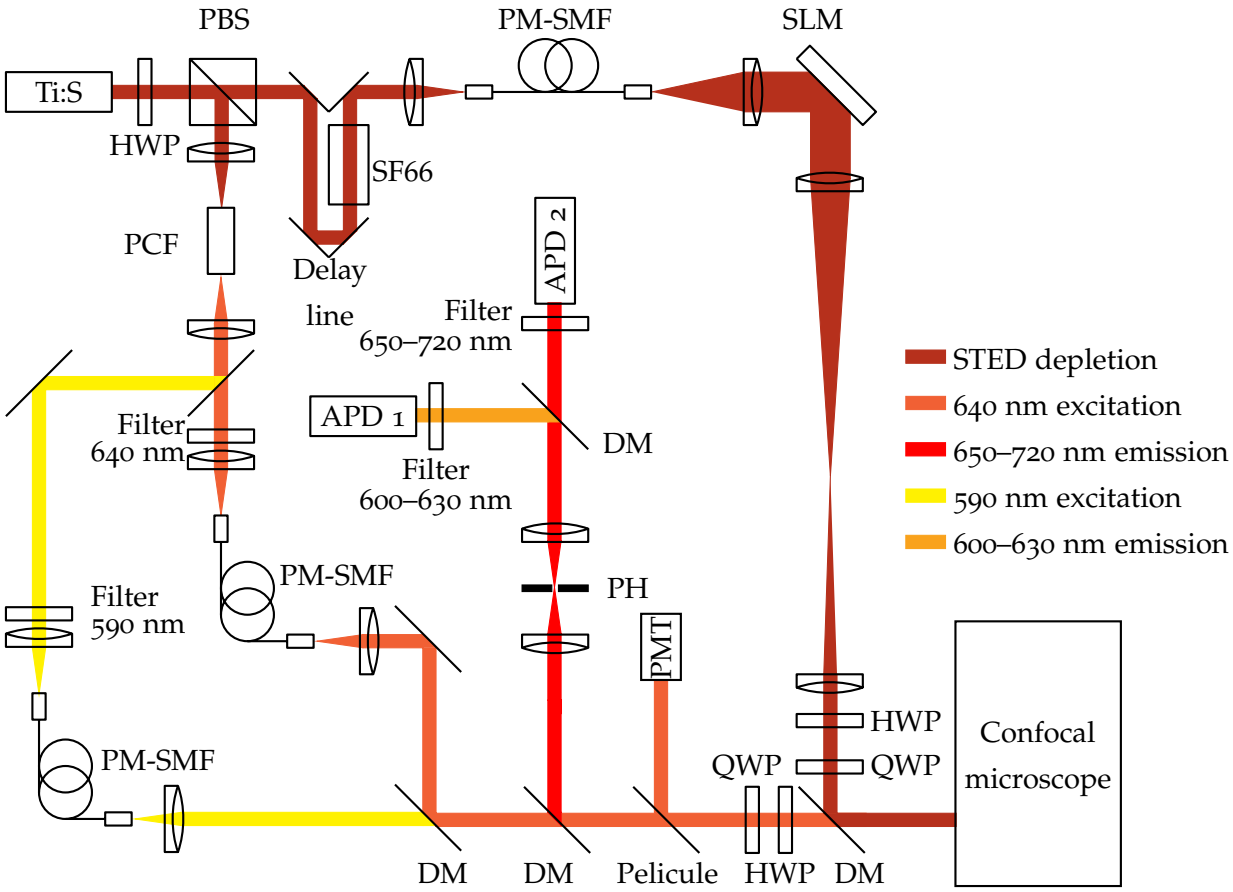

Figure 79: **Design for two-colour STED.** A 590 nm excitation line is also chosen from the supercontinuum source. All three beam paths (590 nm excitation, 640 nm excitation and STED depletion) must be coaligned in space and time. For fine temporal alignment the 590 nm excitation fibre incoupling is mounted on a translation stage (not shown).

An alternative two colour STED approach was proposed by Lukinavicius *et al.* [33]. This uses SiR dyes and the newly derived SiR-700 dye which has a similar excitation spectrum but a larger Stokes shift such that both dyes can be excited and depleted by the same laser, with the two fluorophores separated in detection. This may be a simpler set-up for two colour imaging and would require only changes to the dichroic mirrors and detection filters in this system. Both approaches could be investigated and appropriate modifications made to the system to allow two colour imaging.

8.2.3 *Correlative FLIM and AFM*

A major output of this work was the combination of STED and AFM microscopy leading to two studies that combined super-resolution microscopy and AFM to investigate cell migration. A relatively unexplored technique in correlative advanced microscopy and AFM is the combination of fluorescence lifetime imaging (FLIM) with AFM [66]. A possible reason for this is that AFM is a high-resolution imaging technique whilst FLIM generally requires averaging over large areas to generate sufficient statistics to identify changes in lifetime. However, FLIM, as a quantitative imaging technique that can measure local pH; viscosity or protein–protein interactions, could be combined with mechanical property AFM imaging – particularly on live cells – to read out complementary quantitative information.

In a proposed project FLIM and AFM will be used to investigate the formation of FUS granules in the nucleus and correlate this with changes in mechanical stiffness. Preliminary experiments were performed on AFM and FLIM independently. FLIM experiments were performed by Chetan Poudel and Kevin Feeney on live SHSY5Y cells expressing YFP-FUS. Upon treatment with AdOx, a drug which leads to the formation of FUS granules, the fluorescence lifetime of YFP decreased. Similarly independent AFM experiments on purified nucleii revealed an increase in nuclear stiffness for AdOx treated nucleii. This implies that fluorescence lifetime is a reporter for FUS granule formation and that the formation of granules changes nuclear stiffness. A correlated readout would allow increases in stiffness to be directly correlated with changes in fluorescence lifetime, and therefore the formation of FUS granules.

In future work the AFM will be mounted directly on the FLIM system and used to correlate fluorescence lifetime and mechanical stiffness on the same nucleus. This will provide a unique technology for investigating FUS aggregation and the effects on mechanical properties and could be further applied to investigating different stages in the cell cycle. Further this technique can be further applied to a range of biological systems for instance correlating mechanical stiffness with cell viscocity or the amount of protein aggregation.

BIBLIOGRAPHY

[1] F. A. Azevedo, L. R. Carvalho, L. T. Grinberg, J. M. Farfel, R. E. Ferretti, R. E. Leite, W. J. Filho, R. Lent, and S. Herculano-Houzel. "Equal numbers of neuronal and nonneuronal cells make the human brain an isometrically scaled-up primate brain." In: *Journal of Comparative Neurology* 513.5 (2009), pp. 532–541. DOI: 10.1002/cne.21974.

[2] S. C. Noctor, V. Martínez-Cerdeño, and A. R. Kriegstein. "Contribution of Intermediate Progenitor Cells to Cortical Histogenesis." In: *Archives of Neurology* 64.5 (2007), pp. 639–642. DOI: 10.1001/archneur.64.5.639.

[3] G. Ghézali, G. Dallérac, and N. Rouach. "Perisynaptic astroglial processes: dynamic processors of neuronal information." In: *Brain structure & function* 221.5 (2016), pp. 2427–42. DOI: 10.1007/s00429-015-1070-3.

[4] G. Perea, M. Navarrete, and A. Araque. "Tripartite synapses: astrocytes process and control synaptic information." In: *Trends in Neurosciences* 32.8 (2009), pp. 421–431. DOI: 10.1016/j.tins.2009.05.001.

[5] J Tonnesen, G Katona, B Rozsa, and U. V. Nagerl. "Spine neck plasticity regulates compartmentalization of synapses." In: *Nature neuroscience* 17.5 (2014), pp. 678–85. DOI: 10.1038/nn.3682.

[6] U. Pannasch et al. "Connexin 30 sets synaptic strength by controlling astroglial synapse invasion." In: *Nature Neuroscience* 17.4 (2014), pp. 549–558. DOI: 10.1038/nn.3662.

[7] A. V. Molofsky and B. Deneen. "Astrocyte Development : A Guide for the Perplexed." In: *Glia* 63 (2015), pp. 1320–1329. DOI: 10.1002/glia.22836.

[8] S. Etienne-Manneville. "Actin and microtubules in cell motility: Which one is in control?" In: *Traffic* 5.7 (2004), pp. 470–477. DOI: 10.1111/j.1600-0854.2004.00196.x.

[9] A. Diz-Muñoz, D. A. Fletcher, and O. D. Weiner. "Use the force: Membrane tension as an organizer of cell shape and motility." In: *Trends in Cell Biology* 23.2 (2013), pp. 47–53. DOI: 10.1016/j.tcb.2012.09.006. arXiv: NIHMS150003.

[10] F. Ritort. "Single-molecule experiments in biological physics: Methods and applications." In: *Journal of Physics Condensed Matter* 18.32 (2006). DOI: 10.1088/0953-8984/18/32/R01. arXiv: 0609378 [cond-mat].

[11] K. Haase and A. E. Pelling. "Investigating cell mechanics with atomic force microscopy." In: *Journal of the Royal Society, Interface / the Royal Society* 12.104 (2015), p. 20140970. DOI: 10.1098/rsif.2014.0970.

[12] D. Alsteens, R. Newton, R. Schubert, D. Martinez-Martin, M. Delguste, B. Roska, and D. J. Mueller. "Nanomechanical mapping of first binding steps of a virus to animal cells." In: *Nature Nanotechnology* 12.2 (2016), pp. 177–183. DOI: 10.1038/nnano.2016.228.

[13] C. Kronlage, M. Schäfer-Herte, D. Böning, H. Oberleithner, and J. Fels. "Feeling for Filaments: Quantification of the Cortical Actin Web in Live Vascular Endothelium." In: *Biophysical Journal* 109.4 (2015), pp. 687–698. DOI: 10.1016/j.bpj.2015.06.066.

[14] E. A. Shelden, Z. T. Colburn, and J. C. Jones. "Focusing super resolution on the cytoskeleton." In: *F1000Research* 5.May (2016), p. 998. DOI: 10.12688/f1000research.8233.1.

[15] S. Handschuh-Wang, T. Wang, and X. Zhou. *Recent advances in hybrid measurement methods based on atomic force microscopy and surface sensitive measurement techniques*. Vol. 7. 75. Royal Society of Chemistry, 2017, pp. 47464–47499. DOI: 10.1039/C7RA08515J.

[16] M. Hauser, M. Wojcik, D. Kim, M. Mahmoudi, W. Li, and K. Xu. "Correlative Super-Resolution Microscopy: New Dimensions and New Opportunities." In: *Chemical Reviews* 117.11 (2017), pp. 7428–7456. DOI: 10.1021/acs.chemrev.6b00604.

[17] J. V. Chacko, F. C. Zanacchi, and A Diaspro. "Probing cytoskeletal structures by coupling optical superresolution and AFM techniques for a correlative approach." In: *Cytoskeleton (Hoboken, N.J.)* 70.11 (2013), pp. 729–40. DOI: 10.1002/cm.21139.

[18] P. D. Odermatt, A. Shivanandan, H. Deschout, R. Jankele, A. P. Nievergelt, L. Feletti, M. W. Davidson, A. Radenovic, and G. E. Fantner. "High-Resolution Correlative Microscopy: Bridging the Gap between Single Molecule Localization Microscopy and Atomic Force Microscopy." In: *Nano Letters* 15.8 (2015), pp. 4896–4904. DOI: 10.1021/acs.nanolett.5b00572.

[19] S. Etienne-Manneville. "In vitro assay of primary astrocyte migration as a tool to study Rho GTPase function in cell polarization." In: *Methods in Enzymology* 406.1995 (2006), pp. 565–578. DOI: 10.1016/S0076-6879(06)06044-7.

[20] G Ghezali. "Control of synaptic transmission by astroglial connexin 30 : molecular basis , activity- dependence and physiological implication." PhD thesis. College de France, 2016.

[21] C. Qu, P. Gardner, and I. Schrijver. "The role of the cytoskeleton in the formation of gap junctions by Connexin 30." In: *Experimental Cell Research* 315.10 (2009), pp. 1683–1692. DOI: 10.1016/j.yexcr.2009.03.001.

[22] S. W. Hell and J Wichmann. "Breaking the diffraction resolution limit by stimulated emission: stimulated-emission-depletion fluorescence microscopy." In: *Optics Letters* 19.11 (1994), p. 780. DOI: 10.1364/OL.19.000780.

[23] S. W. Hell. "Far-field optical nanoscopy." In: *Science (New York, N.Y.)* 316.5828 (2007), pp. 1153–8. DOI: 10.1126/science.1137395.

[24] B Harke, J. V. Chacko, H Haschke, C Canale, and A Diaspro. "A novel nanoscopic tool by combining AFM with STED microscopy." In: *Optical Nanoscopy* 1.1 (2012), p. 3. DOI: 10.1186/2192-2853-1-3.

[25] J. V. Chacko, C. Canale, B Harke, and A Diaspro. "Sub-diffraction nano manipulation using STED AFM." In: *PloS one* 8.6 (2013), e66608. DOI: 10.1371/journal.pone.0066608.

[26] J. V. Chacko, B. Harke, C. Canale, and A. Diaspro. "Cellular level nanomanipulation using atomic force microscope aided with superresolution imaging." In: *Journal of biomedical optics* 19.10 (2014), p. 105003. DOI: 10.1117/1.JBO.19.10.105003.

[27] D. Pinotsi, C. H. Michel, A. K. Buell, R. F. Laine, P. Mahou, C. M. Dobson, C. F. Kaminski, and G. S. Kaminski Schierle. "Nanoscopic insights into seeding mechanisms and toxicity of α-synuclein species in neurons." In: *Proceedings of the National Academy of Sciences* 113.14 (2016), pp. 3815–3819. DOI: 10.1073/pnas.1516546113. arXiv: arXiv:1408.1149.

[28] N. Nespovitaya, P. Mahou, R. F. Laine, G. S. K. Schierle, and C. F. Kaminski. "Heparin acts as a structural component of β-endorphin amyloid fibrils rather than a simple aggregation promoter." In: *Chem. Commun.* 47 (2017), pp. 311–320. DOI: 10.1039/C6CC09770G.

[29] H. Schillers, I. Medalsy, S. Hu, A. L. Slade, and J. E. Shaw. "PeakForce Tapping resolves individual microvilli on living cells." In: *Journal of Molecular Recognition* 29.2 (2016), pp. 95–101. DOI: 10.1002/jmr.2510.

[30] G Lukinavicius et al. "A near-infrared fluorophore for live-cell super-resolution microscopy of cellular proteins." In: *Nature chemistry* 5.2 (2013), pp. 132–9. DOI: 10.1038/nchem.1546.

[31] G Lukinavicius et al. "Fluorogenic probes for live-cell imaging of the cytoskeleton." In: *Nature methods* 11.7 (2014), pp. 731–3. DOI: 10.1038/nmeth.2972.

[32] G. Lukinavicius et al. "SiR–Hoechst is a far-red DNA stain for live-cell nanoscopy." In: *Nature communications* 6 (2015), p. 8497. DOI: 10.1038/ncomms9497.

[33] G. Lukinavičius, L. Reymond, K. Umezawa, O. Sallin, E. D'Este, F. Göttfert, H. Ta, S. W. Hell, Y. Urano, and K. Johnsson. "Fluorogenic Probes for Multicolor Imaging in Living Cells." In: *Journal of the American Chemical Society* 138.30 (2016), pp. 9365–9368. DOI: 10.1021/jacs.6b04782.

[34] T. A. Klar and S. W. Hell. "Subdiffraction resolution in far-field fluorescence microscopy." In: *Optics Letters* 24.14 (1999), p. 954. DOI: 10.1364/OL.24.000954.

[35] K. I. Willig, B Harke, R Medda, and S. W. Hell. "STED microscopy with continuous wave beams." In: *Nature methods* 4.11 (2007), pp. 915–8. DOI: 10.1038/nmeth1108.

[36] G Vicidomini, G Moneron, K. Y. Han, V Westphal, H Ta, M Reuss, J Engelhardt, C Eggeling, and S. W. Hell. "Sharper low-power STED nanoscopy by time gating." In: *Nature methods* 8.7 (2011), pp. 571–3. DOI: 10.1038/nmeth.1624.

[37] J. R. Moffitt, C Osseforth, and J Michaelis. "Time-gating improves the spatial resolution of STED microscopy." In: *Optics express* 19.5 (2011), pp. 4242–54.

[38] M Hofmann, C Eggeling, S Jakobs, and S. W. Hell. "Breaking the diffraction barrier in fluorescence microscopy at low light intensities by using reversibly photoswitchable proteins." In: *Proceedings of the National Academy of Sciences of the United States of America* 102.49 (2005), pp. 17565–9. DOI: 10.1073/pnas.0506010102.

[39] M Leutenegger, C Eggeling, and S. W. Hell. "Analytical description of STED microscopy performance." In: *Optics express* 18.25 (2010), pp. 26417–29.

[40] L. G. Rosa and J. Liang. "Atomic force microscope nanolithography: dip-pen, nanoshaving, nanografting, tapping mode, electrochemical and thermal nanolithography." In: *Journal of Physics Condensed Matter* 21.48 (2009). DOI: 10.1088/0953-8984/21/48/483001.

[41] A. Pyne, R. Thompson, C. Leung, D. Roy, and B. W. Hoogenboom. "Single-molecule reconstruction of oligonucleotide secondary structure by atomic force microscopy." In: *Small* 10.16 (2014), pp. 3257–3261. DOI: 10.1002/smll.201400265.

[42] A. L. B. Pyne and B. W. Hoogenboom. "Imaging DNA Structure by Atomic Force Microscopy." In: *Chromosome Architecture: Methods and Protocols*. Ed. by M. C. Leake. New York, NY: Springer New York, 2016, pp. 47–60. DOI: 10.1007/978-1-4939-3631-1_5.

[43] F. J. Giessibl. "AFM's path to atomic resolution." In: *Materials Today* 8.5 (2005), pp. 32–41. DOI: 10.1016/S1369-7021(05)00844-8. arXiv: 0503671 [cond-mat].

[44] F. J. Giessibl. "Subatomic Features on the Silicon (111)-(7x7) Surface Observed by Atomic Force Microscopy." In: *Science* 289.5478 (2000), pp. 422–425. DOI: 10.1126/science.289.5478.422.

[45] S. Hembacher, F. J. Giessibl, J. Mannhart, and C. F. Quate. "Revealing the hidden atom in graphite by low-temperature atomic force microscopy." In: *Proceedings of the National Academy of Sciences* 100.22 (2003), pp. 12539–12542. DOI: 10.1073/pnas.2134173100.

[46] B Cappella and G Dietler. "Force-distance curves by atomic force microscopy." In: *Surface Science Reports* 34.1-3 (1999), pp. 1–104. DOI: 10.1016/S0167-5729(99)00003-5.

[47] N. Jalili and K. Laxminarayana. "A review of atomic force microscopy imaging systems: Application to molecular metrology and biological sciences." In: *Mechatronics* 14.8 (2004), pp. 907–945. DOI: 10.1016/j.mechatronics.2004.04.005.

[48] B Pettinger, N Erina, and C. Su. "Quantitative Mechanical Property Mapping at the Nanoscale with PeakForce QN." In: *Bruker Appl. Note* 128 (2010), pp. 1–12.

[49] S. B. Kaemmer. "Introduction to Bruker's ScanAsyst and PeakForce Tapping AFM Technology." In: *Bruker Appl. Note* 133 (), pp. 1–12.

[50] G. Binnig and C. F. Quate. "Atomic Force Microscope." In: *Physical Review Letters* 56.9 (1986), pp. 930–933. DOI: 10.1103/PhysRevLett.56.930.

[51] C. Goldsbury, J. Kistler, U. Aebi, T. Arvinte, and G. J. Cooper. "Watching amyloid fibrils grow by time-lapse atomic force microscopy." In: *Journal of Molecular Biology* 285.1 (1999), pp. 33–39. DOI: 10.1006/jmbi.1998.2299.

[52] D. J. Mueller, F. A. Schabert, G. Büldt, and A. Engel. "Imaging purple membranes in aqueous solutions at sub-nanometer resolution by atomic force microscopy." In: *Biophysical Journal* 68.5 (1995), pp. 1681–1686. DOI: 10.1016/S0006-3495(95)80345-0.

[53] Y. F. Dufrêne, T. Ando, R. Garcia, D. Alsteens, D. Martinez-Martin, A. Engel, C. Gerber, and D. J. Müller. "Imaging modes of atomic force microscopy for application in molecular and cell biology." In: *Nature Nanotechnology* 12.4 (2017), pp. 295–307. DOI: 10.1038/nnano.2017.45.

[54] J. Adamcik and R. Mezzenga. "Study of amyloid fibrils via atomic force microscopy." In: *Current Opinion in Colloid & Interface Science* 17.6 (2012), pp. 369–376. DOI: 10.1016/j.cocis.2012.08.001.

[55] D. A. Walters, J. P. Cleveland, N. H. Thomson, P. K. Hansma, M. A. Wendman, G. Gurley, and V. Elings. "Short cantilevers for atomic force microscopy." In: *Review of Scientific Instruments* 67.10 (1996), pp. 3583–3590. DOI: 10.1063/1.1147177.

[56] S. Kumar, M. L. Cartron, N. Mullin, P. Qian, G. J. Leggett, C. N. Hunter, and J. K. Hobbs. "Direct Imaging of Protein Organization in an Intact Bacterial Organelle Using High-Resolution Atomic Force Microscopy." In: *ACS Nano* 11.1 (2017), pp. 126–133. DOI: 10.1021/acsnano.6b05647.

[57] H. J. Butt, B. Cappella, and M. Kappl. "Force measurements with the atomic force microscope: Technique, interpretation and applications." In: *Surface Science Reports* 59.1-6 (2005), pp. 1–152. DOI: 10.1016/j.surfrep.2005.08.003.

[58] C. S. Han, S. H. Sanei, and F. Alisafaei. "On the origin of indentation size effects and depth dependent mechanical properties of elastic polymers." In: *Journal of Polymer Engineering* 36.1 (2016), pp. 103–111. DOI: 10.1515/polyeng-2015-0030.

[59] D. N. Ganchev, N. J. Cobb, K. Surewicz, and W. K. Surewicz. "Nanomechanical properties of human prion protein amyloid as probed by force spectroscopy." In: *Biophysical journal* 95.6 (2008), pp. 2909–2915. DOI: 10.1529/biophysj.108.133108.

[60] B. J. Briscoe, K. S. Sebastian, and M. J. Adams. "The effect of indenter geometry on the elastic response to indentation." In: *Journal of Physics D: Applied Physics* 27.6 (1999), pp. 1156–1162. DOI: 10.1088/0022-3727/27/6/013.

[61] I. N. Sneddon. "The relation between load and penetration in the axisymmetric boussinesq problem for a punch of arbitrary profile." In: *International Journal of Engineering Science* 3.638 (1965), pp. 47–57.

[62] B. Poon, D. Rittel, and G. Ravichandran. "An analysis of nanoindentation in linearly elastic solids." In: *International Journal of Solids and Structures* 45.24 (2008), pp. 6018–6033. DOI: 10.1016/j.ijsolstr.2008.07.021.

[63] M. Lekka. "Discrimination Between Normal and Cancerous Cells Using AFM." In: *BioNanoScience* 6.1 (2016), pp. 65–80. DOI: 10.1007/s12668-016-0191-3.

[64] N. Gavara and R. S. Chadwick. "Relationship between cell stiffness and stress fiber amount , assessed by simultaneous atomic force microscopy and live-cell fluorescence imaging." In: *Biomechanics and Modeling in Mechanobiology* 15.3 (2016), pp. 511–523. DOI: 10.1007/s10237-015-0706-9.

[65] Y. M. Efremov, A. A. Dokrunova, A. V. Efremenko, M. P. Kirpichnikov, K. V. Shaitan, and O. S. Sokolova. "Distinct impact of targeted actin cytoskeleton reorganization on mechanical properties of normal andmalignant cells." In: *BBA - Molecular Cell Research* 1853.11 (2015), pp. 3117–3125. DOI: 10.1016/j.bbamcr.2015.05.008.

[66] S. Moreno Flores and J. L. Toca-Herrera. "The new future of scanning probe microscopy: Combining atomic force microscopy with other surface-sensitive techniques, optical microscopy and fluorescence techniques." In: *Nanoscale* 1.1 (2009), p. 40. DOI: 10.1039/b9nr00156e.

[67] A. E. Brown, A. Hategan, D. Safer, Y. E. Goldman, and D. E. Discher. "Cross-Correlated TIRF/AFM Reveals Asymmetric Distribution of Force-Generating Heads along Self-Assembled, "Synthetic" Myosin Filaments." In: *Biophysical Journal* 96.5 (2009), pp. 1952–1960. DOI: 10.1016/j.bpj.2008.11.032.

[68] D. N. Fronczek, C. Quammen, H. Wang, C. Kisker, R. Superfine, R. Taylor, D. A. Erie, and I. Tessmer. "High accuracy FIONA-AFM hybrid imaging." In: *Ultramicroscopy* 111.5 (2011), pp. 350–355. DOI: 10.1016/j.ultramic.2011.01.020.

[69] H. Sanchez, R. Kanaar, and C. Wyman. "Molecular recognition of DNA-protein complexes: A straightforward method combining scanning force and fluorescence microscopy." In: *Ultramicroscopy* 110.7 (2010), pp. 844–851. DOI: 10.1016/j.ultramic.2010.03.002.

[70] A. Monserrate, S. Casado, and C. Flors. "Correlative atomic force microscopy and localization-based super-resolution microscopy: revealing labelling and image reconstruction artefacts." In: *Chemphyschem : a European journal of chemical physics and physical chemistry* 15.4 (2014), pp. 647–50. DOI: 10.1002/cphc.201300853.

[71] E. Yoskovitz, D. Oron, I. Shweky, and U. Banin. "Apertureless Near-Field Distance-Dependent Lifetime Imaging and Spectroscopy of Semiconductor Nanocrystals Apertureless Near-Field Distance-Dependent Lifetime Imaging and Spectroscopy of Semiconductor Nanocrystals." In: *Society* (2008), pp. 16306–16311. DOI: 10.1021/jp8043253.

[72] C. M. Franz. "Analyzing focal adhesion structure by atomic force microscopy." In: *Journal of Cell Science* 118.22 (2005), pp. 5315–5323. DOI: 10.1242/jcs.02653.

[73] J Heuser. "The production of 'cell cortices' for light and electron microscopy." In: *Traffic (Copenhagen, Denmark)* 1.3 (2000), pp. 545–552. DOI: 10.1034/j.1600-0854.2000.010704.x.

[74] G. Abberior Instruments. *Modules for STED/RESOLFT - AFM*. 2017.

[75] T. Staudt, A. Engler, E. Rittweger, B. Harke, J. Engelhardt, and S. W. Hell. "Far-field optical nanoscopy with reduced number of state transition cycles." In: *Optics Express* 19.6 (2011), p. 5644. DOI: 10.1364/OE.19.005644.

[76] J. Heine, M. Reuss, B. Harke, E. D'Este, S. J. Sahl, and S. W. Hell. "Adaptive-illumination STED nanoscopy." In: *Proceedings of the National Academy of Sciences* 11 (2017), p. 201708304. DOI: 10.1073/pnas.1708304114.

[77] J. G. Danzl, S. C. Sidenstein, C. Gregor, N. T. Urban, P. Ilgen, S. Jakobs, and S. W. Hell. "Coordinate-targeted fluorescence nanoscopy with multiple off states." In: *Nature Photonics* 10.2 (2016), pp. 122–128. DOI: 10.1038/nphoton.2015.266.

[78] Y. Wu, X. Wu, R. Lu, J. Zhang, L. Toro, and E. Stefani. "Resonant Scanning with Large Field of View Reduces Photobleaching and Enhances Fluorescence Yield in STED Microscopy." In: *Scientific Reports* 5.October (2015), p. 14766. DOI: 10.1038/srep14766.

[79] F. Göttfert, T. Pleiner, J. Heine, V. Westphal, D. Görlich, S. J. Sahl, and S. W. Hell. "Strong signal increase in STED fluorescence microscopy by imaging regions of subdiffraction extent." In: *Proceedings of the National Academy of Sciences* 114.9 (2017), pp. 2125–2130. DOI: 10.1073/pnas.1621495114.

[80] U. V. Nägerl and T Bonhoeffer. "Imaging living synapses at the nanoscale by STED microscopy." In: *The Journal of neuroscience : the official journal of the Society for Neuroscience* 30.28 (2010), pp. 9341–6. DOI: 10.1523/JNEUROSCI.0990-10.2010.

[81] J. R. Lakowicz. *Principles of Fluorescence Spectroscopy*. Third. New York: Kluwer Academic/Plenum Publishers, 2006.

[82] J Keller, A Schönle, and S. W. Hell. "Efficient fluorescence inhibition patterns for RESOLFT microscopy." In: *Optics express* 15.6 (2007), pp. 3361–71.

[83] E Auksorius. "Multidimensional fluorescence imaging and superresolution exploiting ultrafast laser and supercontinuum technology." PhD thesis. Imperial College London, 2009.

[84] M. O. Lenz, H. G. Sinclair, A Savell, J. H. Clegg, A. C. N. Brown, D. M. Davis, C Dunsby, M. a. a. Neil, and P. M. W. French. "3D stimulated emission depletion microscopy with programmable aberration correction." In: *Journal of biophotonics* 7.1-2 (2014), pp. 29–36. DOI: 10.1002/jbio.201300041.

[85] T. Wilson and C. Sheppard. *Theory and practice of scanning optical microscopy*. Londn: Academic Press, 1984, p. 213.

[86] J. Antonello, E. B. Kromann, D. Burke, J. Bewersdorf, and M. J. Booth. "Coma aberrations in combined two- and three-dimensional STED nanoscopy." In: *Optics Letters* 41.15 (2016), p. 3631. DOI: 10.1364/OL.41.003631.

[87] M. Booth, D. Andrade, D. Burke, B. Patton, and M. Zurauskas. "Aberrations and adaptive optics in super-resolution microscopy." In: *Microscopy* 64.4 (2015), pp. 251–261. DOI: 10.1093/jmicro/dfv033.

[88] M. J. Booth. "Adaptive Optics in Microscopy." In: *Optical and Digital Image Processing: Fundamentals and Applications* September (2011), pp. 295–322. DOI: 10.1002/9783527635245.ch14.

[89] T. J. Gould, D Burke, J Bewersdorf, and M. J. Booth. "Adaptive optics enables 3D STED microscopy in aberrating specimens." In: *Optics express* 20.19 (2012), pp. 20998–1009.

[90] B. R. Patton, D. Burke, R. Vrees, and M. J. Booth. "Is phase-mask alignment aberrating your STED microscope?" In: *Methods and Applications in Fluorescence* 3.2 (2015), p. 024002. DOI: 10.1088/2050-6120/3/2/024002.

[91] X Hao, C Kuang, T Wang, and X Liu. "Effects of polarization on the de-excitation dark focal spot in STED microscopy." In: *Journal of Optics* 12.11 (2010), p. 115707. DOI: 10.1088/2040-8978/12/11/115707.

[92] B Neupane, F Chen, W Sun, D. T. Chiu, and G Wang. "Tuning donut profile for spatial resolution in stimulated emission depletion microscopy." In: *The Review of scientific instruments* 84.4 (2013), p. 043701. DOI: 10.1063/1.4799665.

[93] H. Xie, Y. Liu, D. Jin, P. J. Santangelo, Xi, and Peng. "Analytical description of high-aperture STED resolution with 0– 2π vortex phase modulation." In: *J Opt Soc Am A Opt Image Sci Vis. 2013* August 1.30(8) (2013), pp. 1640–1645. DOI: 10.1126/scisignal.2001449.Engineering. arXiv: 1302.1646.

[94] S Deng, L Liu, Y Cheng, R Li, and Z Xu. "Effects of primary aberrations on the fluorescence depletion patterns of STED microscopy." In: *Optics express* 18.2 (2010), pp. 1657–66.

[95] M. J. Booth and T. Wilson. "Strategies for the compensation of specimen-induced spherical aberration in confocal microscopy of skin." In: *Journal of Microscopy* 200.1 (2000), pp. 68–74. DOI: 10.1046/j.1365-2818.2000.00735.x.

[96] P. S. Salter, M. Baum, I. Alexeev, M. Schmidt, and M. J. Booth. "Exploring the depth range for three-dimensional laser machining with aberration correction." In: *Optics Express* 22.15 (2014), p. 17644. DOI: 10.1364/OE.22.017644.

[97] B Harke, J Keller, C. K. Ullal, V Westphal, A Schönle, and S. W. Hell. "Resolution scaling in STED microscopy." In: *Optics express* 16.6 (2008), pp. 4154–62.

[98] M Reuss, J Engelhardt, and S. W. Hell. "Birefringent device converts a standard scanning microscope into a STED microscope that also maps molecular orientation." In: *Optics express* 18.2 (2010), pp. 1049–58.

[99] D Wildanger, E Rittweger, L Kastrup, and S. W. Hell. "STED microscopy with a supercontinuum laser source." In: *Optics express* 16.13 (2008), pp. 9614–21.

[100] B. R. Patton, D. Burke, D. Owald, T. J. Gould, J. Bewersdorf, and M. J. Booth. "Three-dimensional STED microscopy of aberrating tissue using dual adaptive optics." In: *Optics Express* 24.8 (2016), p. 8862. DOI: 10.1364/OE.24.008862.

[101] F. Bottanelli et al. "Two-colour live-cell nanoscale imaging of intracellular targets." In: *Nature Communications* 7.May 2015 (2016), p. 10778. DOI: 10.1038/ncomms10778.

[102] G Donnert, J Keller, C. A. Wurm, S. O. Rizzoli, V Westphal, A Schönle, R Jahn, S Jakobs, C Eggeling, and S. W. Hell. "Two-color far-field fluorescence nanoscopy." In: *Biophysical journal* 92.8 (2007), pp. L67–9. DOI: 10.1529/biophysj.107.104497.

[103] V Westphal, S. O. Rizzoli, M. a. Lauterbach, D Kamin, R Jahn, and S. W. Hell. "Video-rate far-field optical nanoscopy dissects synaptic vesicle movement." In: *Science (New York, N.Y.)* 320.5873 (2008), pp. 246–9. DOI: 10.1126/science.1154228.

[104] K. Nienhaus and G. U. Nienhaus. "Photoswitchable Fluorescent Proteins: Do Not Always Look on the Bright Side." In: *ACS Nano* 10.10 (2016), pp. 9104–9108. DOI: 10.1021/acsnano.6b06298.

[105] T Grotjohann, I Testa, M Leutenegger, H Bock, N. T. Urban, F Lavoie-Cardinal, K. I. Willig, C Eggeling, S Jakobs, and S. W. Hell. "Diffraction-unlimited all-optical imaging and writing with a photochromic GFP." In: *Nature* 478.7368 (2011), pp. 204–8. DOI: 10.1038/nature10497.

[106] T. Grotjohann, I. Testa, M. Reuss, T. Brakemann, C. Eggeling, S. W. Hell, and S. Jakobs. "rsEGFP2 enables fast RESOLFT nanoscopy of living cells." In: *eLife* 2012.1 (2012), pp. 1–14. DOI: 10.7554/eLife.00248.

[107] M. Ratz, I. Testa, S. W. Hell, and S. Jakobs. "CRISPR/Cas9-mediated endogenous protein tagging for RESOLFT super-resolution microscopy of living human cells." In: *Scientific reports* 5 (2015), p. 9592. DOI: 10.1038/srep09592. arXiv: /www.pubmedcentral.nih.gov/articlerender.fcgi?artid=3006164{\&}tool=pmcentrez{\&}rendertype=abstract. [Figures, S., 2010. Supplementary information. Nature, 1(c), pp.1-7. Available at: http:].

[108] C. A. Wurm et al. "Novel red fluorophores with superior performance in STED microscopy." In: *Optical Nanoscopy* 1.1 (2012), p. 7. DOI: 10.1186/2192-2853-1-7.

[109] W. Wegner, P. Ilgen, C. Gregor, J. van Dort, A. C. Mott, H. Steffens, and K. I. Willig. "In vivo mouse and live cell STED microscopy of neuronal actin plasticity using far-red emitting fluorescent proteins." In: *Scientific Reports* 7.1 (2017), p. 11781. DOI: 10.1038/s41598-017-11827-4.

[110] J.-I. Hotta, E Fron, P Dedecker, K. P. F. Janssen, C Li, K Mullen, B Harke, J Buckers, S. W. Hell, and J Hofkens. "Spectroscopic rationale for efficient stimulated-emission depletion microscopy fluorophores." In: *Journal of the American Chemical Society* 132.14 (2010), pp. 5021–3. DOI: 10.1021/ja100079w.

[111] P. Bosch, I. Corrêa, M. Sonntag, J. Ibach, L. Brunsveld, J. Kanger, and V. Subramaniam. "Evaluation of Fluorophores to Label SNAP-Tag Fused Proteins for Multicolor Single-Molecule Tracking Microscopy in Live Cells." In: *Biophysical Journal* 107.4 (2014), pp. 803–814. DOI: 10.1016/j.bpj.2014.06.040.

[112] F Lavoie-Cardinal, N. A. Jensen, V Westphal, A. C. Stiel, A Chmyrov, J Bierwagen, I Testa, S Jakobs, and S. W. Hell. "Two-Color RESOLFT Nanoscopy with Green and Red Fluorescent Photochromic Proteins." In: *ChemPhysChem* (2014). DOI: 10.1002/cphc.201301016.

[113] S. Wang, X. Chen, L. Chang, R. Xue, H. Duan, and Y. Sun. "GMars-Q Enables Long-Term Live-Cell Parallelized Reversible Saturable Optical Fluorescence Transitions Nanoscopy." In: *ACS Nano* 10.10 (2016), pp. 9136–9144. DOI: 10.1021/acsnano.6b04254.

[114] P. S. Dittrich and P Schwille. "Photobleaching and stabilization of. fluorophores used for single-molecule analysis. with one- and two-photon excitation." In: *Applied Physics B* 73.8 (2014), pp. 829–837. DOI: 10.1007/s003400100737.

[115] J. W. Lichtman and J.-A. Conchello. "Fluorescence microscopy." In: *Nature methods* 2.12 (2005), pp. 910–9. DOI: 10.1038/nmeth817.

[116] C Eggeling, J Widengren, R Rigler, and C. a. Seidel. "Photobleaching of Fluorescent Dyes under Conditions Used for Single-Molecule Detection: Evidence of Two-Step Photolysis." In: *Analytical chemistry* 70.13 (1998), pp. 2651–9. DOI: 10.1021/ac980027p.

[117] C. Eggeling, A. Volkmer, and C. a. M. Seidel. "Molecular photobleaching kinetics of Rhodamine 6G by one- and two-photon induced confocal fluorescence microscopy." In: *Chemphyschem : a European journal of chemical physics and physical chemistry* 6.5 (2005), pp. 791–804. DOI: 10.1002/cphc.200400509.

[118] C. Eggeling, J. Widengren, L. Brand, J. Schaffer, S. Felekyan, and C. A. M. Seidel. "Analysis of photobleaching in single-molecule multicolor excitation and Förster resonance energy transfer measurements." In: *Journal of Physical Chemistry A* 110.9 (2006), pp. 2979–2995. DOI: 10.1021/jp054581w.

[119] J. Fölling, M. Bossi, H. Bock, R. Medda, C. A. Wurm, B. Hein, S. Jakobs, C. Eggeling, and S. W. Hell. "Fluorescence nanoscopy by ground-state depletion and single-molecule return." In: *Nature Methods* 5.11 (2008), pp. 943–945. DOI: 10.1038/nmeth.1257.

[120] G Donnert, C Eggeling, and S. W. Hell. "Major signal increase in fluorescence microscopy through dark-state relaxation." In: *Nature methods* 4.1 (2007), pp. 81–6. DOI: 10.1038/nmeth986.

[121] J. Oracz, V. Westphal, C. Radzewicz, S. J. Sahl, and S. W. Hell. "Photobleaching in STED nanoscopy and its dependence on the photon flux applied for reversible silencing of the fluorophore." In: *Scientific Reports* 7.1 (2017), p. 11354. DOI: 10.1038/s41598-017-09902-x.

[122] A Longin, C Souchier, M Ffrench, and P. A. Bryon. "Comparison of anti-fading agents used in fluorescence microscopy: image analysis and laser confocal microscopy study." In: *Journal of Histochemistry & Cytochemistry* 41.12 (1993), pp. 1833–1840. DOI: 10.1177/41.12.8245431.

[123] T. Cordes, A. Maiser, C. Steinhauer, L. Schermelleh, and P. Tinnefeld. "Mechanisms and advancement of antifading agents for fluorescence microscopy and single-molecule spectroscopy." In: *Physical Chemistry Chemical Physics* 13.14 (2011), p. 6699. DOI: 10.1039/c0cp01919d.

[124] A. V. Mikhailov and G. G. Gundersen. "Centripetal transport of microtubules in motile cells." In: *Cell Motility and the Cytoskeleton* 32.3 (1995), pp. 173–186. DOI: 10.1002/cm.970320303.

[125] A. M. Bogdanov, E. I. Kudryavtseva, and K. A. Lukyanov. "Anti-Fading Media for Live Cell GFP Imaging." In: *PLoS ONE* 7.12 (2012), pp. 1–4. DOI: 10.1371/journal.pone.0053004.

[126] U. V. Nagerl, K. I. Willig, B Hein, S. W. Hell, and T Bonhoeffer. "Live-cell imaging of dendritic spines by STED microscopy." In: *Proceedings of the National Academy of Sciences of the United States of America* 105.48 (2008), pp. 18982–7. DOI: 10.1073/pnas.0810028105.

[127] J Tonnesen and U. V. Nagerl. "Two-color STED imaging of synapses in living brain slices." In: *Nanoimaging*. Ed. by A. A. Sousa and M. J. Kruhlak. Vol. 950. Methods in Molecular Biology. Totowa, NJ: Humana Press, 2013. Chap. 5, pp. 65–80. DOI: 10.1007/978-1-62703-137-0.

[128] K. I. Willig, H. Steffens, C. Gregor, A. Herholt, M. J. Rossner, and S. W. Hell. "Nanoscopy of filamentous actin in cortical dendrites of a living mouse." In: *Biophysical journal* 106.1 (2014), pp. L01–3. DOI: 10.1016/j.bpj.2013.11.1119.

[129] E. D'Este, D. Kamin, F. Gottfert, A. El-Hady, and S. W. Hell. "STED Nanoscopy Reveals the Ubiquity of Subcortical Cytoskeleton Periodicity in Living Neurons." In: *Cell reports* (2015), pp. 1246–1251. DOI: 10.1016/j.celrep.2015.02.007.

[130] K. T. Takasaki, J. B. Ding, and B. L. Sabatini. "Live-cell superresolution imaging by pulsed STED two-photon excitation microscopy." In: *Biophysical journal* 104.4 (2013), pp. 770–7. DOI: 10.1016/j.bpj.2012.12.053.

[131] D. Wildanger, E. Rittweger, L. Kastrup, and S. W. Hell. "STED microscopy with a supercontinuum laser source." In: *Optics express* 16.13 (2008), pp. 9614–21.

[132] G. Donnert, J. Keller, R. Medda, M. A. Andrei, S. O. Rizzoli, R. Lührmann, R. Jahn, C. Eggeling, and S. W. Hell. "Macromolecular-scale resolution in biological fluorescence microscopy." In: *Proceedings of the National Academy of Sciences of the United States of America* 103.31 (2006), pp. 11440–5. DOI: 10.1073/pnas.0604965103.

[133] G. Donnert, C. Eggeling, and S. W. Hell. "Triplet-relaxation microscopy with bunched pulsed excitation." In: *Photochemical & Photobiological Sciences* 8.4 (2009), p. 481. DOI: 10.1039/b903357m.

[134] G. Donnert. "Dual-colour STED-microscopy on the Nanoscale Confocal STED +." PhD thesis. Ruperto-Carola University of Heidelberg, 2007.

[135] S. Waldchen, J. Lehmann, T. Klein, S. Van De Linde, and M. Sauer. "Light-induced cell damage in live-cell super-resolution microscopy." In: *Scientific Reports* 5 (2015), pp. 1–12. DOI: 10.1038/srep15348.

[136] M Dyba and S. W. Hell. "Focal Spots of Size λ/23 Open Up Far-Field Florescence Microscopy at 33 nm Axial Resolution." In: *Physical Review Letters* 88.16 (2002), p. 163901. DOI: 10.1103/PhysRevLett.88.163901.

[137] G Vicidomini, A Schonle, H Ta, K. Y. Han, G Moneron, C Eggeling, and S. W. Hell. "STED nanoscopy with time-gated detection: theoretical and experimental aspects." In: *PloS one* 8.1 (2013), e54421. DOI: 10.1371/journal.pone.0054421.

[138] M. Castello, G. Tortarolo, I. C. Hernández, P. Bianchini, M. Buttafava, G. Boso, A. Tosi, A. Diaspro, and G. Vicidomini. "Gated-sted microscopy with subnanosecond pulsed fiber laser for reducing photobleaching." In: *Microscopy Research and Technique* 79.9 (2016), pp. 785–791. DOI: 10.1002/jemt.22716.

[139] B. R. Rankin, G Moneron, C. a. Wurm, J. C. Nelson, A Walter, D Schwarzer, J Schroeder, D. a. Colón-Ramos, and S. W. Hell. "Nanoscopy in a living multicellular organism expressing GFP." In: *Biophysical journal* 100.12 (2011), pp. L63–5. DOI: 10.1016/j.bpj.2011.05.020.

[140] G Moneron and S. W. Hell. "Two-photon excitation STED microscopy." In: *Optics express* 17.17 (2009), pp. 14567–73.

[141] J. B. Ding, K. T. Takasaki, and B. L. Sabatini. "Supraresolution imaging in brain slices using stimulated-emission depletion two-photon laser scanning microscopy." In: *Neuron* 63.4 (2009), pp. 429–37. DOI: 10.1016/j.neuron.2009.07.011.

[142] I. Coto Hernández, M. Castello, L. Lanzanò, M. D'Amora, P. Bianchini, A. Diaspro, and G. Vicidomini. "Two-Photon Excitation STED Microscopy with Time-Gated Detection." In: *Scientific Reports* 6.1 (2016), p. 19419. DOI: 10.1038/srep19419.

[143] G Vicidomini, I. C. Hernández, M D'Amora, F. C. Zanacchi, P Bianchini, and A Diaspro. "Gated CW-STED microscopy: a versatile tool for biological nanometer scale investigation." In: *Methods (San Diego, Calif.)* 66.2 (2014), pp. 124–30. DOI: 10.1016/j.ymeth.2013.06.029.

[144] M Dyba and S. W. Hell. "Photostability of a fluorescent marker under pulsed excited-state depletion through stimulated emission." In: *Applied optics* 42.25 (2003), pp. 5123–9.

[145] W. R. Zipfel, R. M. Williams, and W. W. Webb. "Nonlinear magic: multiphoton microscopy in the biosciences." In: *Nature biotechnology* 21.11 (2003), pp. 1369–77. DOI: 10.1038/nbt899.

[146] P. Bethge, R. Chéreau, E. Avignone, G. Marsicano, and U. V. Nägerl. "Two-photon excitation STED microscopy in two colors in acute brain slices." In: *Biophysical journal* 104.4 (2013), pp. 778–85. DOI: 10.1016/j.bpj.2012.12.054.

[147] I Coto Hernandez, M D'Amora, A Diaspro, and G Vicidomini. "Influence of laser intensity noise on gated CW-STED microscopy." In: *Laser Physics Letters* 11.9 (2014), p. 095603. DOI: 10.1088/1612-2011/11/9/095603.

[148] T. A. Klar, S. Jakobs, M. Dyba, A. Egner, and S. W. Hell. "Fluorescence microscopy with diffraction resolution barrier broken by stimulated emission." In: *Proceedings of the National Academy of Sciences* 97.15 (2000), pp. 8206–8210. DOI: 10.1073/pnas.97.15.8206.

[149] E Rittweger, K. Y. Han, S. E. Irvine, C Eggeling, and S. W. Hell. "STED microscopy reveals crystal colour centres with nanometric resolution." In: *Nature Photonics* 3.3 (2009), pp. 144–147. DOI: 10.1038/nphoton.2009.2.

[150] C. Wang, A. Fukazawa, M. Taki, Y. Sato, T. Higashiyama, and S. Yamaguchi. "A Phosphole Oxide Based Fluorescent Dye with Exceptional Resistance to Photobleaching: A Practical Tool for Continuous Imaging in STED Microscopy." In: *Angewandte Chemie - International Edition* 54.50 (2015), pp. 15213–15217. DOI: 10.1002/anie.201507939.

[151] C. Wang, M. Taki, Y. Sato, A. Fukazawa, T. Higashiyama, and S. Yamaguchi. "Super-Photostable Phosphole-Based Dye for Multiple-Acquisition Stimulated Emission Depletion Imaging." In: *Journal of the American Chemical Society* 139.30 (2017), pp. 10374–10381. DOI: 10.1021/jacs.7b04418.

[152] S. Hell, S. Jakobs, and L. Kastrup. "Imaging and writing at the nanoscale with focused visible light through saturable optical transitions." In: *Applied Physics A: Materials Science & Processing* 77.7 (2003), pp. 859–860. DOI: 10.1007/s00339-003-2292-4.

[153] T. Grotjohann. "Generation of Novel Photochromic GFPs: Fluorescent Probes for RESOLFT-type Microscopy at Low Light Intensities." PhD thesis. Georg-August-Universitat Gottingen, 2012.

[154] A Chmyrov, J Keller, T Grotjohann, M Ratz, E D'Este, S Jakobs, C Eggeling, and S. W. Hell. "Nanoscopy with more than 100,000 'doughnuts'." In: *Nature methods* 10.8 (2013), pp. 737–40. DOI: 10.1038/nmeth.2556.

[155] E Auksorius, B. R. Boruah, C Dunsby, P. M. P. Lanigan, G Kennedy, M. A. A. Neil, and P. W. French. "Stimulated emission depletion microscopy with a supercontinuum source and

fluorescence lifetime imaging." In: *Optics letters* 33.2 (2008), pp. 113–5.

[156] J. M. Dudley and S Coen. "Supercontinuum generation in photonic crystal fiber." In: *Reviews of Modern Physics* 78.4 (2006), pp. 1135–1184. DOI: 10.1103/RevModPhys.78.1135.

[157] J. M. Dudley, L Provino, N Grossard, H Maillotte, R. S. Windeler, B. J. Eggleton, and S Coen. "Supercontinuum generation in air-silica microstructured fibers with nanosecond and femtosecond pulse pumping." In: *Journal of the Optical Society of America B* 19.4 (2002), p. 765. DOI: 10.1364/JOSAB.19.000765.

[158] A. note 28. *Supercontinuum Generation in SCG-800 Photonic Crystal Fiber*. Tech. rep. Newport Corporation Technology and Applications Center, 2006.

[159] S Galiani, B Harke, G Vicidomini, G Lignani, F Benfenati, A Diaspro, and P Bianchini. "Strategies to maximize the performance of a STED microscope." In: *Optics express* 20.7 (2012), pp. 7362–74.

[160] C. A. Wurm, D Neumann, R Schmidt, A Egner, and S Jakobs. *Live Cell Imaging*. Ed. by D. B. Papkovsky. Vol. 591. Methods in Molecular Biology. Totowa, NJ: Humana Press, 2010, pp. 185–199. DOI: 10.1007/978-1-60761-404-3.

[161] R. F. Laine, A. Albecka, S. Van De Linde, E. J. Rees, C. M. Crump, and C. F. Kaminski. "Structural analysis of herpes simplex virus by optical super-resolution imaging." In: *Nature Communications* 6 (2015), pp. 1–10. DOI: 10.1038/ncomms6980.

[162] P. G. Haydon and G. Carmignoto. "Astrocyte Control of Synaptic Transmission and Neurovascular Coupling." In: *Physiological Reviews* 86.3 (2006), pp. 1009–1031. DOI: 10.1152/physrev.00049.2005.

[163] S. M. Lee, T. H. Nguyen, K. Na, I. J. Cho, D. H. Woo, J. E. Oh, C. J. Lee, and E. S. Yoon. "Nanomechanical measurement of astrocyte stiffness correlated with cytoskeletal maturation." In: *Journal of Biomedical Materials Research - Part A* 103.1 (2015), pp. 365–370. DOI: 10.1002/jbm.a.35174.

[164] A. Panatier, D. T. Theodosis, J. P. Mothet, B. Touquet, L. Pollegioni, D. A. Poulain, and S. H. R. Oliet. "Glia-Derived d-Serine Controls NMDA Receptor Activity and Synaptic Memory." In: *Cell* 125.4 (2006), pp. 775–784. DOI: 10.1016/j.cell.2006.02.051.

[165] S. H. R. Oliet, R. Piet, and D. A. Poulain. "Control of Glutamate Clearance and Synaptic Efficacy by Glial Coverage of Neurons." In: *Science* 292.5518 (2001), pp. 923–926. DOI: 10.1126/science.1059162.

[166] U. Pannasch and N. Rouach. "Emerging role for astroglial networks in information processing : from synapse to behavior." In: *Trends in Neurosciences* 36.7 (2013), pp. 405–417. DOI: 10.1016/j.tins.2013.04.004.

[167] O. A. Bayraktar, L. C. Fuentealba, A. Alvarez-Buylla, and D. H. Rowitch. "Astrocyte development and heterogeneity." In: *Cold Spring Harbor Perspectives in Biology* 7.1 (2015). DOI: 10.1101/cshperspect.a020362.

[168] M. C. Shearer and J. W. Fawcett. "The astrocyte/meningeal cell interface - A barrier to successful nerve regeneration?" In: *Cell and Tissue Research* 305.2 (2001), pp. 267–273. DOI: 10.1007/s004410100384.

[169] H. Zong, R. G. Verhaak, and P. Canoll. "The cellular origin for malignant glioma and prospects for clinical advancements." In: *Expert Review of Molecular Diagnostics* 12.4 (2012), pp. 383–394. DOI: 10.1586/erm.12.30. arXiv: NIHMS150003.

[170] M. Artesi et al. "Connexin 30 expression inhibits growth of human malignant gliomas but protects them against radiation therapy." In: *Neuro-Oncology* 17.3 (2015), pp. 392–406. DOI: 10.1093/neuonc/nou215.

[171] F Princen, P Robe, D Gros, T Jarry-Guichard, J Gielen, M. P. Merville, and V Bours. "Rat gap junction connexin-30 inhibits proliferation of glioma cell lines." In: *Carcinogenesis* 22.3 (2001), pp. 507–513.

[172] S. Etienne-Manneville. "Microtubules in cell migration." In: *Annual review of cell and developmental biology* 29 (2013), pp. 471–99. DOI: 10.1146/annurev-cellbio-101011-155711. arXiv: arXiv:1011.1669v3.

[173] M. Haber, L. Zhou, and K. K. Murai. "Cooperative Astrocyte and Dendritic Spine Dynamics at Hippocampal Excitatory Synapses." In: *Journal of Neuroscience* 26.35 (2006), pp. 8881–8891. DOI: 10.1523/JNEUROSCI.1302-06.2006.

[174] A. Koulakoff, P. Ezan, and C. Giaume. "Neurons control the expression of connexin 30 and connexin 43 in mouse cortical astrocytes." In: *Glia* 56.12 (2008), pp. 1299–1311. DOI: 10.1002/glia.20698.

[175] D. Pesen and J. H. Hoh. "Micromechanical Architecture of the Endothelial Cell Cortex." In: *Biophysical Journal* 88.1 (2005), pp. 670–679. DOI: 10.1529/biophysj.104.049965.

[176] Q. Luo, D. Kuang, B. Zhang, and G. Song. "Cell stiffness determined by atomic force microscopy and its correlation with cell motility." In: *Biochimica et Biophysica Acta - General Subjects* 1860.9 (2016), pp. 1953–1960. DOI: 10.1016/j.bbagen.2016.06.010.

[177] D. A. Fletcher and R. D. Mullins. "Cell mechanics and the cytoskeleton." In: *Nature* 463.7280 (2010), pp. 485–492. DOI: 10.1038/nature08908.

[178] H. Ouyang et al. "Contribution of cytoskeletal elements to the axonal mechanical properties." In: *Journal of Biological Engineering* 7.1 (2013), p. 21. DOI: 10.1186/1754-1611-7-21.

[179] T. D. Pollard and G. G. Borisy. "Cellular motility driven by assembly and disassembly of actin filaments." In: *Cell* 112.4 (2003), pp. 453–465. DOI: 10.1016/S0092-8674(03)00120-X.

[180] T. J. Mitchison and L. P. Cramer. "Actin-based cell motility and cell locomotion." In: *Cell* 84.3 (1996), pp. 371–379. DOI: 10.1016/S0092-8674(00)81281-7.

[181] G. J. Doherty and H. T. McMahon. "Mediation, Modulation, and Consequences of Membrane-Cytoskeleton Interactions." In: *Annual Review of Biophysics* 37.1 (2008), pp. 65–95. DOI: 10.1146/annurev.biophys.37.032807.125912.

[182] H. Yang, A. Ganguly, and F. Cabral. "Inhibition of cell migration and cell division correlates with distinct effects of microtubule inhibiting drugs." In: *Journal of Biological Chemistry* 285.42 (2010), pp. 32242–32250. DOI: 10.1074/jbc.M110.160820.

[183] A. Ganguly, H. Yang, R. Sharma, K. D. Patel, and F. Cabral. "The role of microtubules and their dynamics in cell migration." In: *Journal of Biological Chemistry* 287.52 (2012), pp. 43359–43369. DOI: 10.1074/jbc.M112.423905.

[184] J. V. Small, I. Kaverina, O. Krylyshkina, and K. Rottner. "Cytoskeleton cross-talk during cell motility." In: *FEBS Letters* 452.1-2 (1999), pp. 96–99. DOI: 10.1016/S0014-5793(99)00530-X.

[185] M. F. Carlier, J. Pernier, P. Montaville, S. Shekhar, and S. Kühn. "Control of polarized assembly of actin filaments in cell motility." In: *Cellular and Molecular Life Sciences* 72.16 (2015), pp. 3051–3067. DOI: 10.1007/s00018-015-1914-2.

[186] A. F. Hussain, M. Amoury, and S. Barth. "SNAP-tag technology: a powerful tool for site specific conjugation of therapeutic and imaging agents." In: *Current pharmaceutical design* 19.30 (2013), pp. 5437–42.

[187] E. Dere, M. A. De Souza-Silva, C. Frisch, B. Teubner, G. Söhl, K. Willecke, and J. P. Huston. "Connexin30-deficient mice show increased emotionality and decreased rearing activity in the open-field along with neurochemical changes." In: *European Journal of Neuroscience* 18.3 (2003), pp. 629–638. DOI: 10.1046/j.1460-9568.2003.02784.x.

[188] C. Frisch, M. Theis, M. A. De Souza Silva, E. Dere, G. Söhl, B. Teubner, K. Namestkova, K. Willecke, and J. R. Huston. "Mice with astrocyte-directed inactivation of connexin43 exhibit increased exploratory behaviour, impaired motor capacities, and changes in brain acetylcholine levels." In: *European Journal of Neuroscience* 18.8 (2003), pp. 2313–2318. DOI: 10.1046/j.1460-9568.2003.02971.x.

[189] S. E. Lutz, Y. Zhao, M. Gulinello, S. C. Lee, C. S. Raine, and C. F. Brosnan. "Deletion of astrocyte connexins 43 and 30 leads to a dysmyelinating phenotype and hippocampal CA1 vacuolation." In: *The Journal of neuroscience : the official journal of the Society for Neuroscience* 29.24 (2009), pp. 7743–52. DOI: 10.1523/JNEUROSCI.0341-09.2009. arXiv: NIHMS150003.

[190] R Bernard, I. A. Kerman, R. C. Thompson, E. G. Jones, W. E. Bunney, J. D. Barchas, A. F. Schatzberg, R. M. Myers, H Akil, and S. J. Watson. "Altered expression of glutamate signaling, growth factor, and glia genes in the locus coeruleus of patients with major depression." In: *Molecular Psychiatry* 16.6 (2011), pp. 634–646. DOI: 10.1038/mp.2010.44.

[191] C. Ernst, C. Nagy, S. Kim, J. P. Yang, X. Deng, I. C. Hellstrom, K. H. Choi, H. Gershenfeld, M. J. Meaney, and G. Turecki. "Dysfunction of astrocyte connexins 30 and 43 in dorsal lateral prefrontal cortex of suicide completers." In: *Biological Psychiatry* 70.4 (2011), pp. 312–319. DOI: 10.1016/j.biopsych.2011.03.038.

[192] A. Boudaoud, A. Burian, D. Borowska-Wykręt, M. Uyttewaal, R. Wrzalik, D. Kwiatkowska, and O. Hamant. "FibrilTool, an ImageJ plug-in to quantify fibrillar structures in raw microscopy images." In: *Nature Protocols* 9.2 (2014), pp. 457–463. DOI: 10.1038/nprot.2014.024.

[193] C.-Y. Liu, H.-H. Lin, M.-J. Tang, and Y.-K. Wang. "Vimentin contributes to epithelial-mesenchymal transition cancer cell mechanics by mediating cytoskeletal organization and focal adhesion maturation." In: *Oncotarget* 6.18 (2015), pp. 15966–15983. DOI: 10.18632/oncotarget.3862.

[194] L.-S. Z. Rathje, N. Nordgren, T. Pettersson, D. Ronnlund, J. Widengren, P. Aspenstrom, and A. K. B. Gad. "Oncogenes induce a vimentin filament collapse mediated by HDAC6 that is linked to cell stiffness." In: *Proceedings of the National Academy of Sciences* 111.4 (2014), pp. 1515–1520. DOI: 10.1073/pnas.1300238111.

[195] S. P. Chaki, R. Barhoumi, M. E. Berginski, H. Sreenivasappa, A. Trache, S. M. Gomez, and G. M. Rivera. "Nck enables directional cell migration through the coordination of polarized membrane protrusion with adhesion dynamics." In: *Journal of*

Cell Science 126.7 (2013), pp. 1637–1649. DOI: 10.1242/jcs.119610.

[196] S. Memmel et al. "Migration pattern, actin cytoskeleton organization and response to PI3K-, mTOR-, and Hsp90-inhibition of glioblastoma cells with different invasive capacities." In: *Oncotarget* 8.28 (2017), pp. 45298–45310. DOI: 10.18632/oncotarget.16847.

[197] G. S. Kaminski Schierle, S van de Linde, M Erdelyi, E. K. Esbjörner, T Klein, E Rees, C. W. Bertoncini, C. M. Dobson, M Sauer, and C. F. Kaminski. "In situ measurements of the formation and morphology of intracellular β-amyloid fibrils by super-resolution fluorescence imaging." In: *Journal of the American Chemical Society* 133.33 (2011), pp. 12902–5. DOI: 10.1021/ja201651w.

[198] C. L. Masters, G Simms, N. a. Weinman, G Multhaup, B. L. McDonald, and K Beyreuther. "Amyloid plaque core protein in Alzheimer disease and Down syndrome." In: *Proceedings of the National Academy of Sciences of the United States of America* 82.12 (1985), pp. 4245–9.

[199] S Ahmed. "Nanoscopy of cell architecture: The actin-membrane interface." In: *Bioarchitecture* 1.1 (2011), pp. 32–38. DOI: 10.4161/bioa.1.1.14799.

[200] S. G. Bolder, L. M. C. Sagis, P. Venema, and E. D. Van Linden. "Thioflavin T and birefringence assays to determine the conversion of proteins into fibrils." In: *Langmuir* 23.8 (2007), pp. 4144–4147. DOI: 10.1021/la063048k.

[201] F. T. Chan, D. Pinotsi, S. Gabriele, K. Schierle, and C. F. Kaminski. "Structure-Specific Intrinsic Fluorescence of Protein Amyloids Used to Study their Kinetics of Aggregation." In: *Bio-nanoimaging*. Elsevier, 2014, pp. 147–155. DOI: 10.1016/B978-0-12-394431-3.00013-4.

[202] C. M. Dobson. "Protein folding and misfolding." In: *Nature* 426.6968 (2003), pp. 884–90. DOI: 10.1038/nature02261.

[203] D. Pinotsi, A. K. Buell, C. Galvagnion, C. M. Dobson, G. S. Kaminski Schierle, and C. F. Kaminski. "Direct observation of heterogeneous amyloid fibril growth kinetics via two-color super-resolution microscopy." In: *Nano letters* 14.1 (2014), pp. 339–45. DOI: 10.1021/nl4041093.

[204] G. S. Kaminski Schierle, M. Sauer, and C. F. Kaminski. "Probing Amyloid Aggregation and Morphology In Situ by Multiparameter Imaging and Super-Resolution Fluorescence Microscopy." In: *Bio-nanoimaging*. Elsevier, 2014, pp. 105–120. DOI: 10.1016/B978-0-12-394431-3.00010-9.

[205] C. H. Michel, S Kumar, D Pinotsi, A Tunnacliffe, P St George-Hyslop, E Mandelkow, E.-M. Mandelkow, C. F. Kaminski, and G. S. Kaminski Schierle. "Extracellular monomeric tau protein is sufficient to initiate the spread of tau protein pathology." In: *The Journal of biological chemistry* 289.2 (2014), pp. 956–67. DOI: 10.1074/jbc.M113.515445.

[206] T Staudt, M. C. Lang, R Medda, J Engelhardt, and S. W. Hell. "2,2'-thiodiethanol: a new water soluble mounting medium for high resolution optical microscopy." In: *Microscopy research and technique* 70.1 (2007), pp. 1–9. DOI: 10.1002/jemt.20396.

[207] C. E. Boott, R. F. Laine, P. Mahou, J. R. Finnegan, E. M. Leitao, S. E. Webb, C. F. Kaminski, and I. Manners. "In Situ Visualization of Block Copolymer Self-Assembly in Organic Media by Super-Resolution Fluorescence Microscopy." In: *Chemistry - A European Journal* 21.51 (2015), pp. 18539–18542. DOI: 10.1002/chem.201504100.

[208] N. Rouach, A. Koulakoff, V. Abudara, K. Willecke, and C. Giaume. "Hippocampal Synaptic Transmission." In: *Science (New York, N.Y.)* 322.December (2008), pp. 1551–1555. DOI: 10.1126/science.1164022.

[209] U. Pannasch, L. Vargova, J. Reingruber, P. Ezan, D. Holcman, C. Giaume, E. Sykova, and N. Rouach. "Astroglial networks scale synaptic activity and plasticity." In: *Proceedings of the National Academy of Sciences* 108.20 (2011), pp. 8467–8472. DOI: 10.1073/pnas.1016650108. arXiv: arXiv:1408.1149.

[210] N. T. Urban, K. I. Willig, S. W. Hell, and U. V. Nägerl. "STED nanoscopy of actin dynamics in synapses deep inside living brain slices." In: *Biophysical journal* 101.5 (2011), pp. 1277–84. DOI: 10.1016/j.bpj.2011.07.027.

[211] U. Pannasch, J. Sibille, and N. Rouach. "Dual Electrophysiological Recordings of Synaptically-evoked Astroglial and Neuronal Responses in Acute Hippocampal Slices." In: *Journal of Visualized Experiments* 69 (2012), pp. 1–8. DOI: 10.3791/4418.

[212] F Gottfert, C. a. Wurm, V Mueller, S Berning, V. C. Cordes, A Honigmann, and S. W. Hell. "Coaligned dual-channel STED nanoscopy and molecular diffusion analysis at 20 nm resolution." In: *Biophysical journal* 105.1 (2013), pp. L01–3. DOI: 10.1016/j.bpj.2013.05.029.

COLOPHON

This document was typeset using the typographical look-and-feel `classicthesis` developed by André Miede. The style was inspired by Robert Bringhurst's seminal book on typography "*The Elements of Typographic Style*". `classicthesis` is available for both LaTeX and LyX:

https://bitbucket.org/amiede/classicthesis/

Final Version as of March 1, 2018 (`classicthesis` version 1).